MECHANOCHEMICAL

SYNTHESIS AND MODIFICATION

OF SPIN CROSSOVER MATERIALS

JED HUGH ASKEW

A thesis submitted to the University of Kent in partial fulfilment of
the requirements for the degree of
Doctor of Philosophy at University of Kent

University of Kent
Canterbury
Kent
CT2 7NH

December 2019

Declaration

I declare that the work described herein was carried out at the University of Kent between September 2016 and September 2019 under the supervision of Dr. H. J. Shepherd and Dr. S. J. Holder. Unless stated otherwise, all work is my own and has not been submitted previously for a degree at this or any other university.

Jed H. Askew

X.

Abstract

Spin crossover (SCO) is a phenomenon of some first-row transition metal complexes in which magnetic, optical, and structural properties change as a result of external stimuli. The change in properties is induced by the switching between high-spin (HS) and low-spin (LS) states. Prediction of the presence of SCO-activity is difficult. Therefore, discovery of novel SCO materials requires synthesis of a wide variety of potential SCO-active candidates. Traditional SCO synthesis is done by standard solution-state techniques, which are time consuming and have no guarantee of obtaining a SCO-active material at the end. The pursuit of novel SCO-active materials is therefore extremely slow. Mechanochemistry is an alternative synthetic technique which has recently begun to be applied to a variety of different fields, driven by the extremely short reaction times, alternative reaction products and the ever-increasing importance of green chemistry. The short reaction times make mechanochemistry an ideal solution to synthesis of novel SCO materials.

This study explores the application of mechanochemical synthesis to SCO research for the first time, investigating the viability of the synthetic route for obtaining SCO materials (chapter 2). The known SCO complexes $Fe(phen)_2(NCS)_2$, $[Fe(Htrz)_3](BF_4)_2$, $[Fe(atrz)_3]SO_4$, $Fe(4-phpy)_2[Ni(CN)_4]$ and $Fe(pz)[Au(CN)_2]_2$ were successfully synthesised using mechanochemical techniques. In general, SCO was more gradual, and shifted to a slightly lower temperature with a decrease in hysteresis, as seen in $Fe(phen)_2(NCS)_2$, $Fe(4-phpy)_2[Ni(CN)_4]$ and $Fe(pz)[Au(CN_2)_2$. However, the SCO properties of mechanochemical and solution-state synthesised $[Fe(atrz)_3]SO_4$ were indistinguishable. Further, mechanochemical synthesis of $[Fe(Htrz)_3](BF_4)_2$ yielded a polymorphic mixture.

Additional investigation of the differences in properties between mechanochemical and solution-state synthetic products was undertaken in Chapter 3 and showed the effects of mechanochemical synthesis are not straightforward. Mechanochemical synthesis of both $[Fe(atrz)_3]SO_4$ and $Fe(pz)[Au(CN)_2]_2$ yielded particle sizes smaller than solution-state synthesis, but the transition temperature and SCO properties of only $Fe(pz)[Au(CN)_2]_2$ were effected. Mechanochemical synthesis of $[Fe(atrz)_3](BF_4)_2$ yielded a previously observed but uncharacterised

polymorph. Comparison between manual grinding and ball-milling for different time durations yielded the same product with relatively insignificant differences in SCO properties.

Further application of mechanochemical techniques such as solid-state metathesis, were investigated as alternative synthetic routes within mechanochemical synthesis, Chapter 4, and was used to successfully exchange chloride anions for both bromide and iodide in the complex $[Fe(atrz)_3]Cl_2$. The anion exchange was undertaken by post-synthetic grinding of $[Fe(atrz)_3]Cl_2$ and NaX (where X = Br and I). Further exchange attempts were undertaken using $NaBF_4$, NaSCN and $NaReO_4$ yielded products which underwent partial exchange.

A screening protocol was devised, tested, and optimised for the identification of both thermochromic and non-thermochromic SCO-active materials prepared by mechanochemistry, Chapter 5. The different analytical techniques used for routine analysis of SCO materials were assessed for their speed, cost and the information they can provide, in an attempt to address the change in the rate-limiting step that occurs through the rapid synthesis of materials using mechanochemistry.

Publications and Presentations

Publications:

Mechanochemical Synthesis of Cooperative Spin Crossover Materials. J. H. Askew and H. J. Shepherd, *Chem Comm*, **2018**, 54, p.180-183

Post-synthetic anion-exchange in iron(II) 1,2,4-triazole based spin crossover materials via mechanochemistry. J. H. Askew and H. J. Shepherd, *Dalton Trans,* **2020**, 49, p 2966-2971

Exploring the effects of Synthetic and Post-synthetic grinding on the properties of the spin crossover material [Fe(atrz)$_3$](BF$_4$)$_2$. J. H. Askew, D. M. Pickup, G. O. Lloyd, A. V. Chadwick, H. J. Shepherd, *In Preparation*.

Oral Presentations:

'Mechanochemical Modification of 1,2,4-Triazole Based Spin Crossover Materials' – School of Physical Sciences Postgraduate Colloquium, 2018

'Mechanochemical Synthesis and Post-synthetic Modification of Spin Crossover Materials' – Functional Materials Group Meeting, 2018

Poster Presentations:

'Mechanochemical Modification of 1,2,4-Triazole Based Spin Crossover Materials' – SpinOn Workshop 2018: Multi-Functional Magnetic Materials

'Simple Synthesis of Colour-Changing Compounds' – University of Kent Postgraduate Festival 2018 – Award Received

'Mechanochemical Synthesis of Spin Crossover Materials' – School of Physical Sciences Postgraduate Colloquium, 2017

'Mechanochemical Synthesis of Spin Crossover Materials' – 13th International Conference of Materials Chemistry (MC13), 2017

Acknowledgements

Final thanks go to my parents and sisters for continually supporting me and for making the holidays a much-needed break from the struggles of work. Without their support for the last 25 years of my life, none of this would have been possible. Thank you.

Abbreviations

$\Delta E°_{HL}$ – Difference in energy between high spin and low spin states

Δ_{oct} – Ligand Field splitting energy

ΔT – Difference in temperature between $T_{1/2}\uparrow$ and $T_{1/2}\downarrow$

° – Degrees

Å – Angstroms

AFM – Atomic force microscopy

CCD – Charge coupled device

dc – Direct current

DSC – Differential scanning calorimetry

HS – High spin state

HS* – Metastable high spin state

K – Kelvin

K_B – Boltzmann constant

LAG – Liquid assisted grinding

LCW – Lithographically controlled wetting

LFT – Ligand field theory

LIESST – Light-induced excited spin state trapping

LS – Low spin state

MO – Molecular orbital

M_w – Molecular weight

P – Spin pairing energy

PXRD – Powder X-ray diffraction

Reverse-LIESST – Reverse Light-induced excited spin state trapping

Rf – Radio frequency

SCO – Spin crossover

SQUID – Super conducting quantum interference device

T - Temperature

T(LIESST) – Temperature in which the HS* state relaxes

$T_{1/2}\uparrow$ - Temperature in which 50% of the metal sites are in the HS and LS states on heating

$T_{1/2}\downarrow$ - Temperature in which 50% of the metal sites are in the HS and LS states on cooling

TEM – Transmission electron microscopy

T_g – Glass transition temperature

TGA – Thermogravimetric Analysis

VT Raman – Variable temperature Raman spectroscopy

α - Alpha

β - Beta

γ_{HS} – High spin fraction

η – Ratio between mass of materials and solvent added

θ – Angle of diffraction

$X_M T$ – Molar magnetic susceptibility.

Ligands

Ligand	Abbreviation
1,10'-phenanthroline	phen
2,2'-bipyridyl	bipy
4,4'-dinonyl-2,2'-bipyridyl	Nonyl-bipy
4,7-dimethyl-1,10'-phenanthroline	Me-phen
4,7-diphenyl-1,10'-phenathroline	Ph-phen
4-amino-4H-1,2,4-triazole	atrz
1H-1,2,4-triazole	Htrz
4-phenylpyradine	4-phpy
5,5'-dimethyl-2,2'-bipyridyl	Me-bipy
thiocyanate	NCS
tri(1-pyrazolyl)borohydride	$[HB(pz)_3]$
tri(3,5-dimethyl-1-pyrazolyl)borohydride	$[HB(3,5\text{-dimethyl-pz})_3]$
pyrazine	pz
2,6-bis(1H-pyrazol-3-yl)pyridine	3bpp
2,2'-(pyridine-2,6-diylbis(1*H*-pyrazole-5,3'diyl)diphenol	3bpp-PhOH
2,6-bis(3-(2-methoxyphenyl)-1H-pyrazol-5-yl)pyridine	$3bpp\text{-PhOCH}_3$
2,6-bis(3-(naphthalen-2-yl)-1H-pyrazol-5-yl)pyridine	3-bpp-Napth

List of Sample Names

Compound **1-Mech**: [Fe(phen)$_3$](SCN)$_2$ (Mechanically synthesised)

Compound **1-Heat**: [Fe(phen)$_2$(NCS)$_2$] (Thermolysis)

Compound **1-Wash**: [Fe(phen)$_2$(NCS)$_2$] (Washed)

Compound **2-Mech**: [Fe(Htrz)$_3$](BF$_4$)$_2$ (Mechanically synthesised)

Compound **2-Dried**: [Fe(Htrz)$_3$](BF$_4$)$_2$ (Oven Dried)

Compound **2-Sol**: [Fe(Htrz)$_3$](BF$_4$)$_2$ (Solution Synthesised)

Compound **3-Mech**: [Fe(atrz)$_3$]SO$_4$ (Mechanically synthesised)

Compound **3-Dried**: [Fe(atrz)$_3$]SO$_4$ (Oven Dried)

Compound **3-Wash**: [Fe(atrz)$_3$]SO$_4$ (Washed)

Compound **3-Sol**: [Fe(atrz)$_3$]SO$_4$ (Solution Synthesised)

Compound **4-Mech**: Fe(4-phpy)$_2$[Ni(CN)$_4$] (Mechanically synthesised)

Compound **4-LAG**: Fe(4-phpy)$_2$[Ni(CN)$_4$] (Liquid Assisted Grinding)

Compound **4-Sol**: Fe(4-phpy)$_2$[Ni(CN)$_4$] (Solution Synthesised)

Compound **5-Mech**: Fe(pz)[Au(CN)$_2$]$_2$ (Mechanically synthesised)

Compound **5-Sol**: Fe(pz)[Au(CN)$_2$]$_2$ (Solution Synthesised)

Compound **6-Sol**: [Fe(atrz)$_3$](BF$_4$)$_2$ (Solution synthesised)

Compound **6-Mech**: [Fe(atrz)$_3$](BF$_4$)$_2$ (Mechanically synthesised)

Compound **6-BM10**: [Fe(atrz)$_3$](BF$_4$)$_2$ (Ball milled for 10 minutes)

Compound **6-BM90**: [Fe(atrz)$_3$](BF$_4$)$_2$ (Ball milled for 90 minutes)

Compound **7**: [Fe(atrz)$_3$]Cl$_2$ (Mechanically synthesised)

Compound **7-Cl**: [Fe(atrz)$_3$]Cl$_2$ (SSM with NaCl)

Compound **7-Br**: [Fe(atrz)$_3$]Cl$_2$ (SSM with NaBr) – Likely [Fe(atrz)$_3$]Br$_2$

Compound **7-I**: [Fe(atrz)$_3$]Cl$_2$ (SSM with NaI) – Likely [Fe(atrz)$_3$]I$_2$

Compound **7-F**: [Fe(atrz)$_3$]Cl$_2$ (SSM with NaF) – Likely [Fe(atrz)$_3$]Cl$_2$

Screening Samples:

S1: Fe(BF$_4$)$_2$.6H$_2$O + Htrz

S2: FeCl$_2$.4H$_2$O + Htrz

S3: FeSO$_4$.7H$_2$O + Htrz

S4: $(NH_4)_2Fe(SO_4)_2.6H_2O$ + Htrz

S5: $Fe(BF_4)_2.6H_2O$ + atrz

S6: $FeCl_2.4H_2O$ + atrz

S7: $FeSO_4.7H_2O$ + atrz

S8: $(NH_4)_2Fe(SO_4)_2.6H_2O$ + atrz

S9-1pot: $[Fe(phen)_3](SCN)_2$ (prepared using 1-pot synthesis)

S9-1pot-Heat: $Fe(phen)_2(NCS)_2$ (prepared using 1-pot synthesis then thermally converted)

S9-2pot: $[Fe(phen)_3](SCN)_2$ (prepared using 2-pot synthesis)

S10-As: Homoleptic Ph-phen (As Synthesised)

S10-Heat: Homoleptic Ph-phen (Heated to 150°C for 10hrs)

S11-As: Homoleptic Me-phen (As Synthesised)

S11-Heat: Homoleptic Me-phen (Heated to 150°C for 10hrs)

S12-As: Homoleptic bipy (As Synthesised)

S12-Heat: Homoleptic bipy (Heated to 150°C for 10hrs)

S13-As: Homoleptic Me-bipy (As Synthesised)

S13-Heat: Homoleptic Me-bipy (Heated to 150°C for 10hrs)

S14-As: Homoleptic Nonyl-bipy (As Synthesised)

S14-Heat: Homoleptic Nonyl-bipy (Heated to 150°C for 10hrs)

S15-As: Heteroleptic bipy + Me-bipy (As synthesised)

S15-Heat: Heteroleptic bipy + Me-bipy (Heated to 150°C for 10hrs)

S16-As: Heteroleptic bipy + Nonyl-bipy (As synthesised)

S16-Heat: Heteroleptic bipy + Nonyl-bipy (Heated to 150°C for 10hrs)

S17-As: Heteroleptic Me-bipy + Nonyl-bipy (As synthesised)

S17-Heat: Heteroleptic Me-bipy + Nonyl-bipy (Heated to 150°C for 10hrs)

S18-As: $Fe(BF_4)_2.6H_2O$ + $K[HB(pz)_3]$ (As synthesised)

S18-Sublim: $Fe(BF_4)_2.6H_2O$ + $K[HB(pz)_3]$ (Purified by sublimation)

S19-As: $Fe(BF_4)_2.6H_2O$ + $K[HB(3,5-dimethyl-pz)_3]$ (As synthesised)

S19-Sublim: $Fe(BF_4)_2.6H_2O$ + $K[HB(3,5-dimethyl-pz)_3]$ (Purified by sublimation)

S20-As: $Fe(BF_4)_2.6H_2O$ + $K[HB(pz)_3]$ + $K[HB(3,5-dimethyl-pz)_3]$ (As synthesised)

S20-Sublim: $Fe(BF_4)_2.6H_2O$ + $K[HB(pz)_3]$ + $K[HB(3,5\text{-dimethyl-pz})_3]$ (Purified by sublimation)

S21-BF$_4$: Homoleptic 3-bpp + $Fe(BF_4)_2.6H_2O$

S21-Cl: Homoleptic 3bpp + $FeCl_2.4H_2O$

S21-SO$_4$: Homoleptic 3bpp + $(NH_4)_2Fe(SO_4)_2.6H_2O$

S21-C$_2$O$_4$: Homoleptic 3bpp + $FeC_2O_2.xH_2O$

S22-BF$_4$: Homoleptic 3-bpp-PhOH + $Fe(BF_4)_2.6H_2O$

S22-Cl: Homoleptic 3bpp-PhOH + $FeCl_2.4H_2O$

S22-SO$_4$: Homoleptic 3bpp-PhOH + $(NH_4)_2Fe(SO_4)_2.6H_2O$

S22-C$_2$O$_4$: Homoleptic 3bpp-PhOH + $FeC_2O_2.xH_2O$

S23-BF$_4$: Homoleptic 3-bpp-PhOCH$_3$ + $Fe(BF_4)_2.6H_2O$

S23-Cl: Homoleptic 3bpp-PhOCH$_3$ + $FeCl_2.4H_2O$

S23-SO$_4$: Homoleptic 3bpp-PhOCH$_3$ + $(NH_4)_2Fe(SO_4)_2.6H_2O$

S23-C$_2$O$_4$: Homoleptic 3bpp-PhOCH$_3$ + $FeC_2O_2.xH_2O$

S24-BF$_4$: Homoleptic 3-bpp-Napth + $Fe(BF_4)_2.6H_2O$

S24-Cl: Homoleptic 3bpp-Napth + $FeCl_2.4H_2O$

S24-SO$_4$: Homoleptic 3bpp-Napth + $(NH_4)_2Fe(SO_4)_2.6H_2O$

S24-C$_2$O$_4$: Homoleptic 3bpp-Napth + $FeC_2O_2.xH_2O$

S25: Heteroleptic 3-bpp + 3-bpp-PhOH

S26: Heteroleptic 3-bpp + 3-bpp-PhOCH$_3$

S27: Heteroleptic 3-bpp + 3-bpp-Napth

S28: Heteroleptic 3-bpp-PhOH + 3-bpp-PhOCH$_3$

S29: Heteroleptic 3-bpp-PhOH + 3-bpp-Napth

S30: Heteroleptic 3-bpp-PhOCH$_3$ + 3-bpp-Napth

Table of Contents

Chapter 1: Introduction

1.1. Introduction to Spin Crossover

1.1.1. Ligand Field Theory

Ligand field theory (LFT) is used to describe the bonding in coordination complexes. It is a branch of molecular orbital theory (MO) used to explain the properties of transition metal complexes, providing insight into bonding, complex reactivity and structural factors.[1] Transition metal ions have five d-orbitals which are considered energetically degenerate in spherical ligand fields, when the ligand field is not symmetrical the relative energies of each orbital changes depending on its proximity to those ligands. The geometry of transition metal complexes is therefore important, with significant differences in energy for the different d-orbitals, where electrons in the d-orbitals orientated towards the ligand will be raised in energy and electrons in d-orbitals directed between ligands will be lowered in energy. A representative example of this effect is shown in Figure 1.1 for a transition metal complex with an octahedral ligand field. The total energy of the system in an octahedral ligand field, when all orbitals are occupied, does not change from that of the spherical field case.
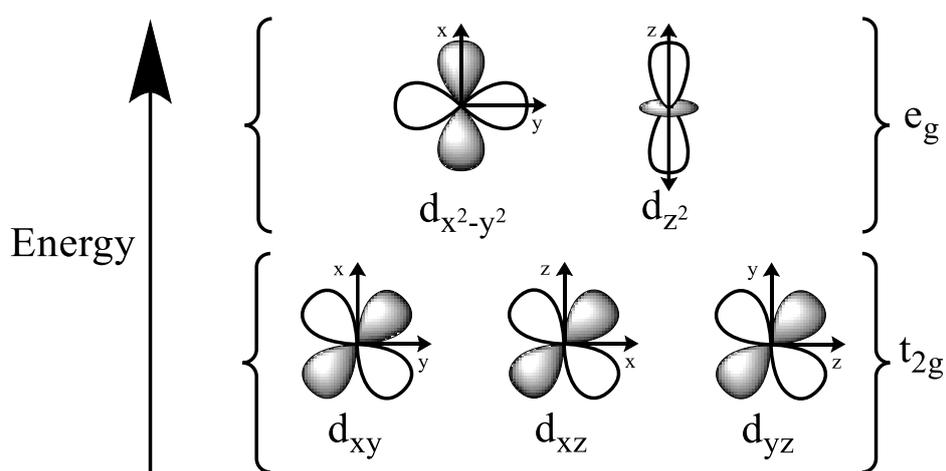
Figure 1.1: The orientation of the d-orbitals for transition metals in an octahedral configuration.

In an octahedral field, ligands are located at the vertices of an octahedron centred on a transition metal centre, as shown in Figure 1.2. Ligands are considered as negative point charges

9

which repel electrons in orbitals that point directly towards them, which increases the energy of these orbitals. As a result, the d-orbitals are split into two sub-sets of degenerate orbitals denoted e_g and t_{2g}. The d_{xy}, d_{xz} and d_{yz} orbitals are orientated between the axes and thus are not pointed towards ligands, therefore they are lower in energy and are described by the symmetry label t_{2g}. The remaining $d_{z^2-y^2}$ and d_{z^2} orbitals are in orientated directly towards ligands, and thus experience electron-electron repulsion from electrons present in the ligands. As such, they are higher in energy and denoted by the symmetry label e_g. The different energy levels are discussed relative to the barycentre, which is described as the proposed energy of the ligand field when the negative charge contribution from the ligands is distributed in a sphere around the transition metal, rather than in localised point charges as described for octahedral ligand fields.
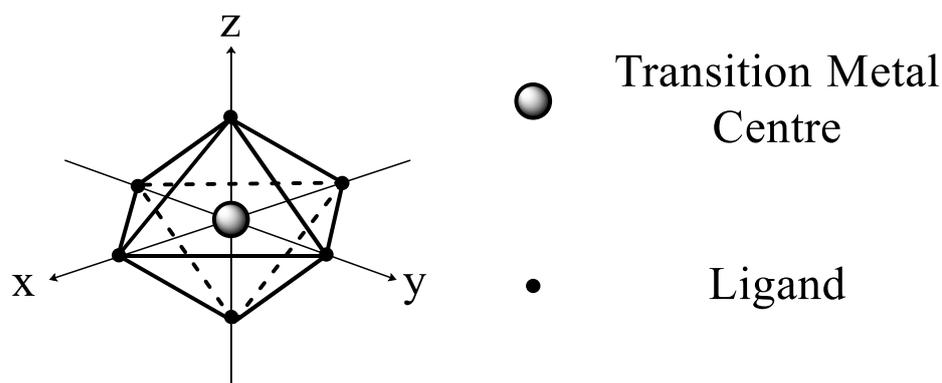
Figure 1.2: Transition metal centre with an octahedral ligand field geometry.

The difference in energy between the t_{2g} and e_g orbitals in an octahedral field are described by the ligand field splitting energy, denoted Δ_{oct}. Factors affecting Δ_{oct} include the specific transition metal centre used, oxidation state and the ligand. For a given metal centre, the strength of Δ_{oct} changes systematically with the ligand as described by the spectrochemical series. Weak field ligands, such as SCN^- and Cl^-, result in low Δ_{oct} and strong field ligands, such as CN^- and CO, have large Δ_{oct}.

MO bonding orbitals are formed by interactions between neighbouring atomic orbitals. When the orbitals have the correct symmetry and are in-phase, they interact and undergo constructive interference forming bonding orbitals. The energy of electron-occupied molecular bonding

orbitals is lower than the corresponding energy of the separate atoms, as shown in Figure 1.3(a). If the orbitals are out-of-phase, then destructive interference occurs. The destructive interference between the out-of-phase atomic orbitals cancels the amplitude of wave function and forms a nodal plane perpendicular to the atom-atom axis, as shown in Figure 1.3(b). Electrons are unable to occupy the nodal plane between atoms and therefore occupy higher energy locations, with increased energy relative to separate atoms, as shown in Figure 1.3(a). If the orbitals do not have the correct symmetry they will not interact or change in energy, they are known as non-bonding orbitals.
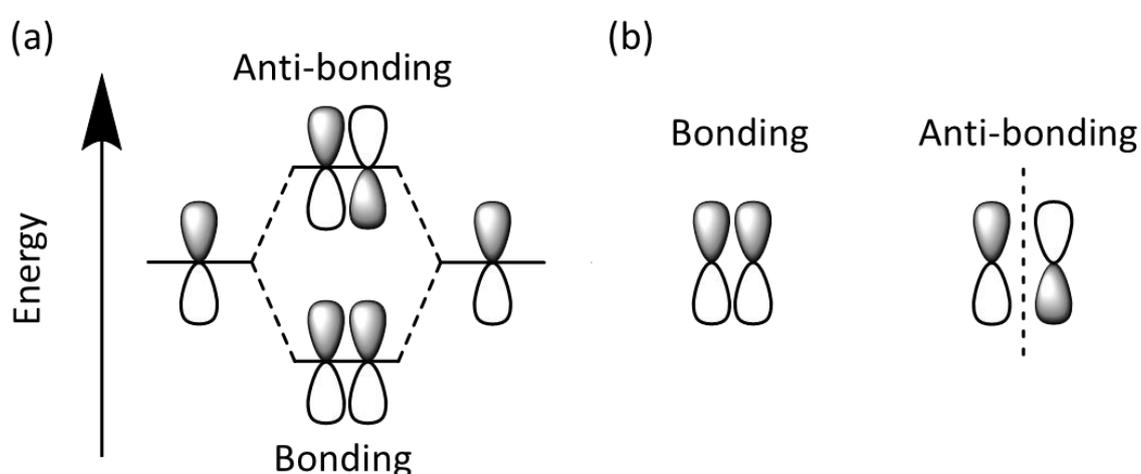
Figure 1.3: (a) Interaction between two p-orbitals with differences in phase identified by differences in colour, denoting bonding and antibonding interactions as a function of energy. (b) The interactions between two p-orbitals with nodal plane identified by a dashed line.

σ-bonding and π-bonding represent two bonding motifs between molecular orbitals. σ-bonding occurs when there is no nodal plane parallel to the atom-atom axis, therefore strong interactions occur. π-bonding occurs with one or more nodal planes in the atom-atom axis, which form weaker interactions than in σ-bonding. Representative examples of σ- and π-bonding using p-orbitals are shown in Figure 1.4, however the formation of σ- and π- bonding can occur between many different orbitals, not only the p-orbitals.
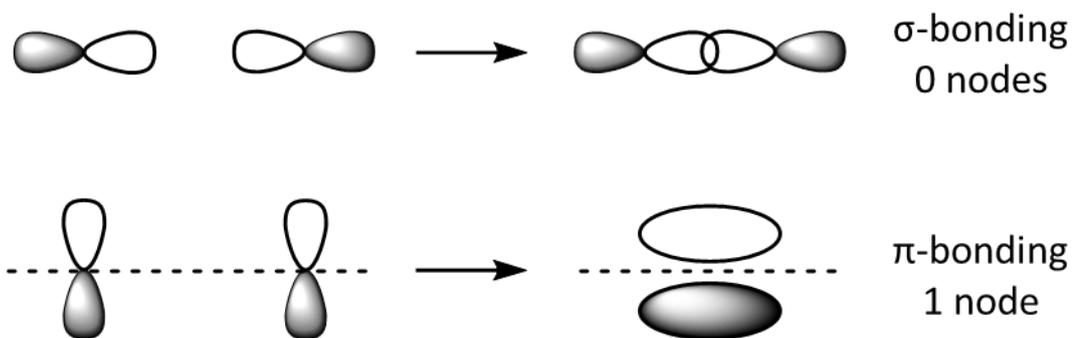
Figure 1.4: Examples of σ-bonding and π-bonding between p-orbitals, with nodal planes denoted by dashed lines.

The distribution of electrons in d-orbitals is determined by two factors, Δ_{oct} as described above and the spin-pairing energy (P). The spin-pairing energy represents the amount of energy associated with paired electrons sharing an orbital. In cases where Δ_{oct} is larger than P, the d-orbitals are filled according to the Aufbau Principle, in which the t_{2g} orbitals are completely filled before the higher energy e_g orbitals, giving the minimum spin multiplicity. However, in instances where Δ_{oct} is smaller than P, the d-orbitals are filled according to Hund's rules. Whereby both the t_{2g} and e_g orbitals are singly occupied before spin-pairing occurs, this gives the maximum spin multiplicity. For metal ions with d^4-d^7 electron configuration, two different ground state electronic configurations can occur, denoted high spin (HS) and low spin (LS). These states have the maximum and minimum spin multiplicity, respectively. The HS and LS electronic configurations for a d^6 metal ion are presented in Figure 1.5. According to the Russell-Saunders notation, the electronic ground state terms for the LS and HS states are $^1A_1$ and $^5T_{2g}$ respectively.
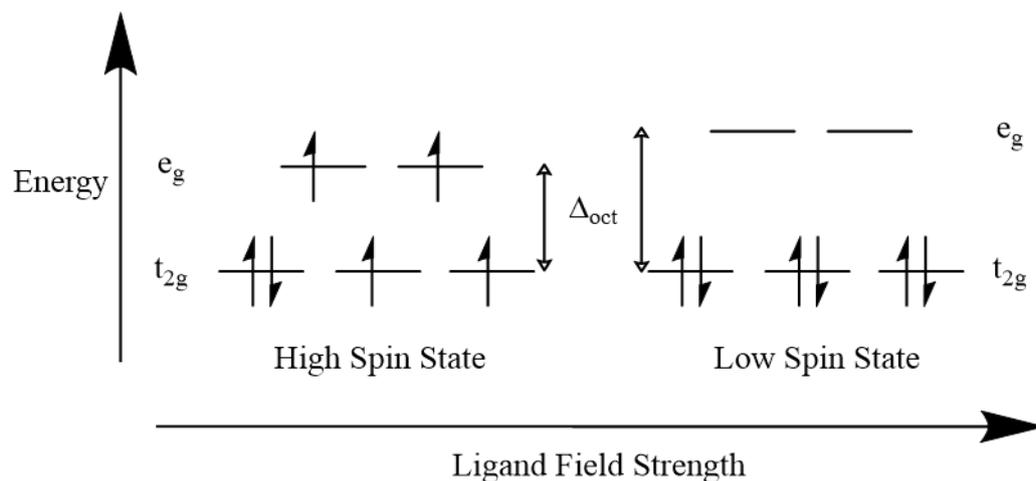
Figure 1.5: Distribution of electrons in *d*-orbitals for d^6 metal ions in the high spin and low spin states, denoting increasing Δ_{oct} with increasing ligand field strength.

The two spin states have several significant differences in properties, including changes in magnetic, structural and optical properties. The larger number of unpaired electrons in the HS state leads to a larger magnetic moment, compared to the LS state. This difference is exemplified in d^6 metal ions, whereby the HS state has four unpaired electrons resulting in a spin-only magnetic moment of 4.8 BM and the LS state has no unpaired electrons and therefore is diamagnetic. The structural differences are induced by consideration of molecular orbital theory. The t_{2g} orbitals are considered largely non-bonding and the e_g orbitals are anti-bonding. As such, the increased occupation of the e_g orbitals in the HS state weaken, and therefore lengthen, the metal-ligand bond.[2] Octahedral complexes with Fe(II) and N-donor ligands have Fe-N bond lengths of ~2.2 Å in the HS state and ~2.0 Å in the LS state, representing a significant difference of ~10% between spin states.[3] The structural differences between spin states can easily be observed by structural investigation techniques such as single crystal and powder X-ray diffraction.[4] Changes in optical properties arise due to the different electronic transitions possible in each spin state. Colour in transition metal complexes arises due to electron transition between energy levels, primarily within the d-orbitals. As such, changing the ground-state electron configuration modifies the spin-allowed electron transitions, resulting in a change in colour. The electronic transitions in *d*-orbitals are controlled by two selection rules; Laporte selection rule, which dictates that for centrosymmetric molecules, transitions between states with the same symmetry are forbidden[5]

and the spin selection rule, which states that no spin in spin multiplication can occur. In the HS state, the number of allowed electronic transitions decreases as a result of the spin selection rule. The optical properties are different in the HS and LS states. The ideal octahedral configuration is distorted in the HS state, which alters Δ_{oct} and changes the wavelength of absorbed light. Another change is an increase in the number of unpaired electrons. In accordance with Hund's Rule of maximum multiplicity all electrons in singly occupied orbitals have the same spin[6] and when considered with the spin selection rule, the HS state has fewer allowed transitions compared to the LS state. When considered together, both the change in Δ_{oct} and difference in allowed electron transitions lead to the HS and LS states having different optical properties.

1.1.2.   Spin Crossover Phenomenon

The spin crossover (SCO) phenomenon describes the change in spin state as a result of external stimuli, such as varying temperature,[7] pressure,[8] irradiating with light,[9] external magnetic field[10] and guest species effects.[11] SCO occurs when the difference in energy between the HS and LS states is sufficiently small to be overcome by changes in external energy. SCO has been observed for several first-row transition metal ions in octahedral complexes with d^4-d^7 electronic configuration. SCO-activity in complexes containing Fe(II), Fe(III), Co(II), Mn(II), Mn(III), Cr(II), Cr(III) and Ni(II) have all been reported, with the majority of reports for Fe(II), Fe(III) and Co(II) complexes.[12,13] The wide availability of Fe(II) salts, the relatively high stability of the resulting complexes under ambient conditions and d^6 transition metals representing the largest difference in properties between the HS and LS states, have resulted in Fe(II) complexes representing the largest proportion of reported SCO-active complexes.

The observation of SCO-activity was first reported by Cambi and Szegö in which they observed anomalous magnetic properties in a Fe(III) tris(dithiocarbamate)-based complex.[14] Initial studies of Co(II) complexes identified SCO-activity denoting the presence of so-called 'electronic isomers'.[15] The SCO phenomenon was not fully described until the term 'spin equilibrium', which was coined to describe the different spin states observed in Ni(II) complexes by Ballhausen *et*

al.,[16] was adopted to describe anomalous magnetic properties in SCO-active complexes. As previously discussed, Fe(II) complexes represent the majority of reported SCO-active materials. The initial reports of SCO-activity in Fe(II) complexes were made by Baker and Bonbonich[17] for the complexes $Fe(phen)_2(NCS)_2$, $Fe(phen)_2(NCSe)_2$ and $Fe(bipy)_2(NCS)_2$ (where phen = 1,10-phenathroline and bipy = 2,2'bypridine), the first of which has been researched extensively using a wide variety of techniques allowing for a thorough solid understanding of the SCO-phenomenon.[18–21]

Interest in SCO materials arise due to the possibility of switching between the HS and LS states and the changes in properties that occur as a result of the switch. The differences in magnetic, optical and structural properties and the occurrence of a transition between two spin states, within easily accessible temperature and pressure ranges, understandably commands a large interest for potential applications, as discussed in 1.1.6. Changes in dielectric constant also occur during SCO, the changing dielectric constant is an artefact of the changes in structure, a LS → HS transition leads to a distortion in local symmetry, which in turn causes a significant change in the dipole moment of the system.[22] This opens up potential applications in technology.

Synthesis of bulk SCO materials has typically been carried out *via* traditional solution state chemistry, although more complex techniques for the production of nanoparticles and thin films have been developed in the last decades, as discussed further in 1.1.7.[23,24] Remarkably, all existing techniques use solvents and can be time-consuming; often they require inert atmospheres and multiple synthetic steps. This aspect is particularly limiting in the search for novel SCO-active materials, due to long reaction times and difficulties in operating under inert conditions.

1.1.2.1.   Inducing Spin Crossover

Due to the relative ease of experimental protocols, a change in temperature is the most widely investigated stimulus for inducing SCO-activity. Thermal SCO occurs when the difference in energy between HS and LS states (ΔE°_{HL}) is approximately equal to ambient thermal energy ($k_B T$, where k_B represents the Boltzmann constant and T is temperature), as shown in Figure 1.6. The

extensive research into thermal-SCO has been extremely fruitful, with the foundations of SCO built on understanding of thermal-SCO activity. This has resulted in great strides towards technological applications of SCO materials, with many complexes that undergo SCO at temperatures around ambient temperature reported.[25,26] However, inducing SCO by other means can provide valuable insight into more fundamental aspects of SCO.
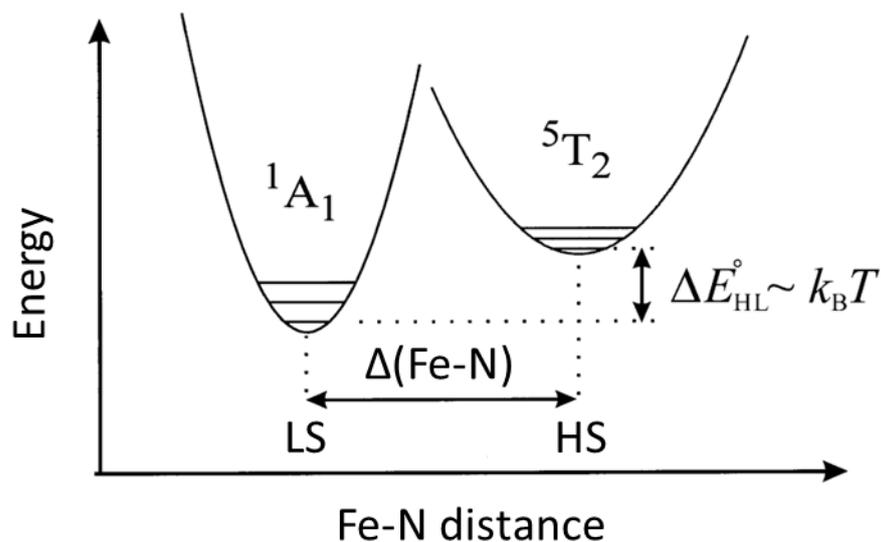
Figure 1.6: Potential wells for LS ($^1A_1$) and HS ($^5T_2$) states in Fe(II) SCO plotted as a function of Fe-N bond distance. The differences in energy between the HS and LS states is denoted $\Delta E°_{HL}$ with k_bT representing the difference in amount of heat between the two states. Adapted with permission from the Royal Society of Chemistry.[27]

Pressure-induced SCO has also been thoroughly investigated, with higher pressures favouring the LS state, by increasing the energy of the HS state, which in turn increases ΔE_{HL}.[8] This may be understood by considering the differences in volume between the LS and HS states. FeN$_6$ octahedral configurations have Fe-N bond lengths of ~2.0 Å and ~2.2 Å in the LS and HS states respectively, increasing the Fe-N bond length results in an increase in the total volume of the material during SCO. This volume for Fe(II) ion in an octahedral complex is expected to be $\approx$ 10 Å^3 in the LS state and $\approx$ 13 Å^3 for the HS state, which manifests at the macroscopic scale as a change in volume of the whole materials of between 1% and 10%.[3] Considering the smaller volume of the LS state, the LS state is expected to be stabilised whilst under high pressure. A representative

example of the stabilisation of the LS state at different pressures using the complex [Fe(hyptrz)$_3$](4-chlorophenylsulfonate).H$_2$O, (where hyptrz = 4-(3'-hydroxproyl)-1,2,4-triazole) is shown in Figure 1.7.[28] Investigation of pressure induced SCO is not a trivial process. The requirement of specialist equipment, such as diamond anvil pressure cells and modification of standard operating procedures significantly hamper accessibility.[8] Although pressure induced SCO can provide valuable insight into many properties and mechanisms behind SCO, pressure studies are not largely considered routine.
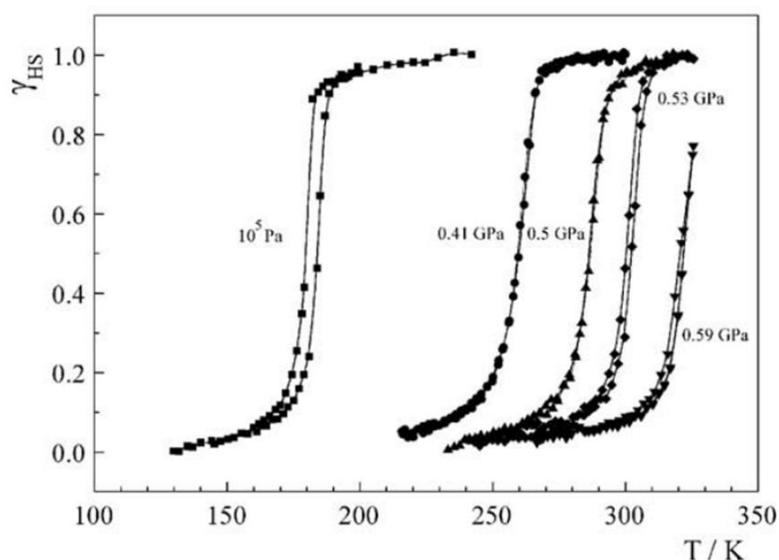
Figure 1.7: Plot of HS fraction (γ_{HS}) vs. temperature at different pressures for [Fe(hyptrz)$_3$](4-chlorophenylsulfonate).H$_2$O, reproduced with permission from reference.[28]

Additional approaches to inducing SCO include the use of hard and soft X-rays[29,30] and changes in external magnetic field,[10] the prospects of which are only beginning to be realised. Light-induced excited spin state trapping (LIESST) is another widely investigated process in which irradiation by light of specific wavelengths can induce the population of a meta-stable HS state (HS*) at low temperatures. LIESST has been observed in variety of complexes which undergo thermal SCO.[31,32] An example of a thermal SCO complex undergoing LIESST at low temperatures for the complex [Fe(dpp)$_2$(NCS)$_2$] (where dpp = dipyrido[3,2-a:2'.3'-c]phenazine), as shown in Figure 1.8.[33] The mechanism behind LIESST was proposed by Hauser *et al.*[34] in 1985. For Fe(II)

complexes, irradiation of a complex at low temperatures with specific wavelengths of light, often green for Fe(II), results in population of the $^1T_1$ energy level *via* spin-allowed excitations. Following this excitation are multiple intersystem crossings (radiationless decay) to the HS* and LS states. The HS* state can have significant relaxation times due the transition between HS* and LS state being spin-forbidden (in accordance to the spin selection rule), therefore the decay can only occur when the thermal barrier between the HS and LS states is overcome.[34] Relaxation of the HS* state at low temperatures can be induced by irradiation with light at a different wavelength, in a process known as reverse-LIESST.[9] As with pressure-induced SCO, experimental research into LIESST requires the use of specialist equipment, in order to irradiate with light at low temperatures, which is often not routinely found outside of specialist labs, which to some extent limits further exploration of the field. Further, a main limitation on the application of LIESST is the instability of the HS* state at high temperatures. The HS* relaxes into the LS state as temperature increases, the temperature in which the HS* relaxes is defined as T(LIESST).
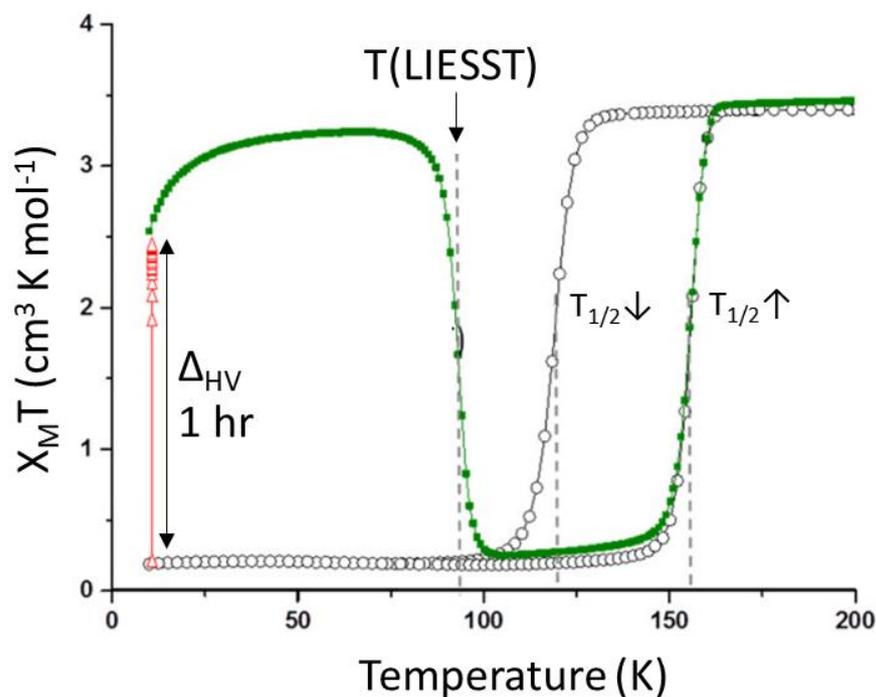
Figure 1.8: Magnetic susceptibility as a function of temperature for $Fe(dpp)_2(NCS)_2$, with thermal magnetic properties and shown for heating and cooling without irradiation (O) and after irradiation for 1 hour with T(LIESST) identified. Adapted under a creative commons' attribution-NonCommercial license from reference.[33]

1.1.3.   Classifying Spin Crossover Systems

The transition between LS and HS states is determined as the temperature in which the material consists of approximately equal part HS and LS sites. This is essentially the mid-point between a fully HS state and a fully LS state. This term is denoted $T_{1/2}\uparrow$ on heating and $T_{1/2}\downarrow$ on cooling, as shown in Figure 1.9(a). The difference in temperature between $T_{1/2}\uparrow$ and $T_{1/2}\downarrow$ characterises the thermal hysteresis in the transition temperature and is reported as ΔT. An additional metric that has been used to quantify the abruptness of transition is the 'smoothness'. 'Smoothness' is defined as the difference in temperature in which 20% (T_{20}) and 80% (T_{80}) of the material is in the HS state, as shown in Figure 1.9(b).[3] Simple characterisation of SCO properties using these metrics assists in characterisation of materials which can undergo more complex SCO-behaviour, such as stepped-transitions or incomplete transitions.
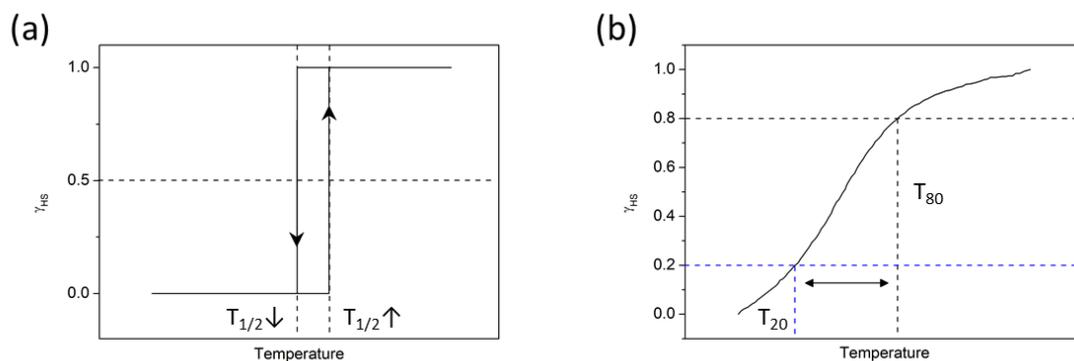
Figure 1.9: (a) Schematic representation of $T_{1/2}\uparrow$ and $T_{1/2}\downarrow$. (b) Schematic representation of the determination of 'smoothness' with the temperature in which 20% of the material in the HS state denoted by T_{20} and the temperature in which 80% of the material is in the HS state denoted by T_{80}.

SCO behaviour can be extremely complex but are generally described by five different characteristics, as illustrated in Figure 1.10. A gradual transition occurs when transition between fully LS and HS states occurs over a wide temperature range as a result of weak interactions between metal centres. Abrupt SCO occurs when a transition between LS and HS states happens over a short temperature range. Stepped transitions, as shown in Figure 1.10(c), can occur when one or more intermediate steps are present in the SCO transition. Stepped transitions can occur in mononuclear and polynuclear materials as a result of the interactions between the metal centres. In mononuclear scenarios, the LS to HS transition can modify the ligand environment of nearby metal centres thus potentially stabilising the LS state. This modification of the local ligand environment can be considered as a short-range interaction which is competing with the general long-range interactions.[35,36] This is evident in the complex [Fe(bapbpy)(NCS)$_2$] (where bapbpy = N6,N6'-di(pyridine-2-yl)-2,2'-bipyridine-6,6'-diamine), which undergoes a phase change resulting in stepped SCO with a HS-LS-LS intermediate phase[37] and the Fe(III) complex [Fe(lig)]ClO$_4$ (where lig = diimine product of N,N'-bis(2-aminoethyl)-1,3-propanediamine and 4,6-dimethoxysalicylaldehyde), which undergoes a symmetry-breaking spin-state stepped-transition with a LS-HS-HS intermediate phase.[38] Polynuclear systems can also undergo stepped SCO with the presence of distinct crystallographic sites with slightly different ligand environments causing different transition temperatures. An extreme example of this is the [Fe$_3$(saltz)$_6$(Pt(CN)$_4$)$_3$].8H$_2$O

system (where saltz = (E)-2-(((4H-1,2,4-triazol-4-yl)imino)methyl)phenyol)) which undergoes a 4-step transition.[39]

Incomplete transitions occur when a complex is unable to reach either a fully HS or fully LS state during SCO. This can occur by thermal spin state trapping, where the cooling rate kinetically traps the relaxation of the metal centre from a HS to LS state,[40] or by structural packing in which the transition to LS state of certain metal sites prevents the transition of other sites due to introduction of structural stress.[41] The final characteristic discussed is hysteresis which is an example of bistability. Hysteresis occurs when $T_{1/2}\uparrow$ is different to $T_{1/2}\downarrow$ and it is a result of cooperativity in the material. Spin crossover behaviour is often complex and can multiple present characteristics. Examples of each of the properties described above are presented in Figure 1.10, which was reproduced with permission from reference.[42]

(a) Gradual   (b) Abrupt   (c) Stepped

(d) Incomplete   (e) Hysteresis
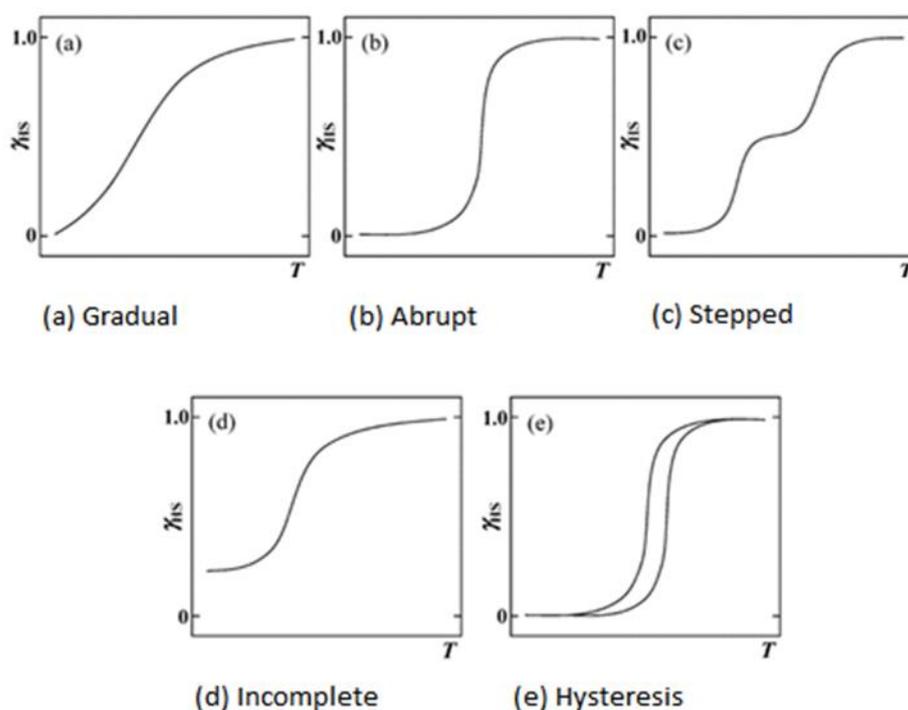
Figure 1.10: Schematic representation of different SCO types denoting HS fraction (γ_{HS}) vs temperature (a) Gradual, (b) Abrupt, (c) Stepped transition, (d) Incomplete and (e) Hysteresis. Reproduced with permission from reference.[42]

Abruptness of transition and ΔT are factors which are strongly dependent on cooperativity in the material. Cooperativity describes the interactions between metal sites, whereby a change in

environment at one metal site is propagated throughout the material as a result of electron-phonon coupling between SCO centres in the solid state through elastic and intermolecular interactions in the lattice.[27] The degree of cooperativity in a material is dependent on these interactions, including van der Waals forces, π-π stacking[43] and hydrogen bonding.[44] The propagation of SCO in a material has been attributed to an 'internal pressure' created by the changing bond lengths between the HS and LS states. The differences in bond lengths induces the formation of a point defect in the lattice which can cascade the transition across the entire matrix.[45,46] Simulations of the propagation of SCO in different particle shapes are presented in Figure 1.11, alongside experimental evidence supporting the modelling. Attempts to improve cooperativity in materials have been made by preparing materials with strong covalent interactions between metal centres in 1-, 2- and 3-dimensional coordination polymers such as: 4-R-1,2,4-triazole 1-dimensional polymers and 2- and 3- dimensional Hofmann-like clathrates.[47–49]
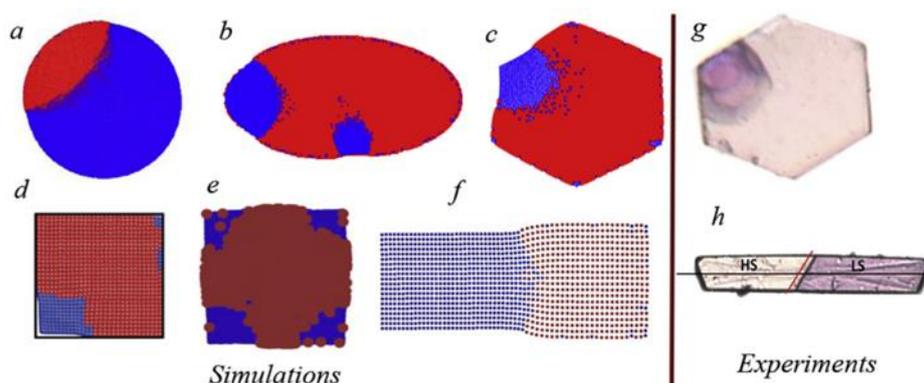
Figure 1.11: Schematic representations of the propagation of SCO. (a-f) simulations of the process in different shapes.[50–54] (g and h) experimental evidence supporting the simulated plots.[54,55] Reproduced with permission from reference.[56]

Further investigation of cooperativity in SCO materials include the use of metal dilution studies. Metal dilution studies seek to investigate the role of internal pressure in the propagation of SCO materials. The changing bonding lengths of the SCO-active metal centres are diluted with metals centres which are not SCO-active. This has the effect of dampening and reducing the internal pressure by preventing the formation of 'point defects' in the matrix. The most commonly used metal for this purpose is Zn(II), which does not undergo SCO-activity due to its d^{10}

electronic configuration. The effect of metal dilution is a decrease in transition completeness with

increasing residual HS fraction and a more gradual SCO, with $T_{1/2}\uparrow$ shifted to lower temperatures,

as shown for the system $[Fe_xNi_{1-x}(phen)_2(NCS)_2]$ in Figure 1.12.[41] This effects has been investigated

in multiple systems, ranging from 0-dimensional systems such as $[Fe_xZn_{1-x}(2\text{-pic})_3]Cl_2 \cdot EtOH$ (where

2-pic = 2-picolylamine)[57] to 3-dimensional coordination polymers such as the Hofmann-like

clathrate compound $[Fe_xNi_{1-x}(pz)][Pt(CN)_4]$ (where pz = pyrazine).[58]
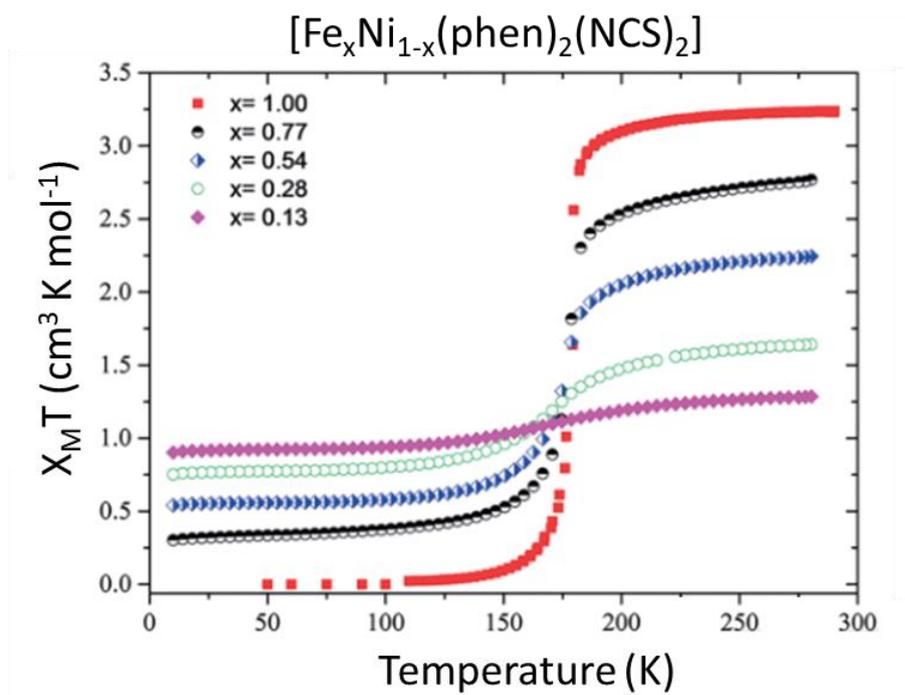
Figure 1.12: Plot of X_MT vs T for $[Fe_xNi_{1-x}(phen)_2(NCS)_2]$ (where phen = 1,10-phenanthroline) with varying degrees of metal dilution. Adapted with permission from reference.[41]

1.1.4. 'Run-in' Effect

The first heating cycle in a SCO-material is often different to resulting cycles due to an effect

known as 'run-in'. Multiple hypothesises have been proposed to describe the origin of this

difference, with a single conclusive description not yet realised.[59–61] Propositions such as the

release of crystalline strain and relaxation of the lattice during the first cycle could explain the

changing properties but experimental evidence supporting the theory is not widely reported.[60,61]

The release of minute quantities of adsorbed solvents and moisture from the material could also

present an explanation for the changing properties, due to the well characterised solvent effects on SCO properties.[62] However, the effect is not fully understood so far. As a result, the first cycle is often omitted from publication with the repeatable and consistent properties of subsequent cycling reported as the materials SCO properties. However, this can lead to inaccurate values for $T_{1/2}\uparrow$ and ΔT for some compounds in the literature.

The 'run-in' effect has been extensively investigated in the complex Fe[HB(pz)$_3$]$_2$, with a significant difference in the first cycle and subsequent cycling observed (>45 K difference). The 'run-in' effect presents itself as a large apparent first hysteresis. A first explanation of this effect was presented by Grandjean *et al* .[63] in which the first heating cycle and SCO transition caused an initial shattering of the microcrystalline sample in a self-grinding process. The initial shattering was consistent with previous literature reports on effects of grinding, which are discussed further in Chapter 3, whereby the transition temperature decreases and becomes more gradual. This theory is consistent with the observations of crystals shattering during SCO.[63] However, reinvestigation of the complex by Bousseksou *et al*.[64] proposed an alternative explanation, instead proposing the occurrence of an irreversible phase change in the first heating cycle. This instead attributes the change in SCO as a result of polymorphism in the sample. Although the Fe[HB(pz)$_3$]$_2$ complex presents an extreme example of the 'run-in' effect it serves to illustrate that the effect may be attributed to several different processes occurring simultaneously and the origin of changing properties in the first cycle may well be material dependent.

1.1.5. Spin Crossover-Active Fe(II) Materials

There are hundreds of known SCO-active Fe(II) materials in the literature including molecular coordination complexes, 1D coordination polymers and 2-/3-dimensional metal organic frameworks, with many novel complexes reported each year.[65,66] Discovery of novel materials is driven by the pursuit of materials with technologically useful properties, such as chemical stability and accessible temperatures of operation, as well as a fundamental understanding of the SCO process itself. Fe(II) SCO materials are often split into distinct families with variation of ligands

incrementally driving the discovery of novel materials. However, in most instances the FeN_6 octahedral configuration is present. Throughout this work, multiple different families of Fe(II) SCO complexes are investigated, including a particular focus on the 4-R-1,2,4-triazoles.

1.1.6. Applications of Spin Crossover Materials

The change in properties of a material resulting from SCO can be extremely significant. The differences in magnetic, optical and structural properties alongside secondary effects such as changing dielectric constant can all occur near or above ambient temperatures. This highlights why SCO materials have seen a surge in interest in recent years. The change in properties induced by SCO give rise to a number of potential applications in sensing,[67] data storage[68,69] and actuator technologies.[70,71]

The sensing aspect of SCO materials is not just limited to temperature sensing, although the use of gradual transitions spread over large temperature ranges could provide sensitive temperature measurements. SCO can also be induced by changes in pressure, which results in a stabilisation of the LS state that can allow visual identification of the increasing pressure, as proposed for the system $[Fe(Htrz)_2(trz)](BF_4)$.[72] Chemical sensing using SCO materials has also been proposed as a viable application, with solvent sensitivity resulting in solvatochromism effects.[73,74] This was proposed for the complex $[Fe_2(L)(CH_3CN)_4](BF_4)_4.2CH_3CN$ (where L = 4-(4-methylphenyl)-3-3(pyridazinyl)-5-pyridyl-4H-1,2,4-triazole), which displays clear colour changes when exposed to various different solvents, as shown in Figure 1.13.[75]
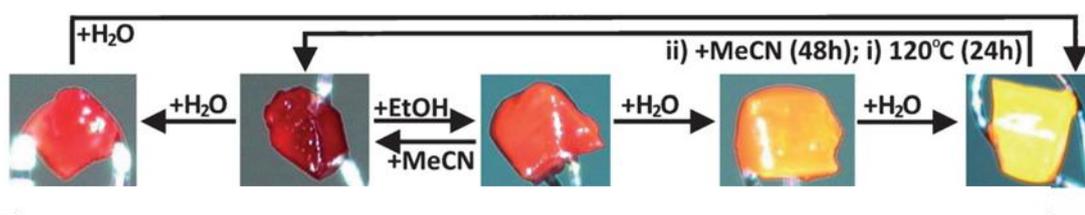
Figure 1.13: Summary of colour changes for $[Fe_2(L)(CH_3CN)_4](BF_4)_4.2CH_3CN$, when exposed to different solvents and conditions. Adapted with permission from reference.[75]

For application in data storage, a material must have two stable states which can be denoted as 'on' and 'off'. The materials must also retain the input state without constant power input, therefore an element of bistability must be present. Kahn et al.[76] explored the possibilities of applications in data storage for SCO materials. For technological applications, the proposed bistability should be sufficiently large enough to present stability in a range of operational temperatures. Kahn et al. proposed bistability of ≈ 50 K as sufficient. However, it has been suggested that for genuine applications a thermal hysteresis of 100 K within the range 253 – 353 K would be required.[68] The switching between states can be initiated by different approaches, depending on the device, with applications of LIESST and reverse-LIESST presenting an approach closest in line with current technologies. Currently, no SCO materials represent an ideal example for application in data storage. However, thermal hysteresis near room temperature has been observed in multiple complexes which represent substantial strides towards future applications.[65,76–78]

Application of SCO materials as molecular actuators is a viable potential application due to the relatively large increase in volume resulting from a LS to HS transition. The fundamental definition of an actuator is to convert a form of energy into kinetic energy. If harnessed, SCO materials could convert thermal, light, pressure and differences in external magnetic field strength into kinetic energy. In order to be an ideal material for molecular actuators, a material needs to be able to undergo reversible switching between states without significant loss of efficiency. As SCO occurs due to a change in spin state, they are not as susceptible to the same loss of efficiency as in materials which undergo chemical reactions as a result of external stimuli.[9] Application of SCO materials in the design and testing of micro- and nano- actuator systems has been carried out using two main techniques. The first of which is the use of single crystals of the corresponding SCO material coupled with an inert substance in a bilayer[70] and the second approach is to form composites of inert polymers doped with SCO-active substances in a similar bilayer architecture.[79,80] The use of a bilayers to amplify small volume changes into significant macroscopic motion have been classically used in materials with different thermal expansion

rates to induce a bend in the bilayer.[79] However, standard differences in thermal expansion rates and corresponding bending are small relative to the 5-13% volume changes possible with the use of SCO materials.[81]

1.1.7.   Nanoparticles and Thin Films

In the majority of potential technological applications of SCO materials, the need for smaller and smaller particle sizes is required for real-world applications, and great strides have been made to achieve this desired miniaturisation. Two avenues of extensive research are underway with focus on synthesis of nanoparticles and preparation of thin films in a controlled manner.[24,82] Synthesis of nanoparticles falls under one of two definitions. The top-down approach, in which bulk materials are broken down into smaller particles, and bottom-up, whereby nanoparticles are formed from smaller constituents. Top-down synthesis of nanoparticles requires physical processing of a solid-state starting material using techniques such as cutting, etching, grinding and lithographic techniques.[24,82] The effects these procedures would have on the SCO properties in a material are largely unrealised, with a consensus on the effects of grinding SCO materials is not yet met and further discussion is undertaken in Chapter 3.

The bottom-up approach requires controlled formation of particles, often in confined spaces, with limited quantities of precursors to control the growth of particles. The bottom-up approach often makes use of templating, such as hard templating using substances such as MOFs[67] and mesoporous silica[83] to control the growth inside pores, as well as soft templating through use of reverse micelle techniques[84] and small 'reactor' vesicles.[85] Template- and surfactant-free methods are also available, such as microfluidics[86] and spray drying.[87] One of the main advantages of using hard templating in nanoparticle synthesis is the possibility to control the particle shape, by altering the templating used, as evidenced by the formation of 1-D chains of SCO-active $[Fe(Htrz)_3](BF_4)_2.H_2O$ embedded in the channels of MCM-41, as shown in Figure 1.14(a).[83] However, one major difficulty in using hard templating techniques is preventing growth of the material outside of the desired pores which requires special consideration to overcome.[82]

Soft templating takes advantage of the many ways in which surfactants and self-assembling polymers can be used to confine growth of materials. One such approach, is the 'reverse micelle' technique which is done by preparing two different water-in-oil microemulsions, in which the reagents are dissolved in water. When combined, the Brownian motion merges pockets of water and the exchange of their contents creates microreactors. In instances where the products are insoluble in water, the product is removed from the microreactor thus preventing further growth. This approach has successfully been used to synthesis sub-50nm particles of $[Fe(atrz)_3]Br_2.3H_2O$.[88] A schematic representation of the use of vesicles for soft templating is shown in Figure 1.14(b).[82]
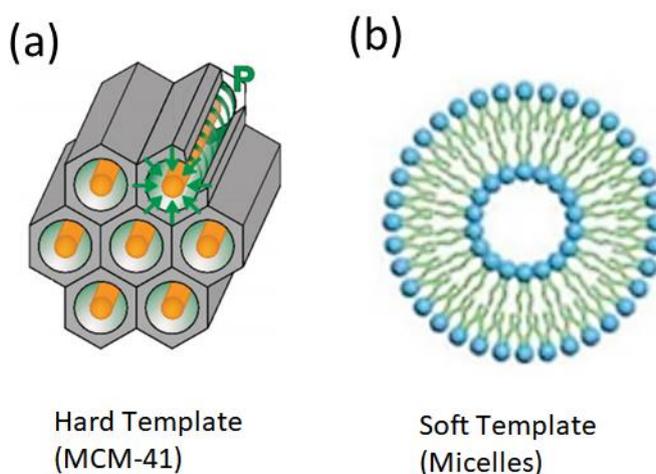
Figure 1.14: Schematic representation of templating nanoparticle growth. (a) Hard templating using MCM-41 (a form of mesoporous silica) in which nano-rods of $[Fe(Htrz)_3](BF_4)_2$ are shown in yellow. Adapted with permission from The Royal Society of Chemistry.[83] (b) Soft templating using vesicles. Adapted with permission from reference.[82]

Thin films represent an ideal approach for deposition of small quantities of materials over large surface areas, which are required for use in many applications.[24] Many techniques have been used to prepare thin films in research laboratories including: vacuum sublimation,[89,90] spin-coating,[91,92] drop casting[93] and multiple patterning approaches using lithographic techniques.[94] The SCO community has developed several families of materials which can exhibit SCO around ambient temperature with many displaying bistability.[65,76–78] Application of multiple methods to prepare thin-films have previously proved successful, such as high vacuum evaporation, which has been used to prepare $[Fe(phen)_2(NCS)_2]$ thin films, as shown in Figure 1.15(a). Various patterning

methods that are crucial for technological applications have also been applied, such as lithographically controlled wetting (LCW), a schematic representation of the procedure is shown in Figure 1.15(b), which was pioneered by Cavallini *et al* to pattern [Fe-(4'-(4'''-pyridyl)-1,2':6'1''-bis-(pyrazolyl) pyridine)$_2$] as shown in Figure 1.15(c). However, the effects of thin film production on the properties of SCO materials is not well understood. It is expected that cooperativity in the thin films will be different from bulk samples. Based on current literature reports general trends are observed but material dependent factors are prevalent, as discussed further in Chapter 3.
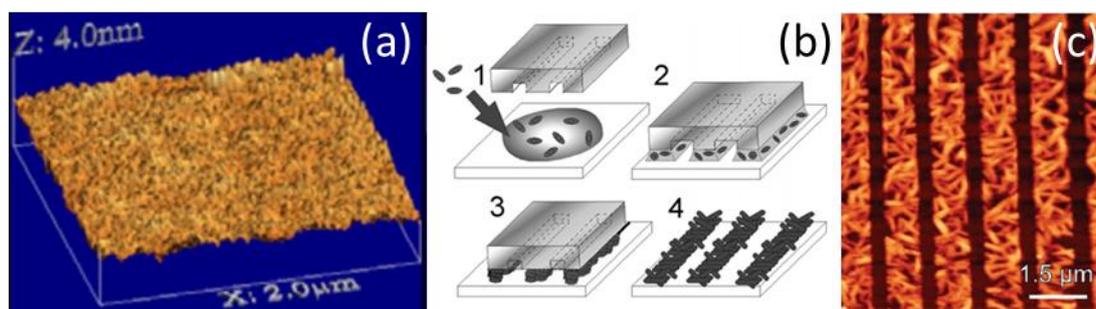
Figure 1.15: (a) AFM images of Fe(phen)$_2$(NCS)$_2$ thin film deposited with a thickness of 280 nm on silicon substrate by high vacuum evaporation. Adapted with permission from reference.[95] (b) Schematic representation of the lithographically controlled wetting (LCW) procedure. Reproduced with permission from reference.[96] (c) AFM morphology of [Fe-(4'-(4'''-pyridyl)-1,2':6'1''-bis-(pyrazolyl) pyridine)$_2$] strips prepared using LCW. Reproduced with permission from reference.[96]

Both nanoparticle and thin film synthesis have proved successful for SCO materials. But, one of the main limitations on applications in technology continues to be a lack of fundamental understanding of the factors affecting cooperativity and how to mitigate them in order to maintain bistability in these systems at lower particle sizes. For technological applications, a deeper understanding of these factors is required and work in this area represents a 'hot topic' for the SCO community.

1.2. Introduction to Mechanochemistry

Mechanochemistry refers to the reaction of materials through the application of mechanical energy, often through grinding in the solid state. While mechanochemistry has long been used in

the synthesis of inorganic materials and composites, in recent years it has also been applied in the synthesis of molecular systems, coordination complexes and frameworks, co-crystals, supramolecular networks and enzymes.[97,98] Mechanistic explanations for the success of the mechanochemical approach are numerous and as yet no single model can be applied to the varied range of systems that can be produced in this manner. One such explanation has been described as the "hot-spot" model[99] in which momentary pulses of significantly increased temperature and pressure are the driving force for mechanochemical reactions. A secondary explanation has also been put forward which has a similar approach, attributing the reaction to temperature and pressure conditions but this approach suggests the formation of momentarily plasma, this is known as the "magma-plasma" model.[97] Both approaches depend on point heating as a result of the grinding. However, it has been suggested that this is not necessarily the case, and in-situ temperature and powder X-ray diffraction studies have questioned both models.[100] Despite the mechanism behind mechanochemistry being not entirely understood, it is clear that the technique has the potential to produce both known and novel materials across diverse areas of chemistry, including spin crossover. In fact, mechanochemistry has been highlighted as one of the IUPAC "10 chemistry innovations that will change the world."[101]

Due to a relatively broad definition of mechanochemistry being 'chemical synthesis enabled or sustained by mechanical force',[102] a number of approaches to apply this mechanical energy have been employed. These range from manual grinding via pestle and mortar to various types of mills (such as planetary and ball mills)[103] and even sonochemical techniques, which supplies mechanical energy via ultrasound. Each milling approach has advantages and preferred applications. But many require the use of specialised equipment. Manual grinding via pestle and mortar is one method which does not require specialised equipment, as pestle and mortars are generally present in standard laboratories. This provides a low-cost approach to explore the application of mechanochemistry to new fields.

One of the major advantages of mechanochemical synthesis over standard synthetic techniques is the relatively short synthetic times. It has been shown that the same reactions can

be carried out by mechanochemical means with only a fraction of time required for the reaction to take place.[104] This makes mechanochemistry an ideal candidate for screening large combinations of varied reagents. Further advantages include the possibility of carrying out reactions completely solvent free. This is an incredibly important aspect is some fields, where solvent effects on the properties of materials are significant, such as in SCO research. This would allow the properties of completely solvent free products to be investigated, allowing for the fundamental effects of solvent presence to be investigated.

The application of mechanochemical synthesis to new fields is currently expanding substantially, with frequent reports of the technique being used in new and exciting ways. As such, certain aspects of the technique are not fully understood. One such aspect is a fundamental understanding of how reactions proceed under mechanochemical conditions, this could give rise to potential issues with reproducibility of results. Additionally, there is not a current standardised approach to undertaking mechanochemistry, with various different devices and equipment applied. Such as manual grinding, ball milling and twin-screw extrusion.[105,106] It is unclear thus far whether mechanochemical synthesis using one technique is comparable to another technique. These are certain problems which will likely be addressed with further research.

1.2.1. Liquid Assisted Grinding

One of the limiting factors of mechanochemistry is a potential lack of 'selectivity'. Although, a wide variety of conditions in standard 'neat grinding' can be modified and controlled, such as milling frequency, milling duration, energy input and container / pestle and mortar materials. The same degree of 'selectivity' available in standard solvent methods cannot readily be achieved by altering the conditions mentioned above. Liquid assisted grinding (LAG) is a potential avenue to achieve this desired selectivity.

LAG is a modification of the standard mechanochemical procedure in which sub-stoichiometric amounts of solvent are added to the reagents during grinding. The presence of small amounts of solvent, in volumes insufficient to dissolve significant quantities of reagents, has

been shown to accelerate mechanochemical reactions in addition to facilitating reactions not possible by 'neat' grinding.[97] The amount of solvent utilised in mechanochemical reactions is described by a variety of terms ranging from 'neat' grinding, 'slurry' and standard solution, as shown schematically in Figure 1.16. In order to be termed LAG, the ratio of solvent (μL) to weight of reactants (mg) known as η should be between 0-1 μL mg^{-1}.[103]

Figure 1.16: The η scale denoting type of reaction relative to solvent contribution, described using μL mg^{-1}.

LAG has seen extensive use in the screening of cocrystals and polymorphs in pharmaceuticals and chemical industries,[102] in part for the possibility of more efficient reactions with significantly reduced reaction times, but also for the possibility cleaner and potentially safer synthesis. The use of a minute quantity of solvent the reagents are not soluble in, may open avenues into introducing previously unseen solvent effects in materials. This could have significant applications in SCO research.

1.3. Overview

The aims of this chapter have been to introduce some fundamental concepts behind SCO, exploring the changing properties and means to induce SCO, as well as describing the ligand field considerations and standard synthetic procedures used in the SCO field. The principles behind mechanochemical synthesis were described with a discussion on the driving forces behind reactions and the absence of a fundamental understanding of the factors controlling mechanochemical synthesis. The analytical techniques used to investigate SCO material properties were described with regard to the information they can provide.

Chapter 3 will describe the combination of SCO and mechanochemistry research for the first time, with mechanochemical synthesis of a range of SCO-active materials. Characterisation of the materials and comparison with solution-synthesised materials is also undertaken. Chapter 3 continues to explore the effects of mechanochemical synthesis on SCO properties, expanding further on particle size, molecular structure, degree of amorphisation, morphology and hydration effects on the SCO properties in different SCO families. In Chapter 4, the mechanochemical technique of solid-state metathesis was explored as a viable method for synthesis of novel SCO materials in the 4-R-1,2,4-triazole family, by exploring the anion exchange potential. Chapter 5 describes the proposition and development of a rapid mechanochemical screening procedure, in which characterisation and identification of SCO-activity was optimised by identifying the most suitable analytical techniques which sufficient information to identify SCO-activity. The developed screening procedures were assessed for their suitability by screening a large quantity of materials in different SCO families, using mechanochemical synthesis. Chapter 6 presents an overall conclusion of the work carried out across all other chapters. The appendix contains additional screening of some samples discussed in Chapter 5.

1.4. References

1   C. A. Daul, *J. Phys. Conf. Ser.*, 2013, **428**, 012023.

2   E. Collet and P. Guionneau, *Comptes Rendus Chim.*, 2018, **21**, 1133–1151.

3   P. Guionneau, M. Marchivie, G. Bravic, J.-F. Létard and D. Chasseau, in *Spin Crossover in Transition Metal Compounds II*, Springer Berlin Heidelberg, Berlin, Heidelberg, 2004, pp. 97–128.

4   A. Adhikary, S. Akhtar, A. Pariyar, A. S. Batsanov and R. Mondal, *ACS Omega*, 2019, **4**, 8731–8738.

5   O. Laporte and W. F. Meggers, *J. Opt. Soc. Am. Rev. Sci. instruments*, 1925, **44**, 459–463.

6   F. Hund, *Zeitschrift für Phys.*, 1925, **33**, 345–371.

7   S. Brooker, *Chem. Soc. Rev.*, 2015, **44**, 2880–2892.

8   A. B. Gaspar, G. Molnár, A. Rotaru and H. J. Shepherd, *Comptes Rendus Chim.*, 2018, **21**, 1095–1120.

9   G. Chastanet, C. Desplanches, C. Baldé, P. Rosa, M. Marchivie and P. Guionneau, *Chem. Squared*, 2018, 1–18.

10   P. O. Ribeiro, B. P. Alho, R. M. Ribas, E. P. Nóbrega, V. S. R. de Sousa and P. J. von Ranke, *J. Magn. Magn. Mater.*, 2019, **489**, 165340.

11   J. Cirera, *Rev. Inorg. Chem.*, 2014, **34**, 199–216.

12   P. N. Martinho, B. Gildea, M. M. Harris, T. Lemma, A. D. Naik, H. Müller-Bunz, T. E. Keyes, Y. Garcia and G. G. Morgan, *Angew. Chemie - Int. Ed.*, 2012, **51**, 12597–12601.

13   J. Sanchez Costa, *Comptes Rendus Chim.*, 2018, **21**, 1121–1132.

14   L. Cambi and L. Szegö, *Berichte der Dtsch. Chem. Gesellschaft*, 1933, **66**, 656–661.

15   R. C. Stoufer, D. H. Busch and W. B. Hadley, *J. Am. Chem. Soc.*, 1961, **83**, 3732–3734.

16   C. J. Ballhausen and A. D. Liehr, *J. Am. Chem. Soc.*, 1959, **81**, 538–542.

17   W. A. Baker and H. M. Bobonich, *Inorg. Chem.*, 1964, **3**, 1184–1188.

18   E. Konig and K. Madeja, *Inorg. Chem.*, 1967, **6**, 48–55.

19   M. Sorai and S. Seki, *J. Phys. Soc. Japan*, 1972, **33**, 575.

20   P. Ganguli, P. Gütlich, E. W. Müller and W. Irler, *J. Chem. Soc. Dalt. Trans.*, 1981, 441.

21   N. Tsuchiya, A. Tsukamoto, T. Ohshita, T. Isobe, M. Senna, N. Yoshioka and H. Inoue, *Solid State Sci.*, 2001, **3**, 705–714.

22   S. Bonhommeau, T. Guillon, L. M. Lawson Daku, P. Demont, J. S. Costa, J. F. Létard, G. Molnár and A. Bousseksou, *Angew. Chemie - Int. Ed.*, 2006, **45**, 1625–1629.

23   F. J. Valverde-Muñoz, A. B. Gaspar, S. I. Shylin, V. Ksenofontov and J. A. Real, *Inorg. Chem.*, 2015, **54**, 7906–7914.

24   T. Mallah and M. Cavallini, *Comptes Rendus Chim.*, 2018, **21**, 1270–1286.

25   M. Seredyuk, A. B. Gaspar, V. Ksenofontov, S. Reiman, Y. Galyametdinov, W. Haase, E. Rentschler and P. Gütlich, *Chem. Mater.*, 2006, **18**, 2513–2519.

26   A. J. Fitzpatrick, P. N. Martinho, B. J. Gildea, J. D. Holbrey and G. G. Morgan, *Eur. J. Inorg. Chem.*, 2016, **2016**, 2025–2029.

27   P. Gütlich, Y. Garcia and H. A. Goodwin, *Chem. Soc. Rev.*, 2000, **29**, 419–427.

28   P. Gütlich, V. Ksenofontov and A. B. Gaspar, *Coord. Chem. Rev.*, 2005, **249**, 1811–1829.

29   G. Vankó, F. Renz, G. Molnár, T. Neisius and S. Kárpáti, *Angew. Chemie - Int. Ed.*, 2007, **46**, 5306–5309.

30   L. Kipgen, M. Bernien, F. Nickel, H. Naggert, A. J. Britton, L. M. Arruda, E. Schierle, E. Weschke, F. Tuczek and W. Kuch, *J. Phys. Condens. Matter*, 2017, **29**, 394003.

31   K. D. Murnaghan, C. Carbonera, L. Toupet, M. Griffin, M. M. Dîrtu, C. Desplanches, Y. Garcia, E. Collet, J. F. Létard and G. G. Morgan, *Chem. - A Eur. J.*, 2014, **20**, 5613–5618.

32   G. Chastanet, M. Lorenc, R. Bertoni and C. Desplanches, *Comptes Rendus Chim.*, 2018, **21**, 1075–1094.

33   N. Paradis, G. Chastanet, T. Palamarciuc, P. Rosa, F. Varret, K. Boukheddaden and J. F. Létard, *J. Phys. Chem. C*, 2015, **119**, 20039–20050.

34   P. Gutlich, S. Decurtins, K. M. Hasselbach, H. Spiering and A. Hauser, *Inorg. Chem.*, 1985, **24**, 2174–2178.

35   A. Bousseksou, J. Nasser, J. Linares, K. Boukheddaden and F. Varret, *J. Phys. I*, 1992, **2**, 1381–1403.

36   H. Romstedt, H. Spiering and P. Gu, *Science.*, 1998, **59**, 1353–1362.

37   S. Bonnet, M. A. Siegler, J. S. Costa, G. Molnár, A. Bousseksou, A. L. Spek, P. Gamez and J. Reedijk, *Chem. Commun.*, 2008, 5619–5621.

38   M. Griffin, S. Shakespeare, H. J. Shepherd, C. J. Harding, J. F. Létard, C. Desplanches, A. E. Goeta, J. A. K. Howard, A. K. Powell, V. Mereacre, Y. Garcia, A. D. Naik, H. Müller-Bunz and G. G. Morgan, *Angew. Chemie - Int. Ed.*, 2011, **50**, 896–900.

39   N. F. Sciortino, K. A. Zenere, M. E. Corrigan, G. J. Halder, G. Chastanet, J. F. Létard, C. J. Kepert and S. M. Neville, *Chem. Sci.*, 2016, **8**, 701–707.

40   A. Arroyave, A. Lennartson, A. Dragulescu-Andrasi, K. S. Pedersen, S. Piligkos, S. A. Stoian, S. M. Greer, C. Pak, O. Hietsoi, H. Phan, S. Hill, C. J. McKenzie and M. Shatruk, *Inorg. Chem.*, 2016, **55**, 5904–5913.

41   M. S. Sylla, C. Baldé, N. Daro, C. Desplanches, M. Marchivie and G. Chastanet, *Eur. J. Inorg. Chem.*, 2018, **2018**, 297–304.

42   P. Gütlich, A. Hauser and H. Spiering, *Angew. Chemie Int. Ed. English*, 1994, **33**, 2024–2054.

43   K. Takahashi, M. Okai, T. Mochida, T. Sakurai, H. Ohta, T. Yamamoto, Y. Einaga, Y. Shiota, K. Yoshizawa, H. Konaka and A. Sasaki, *Inorg. Chem.*, 2018, **57**, 1277–1287.

44   F. X. Shen, Q. Pi, L. Shi, D. Shao, H. Q. Li, Y. C. Sun and X. Y. Wang, *Dalt. Trans.*, 2019, **48**, 8815–8825.

45   H. Spiering and N. Willenbacher, *J. Phys. Condens. Matter*, 1989, **1**, 10089–10105.

46   M. Nishino, C. Enachescu and S. Miyashita, *Phys. Rev. B*, 2019, **100**, 134414.

47   O. Roubeau, J. M. Alcazar Gomez, E. Balskus, J. J. a. Kolnaar, J. G. Haasnoot and J. Reedijk, *New J. Chem.*, 2001, **25**, 144–150.

48   K. Hosoya, S. Nishikiori, M. Takahashi and T. Kitazawa, *Magnetochemistry*, 2016, **2**, 8.

49   K. A. Zenere, S. G. Duyker, E. Trzop, E. Collet, B. Chan, P. W. Doheny, C. J. Kepert and S. M. Neville, *Chem. Sci.*, 2018, **9**, 5623–5629.

50   C. Enachescu, M. Nishino, S. Miyashita, K. Boukheddaden, F. Varret and P. A. Rikvold, *Phys. Rev. B - Condens. Matter Mater. Phys.*, 2015, **91**, 1–9.

51   C. Enachescu, M. Nishino, S. Miyashita, L. Stoleriu and A. Stancu, *Phys. Rev. B - Condens. Matter Mater. Phys.*, 2012, **86**, 1–7.

52   W. Nicolazzi and S. Pillet, *Phys. Rev. B - Condens. Matter Mater. Phys.*, 2012, **85**, 1–13.

53   A. Slimani, K. Boukheddaden, F. Varret, H. Oubouchou, M. Nishino and S. Miyashita, *Phys. Rev. B - Condens. Matter Mater. Phys.*, 2013, **87**, 1–10.

54   A. Slimani, F. Varret, K. Boukheddaden, D. Garrot, H. Oubouchou and S. Kaizaki, *Phys. Rev. Lett.*, 2013, **110**, 1–5.

55   C. Chong, A. Slimani, F. Varret, K. Boukheddaden, E. Collet, J. C. Ameline, R. Bronisz and A. Hauser, *Chem. Phys. Lett.*, 2011, **504**, 29–33.

56   C. Enachescu and W. Nicolazzi, *Comptes Rendus Chim.*, 2018, **21**, 1179–1195.

57   M. Sorai, J. Ensling and P. Gütlich, *Chem. Phys.*, 1976, **18**, 199–209.

58   T. Tayagaki, A. Galet, G. Molnár, M. Carmen Muñoz, A. Zwick, K. Tanaka, J. A. Real and A. Bousseksou, *J. Phys. Chem. B*, 2005, **109**, 14859–14867.

59   O. Roubeau, J. G. Haasnoot, E. Codjovi, F. Varret and J. Reedijk, *Chem. Mater.*, 2002, **14**, 2559–2566.

60   I. V. Ovchinnikov, T. A. Ivanova, V. E. Petrashen', Y. G. Galyametdinov and G. I. Ivanova, *Appl. Magn. Reson.*, 2005, **29**, 325–334.

61   M. Manrique-Juárez, I. Suleimanov, E. Hernández, L. Salmon, G. Molnár and A. Bousseksou, *Materials (Basel).*, 2016, **9**, 537.

62   M. Fumanal, F. Jiménez-Grávalos, J. Ribas-Arino and S. Vela, *Inorg. Chem.*, 2017, **56**, 4474–4483.

63   F. Grandjean, G. J. Long, J. D. Holcomb, B. B. Hutchinson, L. Ohlhausen and P. Neill, *Inorg. Chem.*, 1989, **28**, 4406–4414.

64   L. Salmon, G. Molnár, S. Cobo, P. Oulié, M. Etienne, T. Mahfoud, P. Demont, A. Eguchi, H. Watanabe, K. Tanaka and A. Bousseksou, *New J. Chem.*, 2009, **33**, 1283–1289.

65   V. M. Hiiuk, S. Shova, A. Rotaru, V. Ksenofontov, I. O. Fritsky and I. A. Gural'skiy, *Chem. Commun.*, 2019, **55**, 3359–3362.

66   V. García-López, M. Palacios-Corella, M. Clemente-León and E. Coronado, *Polyhedron*, 2019, **170**, 95–100.

67   A. Tissot, X. Kesse, S. Giannopoulou, I. Stenger, L. Binet, E. Rivière and C. Serre, *Chem. Commun.*, 2019, **55**, 194–197.

68   J.-F. Létard, P. Guionneau and L. Goux-Capes, *Spin Crossover Transit. Met. Compd. III*, 2004, **1**, 221–249.

69   H. Flötotto, T. Secker, P. Kögerler and C. Besson, *Eur. J. Inorg. Chem.*, 2019, 4621–4624.

70   H. J. Shepherd, I. A. Gural'skiy, C. M. Quintero, S. Tricard, L. Salmon, G. Molnár and A. Bousseksou, *Nat. Commun.*, 2013, **4**, 2607.

71   G. Molnár, S. Rat, L. Salmon, W. Nicolazzi and A. Bousseksou, *Adv. Mater.*, 2018, **30**, 1703862.

72   J. Linares, E. Codjovi and Y. Garcia, *Sensors*, 2012, **12**, 4479–4492.

73   R. G. Miller and S. Brooker, *Chem. Sci.*, 2016, **7**, 2501–2505.

74   A. Barker, C. T. Kelly, I. A. Kühne, S. Hill, J. Krzystek, P. Wix, K. Esien, S. Felton, H. Müller-Bunz and G. G. Morgan, *Dalt. Trans.*, 2019, 15560–15566.

75   S. Rodríguez-Jiménez, H. L. C. Feltham and S. Brooker, *Angew. Chemie - Int. Ed.*, 2016, **55**, 15067–15071.

76   O. Kahn, J. Kröber and C. Jay, *Adv. Mater.*, 1992, **4**, 718–728.

77   J. Kröber, E. Codjovi, O. Kahn, F. Grolière and C. Jay, *J. Am. Chem. Soc.*, 1993, **115**, 9810–9811.

78   V. Niel, J. M. Martinez-Agudo, M. C. Muñoz, A. B. Gaspar and J. A. Real, *Inorg. Chem.*, 2001, **40**, 3838–3839.

79   I. A. Gural'skiy, C. M. Quintero, J. S. Costa, P. Demont, G. Molnár, L. Salmon, H. J. Shepherd and A. Bousseksou, *J. Mater. Chem. C*, 2014, **2**, 2949–2955.

80   M. D. Manrique-Juárez, F. Mathieu, A. Laborde, S. Rat, V. Shalabaeva, P. Demont, O. Thomas, L. Salmon, T. Leichle, L. Nicu, G. Molnár and A. Bousseksou, *Adv. Funct. Mater.*, 2018, **28**, 1–7.

81   S. Cobo, D. Ostrovskii, S. Bonhommeau, L. Vendier, G. Molnár, L. Salmon, K. Tanaka and A. Bousseksou, *J. Am. Chem. Soc.*, 2008, **130**, 9019–9024.

82   L. Salmon and L. Catala, *Comptes Rendus Chim.*, 2018, **21**, 1230–1269.

83   T. Zhao, L. Cuignet, M. M. Dîrtu, M. Wolff, V. Spasojevic, I. Boldog, A. Rotaru, Y. Garcia and C. Janiak, *J. Mater. Chem. C*, 2015, **3**, 7802–7812.

84   C. Bartual-Murgui, E. Natividad and O. Roubeau, *J. Mater. Chem. C*, 2015, **3**, 7916–7924.

85   P. Yang, R. Lipowsky and R. Dimova, *Small*, 2009, **5**, 2033–2037.

86   K. Robertson, P.-B. Flandrin, H. J. Shepherd and C. C. Wilson, *Oggi Chem*.

87   N. Daro, L. Moulet, N. Penin, N. Paradis, J. F. Létard, E. Lebraud, S. Buffière, G. Chastanet and P. Guionneau, *Materials (Basel).*, 2017, **10**, 60.

88   T. Forestier, A. Kaiba, S. Pechev, D. Denux, P. Guionneau, C. Etrillard, N. Daro, E. Freysz and J. F. Létard, *Chem. - A Eur. J.*, 2009, **15**, 6122–6130.

89   S. Nishigaki, H. Yoshioka and K. Nakatsu, *Acta Crystallogr. Sect. B Struct. Crystallogr. Cryst. Chem.*, 1978, **34**, 875–879.

90   K. S. Rahman, M. N. Harif, H. N. Rosly, M. I. Bin Kamaruzzaman, M. Akhtaruzzaman, M. Alghoul, H. Misran and N. Amin, *Results Phys.*, 2019, **14**, 102371.

91   O. Klimm, C. Göbel, S. Rosenfeldt, F. Puchtler, N. Miyajima, K. Marquardt, M. Drechsler, J. Breu, S. Förster and B. Weber, *Nanoscale*, 2016, **8**, 19058–19065.

92   D. Tanaka, N. Aketa, H. Tanaka, S. Horike, M. Fukumori, T. Tamaki, T. Inose, T. Akai, H. Toyama, O. Sakata, H. Tajiri and T. Ogawa, *Dalt. Trans.*, 2019, **48**, 7074–7079.

93   R. Torres-Cavanillas, L. Lima-Moya, F. D. Tichelaar, H. W. Zandbergen, M. Giménez-Marqués and E. Coronado, *Dalt. Trans.*, 2019, **48**, 15465–15469.

94   A. Akou, C. Bartual-Murgui, K. Abdul-Kader, M. Lopes, G. Molnár, C. Thibault, C. Vieu, L. Salmon and A. Bousseksou, *Dalt. Trans.*, 2013, **42**, 16021.

95   S. Shi, G. Schmerber, J. Arabski, J. B. Beaufrand, D. J. Kim, S. Boukari, M. Bowen, N. T. Kemp, N. Viart, G. Rogez, E. Beaurepaire, H. Aubriet, J. Petersen, C. Becker and D. Ruch, *Appl. Phys. Lett.*, 2009, **95**, 2–5.

96   M. Cavallini, I. Bergenti, S. Milita, J. C. Kengne, D. Gentili, G. Ruani, I. Salitros, V. Meded and M. Ruben, *Langmuir*, 2011, **27**, 4076–4081.

97   S. L. James, C. J. Adams, C. Bolm, D. Braga, P. Collier, T. Friščić, F. Grepioni, K. D. M. Harris, G. Hyett, W. Jones, A. Krebs, J. Mack, L. Maini, A. G. Orpen, I. P. Parkin, W. C. Shearouse, J. W. Steed and D. C. Waddell, *Chem. Soc. Rev.*, 2012, **41**, 413–447.

98   F. Hammerer, S. Ostadjoo, T. Friščić and K. Auclair, *ChemSusChem*, , DOI:10.1002/cssc.201902752.

99   F. K. Urakaev and V. V. Boldyrev, *Powder Technol.*, 2000, **107**, 93–107.

100   A. Urakawa, W. Van Beek, M. Monrabal-Capilla, J. R. Galán-Mascarós, L. Palin and M. Milanesio, *J. Phys. Chem. C*, 2011, **115**, 1323–1329.

101   F. Gomollón-bel, *Chem. Int.*, 2019, 12–17.

102   J. L. Do and T. Friščić, *ACS Cent. Sci.*, 2017, **3**, 13–19.

103   T. Friščić, S. L. Childs, A. A. Rizvo and W. Jones, *CrystEngComm*, 2009, **11**, 418.

104   J. L. Howard, Q. Cao and D. L. Browne, *Chem. Sci.*, 2018, **9**, 3080–3094.

105   D. E. Crawford and J. Casaban, *Adv. Mater.*, 2016, **28**, 5747–5754.

106   M. Ferguson, M. S. Moyano, G. A. Tribello, D. E. Crawford, E. M. Bringa, S. L. James, J. Kohanoff and M. G. Del Pópolo, *Chem. Sci.*, 2019, **10**, 2924–2929.

Chapter 2 – Experimental Theory and General Methods

2.1. Introduction

2.1.1. Aims

The aims of this chapter are to introduce the experimental theory and synthetic approach used in every other chapter. This begins by introducing the a series of SCO families used throughout the thesis, starting with the 0-D complex $Fe(phen)_2(NCS)_2$ before moving onto to the increasingly complex structures of the 1-D 1,2,4-triazole family and then onto the more structurally complex 2-D and 3-D Hofmann Clathrate-like complexes. The theory behind the instrumentation used was addressed. The methods used for synthesis and modification of the samples will be reported, broken down into each chapter.

2.1.2. Mechanochemical Synthesis

As discussed in 1.2, mechanochemical synthesis has seen a relatively recent resurgence in interest as a viable alternative green synthetic route. The scientific fields in which mechanochemical synthesis can be applied are ever expanding, with research ongoing in a broad range of scientific fields including: cathode/anode material synthesis,[1] metallic alloying,[2] cocrystal formation[3] and organic synthesis.[4] Prior to our work, mechanochemical synthesis had not been applied in spin crossover (SCO) research. The quick reaction times make mechanochemical synthesis ideal for synthesis and screening of potential SCO-active materials. Predicting SCO-activity is extremely difficult, therefore discovery of novel materials requires synthesis of large numbers of compounds. Previous research into the effects of post-synthetic grinding of SCO materials, showing significantly diminished SCO properties has likely played a role in the absence of research into this area.[5]

2.1.3. [Fe(phen)₂(NCS)₂]

One of the most frequently studied Fe^{2+} SCO molecular materials is $[Fe(phen)_2(NCS)_2]$, shown in **Figure 2.1**(a), (where phen = 1,10-phenanthroline, compound **1**). Since its discovery,[6] compound **1** became the most studied SCO material, with significant research into identifying the

magnetic properties[7,8] undertaken including: structural studies,[9] extensive theoretical studies,[10,11] exploration of crystal size and quality effects,[5,12,13] nanoparticle synthesis[12] and testing alternative synthetic routes.[14] At ambient temperature compound **1** is in the HS state and undergoes SCO to the LS state with $T_{1/2}$ of 178 K without any hysteresis.

Early synthetic routes to Fe(phen)$_2$(NCS)$_2$ required the use of template complexes in order to prevent the more favourable formation of [Fe(phen)$_3$](SCN)$_2$, structure shown in **Figure 2.1**(b).[6,8] Reports on the complex from Ganguli *el al.*[15] and Gallois *et al.*[9] identified the significant differences in properties depending on the synthetic route and proposed the possibility of different polymorphs for the complex. Two routes, denoted 'precipitation' and 'extraction', were purported to yield the two different forms. The 'precipitation' route used a template complex, such as Fe(pyz)$_2$(NCS)$_2$ or Fe(py)$_4$(NCS)$_2$ (where pyz = pyrazine and py = pyridine) and required subsequent exchange of ligands in solution. By contrast, the 'extraction' approach removed one phenanthroline ligand from the complex [Fe(phen)$_3$](SCN)$_2$ by continuous extraction using acetone[9] or by thermal decomposition.[14] Both approaches yielded products that display similar transition temperatures ($T_{1/2}\uparrow$ = $T_{1/2}\downarrow$ ≈ 175 K). However, the samples prepared by 'extraction' showed more abrupt transitions and a lower residual HS fraction at low temperatures. The differences between the transition properties were consistent with the effects of differences in crystal quality described by Haddad *et al.* for the [Fe(OCH$_3$-SalEen)$_2$]Y series of SCO complexes (where OCH$_3$-SalEen = 3-methoxysalicylaldhyde and Y = NO$_3$ and PF$_6$).[16]
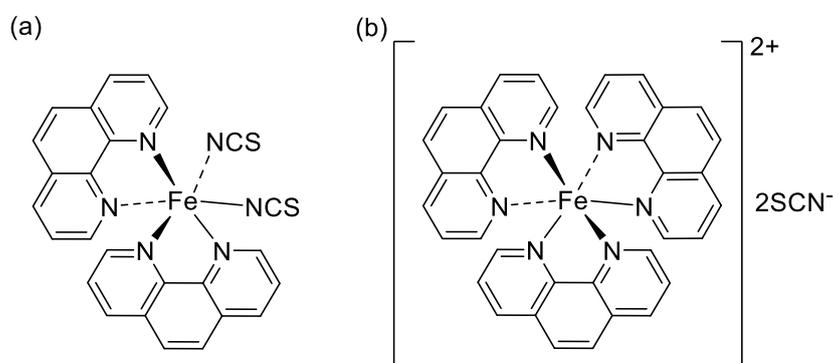
Figure 2.1: (a) Structure of Fe(phen)$_2$(NCS)$_2$. **(b)** Structure of [Fe(phen)$_3$](SCN)$_2$.

The effects of crystal quality on the complex $Fe(phen)_2(NCS)_2$ were further explored by Müller et al.[5] who found reducing crystal quality led to a more gradual transition, higher residual HS fraction at low temperature and a decrease in hysteresis. Further discussion on the effects on SCO of crystal quality in the context of mechanochemistry can be found in Chapter 3. In the absence of any structural evidence in support of polymorphism, it is now largely accepted that only one form of $Fe(phen)_2(NCS)_2$ exists; the differences in magnetic properties are primarily attributed to differences in both crystal quality and particle size.[17] The abruptness of the transition has been shown to be sensitive to varying crystallinity that results from differing preparation methods[6,14] and batch to batch variation has been reported with a wide range of transition temperatures, 165-190 K.[6,8,9,15,18,19]

2.1.4. 4-R-1,2,4-triazoles

4-R-1,2,4-triazoles and Fe(II) materials form one-dimensional chains with the general formula $[Fe(Rtrz)_3](A)_x.nH_2O$ (where Rtrz = 4-substituted-1,2,4-triazoles) represent an incredibly versatile family of SCO-active materials, which have long been a focus of research in SCO and have continue to be relevant to a lot of recent developments.[20–23] The versatility of the triazole family arises due to chemical flexibility with the SCO-properties being dependent on substitution on the 4-position, variation of the anion and the presence of solvents. The SCO complexes exhibit clear thermochromism alongside their transitions, changing from a purple LS state to a white HS state. Due to the use of Fe(II) the LS state is diamagnetic, and the HS state is paramagnetic. Members of the triazole family of SCO materials have been reported to display high temperature transitions with transitions reported above 400 K.[24] The complex $[Fe(Htrz)_2(trz)](BF_4)$ has also been reported to display a large hysteresis of 40 K with transitions above room temperature, which indicates a high degree of cooperativity is obtainable in these materials.[24]

The 4-R-1,2,4-triazole ligands form triply bridged links between Fe(II) centres, forming 'infinite' one-dimensional chains, as shown in **Figure 2.2**. The 'infinite' chains are important for maintaining the ligand field environment required for SCO. In the middle of the chains where the

FeN$_6$ configuration is maintained, SCO of the metal centres can occur. But, in short chain lengths, the end of chains may not be suitable for the occurrence of SCO due to likely solvent and strongly coordination anions 'capping' of the chains, as seen in trimer analogues. The effect is visible in short-chain systems such as the trinuclear complex [Fe(npt)$_6$(EtOH)$_4$(H$_2$O)$_2$](ptol)$_6$.4EtOH (where npt = 4-(4'-nitrophenyl)-1,2,4-triazole and ptol = *p*-tolylsulfonate), in which only one Fe(II) site undergoes SCO.[25]
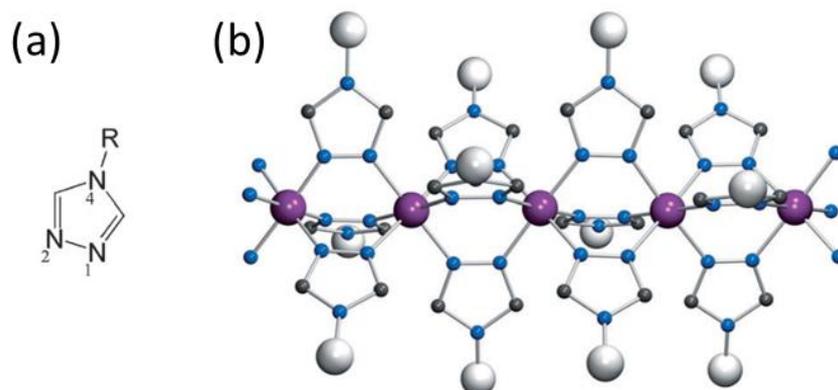
Figure 2.2: Schematic representation of (a) 4-R-1,2,4-triazole with sites numbers. (b) A 4-R-1,2,4-triazole chain in an ideal 1D coordination chain with Fe(II) centres (purple) triply bridged by triazole bridges. Reproduced with permission from reference.[20]

Synthesis of Rtrz complexes with Fe(II) are relatively simple, with the reactions often occurring in water or alcohol-based solvents and consisting of room temperature stirring of the Rtrz ligand and the corresponding Fe(II) salt. However, for more exotic anions the in-situ formation of the appropriate salt is first required, which has been used to prepare iron-triazole complexes with exotic anions such as MF$_6^{2-}$ (where M = Ti, Zr, Sn and Ta).[26] The catalogue of reported SCO-active materials in the iron-triazole family is extensive, with many different substitutions in the 4-position, ranging from simple 1,2,4-triaozle to large aliphatic chains[27] and bulky aromatic regions.[28] The effects of solvents used in the synthesis of iron-triazole complexes can be significant, with the impact of degree of hydration well characterised.[29] The transition temperatures in the family have presented across the board, with transition temperatures lower than 150 K[30] and above 400 K.[24]

2.1.5. Hofmann-type Clathrate Frameworks

Iron(II)-containing Hofmann-type clathrates are 3D framework materials that have also been extensively studied for their attractive SCO properties. These two- and three- dimensional frameworks have the general formula $\{Fe(L)_n[M(CN)_2]_2\}.xH_2O$ (where L = monodentate or bidentate N-donor aromatic ligands, M = Ni(II), Pd(II), Pt(II), Cu(I), Ag(I) or Au(I) and x ≥ 0).[31] Fe(4-phpy)$_2$[Ni(CN)$_4$] (4-phpy = 4-phenylpyridine), compound **4**, and Fe(pz)[Au(CN)$_2$]$_2$ (pz = pyrazine), compound **5**, shown in **Figure 2.3**(b) and (d) respectively. Two-dimensional iron dicyanometallate or tetracyanometallate layers form the basis of the frameworks, which can be pillared by organic bidentate bridging ligands (such as pyrazine) to form three- dimensional frameworks or capped by monodentate ligands (such as 4-phenylpyridine) to form two- dimensional networks.
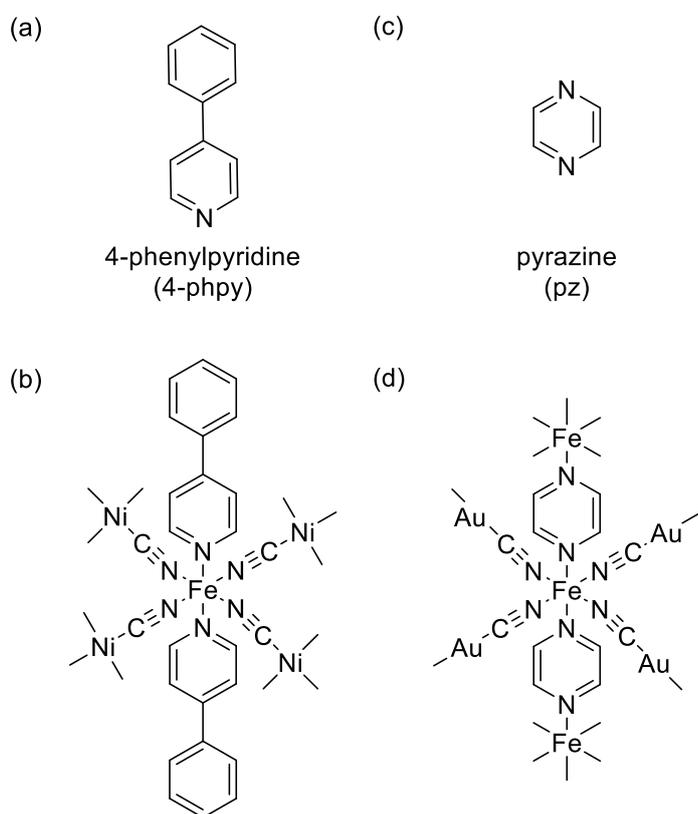
Figure 2.3: (a) Structure of 4-phenylpyridine (4-phpy). **(b)** Schematic representation of the complex Fe(4-Phpy)$_2$[Ni(CN)$_4$] presenting the two- dimensional iron tetracyanometallate layer capped by 4-phenylpyridine. **(c)** Structure of pyrazine (pz) and **(d)** Schematic representation of the complex Fe(pz)[Au(CN)$_2$]$_2$ presenting two-dimensional iron dicyanometallate layers bridged by pyrazine.

Interest in this family arises due to high temperature transitions,[32] high cooperativity,[33] ease of modification[34] and exploitable host-guest properties.[35] Further features include interpenetrating frameworks,[36] porosity,[37] supramolecular isomerism,[38] and both physi- and chemisorption, all of which have an impact on SCO behaviour.[39,40] This family generally displays abrupt SCO transitions at temperatures above room temperature, up to and exceeding 400 K.[41] The high temperature transitions can also be coupled with wide thermal hysteresis and associated bi-stability, attributed to the highly cooperative extended covalent network structure.

2.1.6. Experimental Theory

2.1.6.1. SQUID Magnetometry

Superconducting quantum interference device (SQUID) magnetometry is an incredibly sensitive technique which can be used to investigated magnetic properties in a variety of different materials including those with low magnetic moments such as ultrathin films,[42,43] nanoparticles[44] and dilute magnetic semiconductors.[45] The operating principle behind the technique is the conversion of magnetic flux into voltage through the use of Josephson junctions. A Josephson junction is a device in which two superconducting electrodes are separated by a non-superconducting barrier. Pairs of electrons, known as Cooper pairs, can tunnel through the non-superconducting barrier, with certain frequencies. Two types of SQUID magnetometers are available, radio frequency (rf) and direct current (dc). Rf SQUIDs are made up of one Josephson junction that is mounted on a superconducting ring, magnetic flux is measured by recording the change in voltage on external circuit with an oscillating current. DC SQUIDs are significantly more sensitive and are made with two Josephson junctions in parallel. The tunnelling electrons exhibit quantum interference which is affected by magnetic flux within the loop. A current is generated proportional to the phase difference between the two junctions.

$$X_M T \ (cm^3 \ K \ mol^{-1}) = \left(\frac{Magnetic \ Moment(emu) \ x \ M_w}{Magnetic \ Field \ (Oe) \ x \ Mass(g)} \right) x \ Temperature \ (K)$$

Equation 2. 1

45

SQUID magnetometry is used extensively in SCO research to characterise the transition between spin states by measuring the change in magnetic flux. The difference in magnetic susceptibility between the HS and LS state is orders of magnitude larger than the limit of detection for modern SQUID magnetometers. Molar magnetic susceptibility as a function of temperature ($X_M T$) is calculated using **Equation 2. 1**, long magnetic moment is directly measured by the instrument, molecular weight (M_w), magnetic field strength (Oe) and the sample mass (g). Magnetic susceptibility is plotted as a function of temperatures, this allows for easier identification of SCO-activity as well as minimising the tailing induced by temperature effects. Data can also be plotted as a function HS fraction (γ_{HS}) to emphasise minute differences, limit the effects of impurities or substrates present in the material and to allow comparison between different samples, as shown in **Figure 2.4**.
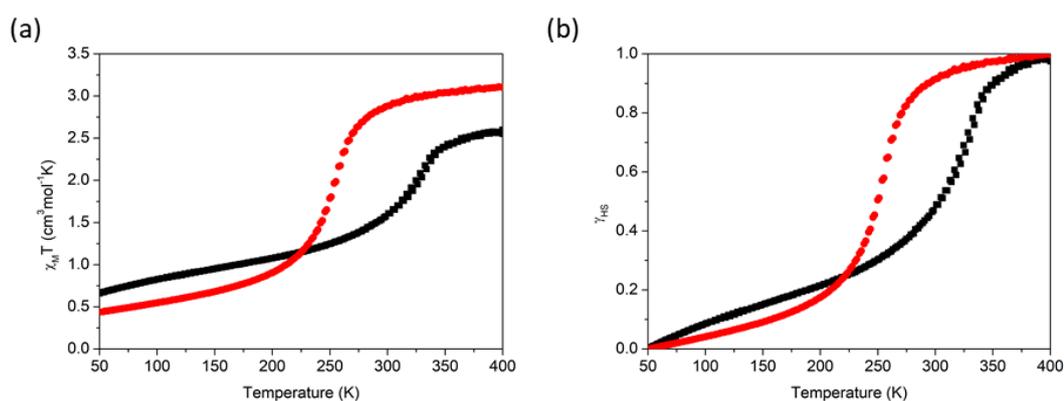
Figure 2.4: Comparison of SQUID data for two materials containing different amounts of impurities. (a) Plotted as a function of magnetic susceptibility ($X_N T$) and (b) plotted as a function of high spin fraction (γ_{HS})

2.1.6.2. Powder X-Ray Diffraction

Powder X-ray diffraction (PXRD) is an analytical technique that is commonly used to investigate the structural properties of a material. It operates on the interactions between X-rays and the atoms present in materials. Electrons in atoms coherently scatter X-rays, therefore the atoms can be considered as point diffraction sources, as shown in **Figure 2.5**(a), atoms need to be ordered in a lattice to provide sufficient diffraction to be measured. PXRD can be used to investigate the structural characteristics of the entire bulk crystalline material. This include the

presence of impurities and can be used determine overall purity through detailed analysis such as Rietveld refinement. Further extensions of PXRD analysis can be collection of data at variable temperatures and the application of particle size estimation techniques such as Scherrer analysis, discussed further in Chapter 3.
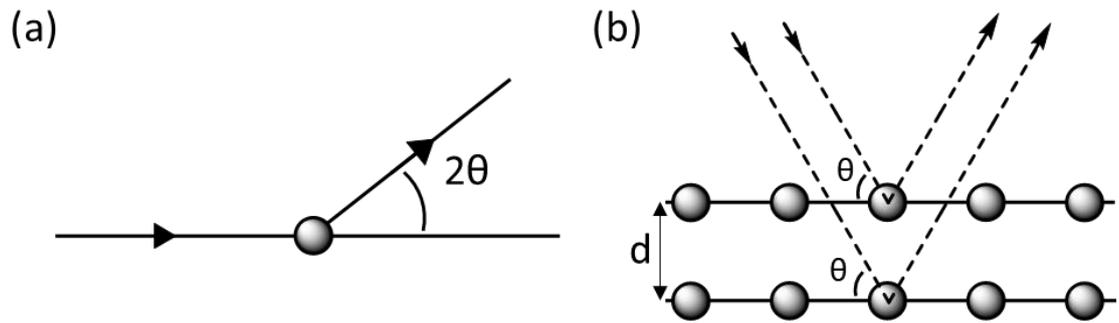
Figure 2.5: (a) Generic scattering of an X-ray by a point atom. (b) Schematic representation of Bragg's Law, denoting two incident X-rays with identical wavelength and phase scattering off different atoms. If the extra distance travelled by the lower beam is equal to 2dsin(θ) then constructive interference occurs.

The basic principle behind PXRD analysis is the incident X-rays are scattered by atoms and either form constructive or destructive interference with each other. Constructive interference results in peaks in diffractions patterns. Constructive interference occurs according to Bragg's Law (Equation 2.2), with a schematic representation shown in **Figure 2.5**(b). The difference in distance travelled by X-rays must be equal to an integer multiple (n) of 2dsin(θ) for constructive interference to occur. Where d represents the difference between planes and θ is the angle of incidence. This description is suitable for idealised scenarios in which discrete planes of atoms exist in a material. However, the reality for most materials are not this simple, with many interacting planes of atoms. This results in patterns with very sharp peaks surrounded with mostly destructive interference.

$$n\lambda = 2dsin(\theta)$$

Equation 2.2

2.1.6.3. Raman Spectroscopy

Raman spectroscopy is a technique that probes inelastic scattering of monochromatic radiation when incident on materials. Incident photons are mostly scattered elastically, known as Rayleigh scattering (same wavelength and energy). But, a small fraction of incident photons, on the order of 1 in 10 million,[46] are scattered inelastically, and this is known as Raman scattering. Raman scattering can either increase in energy (anti-Stokes) or decrease in energy (Stokes) and it can provide information on vibrations within a molecule. The principle has been proposed as a so-called virtual electronic energy level, incident photons are absorbed and excite the molecule into a virtual state.[47] Re-emission of the photon results in either Rayleigh or Raman scattering. Collection of the scattered photons using detectors, such as charge coupled device (CCD) detectors, results in the measurement of a Raman spectrum.

Raman spectra are plotted as a function of wavenumber (cm^{-1}) or λ (nm) and intensity. In instances of relatively simple molecules, with high quality data, it is possible to assign specific peaks to certain bond vibrations. However, for increasingly complex molecules this approach becomes much more complicated. Although possible, the quality of data, time commitments and specific specialities required for full interpretation in this manner make full assignment unviable for routine use in SCO. Therefore, for a large number of materials the Raman spectrum is collected as a 'fingerprint' of the material and they are often stored in large databases which can be used for rapid identification of materials. The fingerprint approach can be used to observe the presence of certain materials in mixtures of compounds. One of the main advantages of Raman spectroscopy over other spectroscopic techniques is the limited sample preparation required, with viable spectra able to be collected through glass sample vials without any special considerations. The technique is non-invasive and can be used in conjunction with temperature-controlled stages on small quantities of material.

In SCO research, Raman spectroscopy can be used to determine differences in spin states as a result of changing bond lengths inducing changing vibrational modes, as shown in **Figure 2.6**. However, the effects of changing bond length can be difficult to observe due to the potential for

'pre-resonance' effects. Pre-resonance occurs when the excitation wavelength is similar to a discrete electronic transition in the material.[48,49] To overcome these difficulties, it is possible to identify specific spin marker bands, separate from metal-ligand stretches, in certain materials. One such example of this is the NCS[-] ligand which is isolated from other vibrations in many materials and it has been used extensively for monitoring of SCO-activity.[14,50,51] It is worth noting potential problems arising from using Raman spectroscopy to investigate SCO materials. One such disadvantage is the potential for localised heating of the sample under laser irradiation. This effect has been observed causing a localised 50 – 60 K beam-induced heating, which is sufficient to induce SCO.[52] Although this is highly dependent on experimental setup (magnification, laser power and wavelength of excitation).
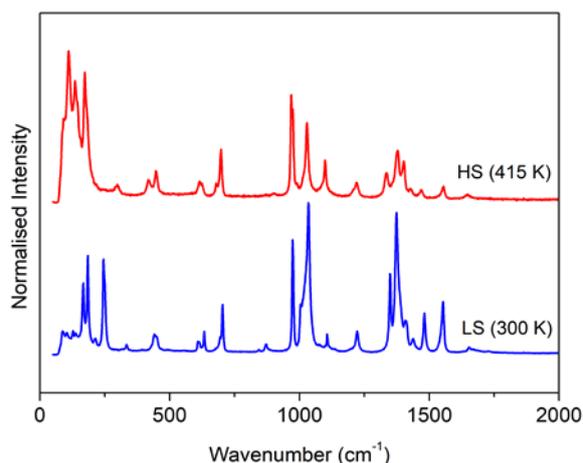
Figure 2.6: Representative example of using Raman spectroscopy in SCO research, showing significant differences in spectra between the HS and LS state for the SCO-active complex [Fe(atrz)$_3$])SO$_4$.

2.1.6.4. Thermogravimetric Analysis and Differential Scanning Calorimetry

Thermogravimetric analysis (TGA) is an analytical technique which records the mass of a sample as a function of temperature. This provides information on solvent and gas adsorption and absorption and degree of hydration in a material. It can also provide insight into thermal stability of a material. TGA is often coupled with the means to record differential scanning calorimetry data (DSC) which records the difference in energy required to heat a sample relative to a

standard. This can provide insight into phase transitions, including glass transitions temperatures (T_g) and SCO transitions.

In SCO research TGA analysis is used to determine amounts of solvent present, which is important considering the significant solvent effects observed for SCO.[53] Differential scanning calorimetry (DSC) can be used to identify SCO transition temperatures and can be used to determine the change in entropy resulting from the SCO transition. However, measurements at temperatures below 100 K after often difficult and the data is strongly dependent on scan-rate, which can lower the sensitivity of the technique if not considered. The combination of TGA and DSC allows rapid study of mass loss, resulting from solvent loss or sample decomposition and phase transitions (such as melting and crystallographic solid-solid) or SCO, a representative example is shown in **Figure 2.7**.
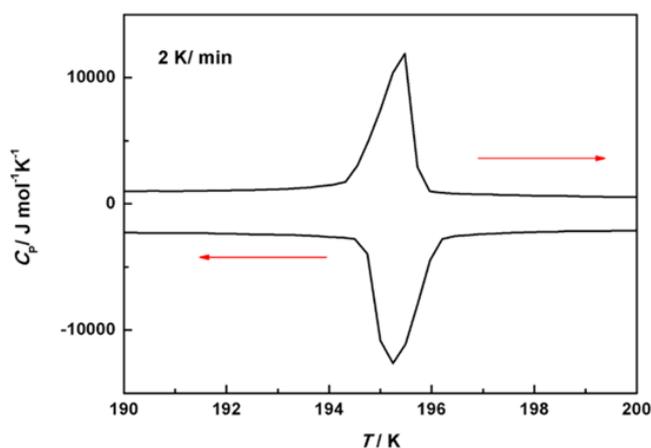
Figure 2.7: Representative example of using DSC to identify and characterise the presence of SCO, for the complex [Fe(H$_2$Bpz$_2$)$_2$(L)] (where L = diisopropyl-2,2'-bipyridine-5,5'-dicarboxylate), reproduced with permission from reference.[54]

2.1.6.5. X-Ray Absorption Spectroscopy

X-Ray absorption spectroscopy (XAS) is an analytical technique that serves to provide element-specific information on local electronic structure. This can provide insight into chemical environment, oxidation state and bonding configuration of a specific atom type without interference from other components present in the system.[55] The X-ray energy used is on the

order of 10^4 eV, which corresponds to wavelengths around 1 Ångstrom. This is of the same order of magnitude as atom-atom separation, which allows XAS to be used to determine local atomic structure.[56] High-energy X-ray excitation of a sample from a synchrotron source causes emission of core electrons and the creation electron holes in the target element. XAS measures the relaxation of the system as a continuous function of energy of the incident X-rays. The XAS spectrum is divided into two regions: X-ray absorption near edge structure (XANES) and extended X-ray fine structure (EXAFS), as shown in **Figure 2.8**.[57]
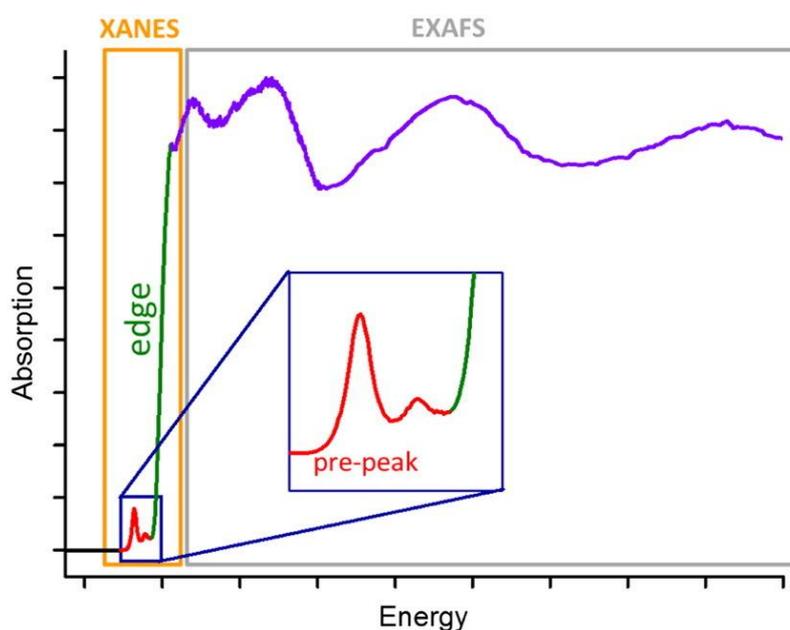
Figure 2.8: X-ray absorption spectrum showing the X-ray absorption region near edge structure (XANES) including the pre-edge-feature and extended X-ray absorption fine structure (EXAFS) region. Reproduced with permission from reference.[57]

2.1.6.5.1.   EXAFS

The extended X-ray absorption fine structure (EXAFS) region is defined between *ca.* 50 eV to 1000 eV above the absorption edge. EXAFS is used to determine the atomic arrangement of neighbouring atoms by investigating oscillations in the intensity of X-ray absorption as a function of energy. The oscillations are the result of interference between outgoing and backscattered photoelectrons, which occur at defined energies. When the outgoing and backscattered photoelectrons are in phase, they result in constructive interference which causes an increase in absorption. Whereas, at other energies the outgoing and backscattered photoelectrons are out of

phase which causes destructive interference, as shown in **Figure 2.9**. As a result of the constructive and destructive interference, atomic structure, coordination number and bond lengths can be determined, making EXAFS a sensitive probe for the local atomic structure. Variation and uncertainty in oscillations allows for disorder and amorphisation to be estimated.

The ability for EXAFS to determine changes in local atomic structure makes EXAFS an ideal method to investigate changes in structure caused by SCO activity. The change in Fe-N bond length resulting from the increased population of the antibonding e_g orbital in the HS state, has been observed and confirmed with confidence using the technique.[58]
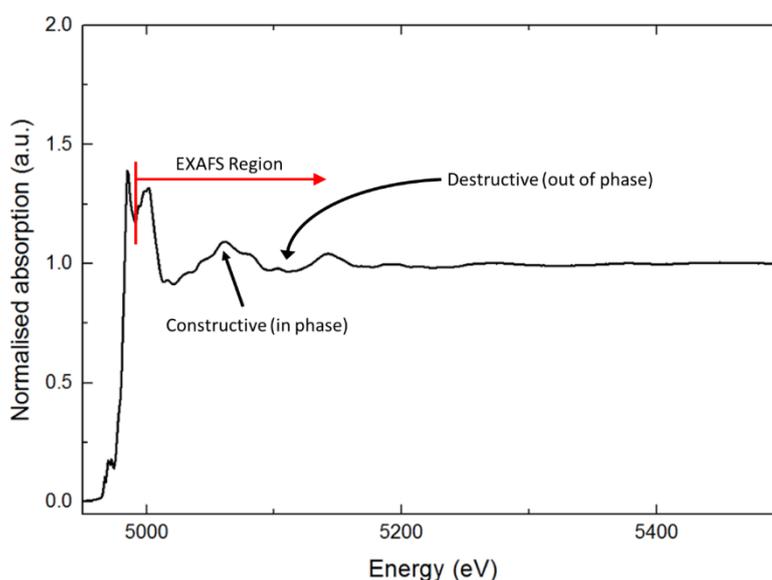
Figure 2.9: Schematic representation of the origin of EXAFS oscillations, showing the constructive and destructive interference of an absorption atom and a neighbouring atom.

Fe-edge EXAFS can be used to probe the short-range structure of a system, providing information on the Fe-atom bond distances. This is particularly important for investigating SCO materials whereby the change in Fe-N distance resulting from SCO can be investigated. Comparison of the Fe-atom bonds between solution-state and mechanochemically synthesised samples provides valuable insight into the structural similarities and differences in the two synthetic procedures. Further, the uncertainty in bond distances represents disorder that can be

used to determine degree of amorphisation in a sample, which is an important consideration in comparing solution-state and mechanochemically synthesised samples.

2.2. Experimental

2.2.1. Material and Equipment

All reagents were bought from either Sigma Aldrich or Fisher Scientific and used without further purification. 1,10' phenanthroline (99+ %, Sigma), 2,2'-bipyridine (99%, Fisher), 4,4' dinonyl-2,2'-dipyridyl (97%, Sigma), 4,7-dimethyl-1,10 phenanthroline (98%, Fisher), 4,7-diphenyl-1,10 phenanthroline (99+%, Fisher), 4-amino-1,2,4-triazole (99 %, Fisher), 1H-1,2,4-triazole (99.5 %, Fisher), 4-phenylpyridine (99 %, Fisher), 5,5'-dimethyl-2,2'-dipyridyl (98%, Sigma), ammonium iron(II) sulphate hexahydrate (99+ %, Fisher), iron(II) chloride tetrahydrate (99+ %, Fisher), iron(II) chloride tetrahydrate (99+%, Fisher), iron(II) oxalate trihydrate (99%, Sigma), iron(II) sulphate heptahydrate (99+ %, Fisher), iron(II) tetrafluoroborate hexahydrate (97 %, Fisher), L-ascorbic acid (99 %, Fisher), potassium thiocyanate (99+ %, Sigma), potassium tri(1-pyrazolyl)borohydride (93%, Sigma), potassium tri(3,5-dimethyl-1-pyrzolyl)borohydride (97%, Sigma) and pyrazine (99 %, Fisher). 2,2'-(pyridine-2,6-diylbis(1H-pyrazole-5,3'diyl)diphenol (**3-bpp-PhOH**) and 2,6-bis(3-(2-methoxyphenyl)-1H-pyrazol-5-yl)pyridine (**3-bpp-PhOCH₃**) and 2,6-bis(3-(naphthalen-2-yl)-1H-pyrazol-5-yl)pyridine (**3-bpp-Napth**) were provided by Dr. P. Rosa from the ICMCB, CNRS, Bordeaux, France.

3-bpp-PhOH ^{1}H NMR 400 MHz (DMSO-d[6]), Figure B.3, found ppm δ: 6.93-7.24 [m, **10H, PhOH, CH**], 7.66-8.08 [m, **5H, py, CH**], 13.79 [s, **2H, NH**].

3-bpp-PhOCH₃ ^{1}H NMR 400 MHz (DMSO-d[6]), Figure B.4, found ppm δ: 3.96 [s, **6H, CH₃],** 7.03-7.21 [m, **4H**, CH₃OC**Ph**CNNHC**CH**PyC**CH**NNC**Ph**COCH₃], 7.32-7.43 [m, **4H,** CH₃OC**Ph**CNNHCCHPyC**CH**NNC**Ph**COCH₃], 7.70-7.89 [m, **5H, Py(3H)** and **Pz(2H)**], 13.12-13.58 [s, **2H, NH**].

3-bpp-Napth ^{1}H NMR 400 MHz (DMSO-d[6]), Figure B.5, found ppm δ: 7.51-7.86 [m, **4H**, **CH**], 7.86-8.14 [m, **11H**, **CH**], 8.43 [s, **6H**, **CH**], 13.69 [s, **2H**, **NH**].

Magnetic susceptibility measurements were carried out using a Quantum Design MPMS SQUID magnetometer. Temperature dependent measurements were made using a 1000 Oe magnetic field across the stated temperature ranges at a rate of 2 K min^{-1}.

Simultaneous thermogravimetric analysis (TGA) and differential scanning calorimetry (DSC) was carried out using a Netzsch STA 409 PC25 under nitrogen with a constant heating rate 5 K min^{-1} within the range 298 – 723 K, using an aluminium crucible. Compound specific isotherms are stated on plots.

Variable temperature Raman spectra were recorded using a Horiba LabRam spectrometer equipped with a 600 grating, x50 LWD NIR objectives and a 632.81 nm laser. The variable temperature stage used to control sample temperature was a Linkam THMS 600 with a heating/cooling rate of 10 K min^{-1}. Measurements were taken at fixed temperatures, after thermal stabilisation at the target temperature for two mins, as shown on Raman plots.

Powder x-ray diffraction data (PXRD) were collected at room temperature using a Rigaku MiniFlex 600 desktop XRD using Cu Kα radiation, λ = 1.54051 Å, 15 mA, 40 KV, 5 − 50° (2θ). Scherrer analysis of compound **7** and compound **7-Cl**, was carried out using PXRD data collected on a Panalytical X'Pert3 using Cu Kα radiation, λ = 1.54051 Å, with a power rating 40 kV and 20 mA. The 2θ range 5 − 40° was recorded with continuous scanning using a step size 0.0041778° with 400 seconds exposure per step. Samples were mounted on a silicon crystal sample holder. A LaB$_6$ standard was used to determine peak broadening originating in the experimental setup. The Scherrer equation includes a dimensionless shape factor which accounts for the shape of the crystallite, the value used in calculations assumes a spherical shape to the particles. Triazole SCO materials have previously been shown to have multiple different shapes depending on the method of synthesis, including spherical, rod-like and plates.[59]

EDX measurements were recorded using a Hitachi-3400n SEM fitted with an Oxford Instruments X-Max 80 mm^2 Silicon drive detector for EDX analysis. The data were recorded in the 0-20 KeV range with 20 s live time, with an accelerating voltage of 20 kV and 5 s processing time. The samples were analysed as rough particles without polishing, consequently the potential error within the reported values is not insignificant. This is evident in the values obtained for standard deviation of the samples. As such, the relative ratios of each element are discussed, rather than the absolute values.

XAS scans were collected for Fe-edge at room temperature on beam line B18 at the Diamond Light Source by Dr. David Pickup and Prof. Alan Chadwick. Data were collected in transmission mode with ion chamber detectors. Continuous scanning (QEXAFS) was employed; an individual scan required 180 s and several scans were performed to improve the signal-to-noise ratio. The synchrotron energy and current were 3 GeV and 300 mA, respectively. The beam size at the sample was 700 × 700 microns. Powdered samples were mixed with polyvinylpyrrolidone (PVP) as a diluent and pressed into 13 mm diameter pellets. The spectra were normalized in Athena[60] and fitted to scattering models in R-space produced by FEFF[61] in Artemis[60] by Dr Dave Pickup.

Transmission Electron Microscopy (TEM) was done using a Jeol 1230 120 kV Transmission Electron Microscope equipped with a Gatan One View 16 MP camera with automatic drift correction. Samples were prepared by adapting the method described by Petri-Fink *et al*.[62] 10 mg was added to MilliQ water (10 mL) and sonicated for 30 minutes. Bovine Serum Albumin (BSA) (15 mg) was dissolved in MilliQ water (10 mL) and sonicated for 15 minutes. An aliquot of the BSA solution (100 μL) was added to an aliquot of the compound solution (100 μL) and sonicated for an additional 15 minutes. 600 Mesh coppers grids purchased from Agar Scientific were coated in ~70 nm of formvar and ~5 nm of evaporated carbon using a QuorumQ150T ES Evaporative coater. 2 μL aliquots of sample/BSA solution were deposited on the copper grids and vacuum dried at 30 °C for 30 minutes.

Elemental analysis was performed by Mr. S. Boyer at the elemental analysis service of London Metropolitan University, U.K. Due to the nature of the mechanochemical procedure, the final products may well contain traces of unreacted starting materials and by-products from the reaction. Calculated values for elemental analysis discussed below were based on likely compositions of the product at each stage but should be interpreted with a degree of caution.

2.2.2. Synthesis

Mechanochemical synthesis of all complexes was carried out using the following procedure, unless otherwise stated below. Reagents were manually ground in stoichiometric ratios for 5-10 minutes in a glass pestle and mortar. A fraction of the resulting powders were dried at 175 °C for 10 hrs. A second fraction was washed using water and ethanol and dried under vacuum at 45 °C overnight. Mechanical synthesis yielded one product which was split into three portions; as synthesised (**x-Mech**), dried (**x-Dried**) and washed (**x-Wash**). Solution synthesis of each complex is described below.

2.2.2.1. Chapter 3: Initial Synthesis and Exploring the Effects of Mechanochemical Synthesis of Spin Crossover Materials

2.2.2.1.1. Mechanochemical Synthesis

Compounds **2**, **3, 5** and **6** were synthesised using the general mechanochemical procedure described above.

3-Mech CHN analysis for $[Fe(atrz)_3](SO_4) \cdot 0.5(NH_4)_2(SO_4) \cdot 2H_2O$ found (calc). C 14.95 (14.24), H 3.97 (3.98), N 35.06 (35.97). **3-Dried** CHN analysis for $[Fe(atrz)_3](SO_4) \cdot 0.5(NH_4)_2(SO_4)$ found (calc). C 14.13 (15.33), H 3.32 (3.43), N 32.52 (38.72). **3-Sol** CHN analysis for $[Fe(atrz)_3](SO_4) \cdot 2H_2O$ found (calc). C 16.66 (16.37), H 4.02 (3.66), N 41.73 (38.19). **5-Mech** CHN analysis for $Fe(pz)[Au(CN)_2]_2 \cdot 0.04KAu(CN)_2 \cdot 2KBF_4 \cdot H_2O$ found (calc). C 9.84 (10.94), H 0.36 (0.68), N 8.79 (6.44).

2.2.2.1.1.1. Fe(phen)₂(NCS)₂ – Compound 1

$[Fe(phen)_3](SCN)_2$ (compound **1-Mech**) was prepared by manually grinding $Fe(BF_4)_2 \cdot 6H_2O$ (0.5 g, 1.5×10^{-3} mol), 1,10'-phenathroline (0.7 g, 3.9×10^{-3} mol) and KSCN (0.3 g, 3.1×10^{-3} mol) for 5

minutes in a glass pestle and mortar. CHN analysis for [Fe(phen)$_3$](NCS)$_2$·0.15(Fe(BF$_4$)$_2$·6H$_2$O·0.63KSCN·2KBF$_4$ found (calc). C 42.50 (41.85), H 2.43 (2.39), N 11.03 (11.50). The calculated formula assumes that everything in the reactants remained in the product. As discussed in 2.1.3, [Fe(phen)$_3$](SCN)$_2$ can be converted into Fe(phen)$_2$(NCS)$_2$ *via* thermolysis.[14] A fraction of the resulting powder was dried at 80 °C for 3 hours then heated to 200 °C for 10 hours (**1-Heat**). CHN analysis for [Fe(phen)$_2$(NCS)$_2$]·0.15(Fe(BF$_4$)$_2$)·0.63KSCN·2KBF$_4$ found (calc). C 34.84 (36.35), H 1.82 (1.83), N 9.74 (10.55). A third of the sample was washed with H$_2$O (300 ml) and ethanol (300 ml) collected by filtration and dried under vacuum at 45 °C (**1-Wash**). CHN analysis for [Fe(phen)$_2$(NCS)$_2$]·KBF$_4$ found (calc). C 46.85 (47.44), H 2.36 (2.45), N 12.97 (12.77).

2.2.2.1.1.2.   Fe(4-phpy)₂[Ni(CN)₄] – Compound 4

Mechanical synthesis of Fe(4-phpy)$_2$[Ni(CN)$_4$] was attempted using the standard procedure described in 2.2.2 yielding compound **4-Mech**.

Fe(4-phpy)$_2$[Ni(CN)$_4$] (compound **4-LAG**) was synthesised by liquid assisted grinding (LAG), the principles of LAG are described in 1.2.1. Fe(BF$_4$)$_2$.6H$_2$O (0.11 g, 3.2x10^{-4} mol), 4-phenyl pyridine (0.10 g, 6.7x10^{-4} mol) and K$_2$Ni(CN)$_4$.xH$_2$O (0.08 g, 3.1x10^{-4} mol) were ground in an agate pestle and mortar with water (72 μl, η = 0.25) for 10 minutes. The resulting yellow powder was dried under vacuum at 45 °C overnight.

2.2.2.1.2.   Solution-State Synthesis

2.2.2.1.2.1.   [Fe(Htrz)₃](BF₄)₂ – Compound 2

[Fe(Htrz)$_3$](BF$_4$)$_2$ (compound **2-Sol**) was prepared by adding 4-H-1,2,4-triazole (0.23 g, 3.3x10^{-3} mol) in methanol (100 ml) to a solution of Fe(BF$_4$)$_2$.6H$_2$O (0.34 g, 1x10^{-3} mol) in methanol (60 ml) at 0°C and stirred for 48hrs. The precipitate was collected by filtration and dried overnight under vacuum at 45 °C, yielding a fine pink powder (0.26 g, 60%).

2.2.2.1.2.2.   [Fe(atrz)₃]SO₄ – Compound 3

[Fe(atrz)₃]SO₄ (compound **3-Sol**) was synthesised by the addition of 4-amino-1,2,4-triazole

(0.51 g, 6.0×10^{-3} mol) in water (1.5 ml) to a stirred solution of $(NH_4)_2Fe(SO_4)_2 \cdot 6H_2O$ (0.41 g, 1.2×10^{-3}

mol) in water (3 ml). The solution was stirred for 30 minutes at room temperature. The resulting

purple precipitate was collected by filtration and dried under vacuum overnight at 45 °C. Yield

(0.35 g, 71%).

2.2.2.1.2.3.   Fe(4-phpy)₂[Ni(CN)₄] – Compound 4

Compound **4-Sol** was prepared using a modified reported synthetic procedure.[31]

$Fe(BF_4)_2 \cdot 6H_2O$ (0.10g, 3.2×10^{-4}mol) in methanol (10 ml) was added to a stirred solution of 4-

phenylpyridine (0.10 g, 6.4×10^{-4} mol) in methanol (10ml). After 1 hour, $K_2[Ni(CN)_4] \cdot xH_2O$ (0.07 g,

2.9×10^{-4} mol) in methanol (10 ml) was added dropwise and stirred for 5 hours. The yellow

precipitate was collected by filtration, washed with methanol, and dried under vacuum at 45 °C

overnight.

2.2.2.1.2.4.   Fe(pz)[Au(CN)₂]₂ – Compound 5

Compound **5-Sol** was synthesised by modifying a reported synthetic procedure.[32] $K[Au(CN)_2]$

(0.50 g, 1.74×10^{-3} mol) in water (10 ml) was added dropwise to a stirred mixture of $Fe(BF_4)_2 \cdot 6H_2O$

(0.29 g, 8.7×10^{-4} mol) and pyrazine (0.07 g, 8.7×10^{-4} mol) in water (30 ml). After stirring for 1 hr,

the red precipitate was collected by filtration, washed with water (30 ml) and methanol (30 ml)

and dried under vacuum at 45 °C overnight. Yield (0.28 g, 50%).

2.2.2.1.2.5.   [Fe(atrz)₃](BF₄)₂ – Compound 6

[Fe(atrz)₃](BF₄)₂ **(6-Sol)** was prepared by dropwise addition of Iron(II) tetrafluoroborate

hexahydrate (0.94 g, 2.8 mM) and L-ascorbic acid (0.05 g) in methanol (100 ml) to 4-amino-4-H-

1,2,4-triazole (0.7 g, 8.3 mM) in methanol (100 ml). The mixture was stirred under ambient

conditions overnight. The white precipitate was collected by filtration and washed with water and

methanol then dried overnight under vacuum yielding a fine white powder (0.88 g, 64%).

2.2.2.1.3.   Automated Milling – Compound 6

Fe(BF$_4$)$_2$.6H$_2$O (1 eqv.) and 4-amino-4H-1,2,4-triazole (atrz, 3 eqv.) were added to Teflon cups with two 7 mm Teflon balls. The cups were inserted into a Retsch MM400 mill and shaken at frequency of 25 Hz for either 10 or 90 minutes. No washing was carried out on mechanically prepared samples, yielding compounds **6-BM10** and **6-BM90** respectively.

2.2.2.2.   Chapter 4: Post-synthetic Solid-State Metathesis of 1,2,4-Triazole Based Spin Crossover Materials

2.2.2.2.1.   Mechanochemical Synthesis

[Fe(atrz)$_3$]Cl$_2$ (compound **7**) was prepared by grinding iron(II) chloride tetrahydrate (4.00 g, 20.12 mM) and 4-amino-4H-1,2,4-triazole (5.10 g, 60.66 mM) in a glass pestle and mortar in the absence of solvent. Within 2 minutes of grinding, the sample became a wet purple paste. Continued grinding for 10 minutes resulted in a dry purple powder. The resulting powder was washed using a 9:1 ratio of methanol and water containing L-ascorbic acid (2% by mass), filtered and dried under vacuum at 45 °C, yielding a fine purple powder (7.20 g, 94.5% yield).

2.2.2.2.2.   Solid State Metathesis

All solid-state metathesis reactions were carried out using the same procedure. Compound **7** (0.5 g, 1.32 mM) and the corresponding sodium salt in a 5x excess (NaReO$_4$ was only used in a 2x excess, due to cost of the starting material) were ground in a glass pestle and mortar in the absence of solvent. After grinding for 15 minutes, the resulting powder was collected and washed using a 9:1 ratio of methanol and water containing L-ascorbic acid (2% by mass), filtered and dried under vacuum at 45°C.

2.2.2.3. Chapter 5: Developing a Systematic Approach to Mechanochemical Screening for New Spin Crossover Materials

2.2.2.3.1. Screening of 1,2,4-Triazole Systems

Preliminary testing on the potential mechanochemical synthesis of triazole systems was carried out using four iron(II) salts, and two triazole ligands known to yield SCO-active products by traditional solution-state methods. The salts used were $Fe(BF_4)_2.6H_2O$, $FeCl_2.4H_2O$, $FeSO_4.7H_2O$ and $(NH_4)_2Fe(SO_4)_2.6H_2O$. The two triazole ligands used were 4-H-1,2,4-triazole (Htrz) and 4-amino-1,2,4-triazole (atrz), the structures of which are shown in Figure 2.10. In all instances, the iron(II) salt (1 eqv.) was manually ground in a pestle and mortar for 5 minutes with the triazole ligand (3 eqv.) yielding samples **S1-8**, whereby S refers to screening sample, actual quantities used during screening are shown in Table 2.1. No washing was carried out on these samples to save time during the screening process. L-ascorbic acid (10% by mass) was added to both $FeCl_2.4H_2O$ reactions, to reduce oxidation of the iron(II) salt.

<div align="center">

(a) 1H-1,2,4-triazole (Htrz)

(b) 4-amino-4H-1,2,4-triazole (atrz)

</div>
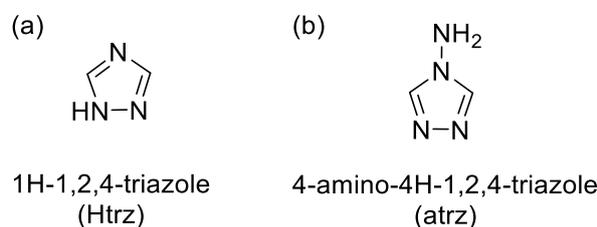
Figure 2.10: (a) Structure of 1H-1,2,4-triazole (Htrz). **(b)** Structure of 4-amino-4H-1,2,4-triazole (atrz).

Table 2.1: Table of quantities used in triazole screening.

4-H-1,2,4-triazole (Htrz)				Sample
Iron Salt	Salt (mol)	Ligand (mol)	L-Ascorbic Acid	
$Fe(BF_4).6H_2O$	$1.5x10^{-4}$	$4.5x10^{-4}$	-	**S1**
$FeCl_2.4H_2O$	$5.0x10^{-4}$	$2.1x10^{-3}$	10%	**S2**
$FeSO_4.7H_2O$	$1.8x10^{-4}$	$8.7x10^{-4}$	-	**S3**
$(NH_4)_2Fe(SO_4)_2.6H_2O$	$2.3x10^{-4}$	$1.1x10^{-3}$	-	**S4**
4-Amino-1,2,4-triazole (atrz)				
$Fe(BF_4).6H_2O$	$2.4x10^{-4}$	$9.5x10^{-4}$	-	**S5**
$FeCl_2.4H_2O$	$2.6x10^{-4}$	$1.1x10^{-3}$	10%	**S6**
$FeSO_4.7H_2O$	$1.6x10^{-3}$	$5.3x10^{-3}$	-	**S7**
$(NH_4)_2Fe(SO_4)_2.6H_2O$	$2.0x10^{-4}$	$9.0x10^{-4}$	-	**S8**

2.2.2.3.2. Screening of 1,10-phenanthroline and 2,2'-bipyridine Derivatives

2.2.2.3.2.1. Fe(phen)$_2$(NCS)$_2$

Screening of Fe(phen)$_2$(NCS)$_2$ was done by both one-pot and two-pot approaches. One-pot synthesis was done by combining (NH$_4$)$_2$Fe(SO$_4$)$_2$.6H$_2$O (0.121 g, 3.1×10^{-4} mol), KSCN (0.094 g, 5.1×10^{-4} mol) and 2 equivalents of 1,10'-phenathroline (0.087 g, 5.2×10^{-4} mol) in a pestle and mortar with manual grinding for 5 minutes, yielding **S9-1pot**. No washing was carried out on the products. A portion of the product (**S9-1pot**) was dried at 80 °C for 3 hours followed by thermal treatment at 200 °C for 10 hours, yielding **S9-1pot-Heat**.

Two-pot synthesis was done by manual grinding of (NH$_4$)$_2$Fe(SO$_4$)$_2$.6H$_2$O (0.102 g, 2.6×10^{-4} mol) with 1,10'-phenanthroline (0.102 g, 6.1×10^{-4} mol) for 5 minutes in an agate pestle and mortar. To the resulting powder, KSCN (0.085 g, 8.7×10^{-4} mol) was added with additional grinding for 5 minutes, yielding **S9-2pot**. No washing was carried out on the products.

2.2.2.3.2.2. 1,10-phenathroline and 2,2'-bipyridine Derivatives

Screening of 1,10-phenanthroline (phen) and 2,2'-bipyridine (bipy) derivatives was carried out using the same synthetic approach. Fe(BF$_4$)$_2$.6H$_2$O (1 eqv.) was ground with KSCN (2 eqv.) and the phen or bipy derivatives (3 eqv.) for 5 minutes, yielding **x-As** (where x is the compound number and -As represents a sample which had not been modified or washed). A portion of **x-As** for each complex was heated to 150 °C for 10 hours, yielding **x-Heat**. Exact quantities used are shown in **Table 2.2**.

Table 2.2: Quantities used in the ligand screening of 4,7-diphenyl-1,10'-phenanthroline (**Ph-phen**), 4,7-dimethyl-1,10'-phenanthroline (**Me-phen**), 2,2'-bipyridyl (**bipy**), 5,5'-dimethyl-2,2'bipyrdyl (**Me-bipy**) and 4,4'-dinonyl-2,2'bipyridyl (**Nonyl-bipy**).

Sample Name	Fe(BF$_4$)$_2$.6H$_2$O	KSCN	Ligand	Quantity
S10	35.0 mg (0.10 mmol)	20.1 mg (0.21 mmol)	Ph-phen	103 mg (0.31 mmol)
S11	57.0 mg (0.17 mmol)	32.8 mg (0.34 mmol)	Me-phen	100 mg (0.48 mmol)
S12	180.0 mg (0.53 mmol)	104.0 mg (1.01 mmol)	bipy	250 mg (1.60 mmol)
S13	153.0 mg (0.45 mmol)	87.9 mg (0.90 mmol)	Me-bipy	250 mg (1.36 mmol)
S14	27.0 mg (0.08 mmol)	15.5 mg (0.16 mmol)	Nonyl-bipy	100 mg (0.25 mmol)

Heteroleptic complex synthesis was attempted using a similar approach. Fe(BF)$_4$.6H$_2$O (1 eqv.), KSCN (2 eqv.) and two bipyridyl derivatives (1.5 eqv. Each) were ground in a glass pestle and mortar for 5 minutes yielding **x-As**. A portion of **x-As** for each complex was heated to 150 °C for 10 hours, yielding **x-Heat**. Exact quantities used are shown in Table 2.3.

Table 2.3: Quantities used in the mixed ligand screening of 2,2'-bipyridyl (**bipy**), 5,5'-dimethyl-2,2'bipyrdyl (**Me-bipy**) and 4,4'-dinonyl-2,2'bipyridyl (**Nonyl-bipy**).

Sample Name	Fe(BF$_4$)$_2$.6H$_2$O	KSCN	Ligand One	Quantity	Ligand Two	Quantity
S15	324.2 mg (0.96 mmol)	186.7 mg (1.92 mmol)	bipy	150.0 mg (0.96 mmol)	Me-bipy	176.9 mg (0.96 mmol)
S16	123.9 mg (0.37 mmol)	71.3 mg (0.73 mmol)	bipy	57.3 mg (0.36 mmol)	Nonyl-bipy	150.0 mg (0.37 mmol)
S17	123.9 mg (0.37 mmol)	71.3 mg (0.72 mmol)	Me-bipy	67.6 mg (0.37 mmol)	Nonyl-bipy	150.0 mg (0.37 mmol)

2.2.2.3.3.   Hydrotris(1-pyrazolyl)borates

Complexes with hydrotris(1-pyrazolyl)borates were prepared using the same approach. Fe(BF$_4$)$_2$.6H$_2$O (1 eqv.) and K[HB(pz)$_3$] (2 eqv.) or K[HB(3,5-dimethyl-pz)$_3$] (2 eqv.) were ground in glass pestle and mortar for 5 minutes. The mixed ligand product was prepared using the same approach but with one equivalent of each ligand, yielding the products labelled **x-As**. A fraction of

x-As was purified by reduced pressure sublimation, yielding **x-Sublim**. Actual reagent quantities are shown in **Table 2.4**.

Table 2.4: Quantities used in screening of Hydrotris(1-pyrazolyl)borates. Potassium tri(3,5-dimethyl-1-pyrzolyl)borohydride, K[HB(pz)3], and potassium tri(1-pyrazolyl)borohydride, K[HB(3,5-(CH3)2-pz)3].

Sample Name	Fe(BF$_4$)$_2$.6H$_2$O	K[HB(pz)$_3$]	K[HB(3,5-(CH$_3$)$_2$-pz)$_3$]
S18	100.4 mg (0.30 mmol)	153.2 mg (0.61 mmol)	-
S19	79.0 mg (0.23 mmol)	-	153.4 mg (0.46 mmol)
S20	200.8 mg (0.59 mmol)	157.0 mg (0.62 mmol)	201.0 mg (0.60 mmol)

2.2.2.3.3.1.   Synthesis of 2,6-di(pyrazol-3-yl)pyridine

2,6-di(pyrzol-3-yl)pyridine was prepared in two steps using a previously reported method, as shown in **Scheme 2.1**.[63] A suspension of 2,6-diacetyl pyridine (5 g, 30 mmol) in dimethylformamide dimethyl acetate (10 ml, 75 mmol) was refluxed for 10 hrs. The solution was cooled, and the solvent removed in *vacuo*. The resulting solid was recrystallized from chloroform, yielding a yellow powder (**3-bpp-Intermediate**, 2.7 g, 32 %). ^{1}H NMR 400 MHz (DMSO-d^6), Appendix B.1, found ppm δ: 2.95-3.20 [s, **12H**, **(CH$_3$)$_2$**NCHCHCOPyCOCHCHN**(CH$_3$)$_2$**], 6.53 [d, **2H**, (CH$_3$)$_2$NCH**CH**COPyCO**CH**CHN(CH$_3$)$_2$] J = 9.8 Hz, 7.85-7.82 [d, **2H**, (CH$_3$)$_2$N**CH**CHCOPyCOCH**CH**N(CH$_3$)$_2$] J = 13.2 Hz, 8.06 [m, **3H**, (CH$_3$)NCHCHCO**Py**COCHCHN(CH$_3$)$_2$, J = 6.7 Hz]. ^{13}C NMR (DMSO-d^6), Appendix B.2., found ppm δ: 36.91, 44.67, 122.74, 137.99, 154.39, 154.46 and 184.32.

To a suspension of **3-bpp-Intermediate** (2.7 g, 10 mmol) in ethanol (15 ml), hydrazine hydrate (51%, 2 ml, 20 mmol) was added dropwise. The resulting solution was stirred at room temperature for 3 hours. Water (70 ml) was added, a light brown precipitate formed and was collected by filtration. The resulting powder was recrystallized in chloroform, yielding a white powder (**3-bpp**, 1.7 g, 80%). ^{1}H NMR 400 MHz (DMSO-d^6), Figure B.2, found ppm δ: 6.91-6.98 [s,

2H, NHNCHC**H**CPyCC**H**CHNNH], 7.59-7.95 [m, **5H**, NHNC**H**CHC**Py**CCHC**H**NNH], 13.01-13.49 [s, **2H,**

N**H**].
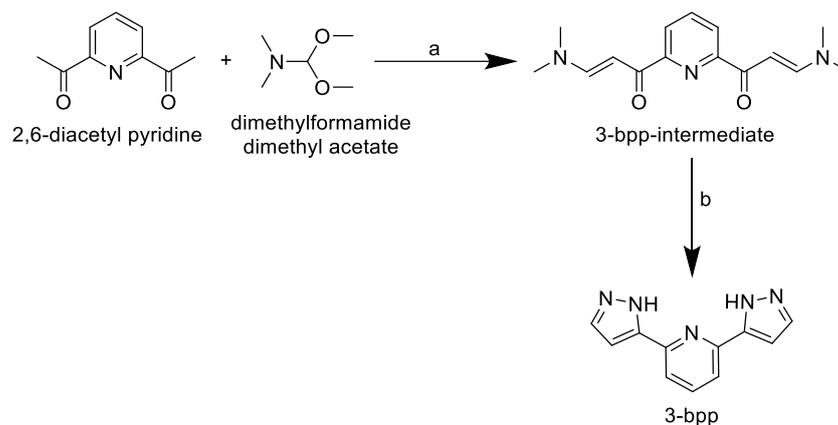
Scheme 2.1: Synthetic route to **3-bpp**. Reaction conditions: (a) Reflux, 10 hours and (b) Room temperature, 3 hours.

2.2.2.3.3.2. Screening of 3-bpp and Derivatives

For all 3-bpp and derivative screening, the same procedure was used, unless otherwise stated. $FeA_x.sH_2O$ (1 eqv.) was ground in a glass pestle and mortar with 3-bpp, or derivatives, (2 eqv.) for 5 minutes. The resulting materials were tested for visually observable thermochromism on heating and/or cooling. Actual quantities used are shown below in **Table 2.5**.

Table 2.5: Quantities used in the screening of 3bpp and its derivatives, using four different iron(II) salts.

Sample Name	$FeA_x.SH_2O$	Quantity	3-bpp
Sample 21-BF$_4$	Fe(BF$_4$)$_2$.6H$_2$O	14.2 mg (0.04 mmol)	19.0 mg (0.09 mmol)
Sample 21-Cl	FeCl$_2$.4H$_2$O	8.8 mg (0.04 mmol)	18.8 mg (0.09 mmol)
Sample 21-SO$_4$	(NH$_4$)$_2$Fe(SO$_4$)$_2$.6H$_2$O	17.7 mg (0.05 mmol)	18.9 mg (0.09 mmol)
Sample 21-C$_2$O$_4$	FeC$_2$O$_4$.2H$_2$O	8.5 mg (0.05 mmol)	18.2 mg (0.09 mmol)

Sample Name	$FeA_x.SH_2O$	Quantity	3-bpp-PhOH (g)
Sample 22-BF$_4$	Fe(BF$_4$)$_2$.6H$_2$O	42.7 mg (0.13 mmol)	100.8 mg (0.26 mmol)
Sample 22-Cl	FeCl$_2$.4H$_2$O	25.1 mg (0.13 mmol)	101.5 mg (0.26 mmol)
Sample 22-SO$_4$	(NH$_4$)$_2$Fe(SO$_4$)$_2$.6H$_2$O	49.6 mg (0.13 mmol)	100.5 mg (0.26 mmol)
Sample 22-C$_2$O$_4$	FeC$_2$O$_4$.2H$_2$O	22.8 mg (0.13 mmol)	102.0 mg (0.26 mmol)

Sample Name	$FeA_x.SH_2O$	Quantity	3-bpp-PhOCH$_3$ (g)
Sample 23-BF$_4$	Fe(BF$_4$)$_2$.6H$_2$O	12.0 mg (0.35 mmol)	31.0 mg (0.72 mmol)
Sample 23-Cl	FeCl$_2$.4H$_2$O	7.0 mg (0.35 mmol)	30.5 mg (0.72 mmol)
Sample 23-SO$_4$	(NH$_4$)$_2$Fe(SO$_4$)$_2$.6H$_2$O	13.9 mg (0.35 mmol)	31.7 mg (0.75 mmol)
Sample 23-C$_2$O$_4$	FeC$_2$O$_4$.2H$_2$O	6.4 mg(0.35 mmol)	30.2 mg (0.71 mmol)

Sample Name	$FeA_x.SH_2O$	Quantity	3-bpp-Napth (g)
Sample 24-BF$_4$	Fe(BF$_4$)$_2$.6H$_2$O	29.1 mg (0.86 mmol)	80.5 mg (0.17 mmol)
Sample 24-Cl	FeCl$_2$.4H$_2$O	17.2 mg (0.87 mmol)	81.0 mg (0.18 mmol)
Sample 24-SO$_4$	(NH$_4$)$_2$Fe(SO$_4$)$_2$.6H$_2$O	33.8 mg (0.86 mmol)	80.4 mg (0.17 mmol)
Sample 24-C$_2$O$_4$	FeC$_2$O$_4$.2H$_2$O	15.5 mg (0.86 mmol)	80.5 mg (0.17 mmol)

Synthesis of heteroleptic ligand (3bpp and derivatives) systems was done using the same synthetic approach. Fe(BF$_4$)$_2$.6H$_2$O (1 eqv.) and one equivalent of two different ligands were ground in a glass pestle and mortar for 5 minutes. In a similar manner to the homoleptic systems

tested above, the resulting complexes were tested for visible thermochromism. Actual quantities

used are shown in **Table 2.6**.

Table 2.6: Quantities used in the mixed ligand screening of 3-bpp, 3-bpp-PhOH, 3-bpp-PhOCH$_3$ and 3-bpp-Napth.

Sample Name	Fe(BF$_4$)$_2$.6H$_2$O	Ligand One	Quantity	Ligand Two	Quantity
Sample **25**	8.0 mg (0.24 mmol)	3-bpp	5.0 mg (0.24 mmol)	3-bpp-PhOH	9.4 mg (0.22 mmol)
Sample **26**	4.1 mg (0.12 mmol)	3-bpp	2.5 mg (0.12 mmol)	3-bpp-PhOCH$_3$	5.0 mg (0.18 mmol)
Sample **27**	8.0 mg (0.24 mmol)	3-bpp	5.0 mg (0.24 mmol)	3-bpp-Napth	11.0 mg (0.24 mmol)
Sample **28**	8.0 mg (0.24 mmol)	3-bpp-PhOH	9.3 mg (0.25 mmol)	3-bpp-PhOCH$_3$	10.0 mg (0.24 mmol)
Sample **29**	8.5 mg (0.25 mmol)	3-bpp-PhOH	5.0 mg (0.13 mmol)	3-bpp-Napth	5.9 mg (0.13 mmol)
Sample **30**	8.0 mg (0.24 mmol)	3-bpp-PhOCH$_3$	10.0 mg (0.24 mmol)	3-bpp-Napth	11.0 mg (0.24 mmol)

2.3. References

1 J. K. Noh, S. Kim, H. Kim, W. Choi, W. Chang, D. Byun, B. W. Cho and K. Y. Chung, *Sci. Rep.*, 2014, **4**, 1–9.

2 S. L. James, C. J. Adams, C. Bolm, D. Braga, P. Collier, T. Friščić, F. Grepioni, K. D. M. Harris, G. Hyett, W. Jones, A. Krebs, J. Mack, L. Maini, A. G. Orpen, I. P. Parkin, W. C. Shearouse, J. W. Steed and D. C. Waddell, *Chem. Soc. Rev.*, 2012, **41**, 413–447.

3 D. Braga, L. Maini and F. Grepioni, *Chem. Soc. Rev.*, 2013, **42**, 7638–7648.

4 D. Tan and T. Friščić, *European J. Org. Chem.*, 2018, **2018**, 18–33.

5 E. W. Müller, H. Spiering and P. Gütlich, *Chem. Phys. Lett.*, 1982, **93**, 567–571.

6 W. A. Baker and H. M. Bobonich, *Inorg. Chem.*, 1964, **3**, 1184–1188.

7 E. König and K. Madeja, *Chem. Commun. (London)*, 1966, **3**, 61–62.

8 E. Konig and K. Madeja, *Inorg. Chem.*, 1967, **6**, 48–55.

9 B. Gallois, J. A. A. Real, C. Hauw and J. Zarembowitch, *Inorg. Chem.*, 1990, **29**, 1152–1158.

10 M. Reiher, *Inorg. Chem.*, 2002, **41**, 6928–6935.

11 S. F. Matar, P. Guionneau and G. Chastanet, *Int. J. Mol. Sci.*, 2015, **16**, 4007–4027.

12 J. Laisney, A. Tissot, G. Molnár, L. Rechignat, E. Rivière, F. Brisset, A. Bousseksou and M.-L. Boillot, *Dalt. Trans.*, 2015, **44**, 17302–17311.

13 F. J. Valverde-Muñoz, A. B. Gaspar, S. I. Shylin, V. Ksenofontov and J. A. Real, *Inorg. Chem.*, 2015, **54**, 7906–7914.

14 E. C. Ellingsworth, B. Turner and G. Szulczewski, *RSC Adv.*, 2013, **3**, 3745.

15 P. Ganguli, P. Gütlich, E. W. Müller and W. Irler, *J. Chem. Soc. Dalt. Trans.*, 1981, 441.

16 M. S. Haddad, W. D. Federer, M. W. Lynch and D. N. Hendrickson, *Inorg. Chem.*, 1981, **20**, 131–139.

17 G. Molnár, S. Rat, L. Salmon, W. Nicolazzi and A. Bousseksou, *Adv. Mater.*, 2018, **30**, 1703862.

18 J. A. Real, B. Gallois, T. Granier, S. P. Franz and J. Zarembowitch, *Inorg. Chem.*, 1992, **31**, 4972–4979.

19 N. Tsuchiya, A. Tsukamoto, T. Ohshita, T. Isobe, M. Senna, N. Yoshioka and H. Inoue, *Solid State Sci.*, 2001, **3**, 705–714.

20 O. Roubeau, *Chem. - A Eur. J.*, 2012, **18**, 15230–15244.

21 H. Voisin, C. Aimé, A. Vallée, T. Coradin and C. Roux, *Inorg. Chem. Front.*, 2018, **5**, 2140–2147.

22 K. A. Zenere, S. G. Duyker, E. Trzop, E. Collet, B. Chan, P. W. Doheny, C. J. Kepert and S. M. Neville, *Chem. Sci.*, 2018, **9**, 5623–5629.

23   R. Torres-Cavanillas, L. Lima-Moya, F. D. Tichelaar, H. W. Zandbergen, M. Giménez-Marqués and E. Coronado, *Dalt. Trans.*, 2019, **48**, 15465–15469.

24   K. Jonas, A. Jean-Paul, C. Renée, C. Epiphane, K. Olivier, J. G. Haasnoot, G. Françoise, J. Charlotte, A. Bousseksou, L. Jorge, V. François and G. V. Anne, *Chem. Mater.*, 1994, **6**, 1404–1412.

25   D. Savard, C. Cook, G. D. Enright, I. Korobkov, T. J. Burchell and M. Murugesu, *CrystEngComm*, 2011, **13**, 5190–5197.

26   M. M. Dîrtu, A. Rotaru, D. Gillard, J. Linares, E. Codjovi, B. Tinant and Y. Garcia, *Inorg. Chem.*, 2009, **48**, 7838–7852.

27   M. Seredyuk, A. B. Gaspar, V. Ksenofontov, S. Reiman, Y. Galyametdinov, W. Haase, E. Rentschler and P. Gütlich, *Chem. Mater.*, 2006, **18**, 2513–2519.

28   M. Seredyuk, A. B. Gaspar, M. C. Muñoz, M. Verdaguer, F. Villain and P. Gütlich, *Eur. J. Inorg. Chem.*, 2007, 4481–4491.

29   M. B. Bushuev, D. P. Pishchur, I. V. Korolkov and K. A. Vinogradova, *Phys. Chem. Chem. Phys.*, 2017, **19**, 4056–4068.

30   Y. Garcia, P. J. van Koningsbruggen, E. Codjovi, R. Lapouyade, O. Kahn and L. Rabardel, *J. Mater. Chem.*, 1997, **7**, 857–858.

31   M. Seredyuk, A. B. Gaspar, V. Ksenofontov, M. Verdaguer, F. Villain and P. Gutlich, *Inorg. Chem.*, 2009, **48**, 6130–6141.

32   I. A. Gural'skiy, B. O. Golub, S. I. Shylin, V. Ksenofontov, H. J. Shepherd, P. R. Raithby, W. Tremel and I. O. Fritsky, *Eur. J. Inorg. Chem.*, 2016, **2016**, 3191–3195.

33   V. Niel, J. M. Martinez-Agudo, M. C. Muñoz, A. B. Gaspar and J. A. Real, *Inorg. Chem.*, 2001, **40**, 3838–3839.

34   J. Cirera, *Rev. Inorg. Chem.*, 2014, **34**, 199–216.

35   N. F. Sciortino, K. A. Zenere, M. E. Corrigan, G. J. Halder, G. Chastanet, J. F. Létard, C. J. Kepert and S. M. Neville, *Chem. Sci.*, 2016, **8**, 701–707.

36   A. Galet, M. C. Muñoz, V. Martínez and J. A. Real, *Chem. Commun.*, 2004, 2268–2269.

37   Y. Meng, Y. J. Dong, Z. Yan, Y. C. Chen, X. W. Song, Q. W. Li, C. L. Zhang, Z. P. Ni and M. L. Tong, *Cryst. Growth Des.*, 2018, **18**, 5214–5219.

38   T. Kosone, I. Tomori, D. Akahoshi, T. Saito and T. Kitazawa, *Crystals*, 2018, **8**, 415.

39   M. Ohba, K. Yoneda, G. Agusti, M. C. Mu??oz, A. B. Gaspar, J. A. Real, M. Yamasaki, H. Ando, Y. Nakao, S. Sakaki and S. Kitagawa, *Angew. Chemie - Int. Ed.*, 2009, **48**, 4767–4771.

40   P. D. Southon, L. Liu, E. A. Fellows, D. J. Price, G. J. Halder, K. W. Chapman, B. Moubaraki, K. S. Murray, J. F. Létard and C. J. Kepert, *J. Am. Chem. Soc.*, 2009, **131**, 10998–11009.

41   M. C. Muñoz and J. A. Real, *Coord. Chem. Rev.*, 2011, 255, 2068–2093.

42   A. Ney, P. Poulopoulos and K. Baberschke, *Europhys. Lett.*, 2001, **54**, 820–825.

43   M. Kuru, E. Ongun, A. Özmetin, M. Hançer and A. E. Özmetin, *Mater. Sci. Forum*, 2018, **915**,

16–21.

44   N. Fontaíña-Troitiño, S. Liébana-Viñas, B. Rodríguez-González, Z. A. Li, M. Spasova, M. Farle and V. Salgueiriño, *Nano Lett.*, 2014, **14**, 640–647.

45   M. Sawicki, T. Devillers, S. Gałęski, C. Simserides, S. Dobkowska, B. Faina, A. Grois, A. Navarro-Quezada, K. N. Trohidou, J. A. Majewski, T. Dietl and A. Bonanni, *Phys. Rev. B - Condens. Matter Mater. Phys.*, 2012, **85**, 1–4.

46   D. C. Harris and M. D. Bertolucci, *Symmetry and Spectroscopy : An Introduction to Vibrational and Electronic Spectroscopy*, Dover Publications Inc., Second., 1989.

47   R. R. Jones, D. C. Hooper, L. Zhang, D. Wolverson and V. K. Valev, *Nanoscale Res. Lett.*, 2019, **14**, 231.

48   S. Yeung, Edward, M. Heiling and G. J. Small, *Spectrochim. Acta*, 1975, **31A**, 1921–1931.

49   Y. A. Tobon, C. Etrillard, O. Nguyen, J.-F. Létard, V. Faramarzi, J.-F. Dayen, B. Doudin, D. M. Bassani and F. Guillaume, *Eur. J. Inorg. Chem.*, 2012, **2012**, 5837–5842.

50   K. L. Ronayne, H. Paulsen, A. Höfer, A. C. Dennis, J. A. Wolny, A. I. Chumakov, V. Schünemann, H. Winkler, H. Spiering, A. Bousseksou, P. Gütlich, A. X. Trautwein and J. J. McGarvey, *Phys. Chem. Chem. Phys.*, 2006, **8**, 4685–4693.

51   Y. Zhang, K. Bennett and S. Mukamel, *J. Phys. Chem. A*, 2018, **122**, 6524–6531.

52   L. Piñeiro-López, N. Ortega-Villar, M. C. Muñoz, G. Molnár, J. Cirera, R. Moreno-Esparza, V. M. Ugalde-Saldívar, A. Bousseksou, E. Ruiz and J. A. Real, *Chem. - A Eur. J.*, 2016, **22**, 12741–12751.

53   M. Fumanal, F. Jiménez-Grávalos, J. Ribas-Arino and S. Vela, *Inorg. Chem.*, 2017, **56**, 4474–4483.

54   S. Xue, Y. Guo, A. Rotaru, H. Müller-Bunz, G. G. Morgan, E. Trzop, E. Collet, J. Oláh and Y. Garcia, *Inorg. Chem.*, 2018, **57**, 9880–9891.

55   H. A. Liebhafsky, H. G. Pfeiffer, E. H. Winslow and P. D. Zemany.W., *X-Ray Absorption and Emission in Analytical Chemistry. Wiley, New York, 1960. 367 pp. Illus.*, 1960, vol. 132.

56   N. Yuan, M. H. Majeed, É. G. Bajnóczi, A. R. Persson, L. R. Wallenberg, A. K. Inge, N. Heidenreich, N. Stock, X. Zou, O. F. Wendt and I. Persson, *Catal. Sci. Technol.*, 2019, **9**, 2025–2031.

57   J. Kowalska and S. DeBeer, *Biochim. Biophys. Acta - Mol. Cell Res.*, 2015, **1853**, 1406–1415.

58   C. Cartier, P. Thuery, M. Verdaguer, J. Zarembowitch and A. Michalowicz, *Le J. Phys. Colloq.*, 1986, **47**, C8-563-C8-568.

59   L. Salmon and L. Catala, *Comptes Rendus Chim.*, 2018, **21**, 1230–1269.

60   B. Ravel and M. Newville, *J. Synchrotron Radiat.*, 2005, **12**, 537–541.

61   J. J. Rehr, J. J. Kas, F. D. Vila, M. P. Prange and K. Jorissen, *Phys. Chem. Chem. Phys.*, 2010, **12**, 5503–5513.

62   B. Michen, C. Geers, D. Vanhecke, C. Endes, B. Rothen-Rutishauser, S. Balog and A. Petri-

Fink, *Sci. Rep.*, 2015, **5**, 9793.

63   Y. Lin and S. A. J. Lang, *J. Heterocycl. Chem*, 1977, **14**, 345.

Chapter 3: Initial Synthesis and Exploring the Effects of Mechanochemical Synthesis of Spin Crossover Materials

3.1. Introduction

3.1.1. Mechanochemical Synthesis

Proof of concept demonstrating the application of mechanochemistry to synthesise SCO materials is presented. Attempted synthesis of known materials is undertaken to determine the applicability of mechanochemical synthesis to several different families of SCO compounds and comparison between mechanochemically synthesised and solution-state synthesised samples will be used to determine any effects on SCO properties resulting from mechanochemical synthesis. The synthesis of several SCO families serves to act as a proof of concept for mechanochemical synthesis and to determine whether a general approach can be used or whether each family requires different mechanochemical approaches.

3.1.2. Effect of Grinding Solution-Synthesised Materials

The effects of grinding solution synthesised SCO materials were first reported by Haddad *et al*. in the ferric complex [Fe(3-OCH$_3$-SalEen)$_2$]PF$_6$ (3-OCH$_3$-SalEen = Schiff base product of 3-methoxy-salicylaldehye and N-ethylethylenediamine). Both manually grinding a portion of the sample in a pestle and mortar and milling a separate fraction in a ball mill caused a decrease in both abruptness and completeness of transition, with a substantial increase in residual HS fraction at low temperatures. Recrystallisation of the ground sample regenerated the original SCO properties, thus, they attributed the changing properties to the grinding process and not an alternative degenerative process, as later confirmed by Sorai *et al*.[2] Continued investigation of the effects of grinding and the related effect of metal dilution in the ferric complexes was carried out by Haddad *at al*.[3,4] Metal-dilution by cobalt doping was observed to cause the same decrease in abruptness and completeness of transition, as well as a decrease in HS fraction at high temperatures. The effects caused by both grinding and metal-dilution were consistent but the effects of grinding were attributed to changes in crystal quality affecting long-range communication between SCO-active sites[4] and the effects of metal dilution is attributed to

reduced communication between SCO-active sites. The same effects of grinding were observed in multiple ferric complexes.[5]

Investigation of the effects of grinding in the extensively studies ferrous complex [Fe(phen)$_2$(NCS)$_2$] was also carried out by Ganguli *et al.*[6], in an attempt to address the discrepancies in SCO properties reported by different synthetic procedures. The complex had been studied using a wide variety of analytical techniques including: SQUID magnetometry,[7–9] Mössbauer spectroscopy,[8,9] IR and Far-IR,[8,10] UV-vis,[8] heat capacity[11] and XRD.[7,8] But the only technique that showed differences between the differently prepared samples was magnetometry, which showed significant differences in transition abruptness and residual HS fraction at low temperatures. Ganguli *et al.*[6] prepared samples using two different reported procedures, 'precipitation' and 'extraction', and investigated the differences in crystal quality and size. This correlated the more gradual transition and increase in residual HS fraction with the smaller crystals and the larger proportion of crystalline defects prepared by the 'extraction' method, as shown in Figure 3.1. The relationship between crystal quality and SCO abruptness and completeness was further confirmed in multiple ferrous complexes.[12–14]
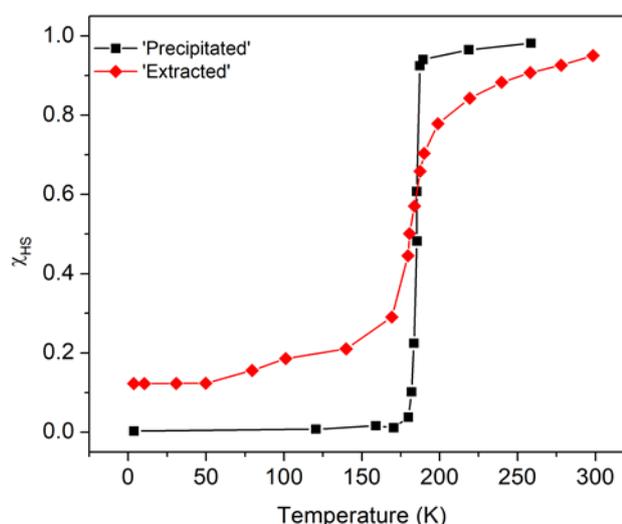

Figure 3.1: HS fraction χ_{HS} from the Mössbauer spectra as a function of temperature of [Fe(phen)$_2$(NCS)$_2$] prepared by 'precipitation' (■) and 'extraction' (◆), digitised from literature.[6]

The effects of particle size on spin crossover properties are of particular importance due to recent interest in preparation and application of nanoparticles.[15] Amongst other methods, synthesis of SCO nanoparticles (SCO NPs) has been carried out using the reverse micelle technique.[16,17] This has provided opportunities to investigate size effects without the corresponding crystalline defects introduced by grinding and milling of macroscopic samples. Forestier *et al.*[18] investigated the effect of particle size in the system $[Fe(atrz)_3]Br_2$, with particles between 1.2 μm and 30 nm. The SCO properties remained consistent between bulk samples and particles in size down to 70 nm, with similar abruptness and hysteresis width. Across all particle sizes, the transitions presented comparable abruptness with relatively insignificant differences in residual HS fraction at low temperature. At sizes around 30-50 nm the hysteresis almost completely disappeared, which was attributed to a proposed 'limit' on the presence of hysteresis that is thought to be dependent on the triazole class of SCO materials owing to different surface chemistry. Further studies on two other members of the triazole family $[Fe(Htrz)_2(trz)](BF_4)_2$ and $[Fe(Htrz)_{2.95}(atrz)_{0.05}](ClO_4)_2$ by Galán-Mascarós *et al.*[19] contradicted these initial reports with nanoparticles as small as 4-18 nm displaying wide hysteresis up to 40 K.

It is clear from literature that the grinding process introduces at least two variables: introduction of crystal defects and reduction of particle size. Introduction of crystalline defects appears to cause a decrease in both abruptness and completeness of transition, with an increase in residual HS fraction at low temperatures.[4,6] However, the effects of reducing particle size are less clear, with an apparently complicated dependence on the changing properties. For $[Fe(atrz)_3]Br_2$, $Fe(Htrz)_2(trz)](BF_4)_2$ and $[Fe(Htrz)_{2.95}(atrz)_{0.05}](ClO_4)_2$ the abruptness of the transitions was maintained down to the smallest particle sizes.[18,19] However, the particle size at which hysteresis was retained varied from sample to sample.

The very fact that mechanochemical synthesis yields crystalline materials indicates some degree of crystallite growth occurring during the grinding process, which is in opposition to the decrease in crystallinity observed for post-synthetic grinding. It is unclear whether the effects of synthetic grinding (mechanochemistry) will be the same as the effects observed for post-synthetic

grinding and milling of macroscopic samples previously reported in literature. All mechanochemical synthesis of spin crossover materials currently reported have been synthesised using manual grinding (by hand).

3.1.3. Aims

In this chapter, mechanochemistry will be used to synthesise SCO-materials for the first time. Synthesis of a simple 0-D structure will be undertaken ([Fe(phen)$_2$(NCS)$_2$]) following by attempted synthesis of increasingly complex structures going from 1-D triazole chains, to 2-D and 3-D Hofmann Clathrate-like materials. Prior to this work, mechanochemical synthesis of SCO materials had not been reported. Previously reported SCO materials were synthesised by both mechanochemistry and solution-state techniques for comparison. The resulting complexes were then analysed by PXRD, VT Raman spectroscopy and SQUID magnetometry to determine if mechanochemistry is possible for SCO materials and to provide an initial evaluation of the effect of the procedure on SCO properties. Following the initial synthesis, detailed analysis of ideal compounds was undertaken to further investigate the effects of mechanochemical synthesis on the properties. Detailed comparison of mechanochemically and solution-state synthesised compounds ([Fe(atrz)$_3$]SO$_4$ and Fe(pz)[Au(CN)$_2$]$_2$) will allow for the effects of mechanochemical synthesis to be investigated. After which, comparison between different mechanochemical techniques (manual grinding and automatic milling for different amounts of time) would allow for effects of different mechanochemical synthetic routes to be observed. Following the discussion, SQUID magnetometry was used to characterise SCO properties, PXRD analysis allowed structural effects and coherent domain size to be investigated. Fe-edge EXAFS was used to investigate short-range structural order and degree of amorphisation, hydration effects were characterised by TGA and particle size and shape was measured by TEM.

3.1.4.   Samples

Below is a list of samples used in this chapter.

Compound **1-Mech**: [Fe(phen)$_3$](SCN)$_2$ (Mechanically synthesised)

Compound **1-Heat**: [Fe(phen)$_2$(NCS)$_2$] (Thermolysis)

Compound **1-Wash**: [Fe(phen)$_2$(NCS)$_2$] (Washed)

Compound **2-Mech**: [Fe(Htrz)$_3$](BF$_4$)$_2$ (Mechanically synthesised)

Compound **2-Dried**: [Fe(Htrz)$_3$](BF$_4$)$_2$ (Oven Dried)

Compound **2-Sol**: [Fe(Htrz)$_3$](BF$_4$)$_2$ (Solution Synthesised)

Compound **3-Mech**: [Fe(atrz)$_3$]SO$_4$ (Mechanically synthesised)

Compound **3-Dried**: [Fe(atrz)$_3$]SO$_4$ (Oven Dried)

Compound **3-Wash**: [Fe(atrz)$_3$]SO$_4$ (Washed)

Compound **3-Sol**: [Fe(atrz)$_3$]SO$_4$ (Solution Synthesised)

Compound **4-Mech**: Fe(4-phpy)$_2$[Ni(CN)$_4$] (Mechanically synthesised)

Compound **4-LAG**: Fe(4-phpy)$_2$[Ni(CN)$_4$] (Liquid Assisted Grinding)

Compound **4-Sol**: Fe(4-phpy)$_2$[Ni(CN)$_4$] (Solution Synthesised)

Compound **5-Mech**: Fe(pz)[Au(CN)$_2$]$_2$ (Mechanically synthesised)

Compound **5-Sol**: Fe(pz)[Au(CN)$_2$]$_2$ (Solution Synthesised)

Compound **6-Sol**: [Fe(atrz)$_3$](BF$_4$)$_2$ (Solution synthesised)

Compound **6-Mech**: [Fe(atrz)$_3$](BF$_4$)$_2$ (Mechanically synthesised)

Compound **6-BM10**: [Fe(atrz)$_3$](BF$_4$)$_2$ (Ball milled for 10 minutes)

Compound **6-BM90**: [Fe(atrz)$_3$](BF$_4$)$_2$ (Ball milled for 90 minutes)

3.2. Results and Discussion

3.2.1. Fe(phen)₂(NCS)₂

Thermogravimetric analysis (TGA) showing the conversion of [Fe(phen)$_3$](SCN)$_2$ to Fe(phen)$_2$(NCS)$_2$ by thermolysis as shown in Figure 3.2, with an overall reaction scheme presented in Scheme 3.1. Water loss at an 80°C isotherm was calculated by assuming all mass lost was due to removal of water and no water remained in the sample. The mass loss corresponds to ≈ 5 H$_2$O. The loss of phenanthroline was calculated using the same assumption that all mass lost by 250°C was due to the removal of phenanthroline. The mass loss indicates the loss of 0.90 moles of phenanthroline per mole of [Fe(phen)$_3$](SCN)$_2$. The loss of phenanthroline is less than 1 equivalent relative to [Fe(phen)$_3$](SCN)$_2$, this is attributed to the presence of impurities in the sample, such as the by-product of the reaction (KBF$_4$) and the possibility of unreacted reagents.

$$\text{Fe(BF}_4)_2.6\text{H}_2\text{O} + 3(\text{phen}) + 2\text{KSCN} \xrightarrow{\;\infty\;} \underset{\text{SCO-Inactive}}{[\text{Fe(phen)}_3](\text{SCN})_2} \xrightarrow{\;\triangle\;} \underset{\text{SCO-Active}}{\text{Fe(phen)}_2(\text{NCS})_2}$$

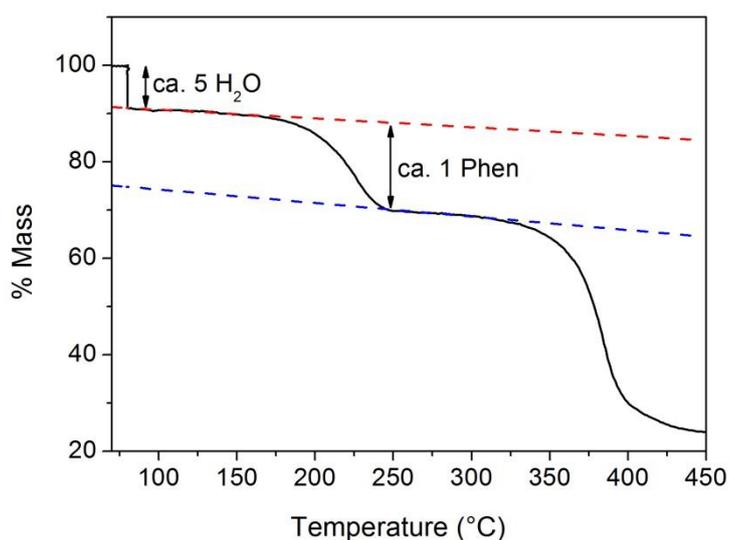**Scheme 3.1**:Mechanochemical synthesis of [Fe(phen)$_3$](SCN)$_2$ and thermolysis to form Fe(phen)$_2$(NCS)$_2$.

Figure 3.2: TGA showing the conversion of **1-Mech** to **1-Heat** *via* Thermolysis.

Formation of the SCO-active complex $Fe(phen)_2(NCS)_2$ was monitored by comparison of PXRD using data simulated from single crystal x-ray diffraction ($Fe(phen)_3](SCN)_2.3H_2O$ CSD Code: KOQDEZ,[20] $Fe(phen)_2(NCS)_2$ – CSD Code: KEKVIF).[20,21] The pattern collected for **1-Mech** shows a combination of $[Fe(phen)_3](SCN)_2$, unreacted reagents and by-products, as shown in Figure 3.3.

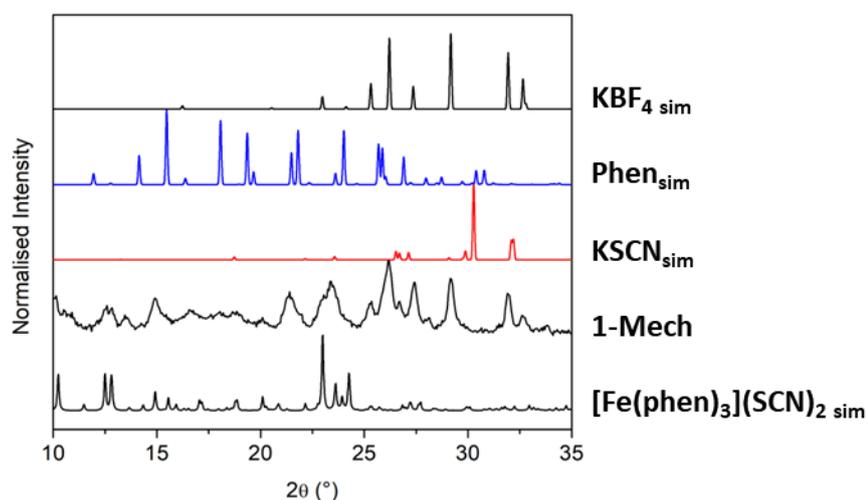**Figure 3.3:** PXRD patterns of compound **1**. Bottom to top: $[Fe(phen)_3](SCN)_2$ simulated from single crystal data (CSD Code: KOQDEZ)[20], **1-Mech**, KSCN simulated from single crystal data,[22] 1,10-phenanthroline simulated from single crystal data (CSD Code: OPENAN)[23] and KBF_4 simulated from single crystal data.[24]

After thermolysis, **1-Heat** yielded a crystalline powder with a qualitative match to the simulated $Fe(phen)_2(NCS)_2$ pattern (denoted Bis_{sim} in Figure 3.4). The magnetic properties of the molecular compound $Fe(phen)_2(NCS)_2$ have not been reported as being sensitive to the presence of solvents, unlike the triazole and clathrate complexes.[25,26] As a consequence, the effect of washing the sample to remove residual impurities was investigated on this sample so as to minimise the possibility of inducing solvent effects. Comparison of powder diffraction patterns before and after washing shows virtually no difference in the composition of the product as a result of washing. The exception is the removal of peaks in the range 25 – 30° on washing, which is attributed to the removal of impurities that are also observed in the PXRD pattern of the **1-Mech** sample. The main impurity was KBF_4, as shown in Figure 3.4. An important factor to consider is that despite grinding for several minutes, the powders remained crystalline.
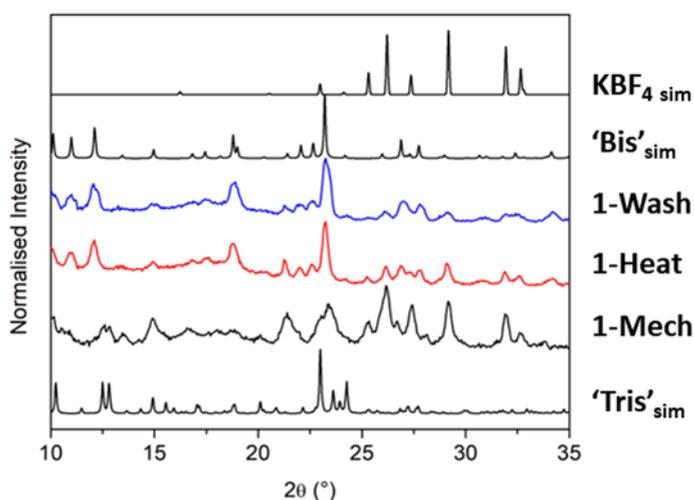
Figure 3.4: PXRD patterns of compound **1**. Bottom to top: [Fe(phen)$_3$](SCN)$_2$, simulated from single crystal data (CSD Code: KOQDEZ)[20], **1-Mech**, **1-Heat**, **1-Wash**, Fe(phen)$_2$(NCS)$_2$ simulated from single crystal data (CSD Code: KEKVIF)[21] and KBF$_4$ simulated from single crystal data.[24]

Variable temperature Raman spectroscopy was used to confirm the presence of SCO activity. Literature has previously reported the transition temperature around 175 K, therefore Raman spectra were collected at 298 K and 130 K. As expected for **1-Mech**, no significant changes in the Raman spectra were observed, see Figure 3.5(a), reflecting the absence of SCO behaviour in this complex. The differences in peak intensities are attributed to temperature effects on the ligand. After thermolysis, **1-Heat** exhibited significant differences in multiple regions of the spectra, as shown in Figure 3.5(b). With notable differences in three regions, 300-800 cm^{-1}, 1200-1700 cm^{-1} and 2000-2200 cm^{-1}. The spectra obtained at 298 K, represents the high spin state of Fe(phen)$_2$(NCS)$_2$ as confirmed by comparison with spectra reported by Bousseksou *et al*.[27] However, the spectra collected at low temperature (130 K) includes characteristic peaks of both spin states, indicating an intermediate temperature. The intermediate state is consistent with observations of Bousseksou *et al*.[27] in which the presence of both spin states was attributed to the fact that spin crossover occurs as a statistical phenomenon in which the proportion of each spin state present at any given temperature may vary smoothly or abruptly, there is no progressive structural change on the molecular level.[28,29] Further discussion on the use of Raman spectroscopy for characterisation of SCO materials is available at 2.1.6.3.
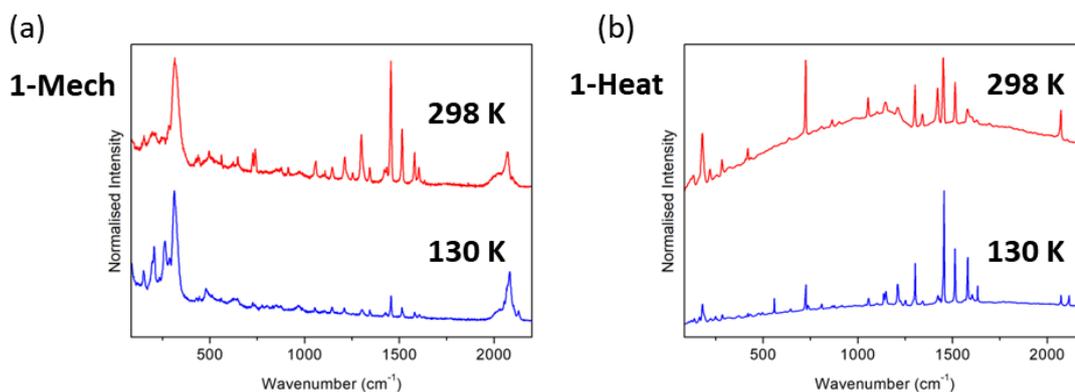
Figure 3.5: Normalised Raman spectra at 298 K and 130 K. **(a) 1-Mech** indicating no SCO activity and **(b) 1-Heat** showing changes attributed to SCO activity.

SQUID magnetometry was used to confirm SCO activity, as shown in Figure 3.6(a). The absence of SCO-activity in **1-Mech** was confirmed by the constant magnetic response across the full temperature range. However, **1-Heat** underwent SCO with $T_{1/2}\uparrow$ = $T_{1/2}\downarrow$ = 174 K and 'smoothness' = 16 K. After washing, the product maintained SCO-activity with a slight increase in transition temperature with $T_{1/2}\uparrow$ = $T_{1/2}\downarrow$ = 175 K and a more abrupt transition, 'smoothness' = 9 K which was tentatively attributed to the potential removal of the smallest particles during the filtering process. **1-Wash** also showed a larger $\Delta\chi_M T$ compared to **1-Heat** which was attributed to the removal of impurities that allowed for a more accurate estimation of M_w, when calculating $\chi_M T$. $T_{1/2}\uparrow$, $T_{1/2}\downarrow$ and ΔT were not significantly altered by the washing process, confirming the insensitivity of $Fe(phen)_2(NCS)_2$ to solvents.
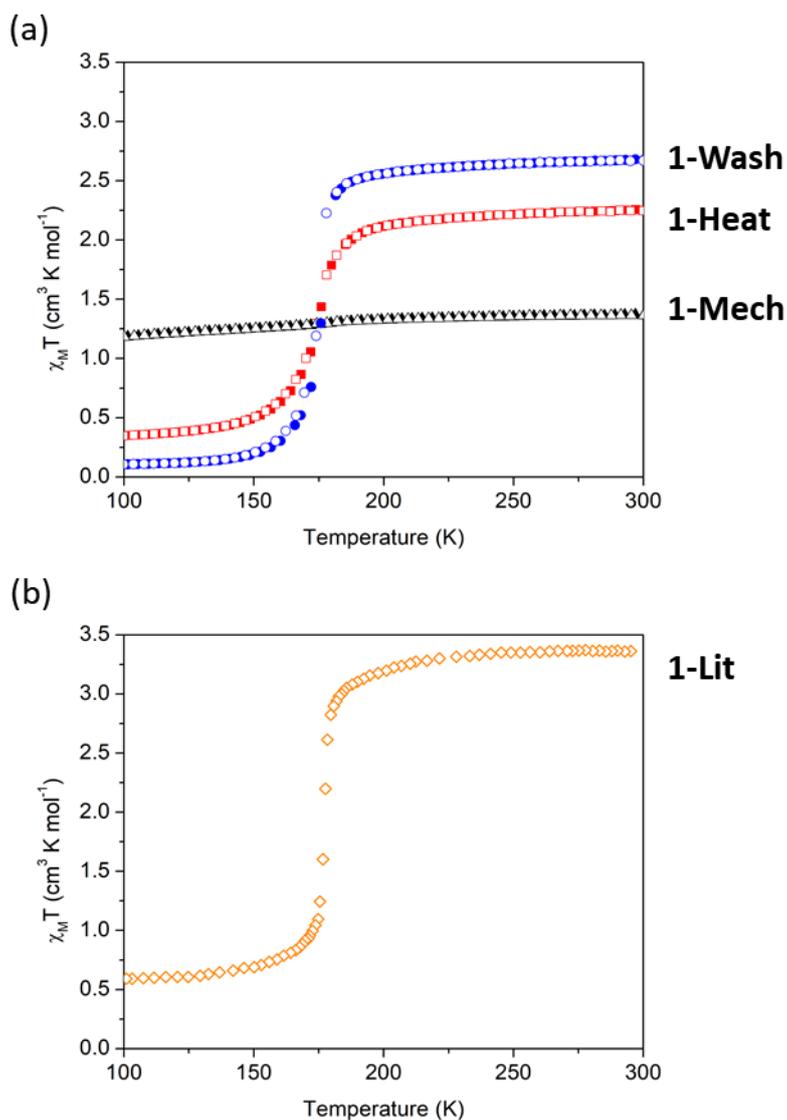
Figure 3.6: Temperature dependent SQUID data (2nd cycle) for compound **1**. (a) Overlaid **1-Mech**, **1-Heat** and **1-Wash**. (b) **1-Lit** digitised plot from literature.[21]

The magnetic properties of both **1-Heat** and **1-Wash** are consistent with previous literature reports ($T_{1/2}\uparrow$ = $T_{1/2}\downarrow$ = 178 K and 'smoothness' = 4 K), as shown in Figure 3.6(b).[21] However, the SCO transition temperatures have shown significant variation between batches in literature (165-190 K)[6,8,21,30,31] The mechanochemically synthesised samples exhibited a slightly lower transition temperature and a more gradual transition than previous reports. This was attributed to differences in crystallinity which are explored further below. The SCO properties of Fe(phen)$_2$(NCS)$_2$ have previously been shown to be significantly dependent on crystal quality and size.[12,32] As crystal size and quality decrease, a decrease in transition temperature and more

gradual transitions have been reported. However, previous reports have also suggested the almost complete loss of SCO properties in samples with prolonged post-synthetic milling.[6,8,21,30,31] By contrast, direct mechanochemical synthesis yielded crystalline products that showed SCO activity comparable to solution synthesised materials. Comparisons of SCO properties prepared by mechanochemistry and literature solution methods are shown in Table 3.1.

Table 3.1: SCO properties for compound **1**. *Values calculated based on data in references.[6,8,21,30,31]

	$T_{1/2}\uparrow$(K)	$T_{1/2}\downarrow$ (K)	ΔT (K)	'Smoothness' (K)
1-Mech	-	-	-	-
1-Heat	174	174	0	16
1-Wash	175	175	0	9
1-Lit*	165 - 190	165 - 190	0	4 - 12

3.2.2. 1-D Coordination Polymers

Triazole-based 1-D SCO coordination polymers have become the subject of a huge number of studies owing to their high temperature range of operation and relative ease of chemical modification, making them extremely attractive from the point of view of applications.[33] Two members of the family were prepared using mechanochemistry, namely [Fe(Htrz)$_3$](BF$_4$)$_2$ (compound **2**) and [Fe(atrz)$_3$]SO$_4$ (compound **3**).

3.2.2.1. [Fe(Htrz)$_3$](BF$_4$)$_2$ (Compound 2)

[Fe(Htrz)$_3$](BF$_4$)$_2$ ($T_{1/2}\uparrow$ = 282 K and $T_{1/2}\downarrow$ = 276 K) and [Fe(Htrz)$_3$](BF$_4$)$_2$.H$_2$O ($T_{1/2}\uparrow$ = 345 K and $T_{1/2}\downarrow$ = 323 K) have been previously reported with different SCO properties.[34] Thermal conversion from the hydrated to dehydrated form occurs above 400 K, with reversion back to the hydrated form over time at room temperature on absorption of atmospheric H$_2$O. The Htrz ligand has also

been shown to deprotonate leading to the complex [Fe(Htrz)$_2$(trz)](BF$_4$) which has two polymorphs. An α phase (T$_{1/2}$↑ = 385 K and T$_{1/2}$↓ = 345 K) and a β phase (T$_{1/2}$↑ = 350 K and T$_{1/2}$↓ = 325 K).[34] Mechanochemical synthesis yielded a purple powder, indicating the presence of a LS species, which underwent a reversible colour change to white on heating.
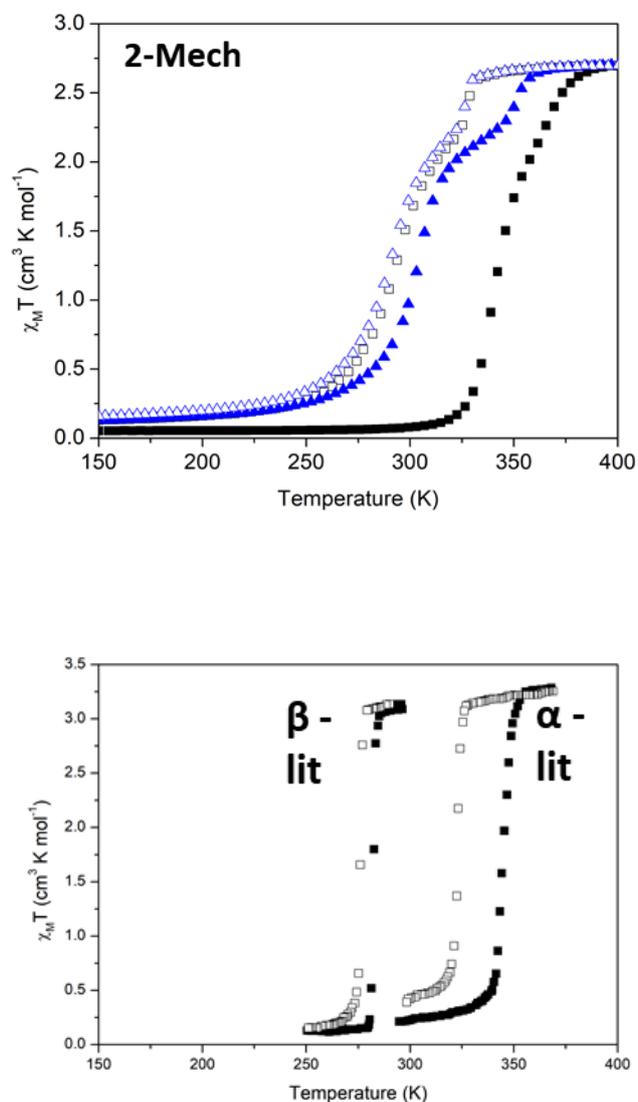

Figure 3.7: (a) Temperature dependent SQUID magnetometry data (2 cycles) for compound **2-Mech**. Cycle 1 Heating ■, Cycle 2 Heating ▲ and Cooling △. **(b)** Digitised plots of [Fe(Htrz)$_3$](BF$_4$)$_2$, α-form denoted **α-lit** and β-form denoted **β-lit**.[34] (Heating ■ and Cooling ▢)

The magnetic properties of the mechanochemically synthesised product are shown in Figure 3.7(a). As previously discussed, the first heating cycle was different to subsequent cycling. The first heating cycle suggested the presence of a two-step transition whereby the low temperature

step represents 80% of the total change and the high temperature step represents the remaining 20% (Low temperature step: $T_{1/2}\uparrow$ = 346 K and High temperature step: $T_{1/2}\uparrow$ = 373 K). The low temperature step was similar to the β-form of [Fe(Htrz)$_2$(trz)](BF$_4$) ($T_{1/2}\uparrow$ = 350 K))[34] and the high temperature step was consistent with the α-form of [Fe(Htrz)$_2$(trz)](BF$_4$) ($T_{1/2}\uparrow$ = 385 K).[34] The presence of a two-step transition strongly supports the formation of at least two reaction products, both of which have previously been reported in literature, as shown in Figure 3.7(b). The second cycle yielded slightly different properties, showing the presence of two forms with (Low temperature step: $T_{1/2}\uparrow$ = 303 K, $T_{1/2}\downarrow$ = 291 K and High temperature step: $T_{1/2}\uparrow$ = 351 K, $T_{1/2}\downarrow$ = 329 K). As with the first heating cycle, the ratio of the two-step transitions was 80:20.
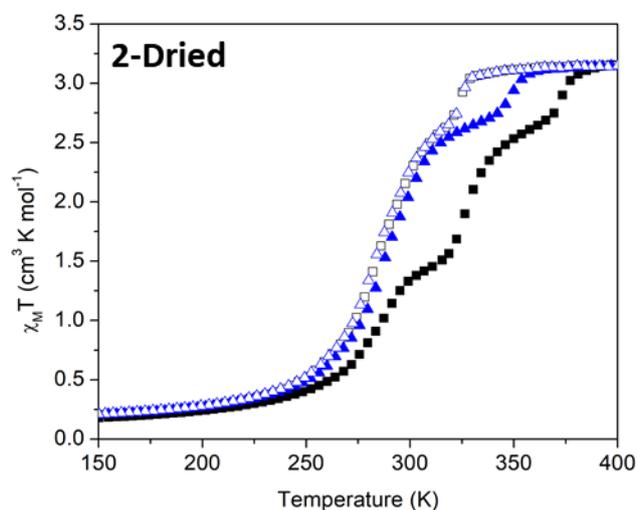

Figure 3.8: Temperature dependent SQUID data (2 cycles) for compound **2-Dried**. Cycle 1 Heating ■ and Cooling □, Cycle 2 Heating ▲ and Cooling △.

2-Mech was dried to reduce potential solvent effects. After drying, **2-Dried** exhibited slightly modified SCO properties, as shown in Figure 3.8. The number of different forms in the sample appeared to increase with the presence of a three-step transition in a 40:50:10 ratio (1: $T_{1/2}\uparrow$ = 280 K, 2: $T_{1/2}\uparrow$ = 330 K and 3: $T_{1/2}\uparrow$ = 373 K). The first step corresponds to the β-form of [Fe(Htrz)$_3$](BF$_4$)$_2$ and the second and third transitions are similar in temperature to the α phases of

[Fe(Htrz)$_3$](BF$_4$)$_2$ and [Fe(Htrz)$_2$(trz)](BF$_4$) respectively, as shown in Figure 3.7(b). The first heating cycle converted the α-form into the β-form, therefore repeated cycling only showed the presence of two different forms. (1: $T_{1/2}\uparrow$ = 295 K, $T_{1/2}\downarrow$ = 291 K and 2: $T_{1/2}\uparrow$ = 350 K, $T_{1/2}\downarrow$ = 326 K). Further research into polymorph selectivity for this complex system would require extensive solution-state and mechanochemical experimentation, with the possibility of applying various liquid assisted grinding and seeding techniques, which was beyond the scope of this work. However, it is clear that the mechanochemical synthesis yielded a SCO-active material that is a mixture of previously reported forms. Due to the presence of multiple forms, further investigation using PXRD was not undertaken.
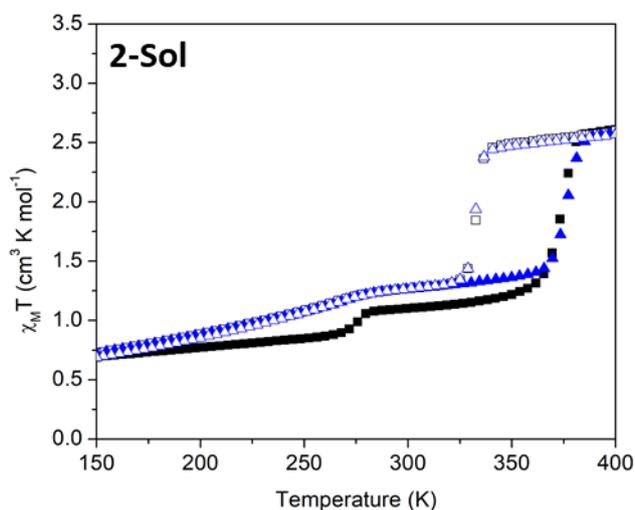

Figure 3.9: Temperature dependent SQUID data (2 cycles) for compound **2-Sol**. Cycle 1 Heating ■ and Cooling □, Cycle 2 Heating ▲ and Cooling △.

The difficulty of polymorph selection was highlighted by the attempted solvent synthesis of [Fe(Htrz)$_3$](BF$_4$)$_2$, resulting in the presence of at least two forms, as shown in Figure 3.9. As with other samples of compound **2**, the first heating cycle is different to subsequent cycling. The first heating shows SCO (1: $T_{1/2}\uparrow$ = 275 K and 2: $T_{1/2}\uparrow$ = 377 K), consistent with [Fe(Htrz)$_3$](BF$_4$)$_2$ and β-[Fe(Htrz)$_2$(trz)](BF$_4$) in a 30:70 ratio. In subsequent cycling, the first transition is significantly more gradual but two transitions remained with a 30:70 ratio (1: $T_{1/2}\uparrow$ = 270 K, $T_{1/2}\downarrow$ = 270 K and 2:

$T_{1/2}\uparrow$ = 377 K, $T_{1/2}\downarrow$ = 332 K). Comparison of SCO properties for **2-Mech**, **2-Dried**, **2-Sol** and literature reports are shown in Table 3.2.

Table 3.2: SCO properties for compound **2**, with comparison with literature.[34] *Represents mixtures of different forms, exhibiting two different transition temperatures.

	Synthesised		
	2nd $T_{1/2}\uparrow$ (K)	2nd $T_{1/2}\downarrow$ (K)	$\Delta T_{1/2}$ (K)
2-Mech*	303 and 351	291 and 329	12 and 22
2-Dried*	295 and 350	291 and 326	4 and 24
2-Sol*	270 and 377	270 and 332	0 and 45
	Literature		
[Fe(Htrz)$_3$](BF$_4$)$_2$	282	276	6
[Fe(Htrz)$_3$](BF$_4$)$_2$.H$_2$O	345	323	18
α-[Fe(Htrz)$_2$(trz)](BF$_4$)	385	345	40
β-[Fe(Htrz)$_2$(trz)](BF$_4$)	350	325	25

The aim for this investigation was to prepare SCO materials mechanochemically; this was shown to be successful. However, further research into the potential for polymorph selectivity was not explored in this instance. Future work with this complex should focus on exploring the possibility of polymorph selectivity, likely by controlling grinding duration or intensity and introducing various solvents to explore their effects in the form of liquid assisted grinding (LAG).

3.2.2.2.   [Fe(atrz)$_3$]SO$_4$ (Compound 3)

[Fe(atrz)$_3$]SO$_4$ (where atrz = 4-amino-1,2- 4-triazole, compound **3**) is a member of the triazole family and has been previously prepared using solution-state techniques.[35] Like other members of this family it shows a pronounced colour change from purple in the LS state at ambient temperature, to white in the HS state above 350 K. Previous solution-state synthesis of [Fe(atrz)$_3$]SO$_4$ used FeSO$_4$.7H$_2$O as the iron salt, while mechanochemical synthesis was carried out using (NH$_4$)$_2$Fe(SO$_4$).6H$_2$O (Mohr's salt). The use of Mohr's salt led to an increase in by-products for the reaction, through the formation of (NH$_4$)$_2$SO$_4$. However, Mohr's salt is less susceptible to oxidation due to the acidic ammonium ions slowing the oxidation process.[36] Due to the stability and ease of use of this compound, a more thorough investigate was undertaken.

As with previously discussed compounds, mechanochemical synthesis yielded crystalline powders suitable for PXRD analysis, as shown in Figure 3.10. No PXRD patterns were previously reported in literature for the complex [Fe(atrz)$_3$]SO$_4$ therefore direct comparison was not possible. However, comparison with the patterns obtained for the solution synthesis sample (**3-Sol**) showed similarities. The pattern of **3-Mech** was consistent with **3-Sol** and after washing (**3-Wash**) impurities were removed. High temperature drying of **3-Mech** yielded **3-Dried** which also had a similar PXRD pattern. However, washing was not carried out on the dried product, due to known effects of water on triazole complexes,[37] and the additional peak at 12° was attributed the presence of impurities, such as (NH$_4$)$_2$SO$_4$, formed during the drying process.
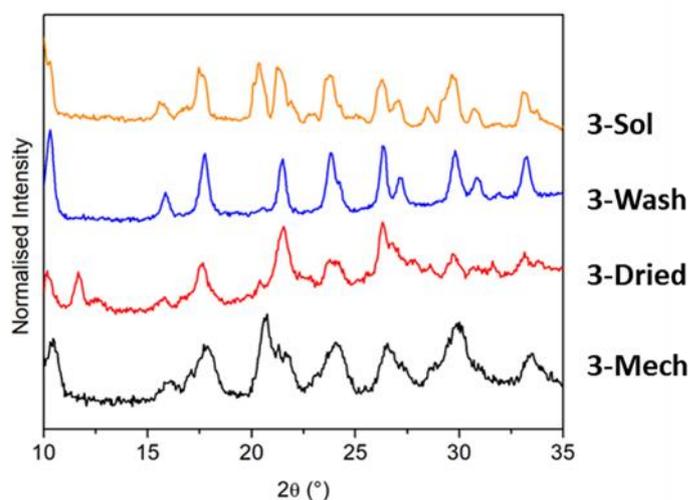
Figure 3.10: PXRD patterns of compound **3.** Bottom to top: **3-Mech**, **3-Dried**, **3-Wash** and **3-Sol**.

Additional PXRD patterns of both **3-Sol** and **3-Mech**, are shown in Figure 3.11 and allow for the use of Scherrer analysis to investigate particle size. Both **3-Sol** and **3-Mech** have similar patterns, with the exception of additional peaks present in **3-Mech** associated with the presence of $(NH_4)_2SO_4$, which is formed as a by-product through the use of $(NH_4)_2Fe(SO_4)_2.6H_2O$ as the iron(II) salt, as confirmed by comparison with the simulated pattern.[38] Both patterns are consistent with the previously reported pattern for solution synthesised $[Fe(atrz)_3]SO_4$.[39] Further analysis of Bragg peak width indicates significant broadening attributable to a reduction in coherent domain size, which was estimated using the Scherrer equation. The crystalline domain size of **3-Mech** was determined to be *c.a.* 30 nm. This value represents a lower estimate for domain size as the equation is unable to differentiate between broadening introduced by crystalline domain size and crystalline defects. Additionally, as the unit cell of the complex is unknown, is it not possible to determine the correct shape-factor contribution for the sample. As a result, the standard shape-factor value was used (0.9) which assumes a spherical shape. Application of the Scherrer equation to **3-Sol** was not possible as the Bragg peaks showed no broadening due to particle size, indicating an exceptionally large domain size. The ability to determine domain size of **3-Mech** *via* Scherrer analysis but not **3-Sol** is clear evidence of the significantly smaller domain sizes in the mechanochemically prepared sample.
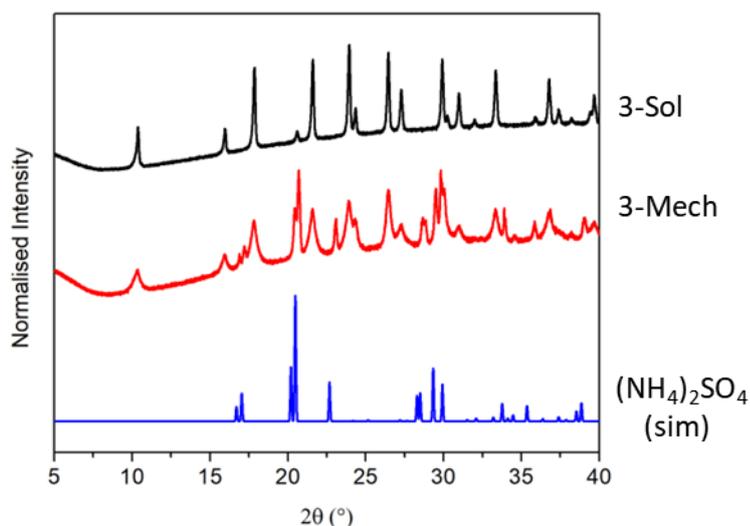
Figure 3.11: Normalised PXRD for [Fe(atrz)₃]SO₄ prepared by solution (Top: **3-Sol**) and mechanochemistry (Middle: **3-Mech**). Bottom: **Simulated (NH₄)₂SO₄.**[38]

Variable temperature Raman spectroscopy was used to characterise the HS and LS species in **3-Mech**, as shown in Figure 3.12. After heating to 415 K, the Raman spectrum was significantly different to the spectrum collected at 300 K, confirming changes in bonding for the system as a function of temperature. The most significant changes in spectra occurred in the ranges 50-300 cm^{-1} and 1250-1500 cm^{-1}. The changes within the range 50-300 cm^{-1} were previously discussed by Urakawa *et al.*[40] where the transition from LS to HS for the complex [Fe(Htrz)₂(trz)]BF₄ caused three bands, previously attributed to Fe-N,[41] to be redshifted, similar changes were observed in Figure 3.12, for **3-Mech**.
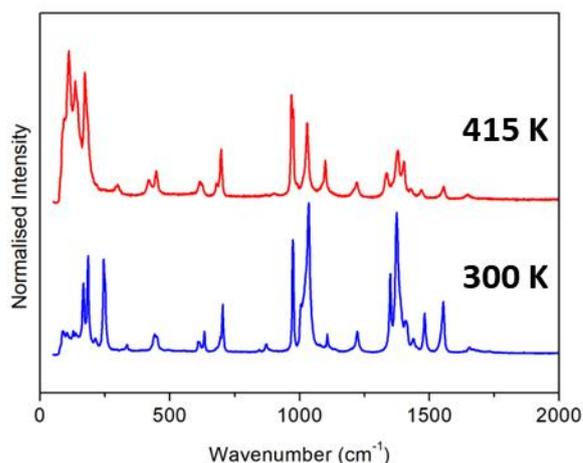
Figure 3.12: Normalised variable temperature Raman spectra at 300 K and 415 K for compound **3-Mech**.

The molar magnetic susceptibility as a function of temperature, also indicated the presence of SCO in **3-Mech**, as shown in Figure 3.13(a). As previously discussed, the first cycle displayed different SCO properties to subsequent cycling ($T_{1/2}\uparrow$ = 365 K), this is primarily attributed to the removal of water from the system (7.5 %), as shown by mass loss *via* TGA (Figure 3.14).
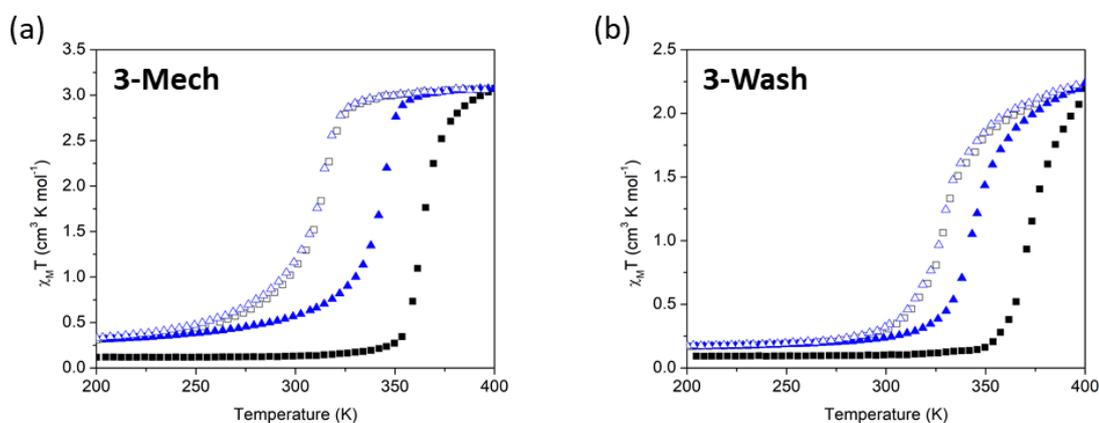
Figure 3.13: Temperature dependent SQUID data, two cycles. Cycle 1 Heating ■ and Cooling □, Cycle 2 Heating ▲ and Cooling △. (a) Mechanochemically synthesised [Fe(atrz)$_3$]SO$_4$, **3-Mech**. (b) Washed version of **3-Mech**, **3-Wash**.

Subsequent cycling resulted in reproducible SCO transitions, ($T_{1/2}\uparrow$ = 346 K, $T_{1/2}\downarrow$ = 315 K and 'smoothness' = 20 K). Triazole systems have previously displayed high sensitivity to the degree of hydration.[25,35,42] Washing **3-Mech** led to significantly modified SCO properties ($T_{1/2}\uparrow$ = 350 K, $T_{1/2}\downarrow$ = 334 K and 'smoothness' = 28 K), as shown in Figure 3.13(b). The addition of water during the

washing procedure increased the transition temperature leading to a potentially incomplete transition at 400 K and a more gradual transition, the extent of the effects water has on the SCO properties was not fully investigated and requires further research. Repeated cycling led to a decrease in transition temperature ($T_{1/2}\uparrow$ = 350 K). Therefore, high temperature drying was used to improve reproducibility of the SCO properties (**3-Dried**).
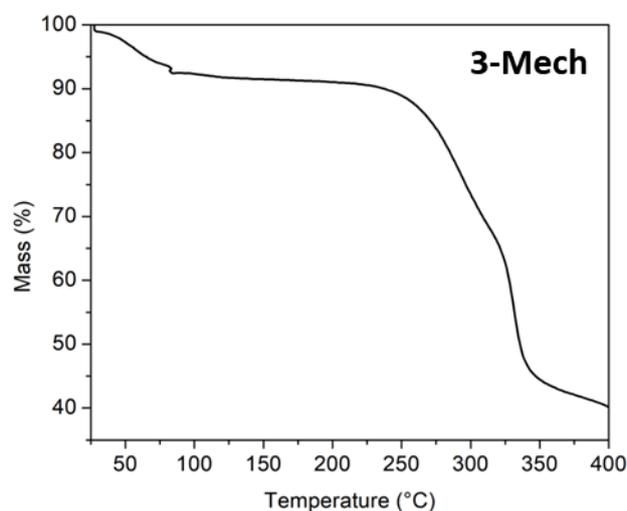
Figure 3.14: TGA plot for **3-Mech**, showing mass loss as a function of temperature with a 1 hr Isotherm at 80 °C.

After drying, the SCO properties were also modified, as shown in Figure 3.15(a). For **3-Dried**, $T_{1/2}\uparrow$ decreased compared to **3-Mech** from 346 K to 338 K and $T_{1/2}\downarrow$ increased from 315 K to 325 K which reduced the width of hysteresis significantly (31 K to 13 K). The SCO properties after drying were significantly more reproducible and comparison with a solution synthesised sample (**3-Sol**) shows similar properties. **3-Dried** transitions were significantly more abrupt ('Smoothness' = 9 K) than **3-Mech** and **3-Wash**, with comparable abruptness to **3-Sol** ('Smoothness' = 12 K), as shown in Figure 3.15(b). A difference between the magnetic properties of the solution and mechanochemically synthesised samples is the calculated values for $\chi_M T$. In **3-Sol**, the values are close to the standard values for an ideal triazole system, between 0 and 3.5 cm3 mol^{-1} K in LS and HS states, respectively. However, **3-Dried** shows both an increase in residual HS at low temperatures and a decrease in $\chi_M T$ at high temperatures, with $\chi_M T$ between 0.75 and 2.25 cm^3 mol^{-1} K for LS and HS states respectively. The increase in residual HS fraction at low temperatures

91

may be attributed to similar causes as in post-synthetic grinding (particle size) but again, absolute X_MT must be interpreted with caution, due to the presence of impurities, which is inevitable without inducing solvent effects through post-synthetic washing.
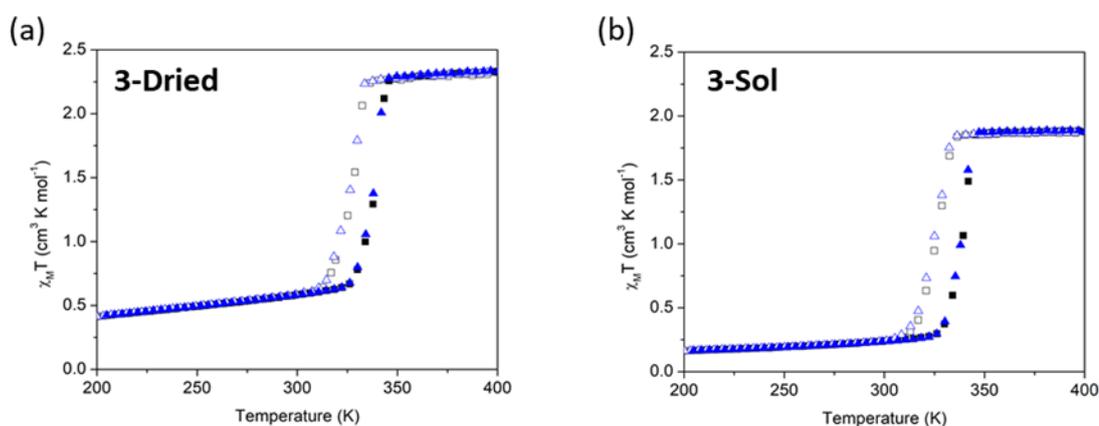

Figure 3.15: Temperature dependent SQUID data, 2 cycles. (a) **3-Dried** and (b) **3-Sol**. Cycle 1 Heating ■ and Cooling □, Cycle 2 Heating ▲ and Cooling △.

The SCO behaviour in $[Fe(atrz)_3]SO_4$ has previously been reported to be highly sensitive to the degree of hydration.[35] This initial literature report stated the presence of a large hysteresis (ΔT = 32 K based on $T_{1/2}\uparrow$ = 355 K and $T_{1/2}\downarrow$ = 323 K). However, this report only showed magnetic data for one heating and cooling cycle; as previously discussed in 1.1.4, due to the 'run-in' effect, it is not uncommon for the first heating cycle to be different from subsequent cycles in many SCO species, with significant differences observed for triazole complexes on cycling with an 'apparent hysteresis' much larger than that observed on subsequent cycling.[43] We previously reported the SCO properties for this complex after vacuum drying and repeated cycling (**3-Lit**), $T_{1/2}\uparrow$ = 338 K, $T_{1/2}\downarrow$ = 325 K (ΔT = 13 K) and a 'smoothness' of 12 K.[39] The observed properties for **3-Sol** are very similar to these values, with only slight differences of 4 K in the absolute temperature values of the transitions. By contrast, the properties of **3-Mech** are moderately different. Both $T_{1/2}\uparrow$ and $T_{1/2}\downarrow$ are shifted to lower temperatures, consistent with previous studies into the effects of post synthetic grinding of SCO active materials.[4] However, **3-Mech** also exhibits an increase in both abruptness and width of hysteresis (ΔT) when compared to **3-Sol**, which indicates an increase in

cooperativity, which is contrary to the effects seen in post-synthetic grinding. Comparison between the SCO properties **3-Sol**, **3-Mech** and **3-Lit** are shown in Table 3.3.

Table 3.3: SCO properties determined by SQUID magnetometry for **3-Sol** and **3-Mech** compared with previous literature reports (**3-Lit**).[39]

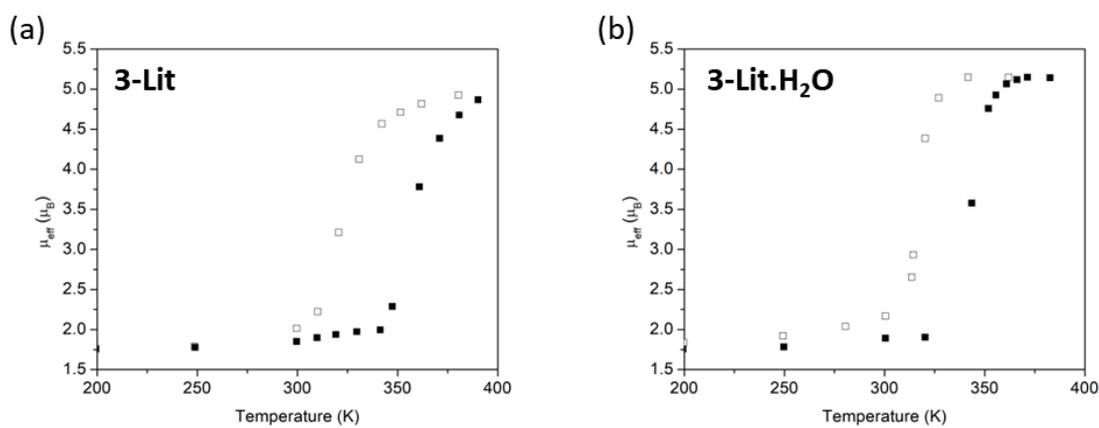| Sample	$T_{1/2}\uparrow$ (K)	$T_{1/2}\downarrow$ (K)	ΔT (K)	'Smoothness'
3-Sol	342	327	15	8
3-Mech	333	315	18	9
3-Lit	338	325	13	12

Figure 3.16: Temperature dependent SQUID data, digitised from literature.[35] (a) **3-Lit** and (b) **3-Lit.H₂O**. On Heating ■ and Cooling □.

Digitised plots of the previously reported effective magnetic moment as a function of temperature, are shown in Figure 3.16.[35] Two forms were proposed, [Fe(atrz)₃]SO₄ (**3-Lit**) and a hydrated form [Fe(atrz)₃]SO₄.H₂O (**3-Lit.H₂O**). **3-Lit** displayed SCO activity with $T_{1/2}\uparrow$ = 355 K, $T_{1/2}\downarrow$ = 323 K and a calculated 'smoothness' = 24 K. Whereas, **3-Lit.H₂O** showed slightly different activity with $\uparrow$ = 346 K, $T_{1/2}\downarrow$ = 319 K and a calculated 'smoothness' = 23 K. Both **3-Lit** and **3-Lit.H₂O** displayed more gradual SCO transitions than **3-Dried**. The differences in properties for **3-Lit** and **3-Lit.H₂O** are relatively small and when differences in particle size and degree of crystallinity are considered, the perceived difference become less significant. The SCO properties of **3-Mech** are similar to both **3-Lit** and **3-Lit.H₂O** with similar transition temperatures, bi-stability

and abruptness. Comparison of magnetic properties for compound **3** with literature are shown in Table 3.4.

Table 3.4: SCO properties for each of compound **3**. *Data taken from [35].

	$T_{1/2}\uparrow$(K)	$T_{1/2}\downarrow$ (K)	ΔT (K)	'Smoothness' (K)
3-Mech	346	315	31	20
3-Dried	338	325	13	9
3-Wash	350	334	16	28
3-Sol	338	325	13	12
3-Lit*	355	323	32	24
3-Lit.H_2O*	346	319	27	23

TEM was used to determine particle morphology and size, as shown in Figure 3.17. Particles of **3-Sol** presented a rod-like morphology, as previously reported for the triazole family.[17] By contrast, the particles of **3-Mech** were a mixture of both rods and spheres. The formation of spherical particles by mechanical synthesis is expected; previous literature reports on the milling of particles with different morphologies have shown a tendency to form spherical particles.[44,45] Due to the rod-like morphology the average length of particles was determined, for **3-Sol** particles of average length 612 ± 371 nm with the range: 130nm to 2030 nm and a median length of 539 nm were measured. For **3-Mech** a significantly smaller average particle size was measured with 92 ± 64 nm calculated with the range: 24 nm to 416 nm and a median length of 73 nm. In both instances a significant particle size distribution was observed.
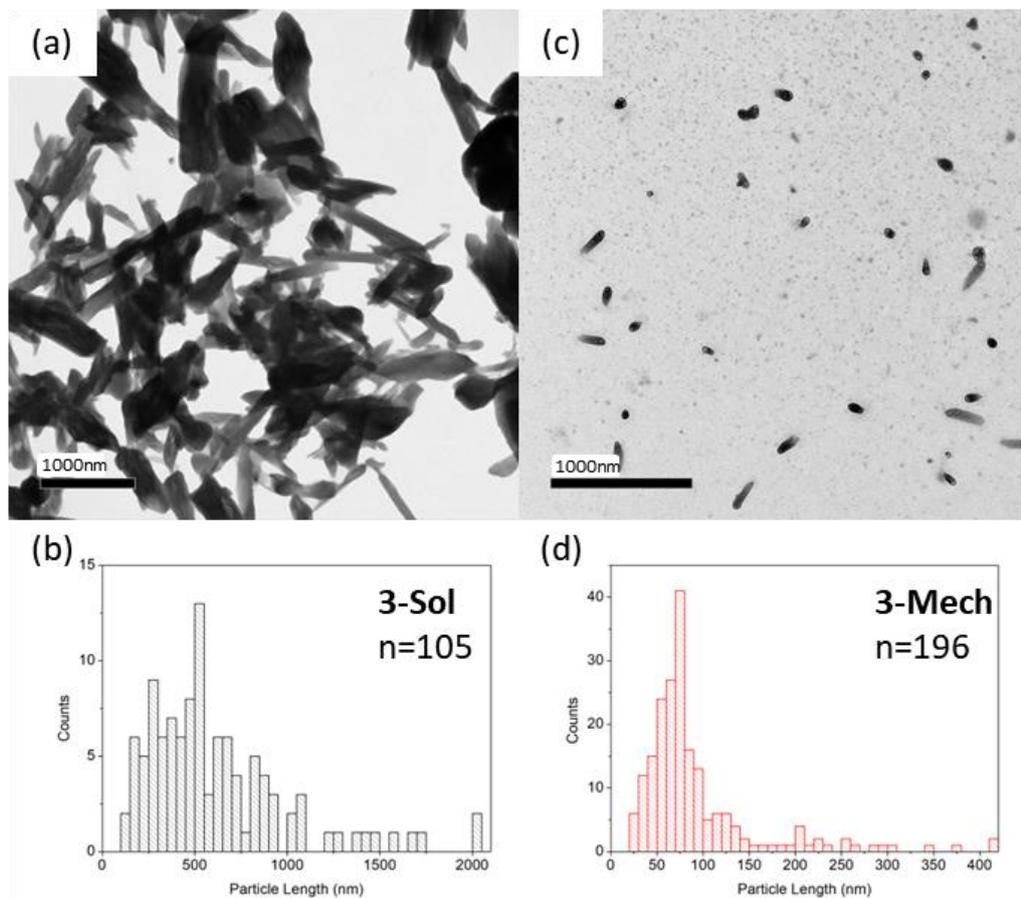
Figure 3.17: (a) Representative TEM image for compound **3-Sol**. **(b)** Particle length distribution for compound **3-Sol**, where n = 105. **(c)** Representative TEM image for compound **3-Mech**. **(d)** Particle length distribution for compound **3-Mech**, where n = 196. Additional images of both **3-Sol** and **3-Mech** are shown in Appendix B.

In both **3-Sol** and **3-Mech**, the particles displayed sensitivity to the electron beam, undergoing apparent decomposition upon exposure, as shown in Figure 3.18. The particles appeared to melt and expand and change shape when exposed to the beam. As a result, the particle sizes determined using this approach represent an upper estimate on the particle size.
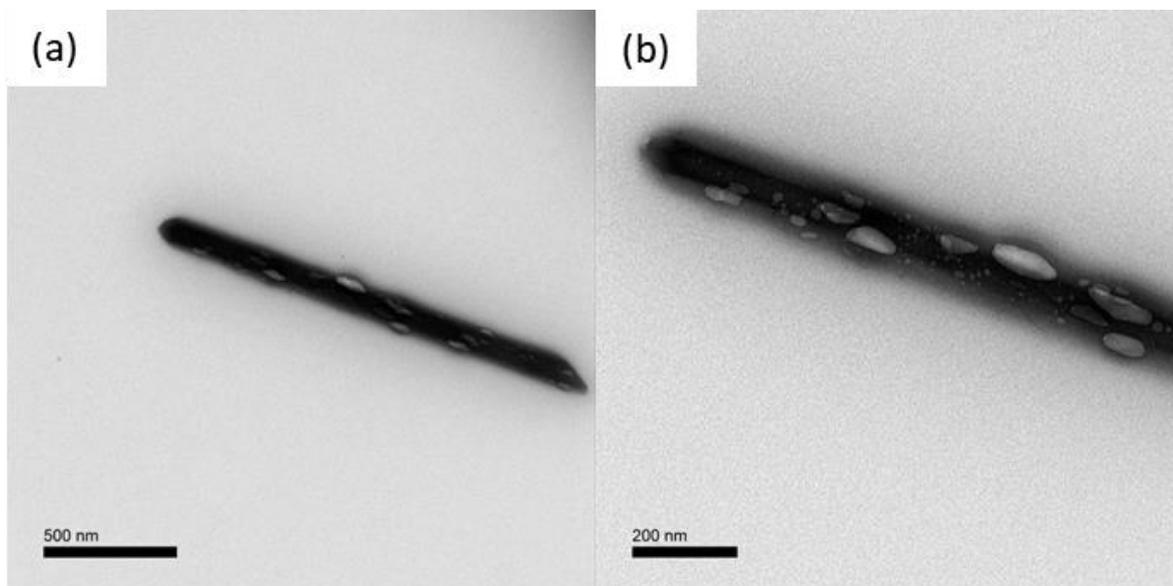
Figure 3.18: Degradation of **3-Sol** in the electron beam. (a) First exposure (b) Second exposure lighter areas are believed to shown regions of melting.

Fe-edge EXAFS data were collected at room temperature in which **3-Sol** and **3-Mech** are in the LS state. The pseudo-radial distribution function (RDF) of Fe for both **3-Sol** and **3-Mech** is shown in Figure 3.19. Both sets of data represent the same short-range structure of the triazole complex. The peak at 1.98(1) Å corresponds to the Fe-N distance, consistent with a Fe^{2+} LS species.[46] The next peaks represent Fe-C (2.98(1) Å), Fe-N (2.99(1) Å) and Fe-Fe (3.65(3) Å) shells. As observed in previous EXAFS studies of SCO Fe^{2+} triazole systems, the peak at *c.a.* 7 Å represents Fe-Fe-Fe multiple scattering, demonstrating the polymeric structure of iron centers bridged by triazole ligands.[47] The presence of the Fe-Fe-Fe multiple scattering peak in both **3-Mech** and **3-Sol** confirms the formation of 1-D triazole chains by both traditional solution and mechanochemical synthetic techniques.
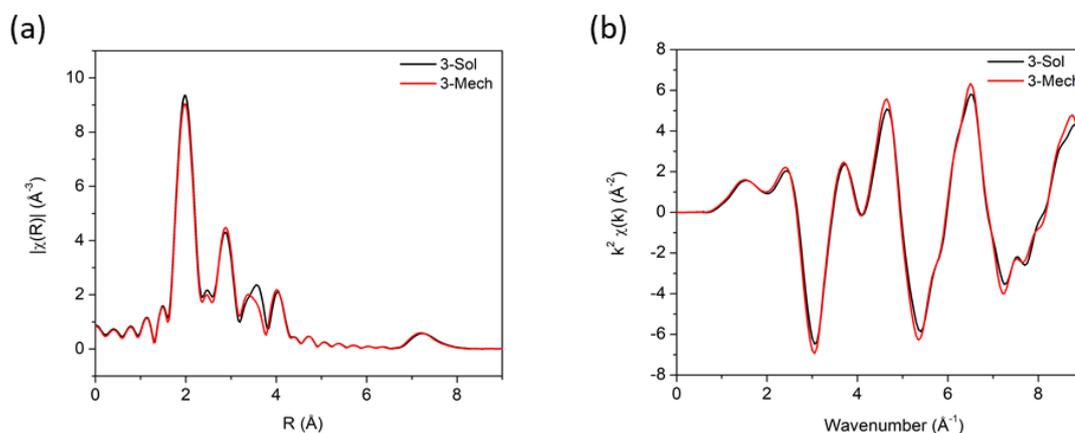
Figure 3.19: (a) k³ weighted R-Space pseudo-radial distribution function of Fe k-Edge spectra for **3-Sol** and **3-Mech**. (b) Combined Fe-Edge k Space EXAFS spectrum (k³ weighted) for **3-Sol** and **3-Mech.**

The only significant difference between the plots is visible at 3.5 Å, which is attributed to the different k-weighting used in fitting EXAFS data, which was performed by Dr. D. Pickup. Different K-weightings are used in data fitting in order to assist in distinguishing different atom types. However, fitting parameters have different k-dependences. As a result, fitting is done by attempting to minimise the differences in raw data and fit for all stated k-weightings. In Figure 3.20, the 3 K-weightings (k^1, k^2 and k^3) used in our fit are plotted against their corresponding calculated fits. The peak of interest at 3.5 Å exhibits a different peak structure for each of the three K weightings. As the k-weight is increased, part of the peak increases in intensity which indicates the shell that the peak represents may include atoms with larger atomic number, such as the Fe-Fe shell. Due to part of the peak decreasing with increasing k-weight, it is likely the peak represents at least two shells; where the second shell corresponds to atoms with smaller atomic number, such as the Fe-C shell. Although the k^3-weighted plot could be visually improved by modifying the fitting parameters, this causes a decrease in the accuracy of the overall fit. The artefact is visible due to standard practice in the field being to represent the data using the k^3 weighted pseudo-RDF plot. However, it is unlikely to represent a significant structural difference due to the consistency of the fitting parameters shown in Table 3.5.
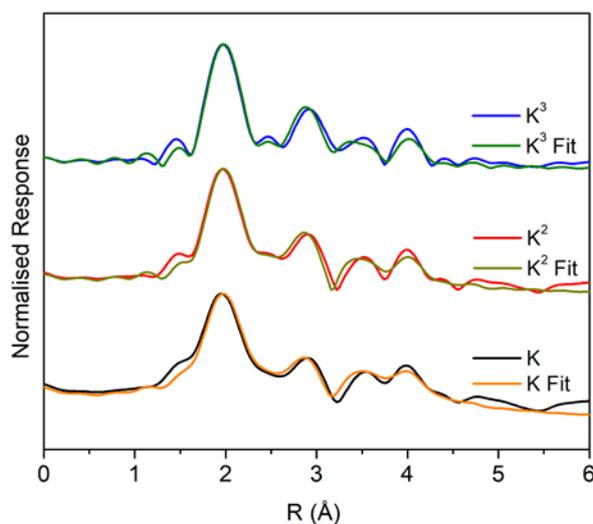
Figure 3.20: Pseudo-RDF for Fe-Edge EXAFS with different k weighting for **3-Mech**.

The degree of amorphisation within the systems was analysed through comparison of the Debye-Waller factors (σ^2), which can be used to describe uncertainty in atomic positions, increased uncertainty indicates a higher degree of disorder. In both cases, the amount of amorphisation is comparable, differences between the values are within error and thus synthesis via mechanochemistry does not introduce increased disorder into this system, at least within the resolution of the EXAFS technique.

Table 3.5: Coordination spheres, interionic distances (R), variance of the absorber-scatterer distances (σ^2), energy shift (E_f) and quality of fit (R-fit) of the EXAFS data for (**3-Sol** and **3-Mech**).

Sample	Neighbour	N	R / Å	σ^2 x10^3 / Å^2	E_f / eV	AFAC	R-fit
3-Sol	N	6	1.98(1)	3.9(10)	1.45(125)	1.45(125)	0.0273
	C	6	2.98(1)	3.1(19)			
	N	6	2.99(1)	8.4(24)			
	Fe	2	3.65(3)	8.1(32)			
	Fe-Fe-Fe linear chain MS	4	7.16(5)	15.0(40)	1.31(98)	0.83(8)	0.0471
3-Mech	N	6	1.98(1)	3.4(11)	1.74(124)	0.74(9)	0.0300
	C	6	2.98(1)	2.0(18)			
	N	6	2.99(1)	7.8(23)			
	Fe	2	3.62(3)	6.9(30)			
	Fe-Fe-Fe linear chain MS	4	7.12(5)	13.8(38)	1.58(93)	0.75(7)	0.0448

The switching properties of the triazole family of SCO materials have previously shown significant dependence on the presence of solvents.[48] The water content for both **3-Sol** and **3-Mech** was determined by TGA, as shown in Figure 3.21. The amount of water present in both samples was very similar with **3-Sol**, Figure 3.21(a), showing a mass loss of 0.4% (< 0.1 H_2O) at 150°C and **3-Mech**, Figure 3.21(b), losing 1.7% (< 0.5 H_2O). In both **3-Sol** and **3-Mech** the mass loss indicates a low presence of water and any water found is likely adsorbed onto the surface rather than a direct stoichiometric component of the system. **3-Mech** was synthesised by neat grinding under atmospheric conditions, potential sources of water include both the hydrated iron(II) salt used and moisture in the air. The plot of **3-Mech** also includes an additional mass loss of ~11% at 280°C consistent with the loss of 0.7 equivalents of ammonium sulphate which decomposes at this temperature.[49] As previously discussed, the presence of 1 eqv. of $(NH_4)_2SO_4$ was expected as a by-product of using $(NH_4)_2Fe(SO_4)_2.6H_2O$ in synthesis, which was used in preference to $FeSO_4.7H_2O$ due to the reduced rate of oxidation. This is attributed to the presence of the slightly acidic ammonium ions and was discussed previously in 2.2.
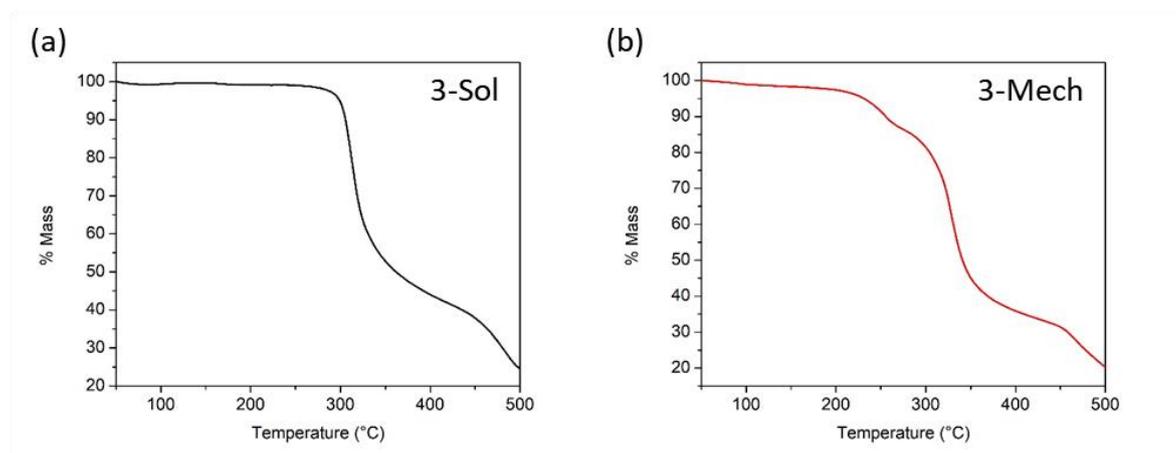

Figure 3.21: TGA plots of % mass vs temperature. Collected between 50-500 °C with a heating rate of 10 K/min. (a) **3-Sol** and (b) **3-Mech**

3.2.3. Fe(4-phpy)$_2$[Ni(CN)$_4$] (Compound 4)

Fe(4-phpy)$_2$[Ni(CN)$_4$] (Compound **4**) is a two-dimensional coordination polymer which undergoes an incomplete SCO transition at low temperatures (T$_{1/2}\uparrow$ = 158 K, T$_{1/2}\downarrow$ = 135 K).[50] Neat grinding to yield compound **4** resulted in a dark green powder which did not display thermochromism on either heating or cooling (**4-Mech**). Liquid assisted grinding, as discussed in 1.2.1, was attempted by the addition of a small quantity of water (η = 0.25) during mechanical synthesis. LAG using H$_2$O modified the product, yielding a fine yellow powder which partially darkened to orange on cooling in liquid nitrogen (**4-LAG**). A solution sample was also synthesised, which yielded a yellow powder that also transitioned to orange on cooling.
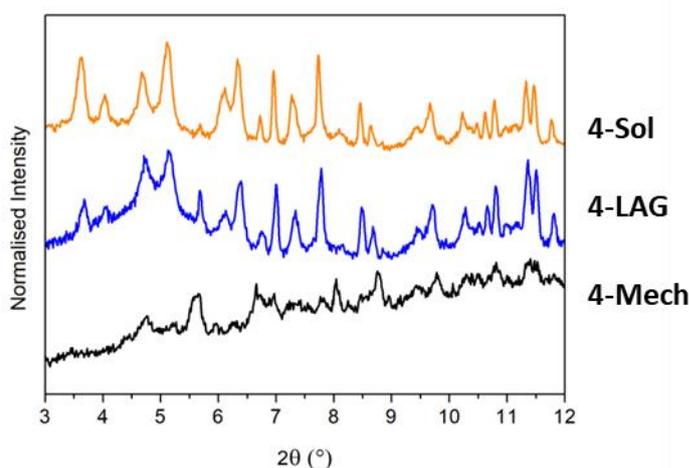

Figure 3.22: PXRD patterns of compound 4. Bottom to top: 4-Mech, 4-LAG and 4-Sol.

PXRD patterns obtained for each sample are shown in . It is clear that **4-Mech** yielded a poorly crystalline powder which was significantly different to **4-Sol**. The patterns for **4-LAG** and **4-Sol** were similar. Comparison with a literature pattern of Fe(Figure 3.224-Phpy)$_2$[Ni(CN)$_4$] reported by Seredyuk *et al.*[50] showed agreement with the collected patterns of both **4-LAG** and **4-Sol**.

Raman spectroscopy was not used to characterise the HS and LS spin states. This was due to limitations of the variable temperature stage used, it was not possible to accurately cool the sample as low enough temperatures to observe the transition. Reported SCO properties indicated gradual SCO transitions with T$_{1/2}\uparrow$ = 158 K and T$_{1/2}\downarrow$ = 135 K.[50] Due to the gradual transition, the

complete LS state was not accessible until significantly lower in temperature (60 K). As such it was not possible to collect a completely LS spectra with the liquid nitrogen cooling stage used.
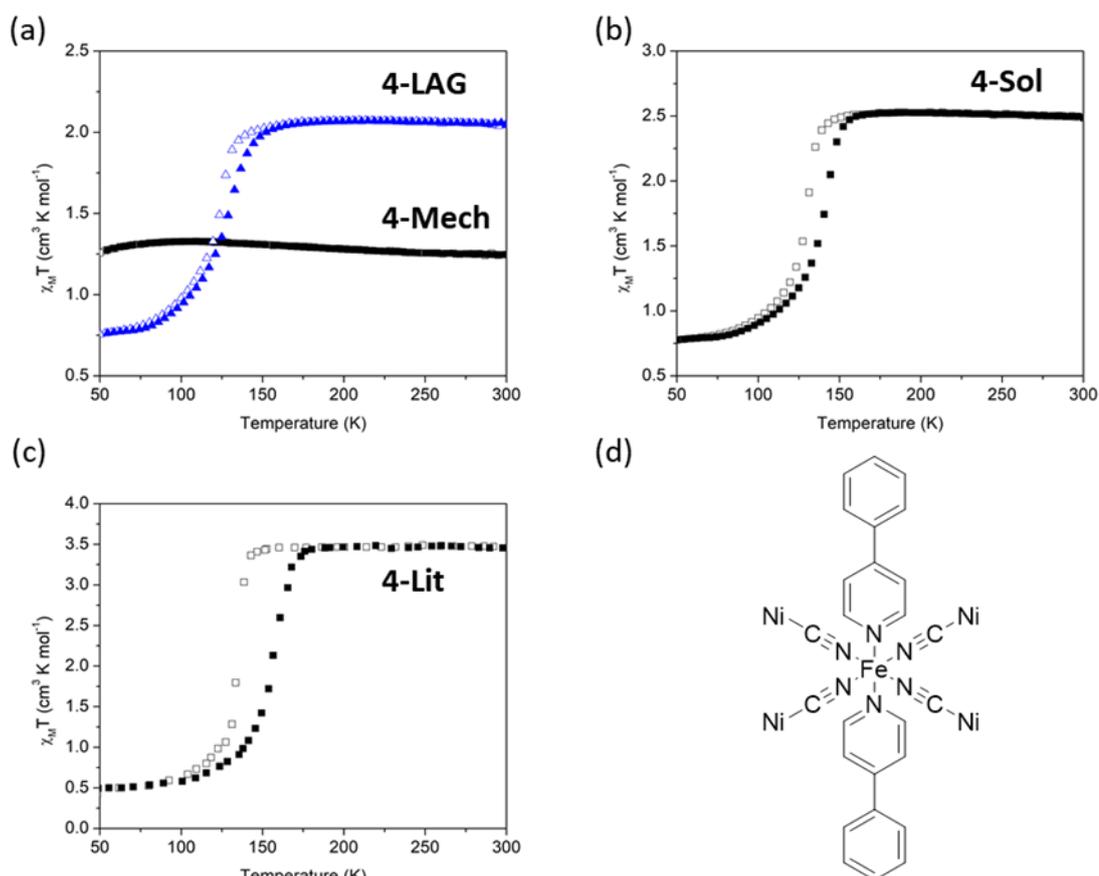

Figure 3.23: : Temperature dependent SQUID data, 2nd cycle. (a) Overlaid **4-Mech** and **4-LAG** (b) **4-Sol**, (c) **4-Lit** digitised from reference [50]. (d) Structure of Fe(4-phpy)$_2$[Ni(CN)$_4$].

The $\chi_M T$ values as a function of temperature were measured using SQUID magnetometry. To improve clarity only the 2nd cycle is shown in Figure 3.23, full measurements are shown in Appendix A. The constant magnetic response across the full temperature range for **4-Mech** confirms the absence of SCO. However, LAG yielded a product which underwent SCO with $T_{1/2}\uparrow$ = 130 K, $T_{1/2}\downarrow$ = 125 K and 'Smoothness' = 27 K. **4-Sol** also presented SCO properties $T_{1/2}\uparrow$ = 140 K, $T_{1/2}\downarrow$ = 135 K and 'Smoothness' = 23 K. Mechanochemistry was used in the successfully synthesis of the 2-D coordination polymer Fe(4-phpy)$_2$[Ni(CN)$_4$] *via* LAG. The structure and magnetic properties were comparable to a solution synthesised sample with a decrease in transition temperature and width of hysteresis. **4-LAG** also showed a slightly more gradual transition (27 K)

compared to **4-Sol** (23 K). The observed differences between **4-LAG** and **4-Sol** are consistent with particle size and crystal quality effects described in 1.1.7. Literature SCO properties for compound **4**, reported a higher transition temperature ($T_{1/2}\uparrow$ = 158 K, $T_{1/2}\downarrow$ = 135 K) and a larger hysteresis (ΔT = 23 K) in comparison to both **4-LAG** (ΔT = 5 K) and **4-Sol** (ΔT = 11 K). These differences were consistent with particle size and crystal quality effects first described by Haddad *et al.*[4] SCO properties of compound **4** are shown in Table 3.6.

Table 3.6: SCO properties for each of compound **4**. *Data taken from reference[50], 'smoothness' calculated using digitised data.

	$T_{1/2}\uparrow$(K)	$T_{1/2}\downarrow$ (K)	ΔT (K)	'Smoothness' (K)
4-Mech	-	-	-	-
4-LAG	130	125	5	27
4-Sol	140	129	11	23
4-Lit*	158	135	23	22

3.2.4.   Fe(pz)[Au(CN)₂]₂ (Compound 5)

Fe(pz)[Au(CN)$_2$]$_2$ (compound **5**) is a three-dimensional Hofmann-type clathrate framework which undergoes SCO transition at high temperatures ($T_{1/2}\uparrow$ = 367 K, $T_{1/2}\downarrow$ = 349 K).[51] Iron-containing dicyanoheterometallic frameworks are a widely studied family of SCO materials. Further investigation into the system was carried out as the 3-D structure represents a highly cooperative network that can display bistability across a wide range of temperatures.[52] This presents an ideal opportunity to investigate the effects mechanochemistry has on cooperativity within a different family to the Fe-triazole complexes. Mechanochemical synthesis yielded a red powder which transitioned to yellow on heating (**5-Mech**). PXRD was used to compare **5-Mech** with a solution synthesised sample (**5-Sol**) and a simulated pattern from SC-XRD data (CSD Code: IRIKUR),[51] as shown in Figure 3.24. PXRD analysis of **5-Sol** and **5-Mech** was carried out and compared with a simulated pattern from SC-XRD data (CSD code: IRIKUR)[51] as shown in Figure 3.24. The patterns for all three were consistent, indicating the formation of the same material. The most significant differences between **5-Sol** and **5-Mech** is the broadening of Bragg peaks in **5-Mech**, which corresponds to a decrease in crystalline domain size. Scherrer analysis was used to

obtain an estimated crystalline domain size for both **5-Sol** obtaining particles *c.a.* 1595 nm and **5-Mech** giving particles of *c.a.* 240 nm. Due to the shape of the particles determined by TEM below, the calculated domain sizes are not reliable due to the spherical shape factor contribution used in the calculation.
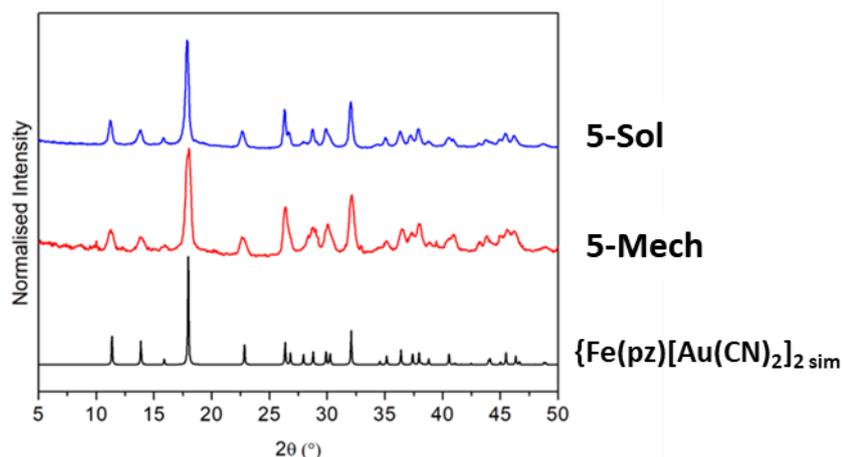

Figure 3.24: PXRD patterns of compound **5.** Bottom: Fe(pz)[Au(CN)$_2$]$_2$ pattern simulated from (CSD code: IRIKUR).[51] Middle: **5-Mech.** Top: **5-Sol**.

Raman spectroscopy was used to characterise HS and LS states in **5-Mech**, see Figure 3.25. After heating to 425 K, the spectrum was significantly altered compared to the spectrum collected at 225 K. The low frequency modes (<200 cm^{-1}) are attributed to FeN$_6$ vibration modes,[53] the differences shown in Figure 3.25, indicate changing bonding interactions in Fe-N. The peaks shown at 1200 cm^{-1} and 1600 cm^{-1} remain consistent across both temperature ranges, indicating the responsible vibration modes are not affected by a change in spin state. Therefore, these peaks are attributed to the pyrazine ligand. Full analysis of the vibrational modes was beyond the scope of this work.
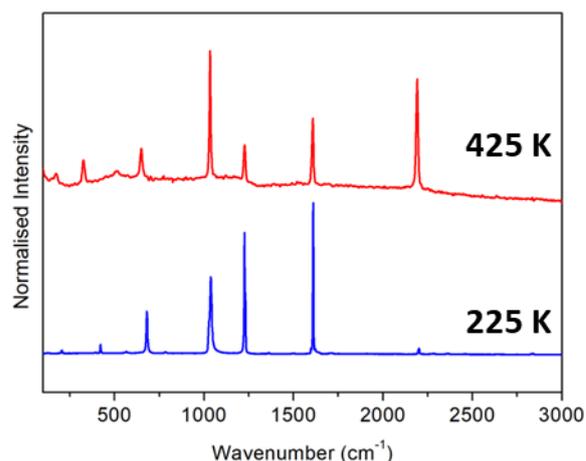
Figure 3.25: Normalised variable temperature Raman spectra at 425 K and 225 K for compound **5-Mech**.

Temperature dependent SQUID magnetometry results are shown in Figure 3.26, where the presence of SCO in both **5-Mech** and **5-Sol** was confirmed. **5-Mech** displayed SCO with $T_{1/2}\uparrow$ = 368 K, $T_{1/2}\downarrow$ = 352 K with 'smoothness' = 10 K. Comparison with **5-Sol** showed similar results $T_{1/2}\uparrow$ = 367 K, $T_{1/2}\downarrow$ = 354 K with a 'smoothness' = 5 K. **5-Sol** displayed a slightly more abrupt transition than **5-Mech** with a similar abruptness to literature reports (**5-Lit**: 'smoothness' = 3 K). Previous literature reports on the $Fe(pz)[Au(CN)_2]_2$ complex (**5-Lit**)[51] exhibit SCO activity consistent with both **5-Mech** and **5-Sol**. Literature reports describe SCO in $Fe(pz)[Au(CN)_2]_2$ with $T_{1/2}\uparrow$ = 369 K, $T_{1/2}\downarrow$ = 349 K and 'smoothness' = 3 K. Both **5-Sol** and **5-Mech** undergo slightly more gradual SCO than the literature report but the differences are relatively small. The biggest differences correspond to the smaller hysteresis in both **5-Sol** and **5-Mech**, these differences are attributed to the use of single crystals for analysis in literature which are expected to be inherently more cooperative. Comparison between **5-Sol** and **5-Mech** with literature reports are shown in Table 3.7.

Table 3.7: SCO properties determined by SQUID magnetometry for **5-Mech** and **5-Sol** compared with previously literature reports for $Fe(pz)[Au(CN)_2]_2$ (**5-Lit**).[51]

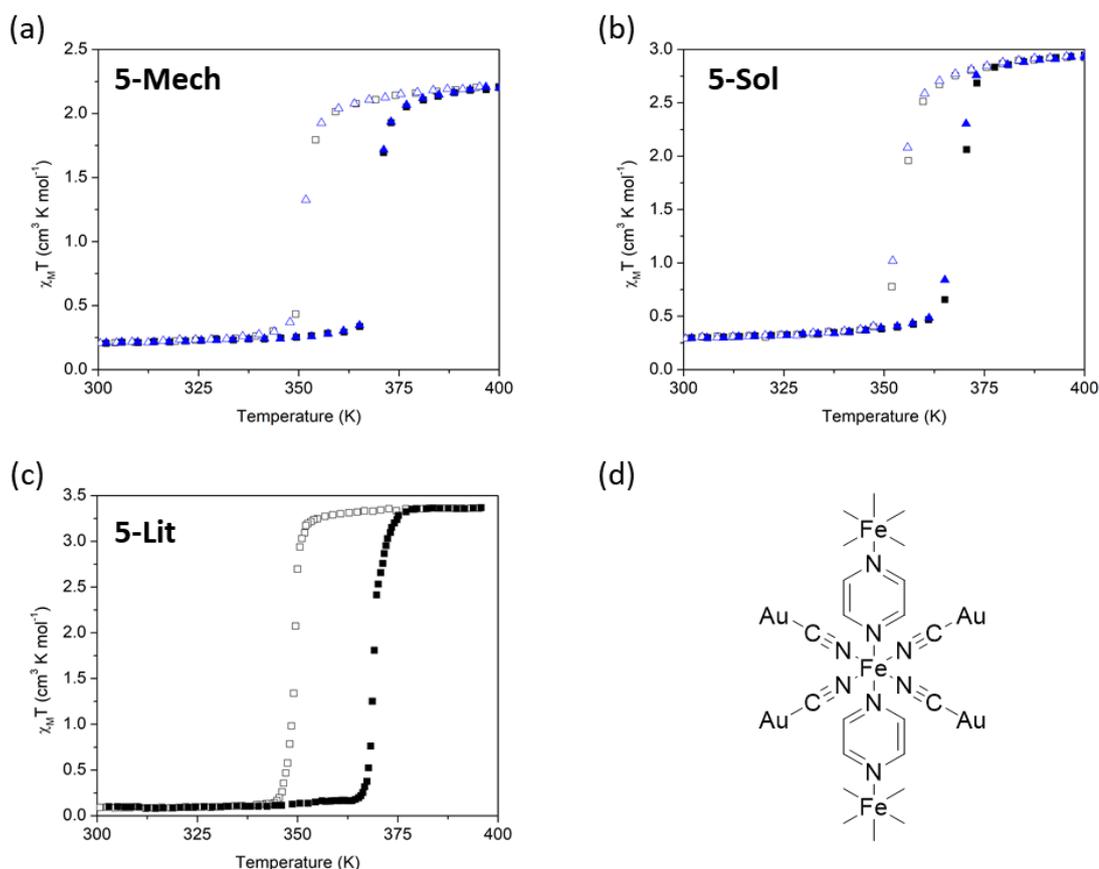| Sample	$T_{1/2}\uparrow$(K)	$T_{1/2}\downarrow$ (K)	ΔT (K)	'Smoothness' (K)
5-Mech	368	352	16	10
5-Sol	367	354	13	5
5-Lit[51]	369	349	20	3

Figure 3.26: $\chi_M T$ verses T for (a) **5-Mech**, (b) **5-Sol** and (c) **5-Lit** Cycle 1 Heating ■ and Cooling □, Cycle 2 Heating ▲ and Cooling △. (d) Structure of Fe(pz)[Au(CN)$_2$]$_2$.

Fe-edge EXAFS data was collected at room temperature, which corresponds to the material being in the LS state for both **5-Sol** and **5-Mech**. The pseudo-radial distribution function (RDF) of Fe for both **5-Sol** and **5-Mech** are shown in Figure 3.27. Both sets of data represent the same short-range structure of the 3-D Hofmann Clathrate-like system. The peak at 1.94(1) Å corresponds to the Fe-N distance, consistent with a Fe^{2+} LS species.[46] The next peaks represent the Fe-C (2.93(1) Å), Fe-C (3.08(1) Å) and Fe-Au (5.04(2) Å) shells. Comparison of **5-Sol** and **5-Mech** appeared to show major differences in the K^3 weighted plots. However, as discussed in 3.2.2.2, the K^3 weighted plots only represent one aspect of the applied fit. The R-space plot shows clear differences in the patterns at low R values, the primary origin of these differences is due to imperfect background subtraction and truncation ripples introduced by the Fourier transform.

Truncation of data is done at a data dependent K_{max} to allow for data fitting to be carried out. Additionally, the sharp peaks present in the K-space plot, Figure 3.27(b), at 6 Å^{-1} are due to well-characterised monochromator glitches originating from the use of double crystal monochromators. The spikes at *c.a.* 6 Å^{-1} correspond to energies in which two or more sets of Bragg planes in the monochromator crystal simultaneously diffract X-rays at the same energy.[54] The imperfect background subtraction does not significantly affect the resulting fitting parameters, this is due to the oscillations below 1.5 Å^{-1} not having a significant weighting for the fitting parameters. Similarly, the monochromator artifacts are well-characterised, and the effects are minimised during fitting.
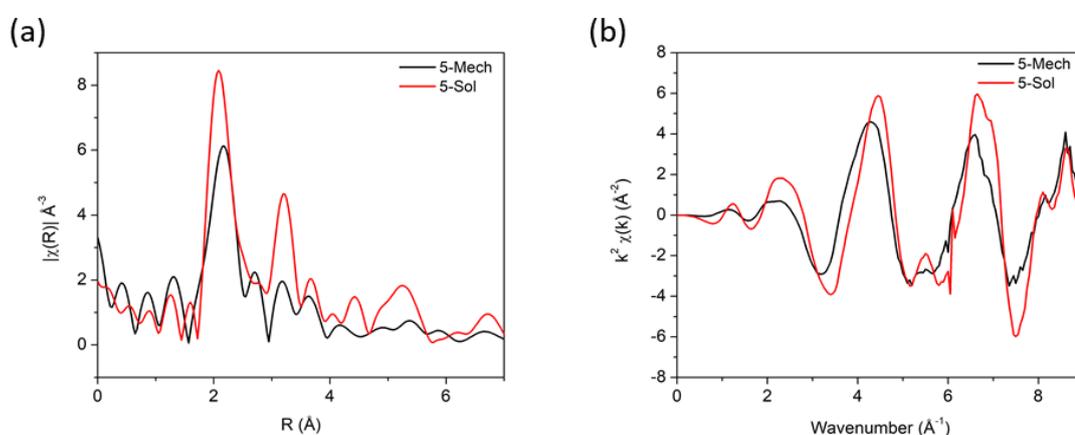

Figure 3.27: (a) K^3 weighted R-Space pseudo-radial distribution function of Fe k-Edge spectra for **5-Sol** and **5-Mech**. (b) Combined Fe-Edge K-Space EXAFS spectrum (k^3 weighted) for **5-Sol** and **5-Mech.**

The degree of amorphisation within the systems was compared by analysis of the Debye-Waller factors (σ^2). In the mechanically synthesised system, **5-Mech**, the degree of amorphisation was larger than in **5-Sol** with variation outside the error potential, significantly greater differences in disorder than observed in compound **9**. Full fitting data is shown in Table 3.8.

Sample	Neighbour	N	R / Å	$\sigma^2 \times 10^3$ / Å^2	E_f / eV	AFAC	R-fit
5-Sol	N	6	1.94(1)	5.7(12)	0.81(152)	0.94(14)	0.0244
	C	4	2.93(1)	4.4(25)			
	C	4	3.08(1)	7.4(46)			
	Au	4	5.04(2)	5.5(16)			
5-Mech	N	6	1.95(1)	7.5(11)	-2.97(147)	0.90(9)	0.0122
	C	4	2.94(1)	14.6(60)			
	C	4	3.10(1)	4.6(23)			
	Au	4	4.88(2)	8.0(24)			

The water content for both **5-Sol** and **5-Mech** was calculated using TGA, as shown in Figure 3.28. At 150 °C, **5-Sol** showed a 0.4% mass loss which approximately 0.2 equivalents of H_2O. Both **5-Sol** and **5-Mech** begin to undergo significant mass loss at *c.a.* 300 °C. **5-Sol** also displayed an additional stepped ≈3% mass loss between 364 °C and 396 °C. The stepped decomposition is consistent with the removal of all non-metal atoms (pyrazine and cyanides) with 22% mass loss similar to observations with the Cobalt analogue (Co(pz)[Au(CN)$_2$]$_2$).[55] The mechanically synthesised sample, **5-Mech** displayed a 0.7% mass loss which is consistent with the presence of 0.3 equivalents of H_2O. However, it is also possible that this corresponds to the removal of unreacted pyrazine remaining the pores, Unlike **5-Sol**, **5-Mech** did not undergo a clear stepped decomposition between 364 °C and 396 °C and only displayed a total mass loss of 18% attributed to the removal of all non-metal atoms. The origin of the difference between total mass loss is attributed to the presence of by-products in **5-Mech**, such as KBF_4 which does not thermally decompose until temperatures higher than 500 °C.[56] The absence of a stepped transition is consistent with the nickel analogue (Ni(pz)[Au(CN)$_2$]$_2$)[55] but the origin of difference between **5-Sol** and **5-Mech** is unclear.
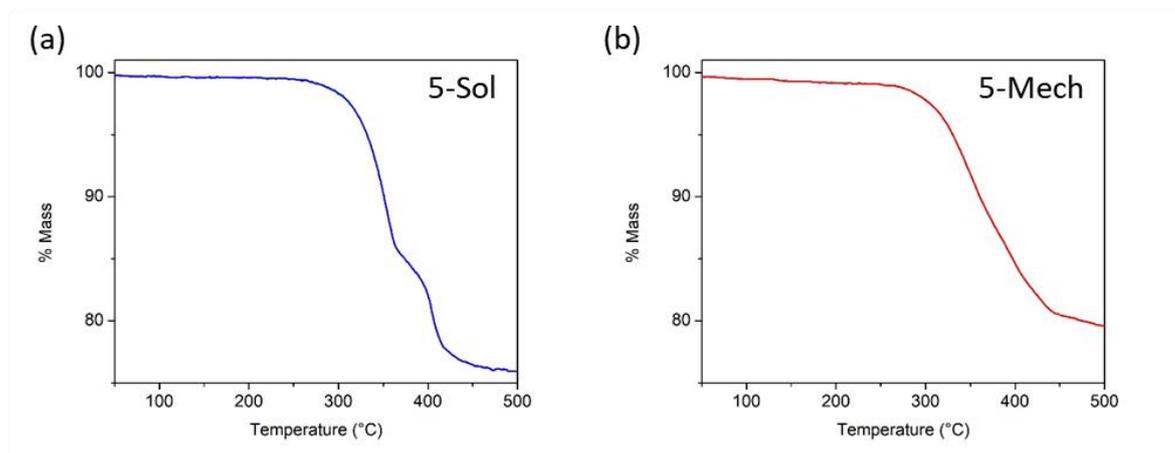
Figure 3.28: TGA plots of % mass vs temperature. Collected between 50-500 °C with a heating rate of 10 K/min. (a) **5-Sol** and (b) **5-Mech**.

Particle size for **5-Sol** and **5-Mech** was determined by TEM, as shown in Figure 3.29. The particles of **5-Sol** had an average particle size of 1282 ± 391 nm, but the large particles were 2-D plates, circular or elliptical in appearance, but due to their size, it was difficult to obtain measurements from a large number of particles. The **5-Mech** particles were significantly smaller, with an average size of 59 ± 24 nm. The majority of particles in **5-Mech** were circular with a small proportion with a similar elliptical shape to **5-Sol**. Particles of **5-Mech** also appeared to aggregate significantly, even after application of BSA to reduce the aggregation, as shown in Figure 3.29(c).
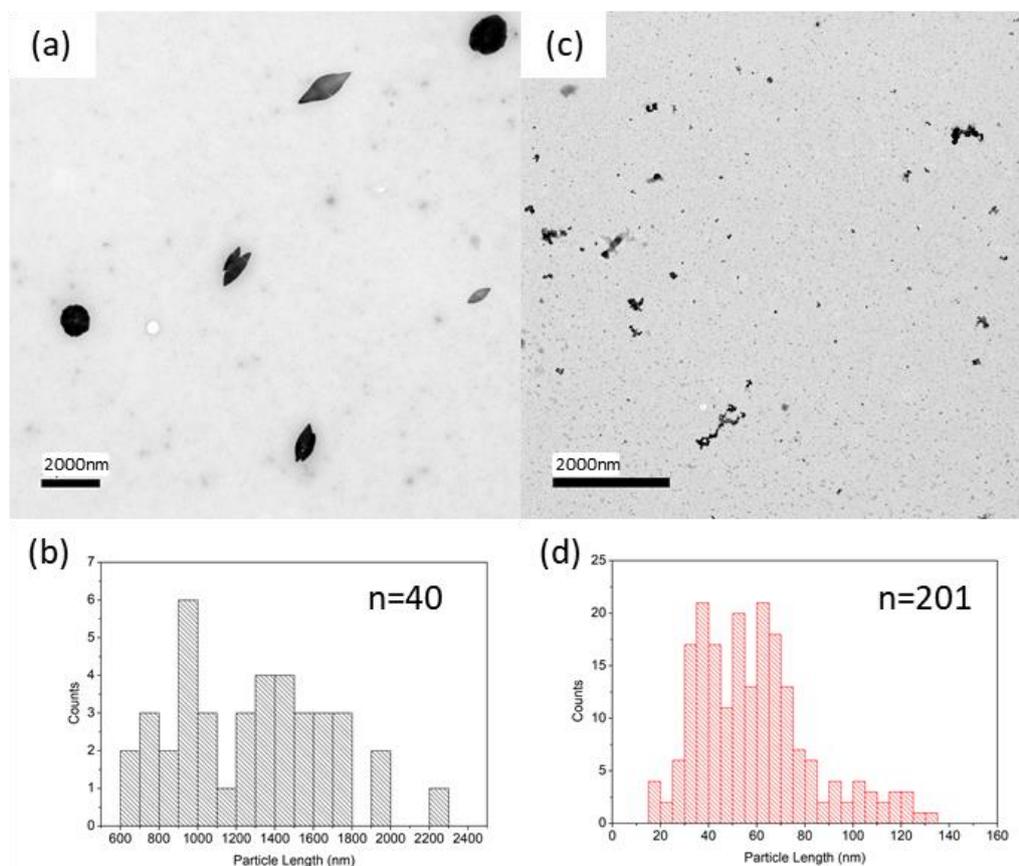
Figure 3.29: (a) Representative TEM image for compound **5-Sol**. **(b)** Particle length distribution for compound **5-Sol**, where n = 40. **(c)** Representative TEM image for compound **5-Mech**. **(d)** Particle length distribution for compound **5-Mech**, where n = 201.

Mechanochemistry was used to synthesise the 3-D Hofmann Clathrate-like system $Fe(pz)[Au(CN)_2]_2$ by neat mechanochemical synthesis. Comparisons of properties were made with both a solution synthesised product and with previous literature report. PXRD analysis showed similar patterns across all three samples. Red → Yellow thermochromism indicated SCO-activity in **5-Mech** which was confirmed by variable temperature Raman spectroscopy and SQUID magnetometry. SCO properties were consistent across the samples with characteristic decrease in transition temperature, width of hysteresis and abruptness of transition observed for the mechanical sample as a result of decreases in particle size and crystal quality.[4]

3.2.5. Summary

Mechanical synthesis of multiple different families of SCO materials was successfully carried out. In the past, post-synthetic grinding of SCO materials has primarily been used to decrease

grain size, such as in the grinding of single crystals for PXRD analysis.[12] The synthesis of materials containing long range coordination networks, such as the one-dimensional triazole family and both two and three-dimensional iron(II) containing cyanaoheterometallic frameworks, indicates the presence of a growth-phase during the mechanochemical procedure.

Literature reports on the effects of post-synthetic grinding SCO-active materials indicate a number of changes in properties.[12] The general described trend is a decrease in transition temperature, width of hysteresis, abruptness of transition and an increase in residual HS fraction at low temperatures.[4,6,12] For all materials discussed in this work, the second heating cycle is used for interpretation. This is due to the potential for changing properties caused by the 'run-in' effect, which is described in detail in 1.1.4. Where possible, comparison with literature is done using the second cycle. However, it is not always clear in the literature which cycle is being reported. As discussed in 2.1, both the triazole and cyanoheterometallic families can display solvent sensitivity. Therefore, the degree of hydration is also an important factor to consider.

Compounds **1**, **2** and **4** displayed a decrease in transition temperature, width of hysteresis, abruptness of transition and an increase in residual HS fraction at low temperature. However, for compounds **3** and **5** one or more of the predicted effects was not observed. Compound **3** displayed properties consistent with a solution synthesised sample with the indication of a slightly more abrupt transition. Compound **5** on the other hand had a more gradual transition, but the transition temperatures were not significantly affected. In fact, **5-Mech** showed SCO-activity with an increased ΔT compared to **5-Sol**, with transition temperatures closer to literature reports.

The effects of mechanochemical synthesis on SCO materials at this stage appear to be system and sample dependent, there does not appear to be a definitive trend in the effects. Properties such as the inherent cooperativity in the systems show a significant effect on SCO behaviour. It is worth noting the differences observed in some systems prepared by mechanochemistry is no greater than differences observed between different batches prepared using the same solution-state procedure, illustrated, for example, by the wide range of transition temperatures reported

for the $Fe(phen)_2(NCS)_2$ system ($T_{1/2}\uparrow$ = 165 − 190 K).[6–8,21,30,57] Similarly, different reports on SCO properties for the complex $Fe(4-phpy)_2[Ni(CN)_4]$ (compound **4**) have reported different SCO transition temperatures ($T_{1/2}\uparrow$ = 150 − 158 K).[50,58] This was further evidenced with synthesis of a comparative solution synthesised sample (**4-Sol**) in which $T_{1/2}\uparrow$ = 140 K.

For compound $[Fe(atrz)_3]SO_4$ (compound **3**), the different synthetic routes had a small effect on the magnetic properties. The transition temperature for the mechanically synthesised sample (**3-Mech**) was at a slightly lower temperature and underwent a slightly more gradual transition than the solution-state sample (**3-Sol**). Analysis by PXRD and EXAFS confirmed the same structure for both types of synthesis with no significant increase in the degree of amorphisation. No differences in degree of solvation were observed by TGA, confirming the differences in magnetic properties are not due to hydration. However, TEM analysis showed differences in morphology and particle size between the samples. **3-Sol** exhibited an elliptical morphology whereas **3-Mech** was a mixture of elliptical and circular particles. The particle size for **9-Sol** (612 ± 371 nm) was significantly greater than **3-Mech** (92 ± 64 nm). Scherrer analysis confirmed a significant difference in coherent domain length between the two samples with a lower limit of 30 nm for **3-Mech**. The differences in magnetic properties were thus attributed to differences in particle size and morphology. However, it is worth noting the smaller particle size did not result in a complete loss of hysteresis with an apparent increase recorded, emphasising the maintenance of cooperativity in the mechanical sample, which has been seen previously in the Fe-trz family.[18]

Similarly, for $Fe(pz)[Au(CN)_2]_2$ (compound **5**), synthesis by both solution-state (**5-Sol**) and mechanochemical synthesis (**5-Mech**) yielded products which displayed similar SCO activity. **5-Mech** underwent a slightly more gradual transition than **5-Sol**. Analysis by PXRD and EXAFS confirmed the formation of the same product, with an increased degree of amorphisation observed in **5-Mech**. The possibility of solvent effects was again eliminated by TGA, with no significant differences in degree of hydration observed. Particle size determination was carried out using TEM, with particle sizes of 59 ± 24 nm measured for **5-Mech** and significantly larger

particles of 1282 ± 391 nm for **5-Sol**. The slightly more gradual transition observed in **5-Mech** was thus attributed to a decrease in particle size and a slight increase in the degree of amorphisation.

The effects observed for mechanochemical synthesis of both compounds **3** and **5** corroborate previous literature reports, which state the effects of grinding vary between each family.[2,4,12] Although the effects of mechanochemical synthesis vary between compounds, in general, the effects are relatively small compared to post-synthetic grinding for several hours as described in literature.[12]

3.2.6.   Effects of Duration of Grinding

$[Fe(atrz)_3](BF_4)_2$ was synthesised by mechanochemistry yielding a compound which displays significantly different SCO properties to a solution synthesised sample, with a large decrease in $T_{1/2}\uparrow$ <40 K. This decrease in $T_{1/2}\uparrow$ was significantly greater than previously observed decreases in $T_{1/2}\uparrow$ after post-synthetic grinding and milling. Initial synthesis also indicated the presence of only one step in the SCO. Here, $[Fe(atrz)_3](BF_4)_2$ was prepared using manual grinding in a pestle and mortar and by a previously reported solution-state technique in order to identify the effects of mechanochemical synthesis on $[Fe(atrz)_3](BF_4)_2$. Further mechanochemical synthesis of $[Fe(atrz)_3](BF_4)_2$ was done using a ball mill with two different milling times, which allows for investigation of size control and the effects of prolonged mechanical synthesis. The complexes were analysed using SQUID magnetometry, PXRD, TGA, Fe-edge EXAFS and TEM.

3.2.6.1. $[Fe(atrz)_3](BF_4)_2$ Compound 6

Literature reports on $[Fe(atrz)_3](BF_4)_2$ present a complex situation with multiple reported temperature ranges for the SCO identified[25,59–61] and significant potential for solvent effects.[33] The properties measured for **6-Sol** are consistent with previously reported literature values for the $[Fe(atrz)_3](BF_4)_2$ complex first described by Kahn[59] then confirmed by both Roubeau[25] and Grosjean,[62] which exhibits SCO with $T_{1/2}\uparrow$ = 260 K and $T_{1/2}\downarrow$ = 250 K, as shown in Figure 3.30(a). A second form of $[Fe(atrz)_3](BF_4)_2$ with $T_{1/2}\uparrow$ = 245 K and $T_{1/2}\downarrow$ = 239 K was observed by Grosjean.[63] However, in the latter study, the authors were only able to observe a polycrystalline mixture of

forms, and were unable to isolate either form; the two-step SCO behaviour is shown in Figure 3.30(b). The form with a higher transition temperature, hereby denoted the 'α-form', was significantly more crystalline and allowed for structural analysis. Whereas the form with a lower transition temperature, hereby denoted the 'β-form', was weakly crystalline and no structural characterisation was possible. It is worth noting the possibility of a third SCO transition temperature, which has been previously reported in literature with $T_{1/2}\uparrow$ = 312 K and $T_{1/2}\downarrow$ = 302 K.[60] However, in that report the difference in transition temperature was noted but no explanation for the difference was suggested. No subsequent literature on this complex has shown SCO at $T_{1/2}\uparrow$ = 312 K and $T_{1/2}\downarrow$ = 302 K.
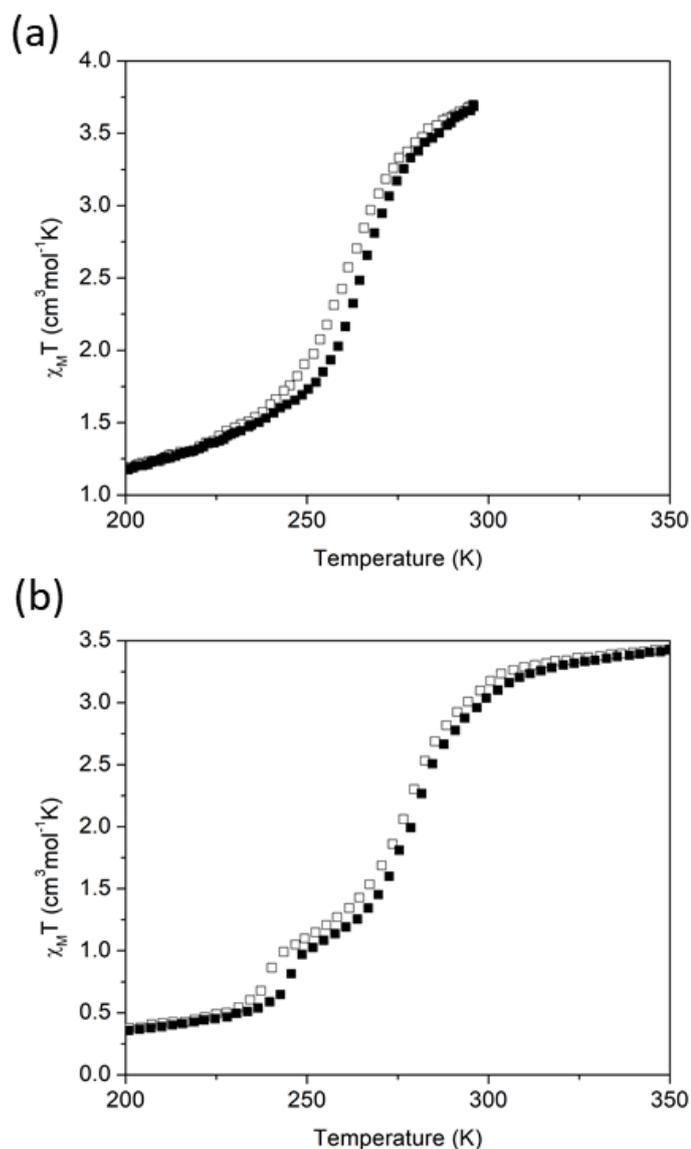
Figure 3.30: Plots of $\chi_M T$ vs T for literature reported versions of [Fe(atrz)$_3$](BF$_4$)$_2$. (a) α only form digitised from reference.[59] (b) Polycrystalline mixture showing the presence of two-step SCO, digitised from reference.[62] One Cycle: heating ■, cooling □.

[Fe(atrz)$_3$](BF$_4$)$_2$ (compound **6**) was synthesised using four different synthetic routes. **6-Sol** was prepared by a traditional solution-based method. **6-Mech** was prepared by manual grinding of the reagents in a pestle and mortar. **6-BM10** and **6-BM90** were synthesised in a ball mill for 10 and 90 minutes respectively. All four synthetic routes yielded white powders that underwent a characteristic HS to LS transition on cooling accompanied by a change in colour to purple. The variable temperature magnetic properties for each product were recorded by SQUID magnetometry, as shown in Figure 3.31. **6-Sol** exhibited a relatively gradual transition with a

'smoothness' of 39 K, $T_{1/2}\uparrow$ = 251 K and $T_{1/2}\downarrow$ = 250 K, as shown in Figure 3.31(a). Consistent with the α-form.
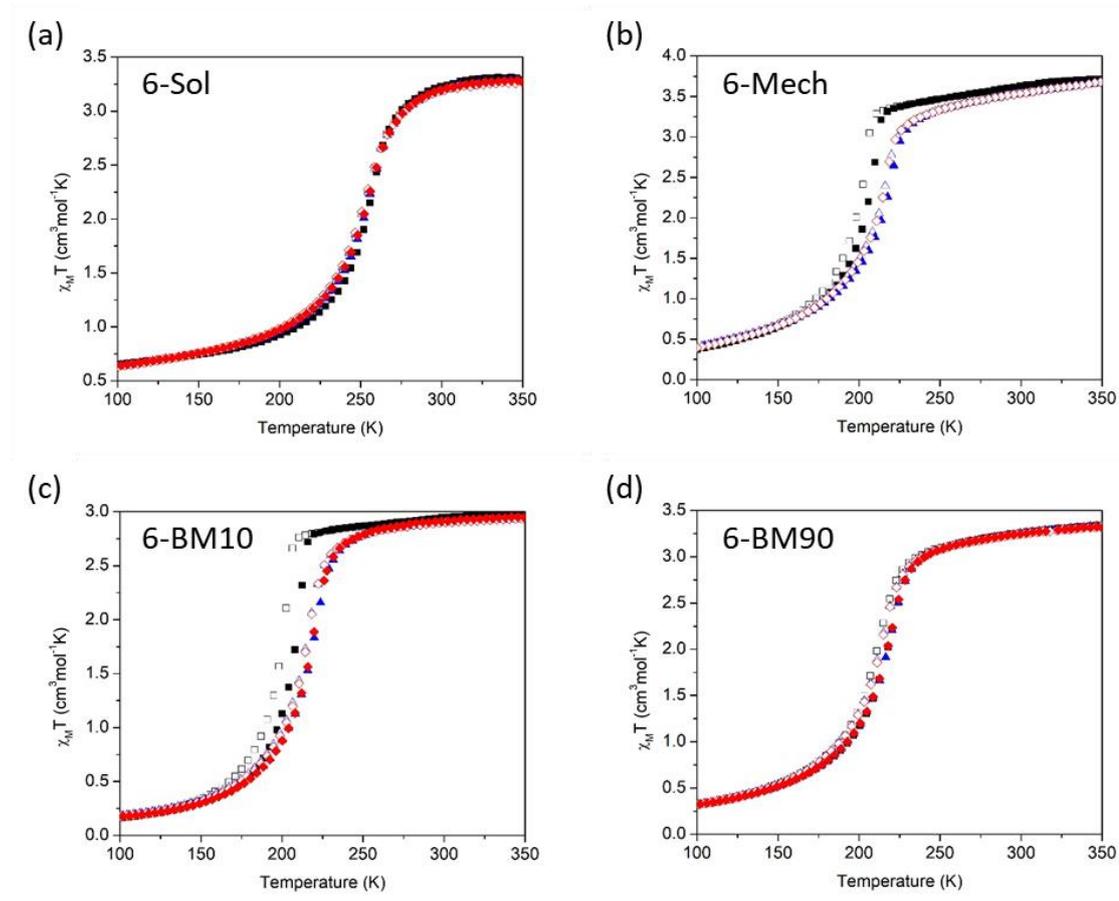

Figure 3.31: Plots of $\chi_M T$ vs T for compound **6** three cycles. (a) **6-Sol**, (b) **6-Mech**, (c) **6-BM10** and (d) **6-BM90**. First cycle: heating ■, cooling □. Second cycle: heating ▲, cooling △. Third cycle: heating ▲ and cooling △.

All three mechanically synthesised samples underwent SCO at a significantly lower temperature (>30 K) than **6-Sol**. **6-Mech** underwent a more abrupt transition than **6-Sol** ('Smoothness' = 31 K) with $T_{1/2}\uparrow$ = 215 K and $T_{1/2}\downarrow$ = 212 K, as shown in Figure 3.31(b). **6-BM10** also showed a more abrupt transition than **6-Sol** ('Smoothness' = 30 K) with transition temperatures comparable to **6-Mech** ($T_{1/2}\uparrow$ = 216 K and $T_{1/2}\downarrow$ = 212 K), as shown in Figure 3.31(c). Finally, **6-BM90** exhibited similar transition properties to other mechanically synthesised samples ('Smoothness' = 30 K) centred on $T_{1/2}\uparrow$ = 215 K and $T_{1/2}\downarrow$ = 211 K, consistent with the β-form, as shown in Figure 3.31(d). To emphasise similarities between the mechanically prepared samples and the corresponding differences to **6-Sol**, the second heating cycles were normalised

between 0 and 1, and overlaid, as shown in Figure 3.32. In all four of our samples, only one SCO transition is visible in the magnetic data. This strongly indicates the presence of one form in each sample. Comparison of SCO activity for all four samples and both the α-form and β-form are shown in Table 3.9.
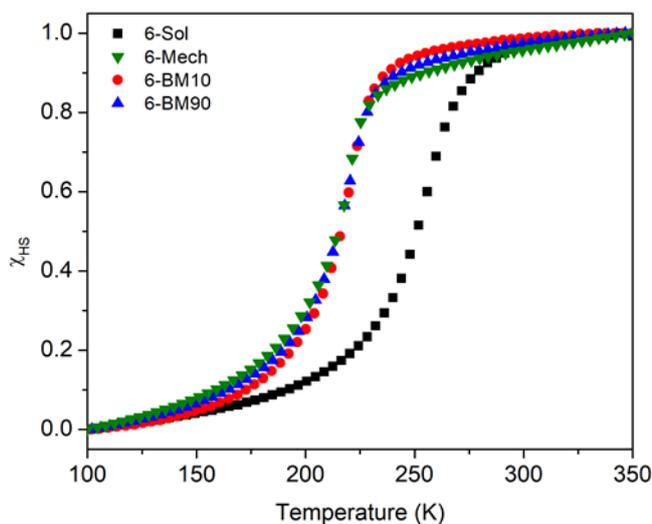

Figure 3.32: Normalised $\chi_M T$ vs Temperature plots, second heating cycles, for **6-Sol** (■), **6-Mech** (▼), **6-BM10** (●) and **6-BM90** (▲).

Table 3.9: SCO properties determined by SQUID magnetometry for **6-Sol**, **6-Mech**, **6-BM10** and **6-BM90**. Compared with previous literature reports on the α-form and β-form.[62]

Sample	$T_{1/2}\uparrow$ (K)	$T_{1/2}\downarrow$ (K)	ΔT (K)	'Smoothness'
6-Sol	251	250	1	39
6-Mech	215	212	3	31
6-BM10	216	212	4	30
6-BM90	215	211	4	30
α-Form Literature[62]	260	250	10	18
β-Form Literature[62]	245	239	6	8

PXRD was carried out on each sample, as shown in Figure 3.33. The pattern for **6-Sol** closely resembles that described by Grosjean,[62] thus confirming the solution-state formation of the α-form. However, the patterns for all three mechanically synthesised samples are virtually

identical to each other but significantly different to the solution synthesised sample. In the pattern described by Grosjean, a number of peaks present in the pattern are outside of the proposed fit. These additional peaks correlate well with the patterns collected for **6-Mech**, **6-BM10** and **6-BM90**, therefore supporting the formation of the β-form by mechanical synthesis. Additionally, the signal: noise ratio is significantly worse in **6-Mech**, **6-BM10** and **6-BM90**, this is consistent with reduced crystallinity, as suggested by Grosjean. The PXRD patterns for **6-Mech**, **6-BM10** and **6-BM90** were not suitable for size determination by Scherrer analysis, this was due to the significant splitting in the Bragg peaks preventing accurate determination of full width half maximum (FWHM) thus preventing particle size determination.
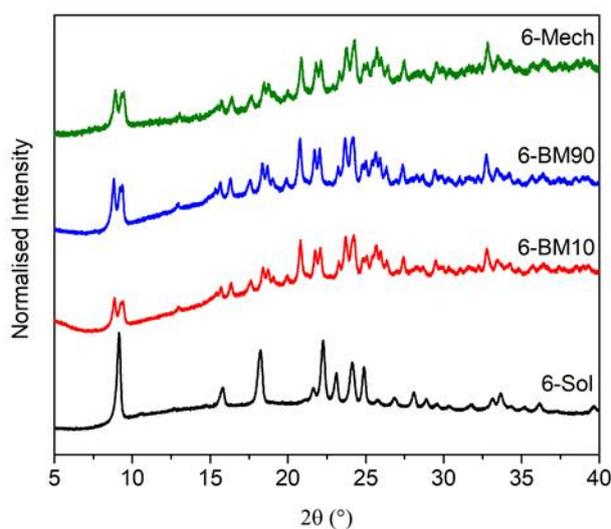

Figure 3.33: Normalised PXRD for **6-Sol**, **6-Mech**, **6-BM10** and **6-BM90**.

The Fourier transform of Fe-edge EXAFS data are shown in Figure 3.34. The data were collected at room temperature in which the complex is in the HS state, in both α and β forms. Data show that all of the samples have the same short-range order. The peak at 2.20(1) Å corresponds to the Fe-N distance, consistent with a Fe^{2+} HS species.[47] The following peaks represent the Fe-C (3.17(1) Å), Fe-C (3.18(1) Å) and Fe-Fe (3.90(5) Å) shells. It is not possible to observe Fe-Fe-Fe multiple scattering in any of the samples of compound **6**, the absence of such a

peak in the HS state is expected and has been discussed extensively in literature, owing to a greater Fe-N bond length distribution as a result of the degenerate $^5T_{1g}$ state.[47,64]
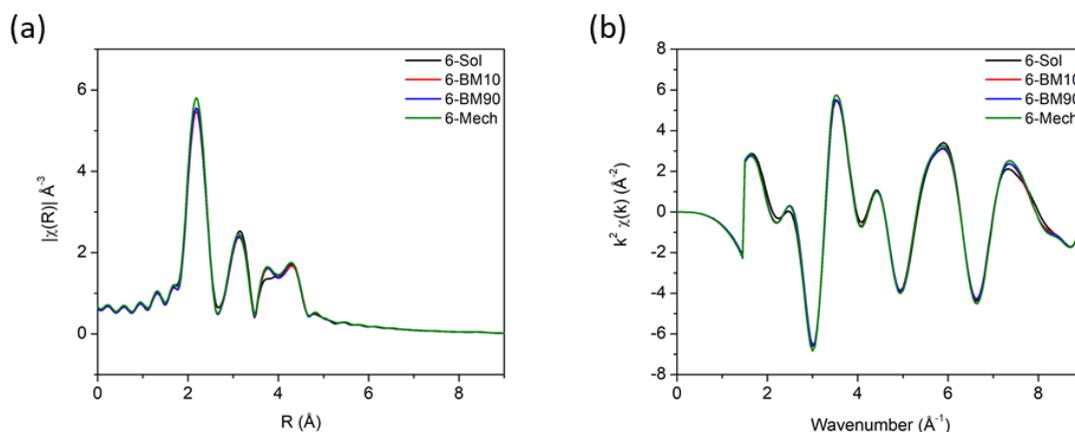

Figure 3.34: K^3 weighted pseudo-radial distribution function of R-Space Fe-Edge spectra for **6-Sol**, **6-BM10**, **6-BM90** and **6-Mech**. **(b)** Combined Fe-Edge k Space EXAFS spectrum (k^3 weighted) for **6-Sol**, **6-BM10**, **6-BM90** and **6-Mech**. the difference at 3.8 Å is attributed to a fitting artefact as discussed in 2.2.1.

As discussed previously, the degree of amorphisation was compared by analysis of the Debye-Waller factors (σ^2). In all four cases, the amount of amorphisation is comparable; differences between the values are within the error or the measurement. Therefore, synthesis via mechanochemistry does not introduce amorphisation into this system; even after prolonged grinding in a ball mill as seen in **6-BM90**. Full fitting data and associated Debye-Waller factors are shown in Table 3.10.

Sample	Neighbour	N	R / Å	σ^2 x10^3 / Å^2	E_f / eV	AFAC	R-fit
6-Sol	N	6	2.19(1)	7.4(11)	8.3(6)	0.88(8)	0.0135
	C	6	3.17(1)	7.7(28)			
	N	6	3.18(1)	10.8(28)			
	Fe	2	3.90(5)	25.6(146)			
6-Mech	N	6	2.20(1)	6.4(12)	8.1(7)	0.85(9)	0.0189
	C	6	3.16(1)	7.9(40)			
	N	6	3.17(1)	10.1(31)			
	Fe	2	3.89(6)	17.4(85)			
6-BM10	N	6	2.20(1)	6.5(12)	8.4(6)	0.81(8)	0.0178
	C	6	3.17(1)	7.5(35)			
	N	6	3.18(1)	10.2(29)			
	Fe	2	3.91(6)	16.6(75)			
6-BM90	N	6	2.20(1)	6.2(12)	8.3(7)	0.80(8)	0.0176
	C	6	3.16(1)	7.7(39)			
	N	6	3.18(1)	9.6(29)			
	Fe	2	3.89(6)	16.4(75)			

Solvent effects on SCO properties were explored by TGA, as shown in Figure 3.35. The mechanically synthesised samples showed a slight variation in mass loss with **6-Mech** losing 2.3% (0.6 eqv. H_2O), **6-BM90** losing 2.6% (0.7 eqv. H_2O) and **6-BM10** losing the least at 0.9% (0.2 eqv. H_2O). The difference in water content for mechanically synthesised samples has proved insignificant with regard to their SCO properties. The water content for **6-Sol** was slightly greater than **6-BM10** at 1.5% (0.4 eqv. H_2O), but still remained lower than both **6-Mech** and **6-BM90**; all calculated mass loss remains within potential error of the calculation. As such the differences in magnetic properties are not attributed to differences in hydration and previously reported effects of hydration are not observed in these samples. The amount of water varied between samples without affecting the properties as such this water was likely adsorbed onto the surface of the material rather than a stoichiometric component of the complex.
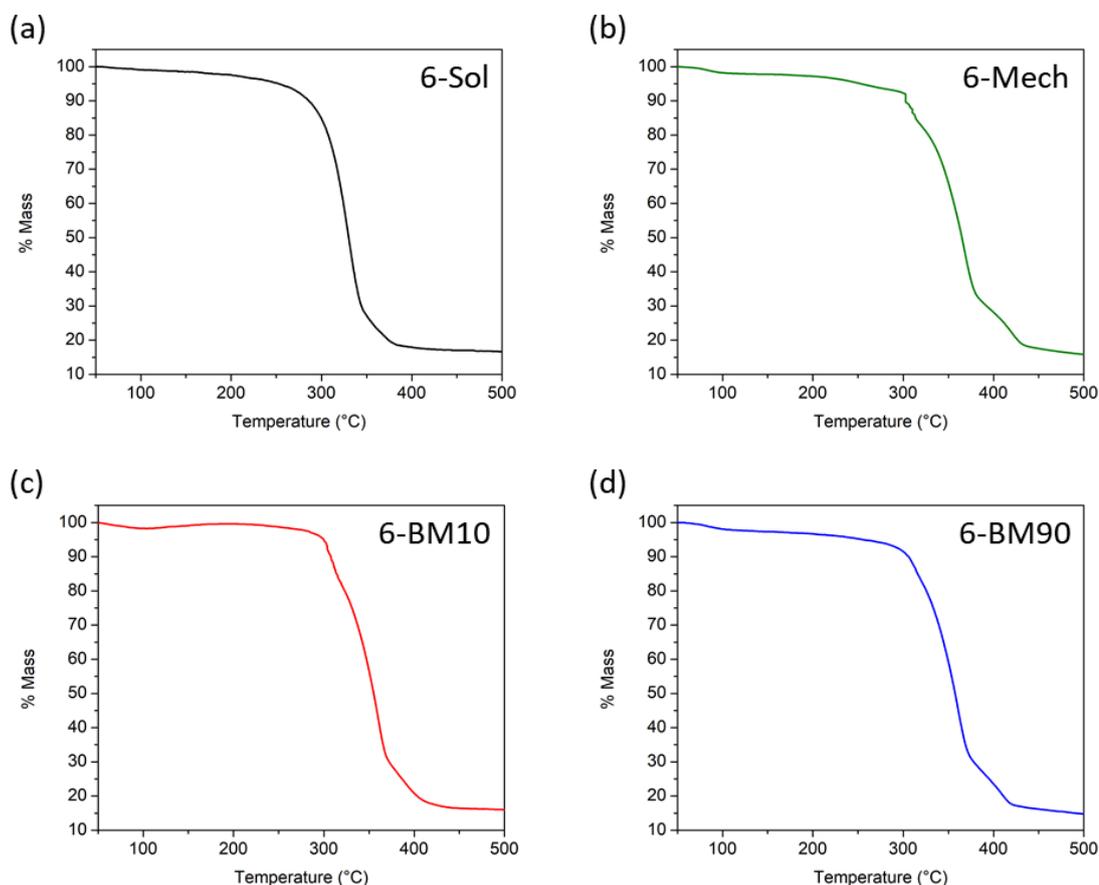
Figure 3.35: TGA plots of % mass vs temperature. (a) **6-Sol** (b) **6-Mech** (c) **6-BM10** (d) **6-BM90**.

Particle size and morphology was determined by TEM, as shown in Figure 3.36 and Figure 3.37. In all four samples, the particles had a spherical morphology. Particles of **6-Sol** were determined to be 48 ± 22 nm in diameter and **6-Mech** particles were measured at 53 ± 20 nm. Both **6-Sol** and **6-Mech** showed large particle size distribution with similar particle sizes, strongly indicating the differences in magnetic properties are not due to size effects. Both **6-BM10** and **6-BM90** showed smaller particle sizes than **6-Sol**, with **6-BM10** = 27 ± 11 nm and **6-BM90** = 22 ± 7 nm. The variation in particle size observed in the mechanically synthesised samples is not accompanied by differences in magnetic properties, aside from the irreversible first cycle observed for **6-BM10** which is attributed to the 'run-in' effect discussed in 1.1.4. However, longer grinding of the samples led to a slight decrease in both particle size and particle size distribution which remained within the potential error, whilst maintaining magnetic properties. There is a visible decrease in size distribution between ball milled samples.
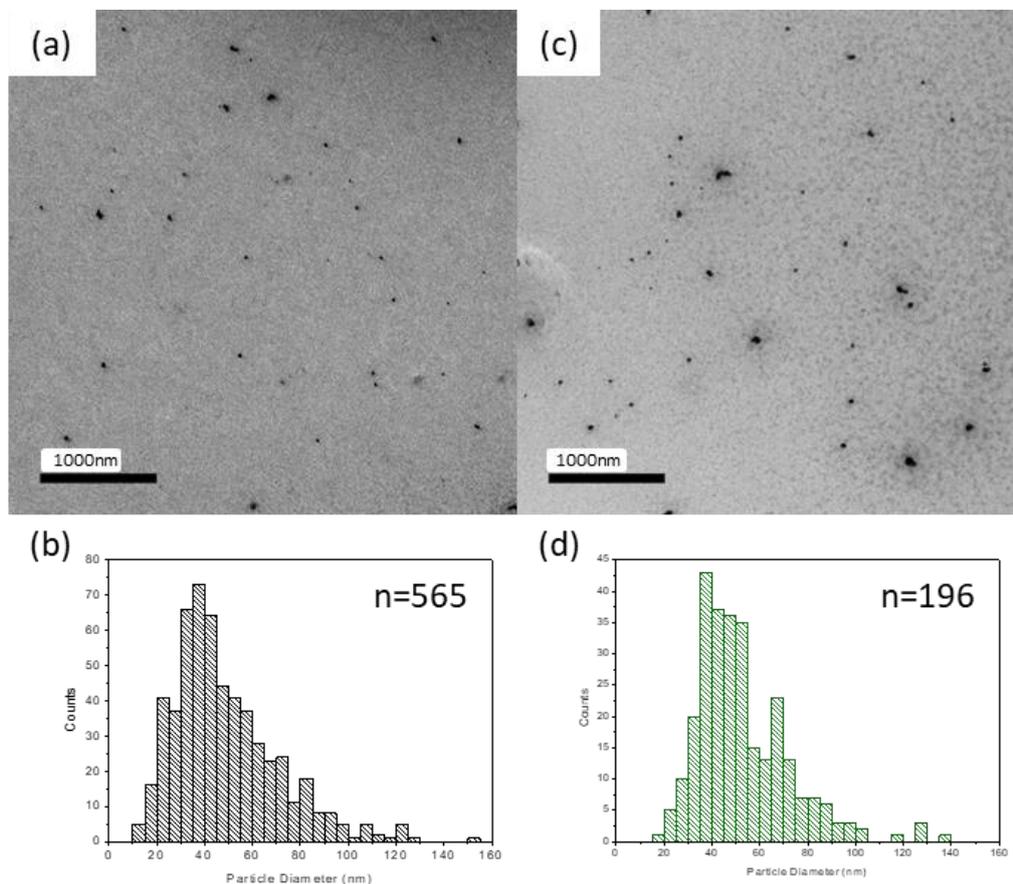
Figure 3.36: (a) Representative TEM image for compound **6-Sol**. **(b)** Particle length distribution for compound **6-Sol**, where n = 565. **(c)** Representative TEM image for compound **6-Mech**. **(d)** Particle length distribution for compound **6-Mech**, where n = 284.
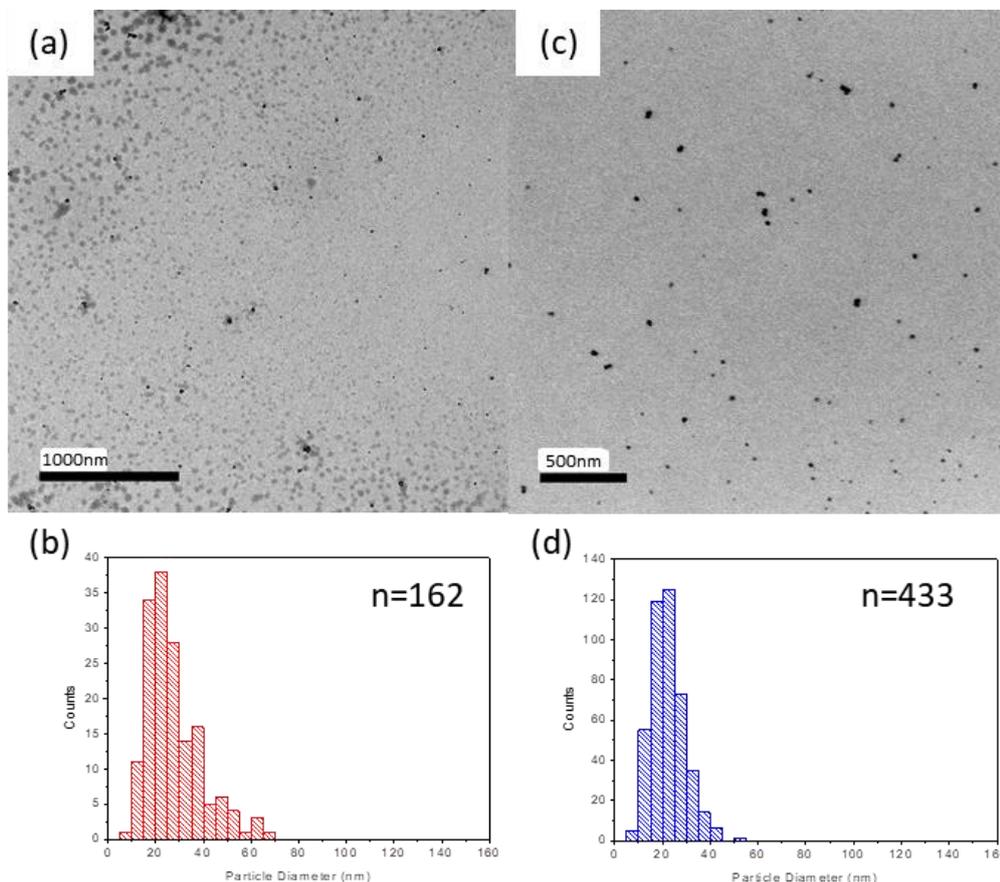
Figure 3.37: (a) Representative TEM image for compound **6-BM10**. **(b)** Particle length distribution for compound **6-BM10**, where n = 162. **(c)** Representative TEM image for compound **6-BM90**. **(d)** Particle length distribution for compound **6-BM90**, where n = 433.

3.2.6.1.1.   Post-synthetic *vs.* Synthetic Grinding

Conversion between the two polymorphs of $[Fe(atrz)_3](BF_4)_2$ was attempted by post-synthetic grinding a sample of **6-Sol** for 10 minutes, in attempt to replicate the conditions of the synthetic grinding process of **6-Mech**, yielding **6-Sol-10**. The magnetic properties of **6-Sol-10** were recorded by SQUID magnetometry as shown in Figure 3.38(a). After grinding, **6-Sol-10** displayed a two-step transition, as indicated by the first derivative Figure 3.38(c), with the first-step $T_{1/2}\uparrow = T_{1/2}\downarrow = 212$ K representing ≈ 60% of the sample and the second-step $T_{1/2}\uparrow = T_{1/2}\downarrow = 252$ K representing the remaining ≈ 40%. The former is consistent with the transition temperature measured for the β-form in the mechanochemically synthesised samples (**6-Mech**, **6-BM10** and **6-BM90**) and the latter is similar in temperature to **6-Sol** prior to grinding, the α-form. **6-Sol-10** was ground for an additional 20 minutes, yielding **6-Sol-30**. **6-Sol-30** displayed two-step SCO with the first-step

consistent with **6-Sol-10**, $T_{1/2}\uparrow = T_{1/2}\downarrow = 212$ K representing an increased proportion of the transition (75%) and the second-step $T_{1/2}\uparrow = T_{1/2}\downarrow = 252$ K representing the remaining 25%, as shown in Figure 3.38(b) with the first derivative included in Figure 3.38(d) to emphasise the two-step transition. Thus, as grinding time increases, the conversion of the α-form into the β-form increases.
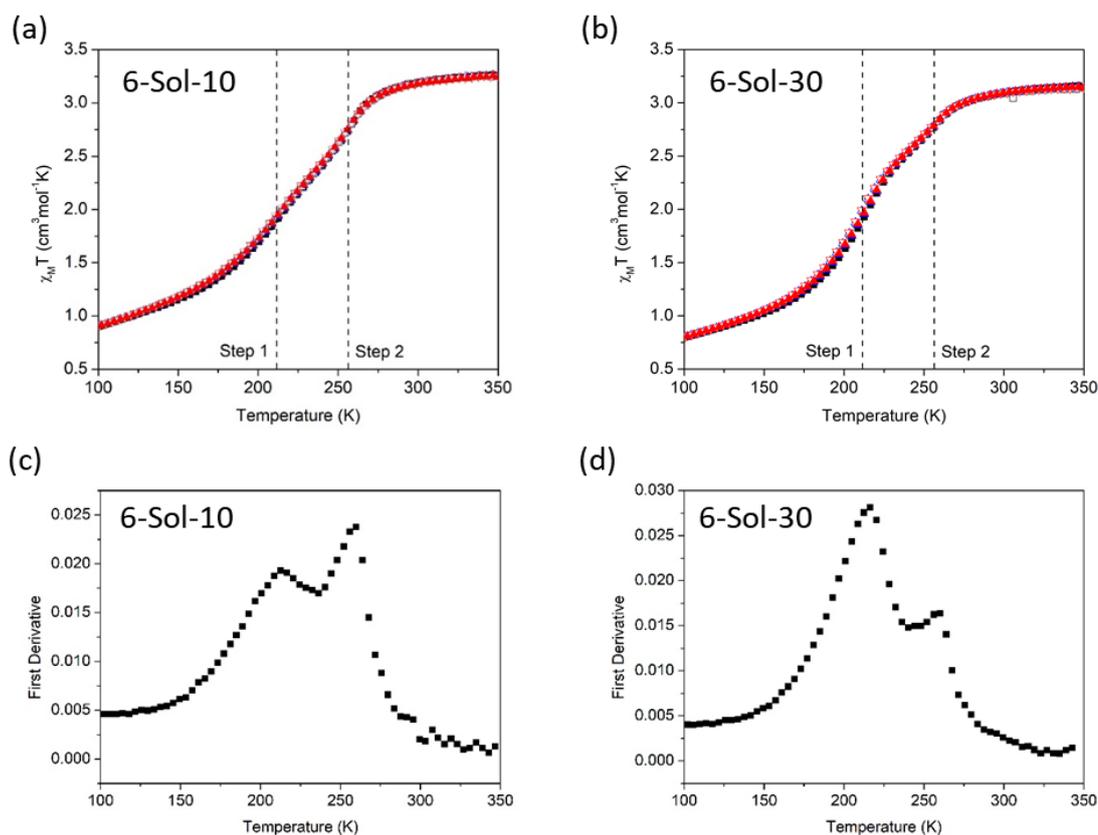

Figure 3.38: Plots of $\chi_M T$ vs T for compound three cycles, with the stepped transitions indicated by dashed lines. First cycle: heating ■, cooling □ Second cycle: heating ▲, cooling △ Third Cycle: Heating ▼ and cooling ▽. (a) **6-Sol-10** (b) **6-Sol-30**. First derivative of 2nd heating cycle. (c) **6-Sol-10** and (d) **6-Sol-30**.

Due to the solution-state synthesis of **6-Sol** including a washing step to remove impurities and both **6-Sol-10** and **6-Sol-30** originating from the same original sample, the absolute $\chi_M T$ values and their relative changes can be used to investigate the change in residual HS fraction, induced by post-synthetic grinding. The residual HS fraction remaining at 100 K for **6-Sol** was a value of 0.6 $cm^3mol^{-1}K$ which slightly increased in **6-Sol-10** with a 0.9 $cm^3mol^{-1}K$ and a similar value in **6-Sol-30** (0.8 $cm^3mol^{-1}K$) . It is worth noting the residual HS fractions for **6-Mech** (0.4 $cm^3mol^{-1}K$),

6-BM10 (0.2 cm^{3}mol^{-1}K) and **6-BM90** (0.3 cm^{3}mol^{-1}K) do not indicate that the β-form inherently contains a higher residual HS fraction. Therefore, this increase in residual HS fraction is likely attributed to a decrease in particle size caused by the grinding process and not an inherent property of the β-form. Further investigation *via* Mössbauer spectroscopy could provide crucial insight into these effects.

The conversion of the α-form into the β-form, shown in Figure 3.38, was also monitored by PXRD analysis, as shown in Figure 3.39, which showed the structure remained mostly unchanged after grinding for 10 minutes (**6-Sol-10**). The majority of the peaks remained consistent with the exception of the presence of a shoulder on the peak at 8° 2θ and the appearance of two peaks at 13° and 21° 2θ. Continued grinding for a total of 30 minutes increased the size of the shoulder at 8° 2θ. The size of the peaks at 13° and 21° 2θ further increased after 30 minutes of grinding. The peaks and peak splitting present after 30 minutes of grinding are consistent with the pattern collected for **6-Mech**. Grinding **6-Sol** also decreased the signal-noise ratio, which is attributed to a lower crystallinity for the β-form, as previously discussed by Grosjean.[62] The pattern for **6-Sol-30** appears to be a mixture of the patterns for **6-Sol** and **6-Mech**.
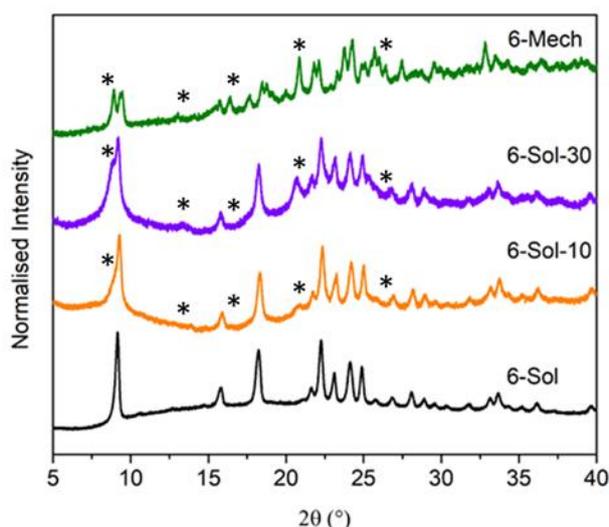

Figure 3.39: Normalised PXRD for **6-Sol**, **6-Sol-10**, **6-Sol-30** and **6-Mech**. * denotes some of the key peaks in **6-Mech** that are visible after grinding.

As previously discussed, when comparing **6-Sol** with the three mechanically prepared samples, the degree of hydration was investigated by TGA analysis, as shown in Figure 3.40. At 150 °C, **6-Sol-10** lost 3.5% mass which is equivalent to 0.9 H_2O and **6-Sol-30** lost 4.2% mass which is equivalent 1.0 H_2O. Both **6-Sol-10** and **6-Sol-30** showed a mass loss greater than **6-Sol** indicating the moisture content increased during the grinding process. This may indicate a link between moisture content and the polymorph identified. However, initial comparisons between **6-Sol** and the three mechanically prepared samples indicated water content was not a significant factor affecting the form observed, as shown in Table 3.11. Therefore, the increased water content observed for **6-Sol-10** and **6-Sol-30** is tentatively attributed to external factors , such as variation in environmental humidity. However, further investigation into the effects of hydration should be carried out in future work, to confirm this conclusion.
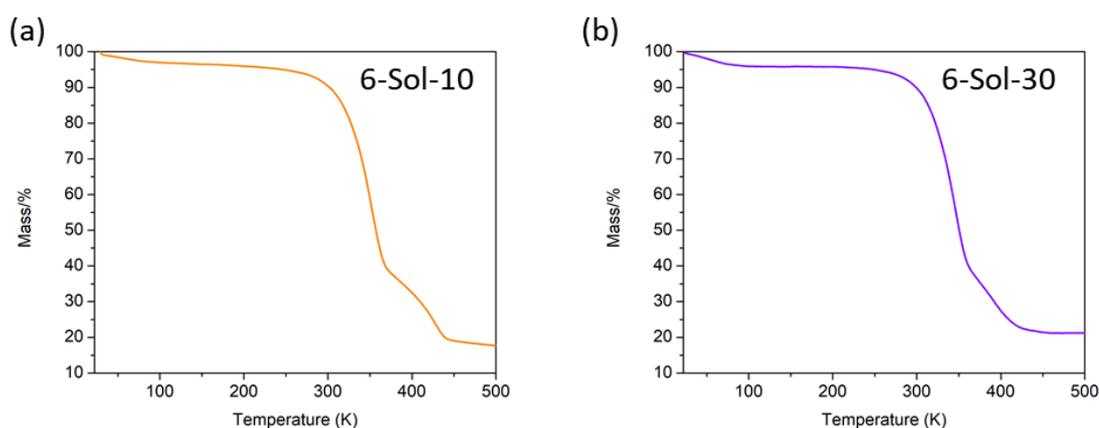

Figure 3.40: TGA plots of % mass vs temperature. (a) **6-Sol-10** (b) **6-Sol-30.**

Table 3.11: Mass loss at 150 °C determined by TGA with corresponding equivalence of H_2O per complex, for **6-Mech**, **6-BM10**, **6-BM90**, **6-Sol**, **6-Sol-10** and **6-Sol-30**.

Sample	Mass Loss (%)	Stoichiometric Ratio of Water
6-Mech	2.3	0.6
6-BM10	0.9	0.2
6-BM90	2.6	0.7
6-Sol	1.5	0.4
6-Sol-10	3.5	0.9
6-Sol-30	4.2	1.0

3.2.6.1.2. Summary

Synthesis of the [Fe(atrz)$_3$](BF$_4$)$_2$ complex was carried out using a previously reported solution-state procedure and three different mechanochemical techniques (manual grinding, ball milling for 10 minutes and ball milling for 90 minutes). The solution synthesised product displayed SCO consistent with previously literature reports (T$_{1/2}$↑ = 251 K and T$_{1/2}$↓ = 250 K), hereby denoted the α-form. All three mechanically synthesised products displayed SCO activity at 40 K lower (T$_{1/2}$↑ = 216 K and T$_{1/2}$↓ = 212 K), which was consistent with a previously reported but uncharacterised second form, hereby denoted the β-form. Characterisation of all four products was carried out using SQUID magnetometry, PXRD, Fe-Edge EXAFS, TGA and TEM and indicated the presence of only one polymorph in each sample. PXRD analysis confirmed the formation of same polymorph in all three mechanically prepared samples with a different form in the solution-state synthesised sample. EXAFS analysis confirmed the same short-range order for all four samples with comparable degrees of amorphisation. TGA analysis showed the absence of significant solvents contributions to differences in SCO properties. Similarly, variation in particle sizes did not contribute to changes in SCO properties. Conversion of the α-form to the β-form was possible through manually grinding **6-Sol** in a pestle and mortar, yielding a 75% conversion after 30 minutes.

As discussed for compounds **3** and **5**, the effects of mechanochemical synthesis on the SCO properties was investigated by synthesising *via* manual mechanochemistry and solution-state techniques. The effects for [Fe(atrz)$_3$](BF$_4$)$_2$ were significantly greater than observed for any other compounds. The mechanochemical product (**6-Mech**) displayed SCO behaviour at < 40 K lower than **6-Sol**. However, no significant differences in particle size, short-range structural order or hydration were observed, which showed the decrease in transition temperature was not due to differences in crystal quality, that were previously discussed for compounds **3** and **5**. This indicated mechanochemical synthesis yielded a different polymorph to solution-state synthesis. To investigate the effects of automatic milling on the reaction products, [Fe(atrz)$_3$](BF$_4$)$_2$ was synthesised using a ball mill (**6-BM10**). No significant differences in properties were observed

between **6-Mech** and **6-BM10**. In a similar vein, the effects of prolonged synthetic grinding were investigated by comparing the products of automated milling for 10 minutes (**6-BM10**) and 90 minutes (**6-BM90**) of synthesis. For both **6-BM10** and **6-BM90** the SCO properties remained relatively unchanged, aside from the first cycle in which the 'run-in' effect was reduced in **6-BM90**. The particle size and morphology remained largely unchanged with prolonged grinding, indicating the effects of prolonged synthetic grinding are relatively insignificant.

3.3. Conclusions and Prospects

Mechanochemistry was used to synthesise a range of SCO-active materials. The molecular system $Fe(phen)_2(NCS)_2$, two 1-D triazole complexes ($[Fe(Htrz)_3](BF_4)_2$ and $[Fe(atrz)_3]SO_4$) and both two- ($Fe(4\text{-}phpy)_2[Ni(CN)_4]$) and three- ($Fe(pz)[Au(CN)_2]_2$) dimensional Hofmann-type clathrates were synthesised and analysed by SQUID magnetometry, Raman spectroscopy and PXRD. Comparison with both solvent synthesised and, where possible, literature reported properties was made. Mechanically synthesised $Fe(phen)_2(NCS)_2$ displayed similar SCO properties to literature reports, with slight variations in temperatures observed. The differences in properties were within the range of temperatures previously reported for the system. The wide range of temperatures reported for $Fe(phen)_2(NCS)_2$, show significant variation in the properties between different batches prepared using the same synthetic technique (165-190 K)[6,8,21,30,31], in addition to the differences observed for alternative synthetic approaches. This is important for this study because the variation in properties between batches may potentially mask changes in properties resulting from mechanochemical synthesis. Mechanochemical synthesis of $[Fe(Htrz)_3](BF_4)_2$ yielded a product which was polymorphic, showing multiple different forms present in the magnetic data. Attempts to convert the product into one form by extended drying in an oven, yielded a three-component mixture. Further analysis of $[Fe(Htrz)_3](BF_4)_2$ was not carried out. Mechanical synthesis of $[Fe(atrz)_3]SO_4$ highlighted hydration effects, indicating the importance of water content. But, after drying, the SCO properties were almost identical to a solvent synthesised sample.

Synthesis of the two- dimensional Hofmann-type Clathrate compound $Fe(4\text{-}phpy)_2[Ni(CN)_4]$ by neat grinding was unsuccessful and required the addition of a small quantity of water to the grinding process (LAG). After LAG synthesis, magnetic properties were similar to a solution synthesised sample. However, synthesis of the three-dimensional Hofmann-type Clathrate complex $Fe(pz)[Au(CN)_2]_2$ by neat grinding was possible, indicating the required addition of water may be dependent on the specific complex and not a requirement for synthesis of two- and three-dimensional Hofmann-type clathrate networks.

Mechanochemistry was used successful in the synthesis of 0-D, 1-D, 2-D and 3-D networks of SCO-active materials. The products were crystalline and display SCO properties consistent with solution synthesised samples. Although a general trend that showed decreases in both $T_{1/2}\uparrow$ and $T_{1/2}\downarrow$, a decrease in ΔT and more gradual SCO behaviour was seen, this is not a rule, as demonstrated by $[Fe(atrz)_3]SO_4$, which showed that the SCO properties of mechanochemically synthesised products are not always worse than solution synthesised products. In conclusion, three different complexes were more thoroughly investigated and synthesised using solution-state and mechanochemical synthetic procedures to investigate the effects of mechanochemical synthesis on the structure and properties of the materials. Analysis was carried out by SQUID magnetometry, PXRD, TGA, Fe-Edge EXAFS and TEM. Two of the complexes, $[Fe(atrz)_3]SO_4$ (compound **3**) and $Fe(pz)[Au(CN)_2]_2$ (compound **5**) yielded the same compound using both synthetic techniques. But, $[Fe(atrz)_3](BF_4)_2$ (compound **6**) prepared by mechanochemistry resulted in a different polymorph than the solution-state product.

Analysis of $[Fe(atrz)_3]SO_4$ (compound **3**) and $Fe(pz)[Au(CN)_2]_2$ (compound **5**) has indicated that the effects of mechanochemical synthesis are not straightforward. In both cases, mechanochemical synthesis yielded smaller particle sizes and slightly more gradual SCO transitions. But, only in $[Fe(atrz)_3]SO_4$ (compound **3**) was the transition temperature affected. Therefore, the effects of mechanochemical synthesis appear to be dependent on the specific complex.

Mechanochemical synthesis of $[Fe(atrz)_3](BF_4)_2$ (compound **6**) yielded a previously observed but uncharacterised polymorph. Comparison of mechanochemical synthesis by manual grinding and ball-milling for two different time periods indicated the synthesis of the same product with relatively insignificant differences in degree of hydration, amorphisation and SCO properties. The magnetic properties of all three mechanically prepared samples indicated the presence of only one polymorph with a $T_{1/2}\uparrow \approx 40$ K lower in temperature. No significant differences in hydration were observed for either synthetic approach, proving reaction products of manual mechanochemical synthesis can be representative of products obtained by ball-milling. Similarly, prolonged synthetic grinding did not significantly affect the SCO properties. Both polymorphs possessed the same short-range order and comparable amorphisation, as confirmed by EXAFS. Conversion of the α-form to the β-form was possible by manually grinding **6-Sol** in a pestle and mortar, yielding a 60% conversion in 10 minutes and an increase to 75% conversion after 30 minutes.

The potential applications of mechanochemistry in the field of SCO research are vast. The short reaction times are ideal for the rapid screening of potential SCO materials, as explored in Chapter 5. As previously discussed, many SCO materials have high solvent sensitivity, and mechanochemical synthesis represents an ideal method for solvent free synthesis, allowing solvent effects to be systematically explored. Mechanical synthesis could also represent an opportunity for particle size-control without the use of surfactants, an important requirement for potential applications. Mechanochemical synthesis, either manual grinding or automated milling, has some exciting prospects for discovery of novel SCO materials. The effects of mechanical synthesis on the SCO properties of known materials appears to be complex-dependent and further research into the changing properties could provide valuable insight. It has been shown that mechanochemistry can produce materials with comparable properties to solution methods, but much more rapidly. There is also a possibility of identifying further novel polymorphs of known materials, which may not be accessible by solution-state approaches, opening an exciting avenue for future SCO research.

3.4. References

1   M. S. Haddad, W. D. Federer, M. W. Lynch and D. N. Hendrickson, *J. Am. Chem. Soc.*, 1980, 102, 1468–1470.

2   M. Sorai, R. Burriel, E. F. Westrum and D. N. Hendrickson, *J. Phys. Chem. B*, 2008, **112**, 4344–4350.

3   M. S. Haddad, M. W. Lynch, W. D. Federer and D. N. Hendrickson, *Inorg. Chem.*, 1981, **20**, 123–131.

4   M. S. Haddad, W. D. Federer, M. W. Lynch and D. N. Hendrickson, *Inorg. Chem.*, 1981, **20**, 131–139.

5   M. D. Timken, S. R. Wilson and D. N. Hendrickson, *Inorg. Chem.*, 1985, **24**, 3450–3457.

6   P. Ganguli, P. Gütlich, E. W. Müller and W. Irler, *J. Chem. Soc. Dalt. Trans.*, 1981, 441.

7   W. A. Baker and H. M. Bobonich, *Inorg. Chem.*, 1964, **3**, 1184–1188.

8   E. Konig and K. Madeja, *Inorg. Chem.*, 1967, **6**, 48–55.

9   I. Dézsi, B. Molnár, T. Tarnóczi and K. Tompa, *J. Inorg. Nucl. Chem.*, 1967, **29**, 2486–2490.

10   J. H. Takemoto and B. Hutchinson, *Inorg. Chem.*, 1973, **12**, 705–708.

11   M. Sorai and S. Seki, *J. Phys. Chem. Solids*, 1974, **35**, 555–570.

12   E. W. Müller, H. Spiering and P. Gütlich, *Chem. Phys. Lett.*, 1982, **93**, 567–571.

13   E. Konig, G. Ritter and S. K. Kulshreshtha, *Inorg. Chem.*, 1984, **23**, 1144–1148.

14   E. König, G. Ritter, S. K. Kulshreshtha and N. Csatary, *Inorg. Chem.*, 1984, **23**, 1903–1910.

15   L. Salmon and L. Catala, *Comptes Rendus Chim.*, 2018, **21**, 1230–1269.

16   E. Coronado, J. R. Galán-Mascarós, M. Monrabal-Capilla, J. García-Martínez and P. Pardo-Ibáñez, *Adv. Mater.*, 2007, **19**, 1359–1361.

17   L. Moulet, N. Daro, C. Etrillard, J.-F. Létard, A. Grosjean and P. Guionneau, *Magnetochemistry*, 2016, **2**, 10.

18   T. Forestier, A. Kaiba, S. Pechev, D. Denux, P. Guionneau, C. Etrillard, N. Daro, E. Freysz and J. F. Létard, *Chem. - A Eur. J.*, 2009, **15**, 6122–6130.

19   J. R. Galán-Mascarós, E. Coronado, A. Forment-Aliaga, M. Monrabal-Capilla, E. Pinilla-Cienfuegos and M. Ceolin, *Inorg. Chem.*, 2010, **49**, 5706–5714.

20   G. Hoshina, S. Ohba and N. Tsuchiya, *Acta Crystallogr. Sect. C*, 2000, **C56**, 191–192.

21   B. Gallois, J. A. A. Real, C. Hauw and J. Zarembowitch, *Inorg. Chem.*, 1990, **29**, 1152–1158.

22   C. Akers, S. W. Peterson and R. D. Willett, *Acta Cryst*, 1968, **24**, 1125.

23   S. Nishigaki, H. Yoshioka and K. Nakatsu, *Acta Crystallogr. Sect. B Struct. Crystallogr. Cryst. Chem.*, 1978, **34**, 875–879.

24   G. Brunton, *Acta Crystallogr. Sect. B Struct. Crystallogr. Cryst. Chem.*, 1969, **25**, 2161–2162.

25   O. Roubeau, *Chem. - A Eur. J.*, 2012, **18**, 15230–15244.

26   K. Hosoya, S. Nishikiori, M. Takahashi and T. Kitazawa, *Magnetochemistry*, 2016, **2**, 8.

27   A. Bousseksou, J. J. McGarvey, F. Varret, J. A. Real, J.-P. Tuchagues, A. C. Dennis and M. L. Boillot, *Chem. Phys. Lett.*, 2000, 409–416.

28   P. Gütlich, *Spin Crossover in Iron(II)-Complexes*, Springer, Berlin, Heidelberg, 1981, vol. 44.

29   E. König, G. Ritter and S. K. Kulshreshtha, *Chem. Rev.*, 1985, **85**, 219–234.

30   J. A. Real, B. Gallois, T. Granier, S. P. Franz and J. Zarembowitch, *Inorg. Chem.*, 1992, **31**, 4972–4979.

31   N. Tsuchiya, A. Tsukamoto, T. Ohshita, T. Isobe, M. Senna, N. Yoshioka and H. Inoue, *J. Solid State Chem.*, 2000, **153**, 82–91.

32   J. Laisney, A. Tissot, G. Molnár, L. Rechignat, E. Rivière, F. Brisset, A. Bousseksou and M.-L. Boillot, *Dalt. Trans.*, 2015, **44**, 17302–17311.

33   O. Kahn and C. J. Martinez, *Science.*, 1998, **279**, 44–48.

34   K. Jonas, A. Jean-Paul, C. Renée, C. Epiphane, K. Olivier, J. G. Haasnoot, G. Françoise, J. Charlotte, A. Bousseksou, L. Jorge, V. François and G. V. Anne, *Chem. Mater.*, 1994, **6**, 1404–1412.

35   L. G. Lavrenova, O. G. Shakirova, V. N. Ikorskii, V. A. Varnek, L. A. Sheludyakova and S. V. Larionov, *Russ. J. Coord. Chem. Khimiya*, 2003, **29**, 22–27.

36   B. Morgan and O. Lahav, *Chemosphere*, 2007, **68**, 2080–2084.

37   T. Zhao, L. Cuignet, M. M. Dîrtu, M. Wolff, V. Spasojevic, I. Boldog, A. Rotaru, Y. Garcia and C. Janiak, *J. Mater. Chem. C*, 2015, **3**, 7802–7812.

38   E. O. Schlemper and W. C. Hamilton, *J. Chem. Phys.*, 1966, **44**, 4498–4509.

39   J. H. Askew and H. J. Shepherd, *Chem. Commun.*, 2018, **54**, 180–183.

40   A. Urakawa, W. Van Beek, M. Monrabal-Capilla, J. R. Galán-Mascarós, L. Palin and M. Milanesio, *J. Phys. Chem. C*, 2011, **115**, 1323–1329.

41   E. Smit and D. De Waal, *J. RAMAN Spectrosc.*, 2001, **32**, 339–344.

42   P. J. van Koningsbruggen, Y. Garcia, E. Codjovi, R. Lapouyade, O. Kahn, L. Fournès, L. Rabardel, C. Jay, A. Bousseksou, J. Linarès, F. Varret and A. Gonthier-Vassal, *J. Mater. Chem.*, 1997, **7**, 2069–2075.

43   O. Roubeau, J. G. Haasnoot, E. Codjovi, F. Varret and J. Reedijk, *Chem. Mater.*, 2002, **14**, 2559–2566.

44   B. Tomiczek, L. A. Dobrzański, M. Adamiak and K. Labisz, *Procedia Manuf.*, 2015, **2**, 402–407.

45   Y. Zheng, Z. Fu, D. Li and M. Wu, *Materials (Basel).*, 2018, **11**, 1–13.

46   A. M. Greenaway and E. Sinn, *J. Am. Chem. Soc.*, 1978, **100**, 8080–8084.

47   A. Michalowicz, J. Moscovici, B. Ducourant, D. Cracco and O. Kahn, *Chem. Mater.*, 1995, **7**, 1833–1842.

48   M. B. Bushuev, D. P. Pishchur, I. V. Korolkov and K. A. Vinogradova, *Phys. Chem. Chem. Phys.*, 2017, **19**, 4056–4068.

49   D. R. Lide, *Physical Constants of Inorganic Compounds - Ammonium Sulfate*, 2005, vol. Internet.

50   M. Seredyuk, A. B. Gaspar, V. Ksenofontov, M. Verdaguer, F. Villain and P. Gutlich, *Inorg. Chem.*, 2009, **48**, 6130–6141.

51   I. A. Gural'skiy, B. O. Golub, S. I. Shylin, V. Ksenofontov, H. J. Shepherd, P. R. Raithby, W. Tremel and I. O. Fritsky, *Eur. J. Inorg. Chem.*, 2016, **2016**, 3191–3195.

52   V. Niel, J. M. Martinez-Agudo, M. C. Muñoz, A. B. Gaspar and J. A. Real, *Inorg. Chem.*, 2001, **40**, 3838–3839.

53   K. L. Ronayne, H. Paulsen, A. Höfer, A. C. Dennis, J. A. Wolny, A. I. Chumakov, V. Schünemann, H. Winkler, H. Spiering, A. Bousseksou, P. Gütlich, A. X. Trautwein and J. J. McGarvey, *Phys. Chem. Chem. Phys.*, 2006, **8**, 4685–4693.

54   G. G. Li, F. Bridges and X. Wang, *Nucl. Inst. Methods Phys. Res. A*, 1994, **340**, 420–426.

55   D. B. Leznoff, B. Y. Xue, C. L. Stevens, A. Storr, R. C. Thompson and B. O. Patrick, *Polyhedron*, 2001, **20**, 1247–1254.

56   R. Dewitt, L. J. Wittenberg and S. Cantor, *Phys. Chem. Liq.*, 1974, **4**, 113–123.

57   N. Tsuchiya, A. Tsukamoto, T. Ohshita, T. Isobe, M. Senna, N. Yoshioka and H. Inoue, *Solid State Sci.*, 2001, **3**, 705–714.

58   A. B. Gaspar, G. Levchenko, S. Terekhov, G. Bukin, J. Valverde-Muñoz, F. J. Muñoz-Lara, M. Seredyuk and J. A. Real, *Eur. J. Inorg. Chem.*, 2014, 429–433.

59   O. Kahn, J. Kröber and C. Jay, *Adv. Mater.*, 1992, **4**, 718–728.

60   V. A. Varnek and L. G. Lavrenova, *J. Struct. Chem.*, 1995, **36**, 120–127.

61   N. Daro, L. Moulet, N. Penin, N. Paradis, J. F. Létard, E. Lebraud, S. Buffière, G. Chastanet and P. Guionneau, *Materials (Basel).*, 2017, **10**, 60.

62   A. Grosjean, L'UNIVERSITÉ BORDEAUX, 2013.

63   A. Grosjean, P. Négrier, P. Bordet, C. Etrillard, D. Mondieig, S. Pechev, E. Lebraud, J.-F. Létard and P. Guionneau, *Eur. J. Inorg. Chem.*, 2013, **2013**, 796–802.

64   A. Michalowicz, J. Moscovici and O. Kahn, *Le J. Phys. IV*, 2009, **7**, C2-633-C2-635.

.

Chapter 4: Post-synthetic Solid-State Metathesis of 1,2,4-Triazole Based Spin Crossover Materials

4.1. Introduction

4.1.1. Solid State Metathesis

Solid state metathesis (SSM) is a technique commonly used in the synthesis of inorganic materials.[1,2] The technique is a 'double displacement' reaction carried out in the solid state that can be initiated by external stimuli such as ignition sources, mechanical or microwave energy.[3] SSM reactions use intrinsically available energy of reacting species to promote the exchange of ions between compounds. Activation energy barriers in SSM reactions are initially overcome by external stimuli as described above. The process then proceeds as a chain reaction, whereby the released energy is sufficient to sustain anion metathesis.[4] Applications of SSM thus far are mostly limited to the synthesis of solid state materials including metal borides,[5–7] nitrides[8–10] and carbides,[11,12] with particular interest in the synthesis of novel rare earth salts such as nitridoborates and carbodiimides, in yields and speeds inaccessible via direct synthetic routes.[13] In most SSM reactions, the formation of highly stable alkali halide salts acts as the major driving force for the reaction.[1] The majority of successful SSM reactions are the result of very large enthalpies of reaction ($\Delta H_{rxn}°$) resulting in a huge amount of energy released as the reaction proceeds. Due to this, the reactions are usually exceptionally quick and self-sufficient.[5] The application of SSM to SCO material synthesis has not previously been investigated. However, the possibility of introducing alternative anions to known SCO materials could allow for the identification of a significant number of novel compounds. However, application of SSM requires consideration of thermodynamic properties, as discussed below.

4.1.2. Thermodynamic Properties

4.1.2.1. Enthalpy

Enthalpy is a thermodynamic expression representing the total heat content within a system.[14] Total enthalpy of a system is calculated according to (Equation 4.1). Enthalpy (H) is defined by the internal energy of the system (U), pressure (p) and volume of the system (V), as shown.

$$H = U + pV$$

(Equation 4.1)

Change in enthalpy (ΔH) is used to observe the change of energy in a system after undergoing a transformation or chemical reaction. The standard enthalpy change, $\Delta H°$, describes the change in enthalpy under standard conditions.[15] Depending on the process undertaken, multiple terms are used to describe the change in energy. For example, standard enthalpy change of combustion ($\Delta H_C°$) is used to describe the enthalpy change when a substance undergoes complete combustion at standard temperature and pressure, and standard enthalpy of reaction ($\Delta H_{rxn}°$) is used to describe the change in enthalpy when one mole of a substance reacts completely.

4.1.2.2. Total Lattice Potential Energies

Multiple different terms relating to the 'lattice energy' for a system have been proposed. These include; lattice formation enthalpy, which represents the change in energy when one mole of the ionic solid is formed from scattered gaseous ions, and lattice dissociation enthalpy, which represents the energy required for the conversion of one mole of the ionic solid into scattered gaseous ions. The suitability of both terms for application in determining changes in energy, generally depends on the presence of monoatomic ionic species, whereby the ions are treated as point charges. In instances with polyatomic ions, the formation of the ion itself requires significant energy. The energy contributions for the formation of polyatomic ions skew the formation and dissociation energies, which prevents stability comparisons between materials with monoatomic and polyatomic anions using these metrics. [16]

In polyatomic ions the charge distribution often prevents the point charge assumptions being made. As such, sophisticated calculations are required to correctly assign the total ion charge distribution between the atomic components of the complex polyatomic ions, which allows the lattice energy to be calculated.[17] Total lattice potential energy (U_{POT}) is the term used to represent the relative stability of ionic solids when comparing lattice energies of both monoatomic and polyatomic atoms. It represents the energy 'stored' within the lattice. As a simple assumption, the larger the values for U_{POT}, the more stable the lattice.[16]

4.1.2.2.1.   Kapustinskii Equation Estimates

The Kapustinskii equation is used to obtain an estimate value for total lattice potential energy, as shown in (Equation 4. 2). The requirement for such an equation arises due to inherent difficulties in determining lattice energies for ionic crystals. Calculating U_{POT} using the equation requires multiple terms including elementary charge of the cation (z_α) and anion (z_β), number of ions in the empirical formula (v) and the ionic radii of the cation (r_α) and anion (r_β).[16]

$$U_{POT} = \frac{121.4 z_a z_b v}{(r_a + r_b)} \left(1 - \frac{0.0345}{(r_a + r_b)} \right)$$

<div align="right">(Equation 4. 2)</div>

4.1.3.   Anions in [Fe(atrz)$_3$](A)$_x$

The Fe(II) 4-R-1,2,4-triazole (Rtrz) family of SCO materials has been prepared using a wide variety of anions, ranging from simple monoatomic anions such as the halides[18] (Cl, Br and I) to large polyatomic sulfonates such as $C_{18}H_{37}SO_3^-$.[19] A significant number of the 4-amino-4-H-1,2,4-triazole complexes reported with different anions display different SCO properties, the 1-D Fe-triazole chain structure is shown in Figure 4.1.
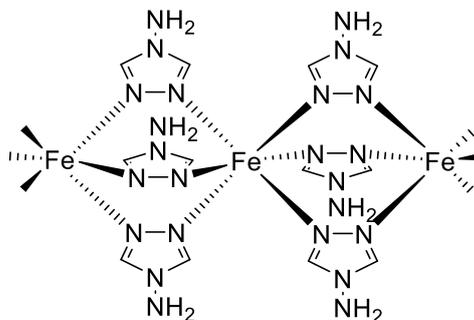
Figure 4.1: Structural representation of the 1-D triazole chains formed for [Fe(atrz)$_3$]$^{2+}$.

4.1.3.1. Halogens

Spin crossover behaviour has previously been reported for [Fe(atrz)$_3$]A$_x$ (where A = anion) with three halogens, Cl,[20] Br[21,22] and I.[23] [Fe(atrz)$_3$]Cl$_2$ was first reported by Lavrenova *et al*.[20] displaying a relatively abrupt transition centred at T$_{1/2}$↑ = 355 K. However, the subsequent cooling cycle shown by Lavrenova *et al*. suggested a significant decrease in the transition temperature, T$_{1/2}$↓ = 300 K with an apparent hysteresis of 55 K, as shown in Figure 4.2(a). In that study, this change in transition temperature was accompanied by an increase in residual HS fraction on cooling, demonstrating the occurrence of a quasi-irreversible process. The proposed hydrated form, [Fe(atrz)$_3$]Cl$_2$.2H$_2$O, showed T$_{1/2}$↑ = 315 K, T$_{1/2}$↓ = 306 K with no significant change in residual HS fraction on cooling, as shown in Figure 4.2(b). In the work by Lavrenova *et al*. only one heating and cooling cycle is shown, but it is common for the first heating cycle to be different from subsequent cycles in many SCO species, particularly the triazole family of complexes, due to the 'run-in' effect discussed further in 1.1.4. Differences in transition temperature between the first and subsequent heating cycles of up to 40 K were previously observed.[24] The absence of subsequent cycles in reported literature highlights the difficulty in comparison with SCO properties for compound **7**.
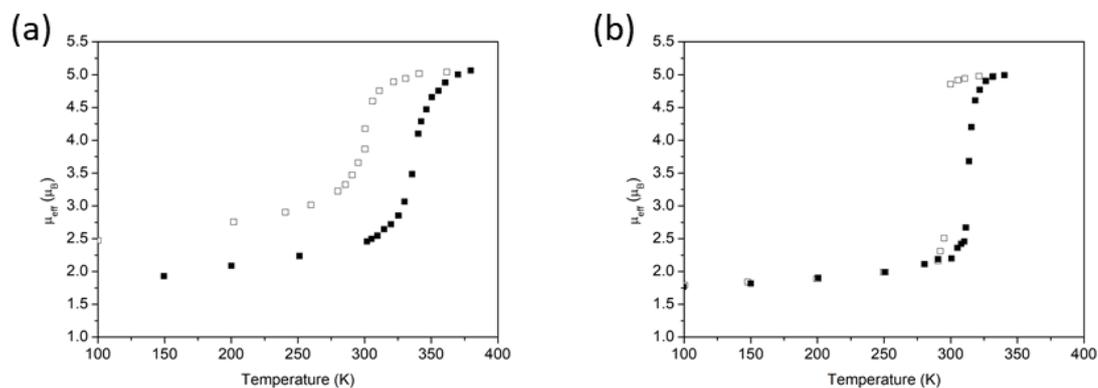
Figure 4.2: (a) Digitised variable temperature magnetic data for [Fe(atrz)$_3$]Cl$_2$ from literature.[20] (b) Digitised variable temperature magnetic data for [Fe(atrz)$_3$]Cl$_2$.2H$_2$O from literature.[20] Heating ■,Cooling □.

The complex [Fe(atrz)$_3$]Br$_2$ was first reported by Lavrenova *et al*. with T$_{1/2}$↑ = 312 K.[25] It displays significant particle size dependence, where decreasing particle size was accompanied by a clear decrease in the width of hysteresis.[21] Additional literature reports on the complex have shown SCO behaviour with significantly different SCO temperatures with Kahn *et al*.[26] giving values of T$_{1/2}$↑ = 307 K and T$_{1/2}$↓ = 279 K, as shown in Figure 4.3. The particle size effects were explored with particles ranging from >1000 nm to 30-70 nm, displaying SCO activity within the range: T$_{1/2}$↑ = 312 K − 320 K and T$_{1/2}$↓ = 304 K − 313 K.[21] The range of SCO temperatures emphasises the sensitivity of these complexes to different synthetic techniques. The [Fe(atrz)$_3$]Br$_2$ complex was also reported as being prone to oxidation by Kahn *et al.* with a chemical stability reported as lower than two comparable complexes [Fe(atrz)$_3$](BF$_4$)$_2$ and [Fe(trz)(Htrz)$_2$](BF$_4$).[26]
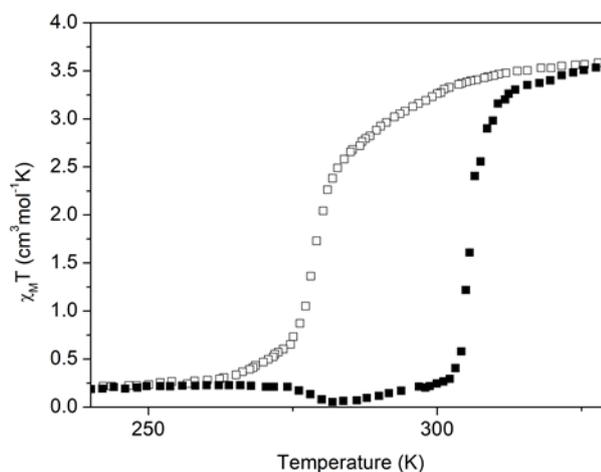
Figure 4.3: Digitised variable temperature magnetic data plot for [Fe(atrz)$_3$]Br$_2$.H$_2$O from literature.[26] Heating ■, Cooling □.

[Fe(atrz)$_3$]I$_2$ was first reported by Lavrenova *et al.*,[23] and synthesis of the complex required the multistep generation of FeI$_2$ from FeSO$_4$.7H$_2$O. The resulting complex displayed SCO behaviour with T$_{1/2}$↑ = 270 – 280 K and T$_{1/2}$↓ = 260 – 278 K, as shown in Figure 4.4.
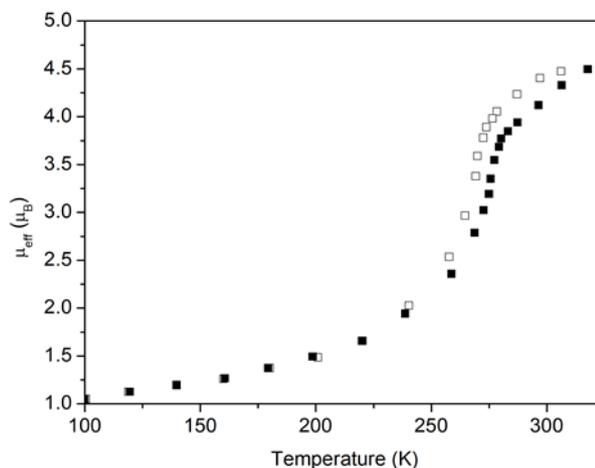
Figure 4.4: Digitised variable temperature magnetic data for [Fe(atrz)$_3$]I$_2$ from literature.[23] Heating ■, Cooling □.

4.1.3.2. Perrhenate

The complex [Fe(atrz)$_3$](ReO$_4$)$_2$ was previously reported by Lavrenova *et al.*[27] with T$_{1/2}$↑ = 228 K, T$_{1/2}$↓ = 223 K, as shown in Figure 4.5. In a similar manner to [Fe(atrz)$_3$]I$_2$, synthesis of [Fe(atrz)$_3$](ReO$_4$)$_2$ required the in-situ formation of Fe(ReO$_4$)$_2$ from NaReO$_4$, FeSO$_4$.7H$_2$O and

Ba(NO$_3$)$_2$. The perrhenate complex was reported as showing a substantial residual HS fraction at low temperatures, which was attributed to the possibility of two structurally non-equivalent forms of the complex. However, no structural investigation of [Fe(atrz)$_3$](ReO$_4$)$_2$ was presented so it is impossible to evaluate the validity of this claim. Another explanation is that partial oxidation of the iron occurred, or impurities remained in the sample, either unreacted reagents or reaction by-products. Further, it is also possible that the complex undergoes an incomplete transition.[28]
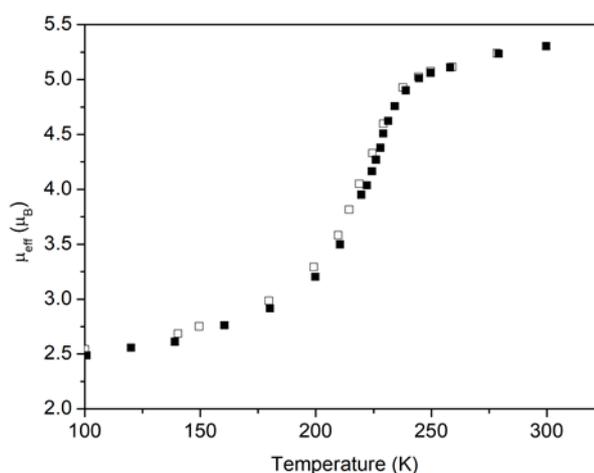
Figure 4.5: Digitised variable temperature magnetic data for [Fe(atrz)$_3$](ReO$_4$)$_2$ from literature.[27] Heating ■, Cooling □.

4.1.3.3. Thiocyanate

Thiocyanate (NCS) is an ambidentate ligand that can act as a nucleophile at either the sulphur or nitrogen. In some instances, the thiocyanate anion can bridge Fe(II) centers, which results in usual FeN$_5$S coordination environments and lead to the formation of 1-D coordination polymers.[29] In most instances, for a complex with thiocyanate as the anion to be SCO active, the anion binds through the nitrogen. The thiocyanate anion strongly coordinates to hard acids such as iron. The strong coordination can cause the anion to cap the growth of 'infinite' 1-D chains, of the type shown in Figure 4.1. The strongly coordinating anions can prevent the potential for obtaining long chain complexes with triply bridged triazole chains, this has been observed in which complexes with strongly coordinating anions preferably form short chain complexes such as dimers[30–32] and

trimers.[31,33] $[Fe(atrz)_3]Cl_2$ could potentially be used as a template for the synthesis of long 1-D triazoles chains and then exchange the Cl anions for the thiocyanate anions. This could be used as a strategy to synthesise long 1-D triazole chains with thiocyanate anions, which could possibly improve cooperativity in the system and lead to a more abrupt transition and potentially modify the transition temperature compared to short chains accessible *via* solution synthetic methods.
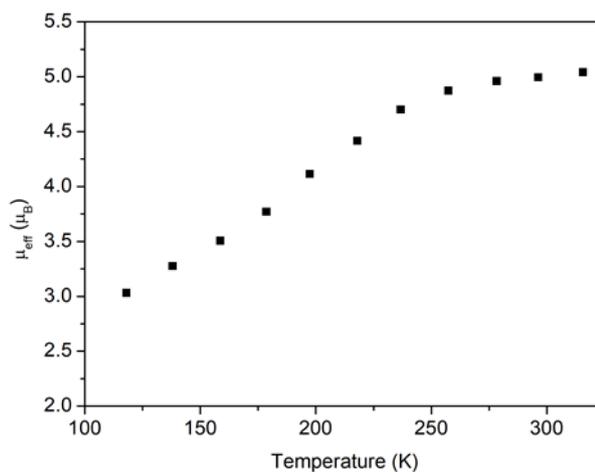

Figure 4.6: Digitised variable temperature magnetic data for $[Fe(atrz)_3](NCS)_2$ from literature.[23]

A complex with the proposed formula $[Fe(atrz)_3](NCS)_2$ was first reported by Lavrenova *et al*.[23] with a gradual SCO, $T_{1/2}\uparrow$ = 200 K, $T_{1/2}\downarrow$ = 200 K, as shown in Figure 4.6. However, no structural characterisation was presented. The thiocyanate complex included a large residual HS fraction at low temperatures. The complex was analysed using Mössbauer spectroscopy and similarities in the HS octahedral distortion to the dimeric complex, $Mn_2(4\text{-methyl-1,2,4-triazole})_5(NCS)_4$ were identified. Therefore, the residual HS fraction at low temperature is likely due to only some of the Fe-centres being SCO active. Further examples of short chain Fe(II) complexes with the NCS^- anion include $[Fe_2(4Phtrz)_5(NCS)_4](H_2O)_{2.5}$ (where 4-Phtrz = 4-phenyl-1,2,4-triazole)[34] and $[Fe_5(4^PTotrz)_{12}(NCS)_{10}(H_2O)_2]$ (where 4^PTotrz = 4-^{P}toluyl-1,2,4-triazole).[30]

4.1.4.   Aims

In this chapter, solid state metathesis will be explored as a technique to introduce novel anions to 1,2,4-triazole based SCO materials. This will be done by attempting the exchange of

halogens in the material [Fe(atrz)$_3$]Cl$_2$ (where atrz = 4-amino-4H-1,2,4-triazole) using sodium halide salts. This method would allow for the exchange potential to be investigated and the properties of the products to be compared to literature reported properties for the expected products.

4.2. Results and Discussion

4.2.1. [Fe(atrz)$_3$]Cl$_2$

4.2.1.1. Mechanochemical Synthesis

[Fe(atrz)$_3$]Cl$_2$ (compound **7**) exhibits SCO with T$_{1/2}$↑ = 334 K, T$_{1/2}$↓ = 328 K, showing a narrow hysteresis of 6 K, as shown in Figure 4.7(a). The abruptness of the transition was defined by the 'smoothness', which was calculated as 39 K, repeated cycling of the system showed consistent SCO properties after the first heating cycle. As discussed above, literature reports for the complex [Fe(atrz)$_3$]Cl$_2$.xH$_2$O (where x = 0 or 2).[20] reported T$_{1/2}$↑ = 355 K, with significant cycling dependence. In this work, magnetic properties were collected for three heating and cooling cycles, to ensure consistency, with only the second cycle shown for clarity in Figure 4.7. The differences in properties for compound **7** and the previous literature report are attributed to run-in effects described in 1.1.4.
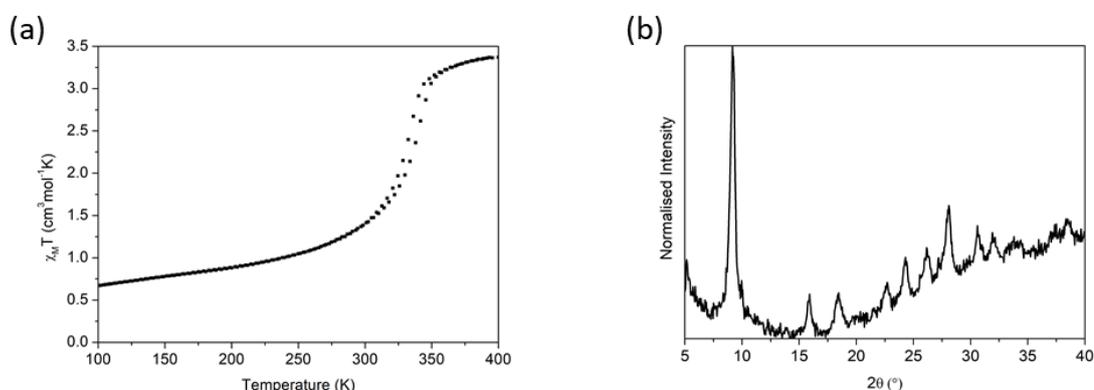

Figure 4.7: (a) Plot of X$_M$T vs T for compound **7**, second cycle. **(b)** Normalised PXRD data for compound **7**.

The PXRD data for compound **7** is shown in Figure 4.7(b). Previous literature reports on the complex have not presented PXRD data therefore comparison was not possible. However, the pattern clearly shows mechanochemical synthesis yielded a crystalline powder.

4.2.1.2. Effects of Grinding

The effects of grinding are investigated further in 3.2.6. For members of the 4-R-1,2,4-triazole family of SCO materials the effects of post-synthetic grinding generally follow the same trend, a slight decrease in both $T_{1/2}\uparrow$ and $T_{1/2}\downarrow$ as well as a slightly more gradual transition.

The applied SSM procedure required the further grinding of the mechanically synthesised compound **7**, in the presence of various sodium salts. Therefore, the effects of this additional grinding on [Fe(atrz)$_3$]Cl$_2$ were investigated using a control experiment. Compound **7** was ground in the presence of NaCl for 15 minutes, yielding compound **7-Cl**. This procedure should not lead to a change in the anion composition of the compound, due to both NaCl and compound **7** containing the same anion (Cl$^-$). Therefore, it was possible to isolate and evaluate the effects of grinding and anion exchange individually. The inclusion of the inactive salt, NaCl, allowed close simulation of the experimental conditions for other SSM experiments.

After grinding with NaCl and washing, the PXRD pattern for **7-Cl** was collected. The pattern is almost identical to compound **7**, as shown in Figure 4.8, indicating that the overall structure of compound **7** is retained after grinding. Crystallite size was estimated from peak broadening using the Scherrer equation, this allowed for domain sizes to be determined rather than aggregated particle size. The average domain size for **7** was calculated to be 62 nm and 40 nm for **7-Cl**, revealing a significant reduction in particle size resulting from the SSM procedure.
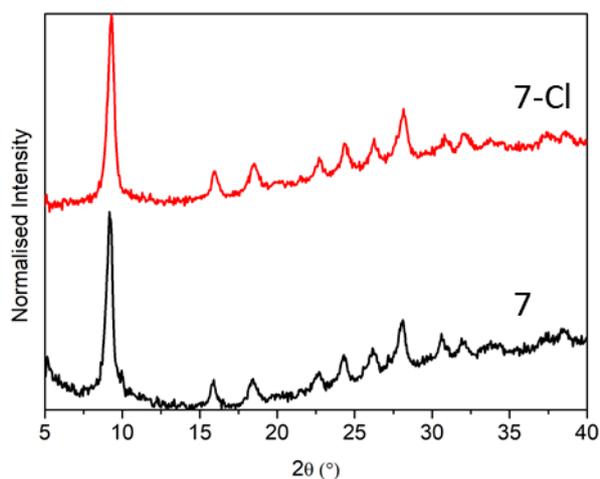
Figure 4.8: Comparison of normalised PXRD data for compound **7** and **7-Cl**.

As seen from the magnetic data in Figure 4.9, the reduction in particle size in **7-Cl** results in a decrease in transition temperature ($T_{1/2}\uparrow$ = 334 K to 318 K and $T_{1/2}\downarrow$ = 328 K to 316 K), decrease in width of hysteresis (5 K to 2 K) and a more gradual transition, with a calculated 'smoothness' of 55 K compared to 39 K prior to grinding. This is within expectation of literature reports[37] and our own investigation in 3.2.6. Comparison of the SCO properties for **7** and **7-Cl** with literature reports are presented in Table 4.1.
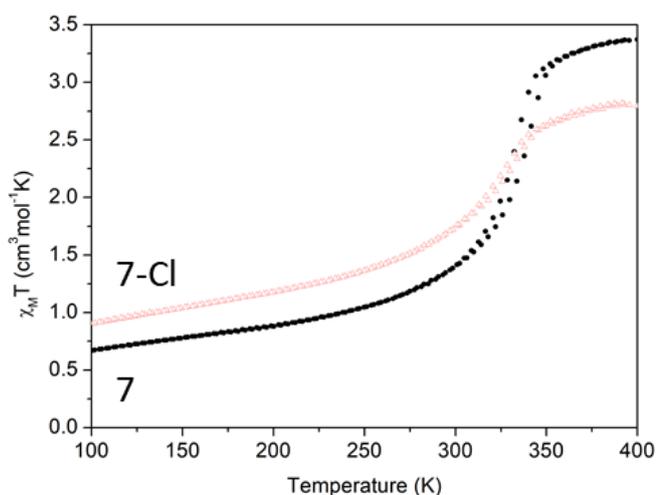

Figure 4.9: Comparison of $\chi_M T$ vs T for compound **7** and **7-Cl**, second cycle.

Table 4.1: Spin crossover properties of **7**, **7-Cl** and literature properties for [Fe(atrz)$_3$]Cl$_2$ and [Fe(atrz)$_3$]Cl$_2$.2H$_2$O.[20]

*Apparent hysteresis, as discussed in 4.1.3.1.

	T$_{1/2}$↑ (K)	T$_{1/2}$↓ (K)	ΔT (K)
7	334	325	6
7-Cl	318	316	2
Lit [Fe(atrz)$_3$]Cl$_2$	355	300	55*
Lit [Fe(atrz)$_3$]Cl$_2$.2H$_2$O	315	306	9

Transmission electron microscopy (TEM) was used to further explore particle size and morphology, for compound **7** (Figure 4.10(a)) and compound **7-Cl** (Figure 4.10(c)). As shown in Figure 4.10(b), compound **7** shows a wide distribution of particle sizes, ranging from 10 nm to 89 nm, with an average particle size of 28 ± 19 nm. The size distributions for 7-Cl (Figure 4.10(d)) were smaller, ranging from 5 nm to 42 nm, with the mean particle also decreasing to 19 ± 8 nm. Further analysis on the effects of mechanochemistry on the synthesis and modification are discussed in 3.2.6.
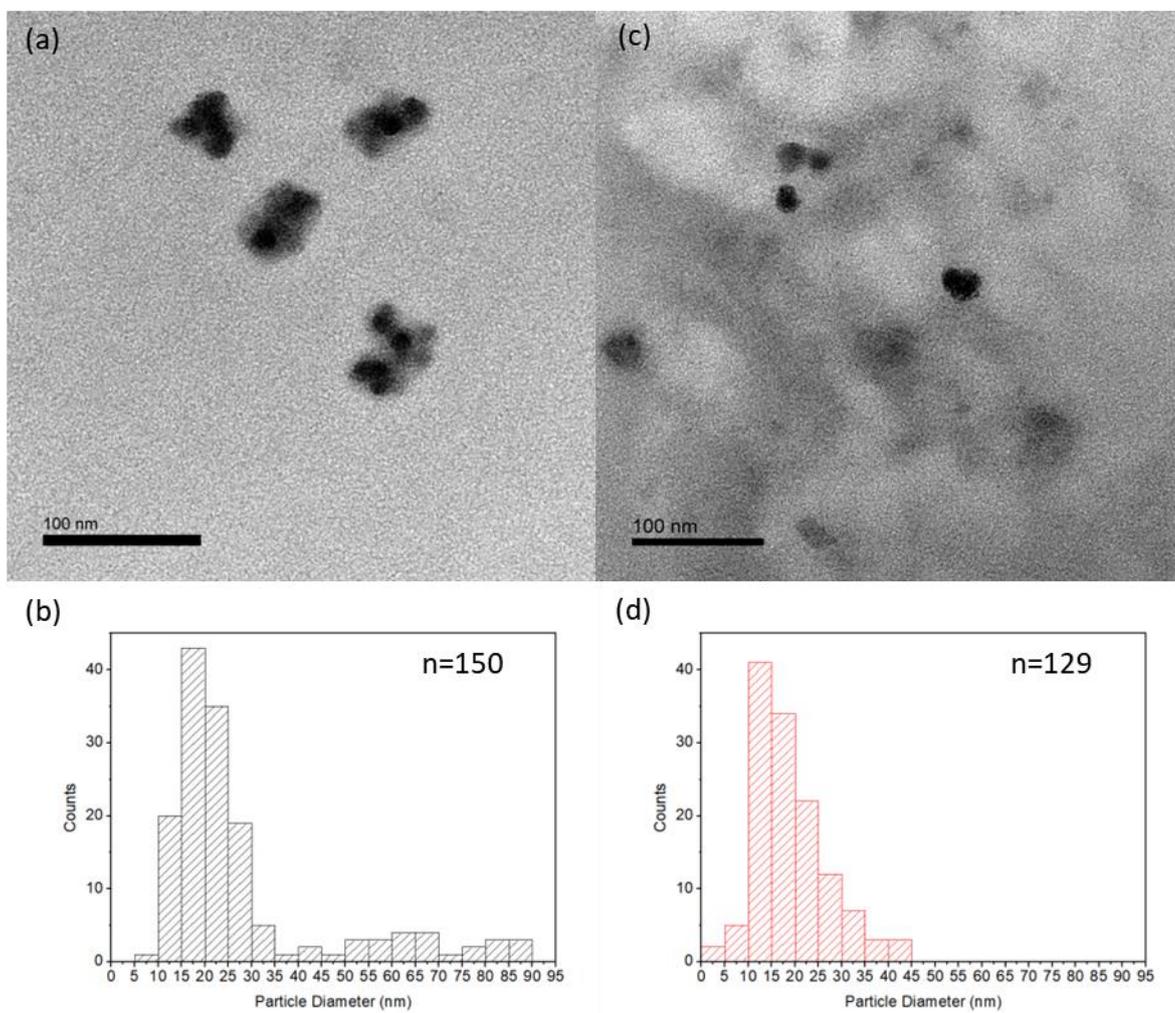
Figure 4.10: (a) Representative TEM image for compound **7**. **(b)** Particle size distribution for compound **7**, where n = 150. **(c)** Representative TEM image for compound **7-Cl**. **(d)** Particle size distribution for compound **7-Cl**, where n = 129. In both compound **7** and **7-Cl**, the observed particles were spherical and prone to forming aggregates. To reduce the formation of aggregates, bovine serum albumin (BSA) was added according to the method described in 2.2.1, the presence of which is visible in the background of **(c)**.

4.2.2. Halogen Exchange

4.2.2.1. Bromide

Solid state metathesis of compound **7** was carried out using an excess of NaBr, yielding product **7-Br**. The magnetic properties were measured, which showed significantly different SCO properties from the control sample **7-Cl**, $T_{1/2}\uparrow$ = 318 K to 298 K and $T_{1/2}\downarrow$ = 316 K to 295 K, as shown in Figure 4.11(a). The width of hysteresis slightly increased (2 K to 3 K) and abruptness of

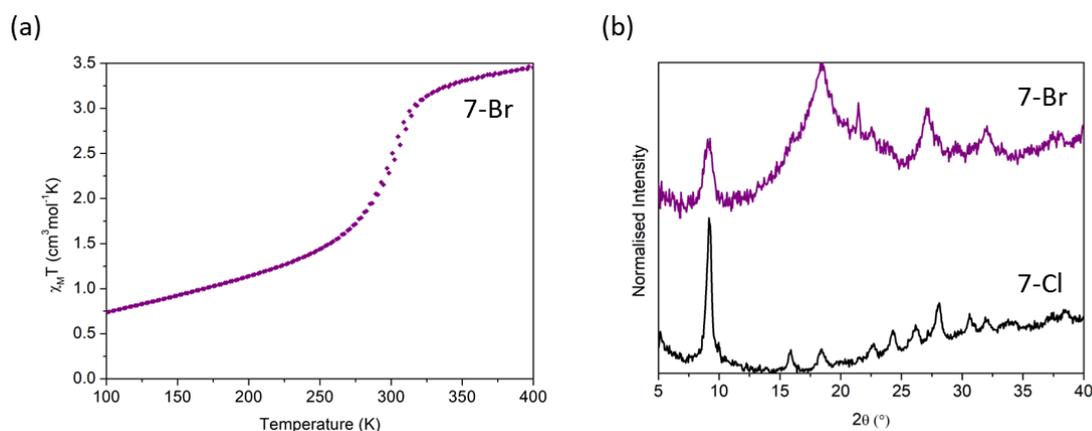the transition remained similar with a calculated 'smoothness' of 41 K compared to 39 K prior to SSM.

Figure 4.11: (a) $X_M T$ vs T for compound **7-Br**, second cycle. **(b)** Comparison of normalised PXRD data for compound **7-Br** and **7-Cl**.

The SCO properties were similar to previously reported transitions for the $[Fe(atrz)_3]Br_2$ complex, as discussed in 4.1.3.1, significant size dependence on SCO properties with a range on temperatures reported ($T_{1/2}\uparrow$ = 312 K – 320 K and $T_{1/2}\downarrow$ = 304 K – 313 K). The width of hysteresis for this complex was also previously observed as having considerable dependence on particle size, with ΔT being observed as low as 2 K for the smallest particles synthesised by traditional solution methods.[21] The observed hysteresis for **7-Br** (3 K) was within previously reported values; complete comparison between experimental and literature values for SCO properties are shown in Table 4.2.

Table 4.2: Spin crossover properties of **7-Cl**, **7-Br** and literature properties for $[Fe(atrz)_3]Br_2$.[21]

	$T_{1/2}\uparrow$ (K)	$T_{1/2}\downarrow$ (K)	ΔT (K)
7-Cl	318	316	2
7-Br	298	295	3
Lit [Fe(atrz)₃]Br₂	Range: 312 to 320	Range: 304 to 313	Range: 1 to 16

The PXRD pattern collected for the bromide exchange showed significant changes in the structure of the product when compared with **7-Cl**, as shown in Figure 4.11(b). The collected PXRD

pattern was similar to previously reported patterns for the complex [Fe(atrz)$_3$]Br$_2$.[21] The broadening of the peaks was an expected effect of the reduction in the crystallinity, crystalline domain size and the increase in crystalline defects resulting from the grinding process, as discussed in section 4.2.1.2. The large broad peak centred on 2θ = 18° indicates the presence of an amorphous material, further investigation on the origin of this was not undertaken.

4.2.2.2. Iodide

Repeating the SSM procedure using NaI yielded a white powder, compound **7-I**. A below room temperature transition was then confirmed by analysis of the magnetic properties as shown in Figure 4.12(a). **7-I** displayed SCO properties $T_{1/2}\uparrow$ = 253 K, $T_{1/2}\downarrow$ = 251 K and in contrast to the reported effects of grinding on SCO materials, the product maintained abruptness, with a calculated 'smoothness' = 39 K, equivalent to compound **7**, prior to exchange attempts. The resulting SCO properties showed a significant difference from the properties of compound **7**, with changes in both $T_{1/2}\uparrow$ >70 K, $T_{1/2}\downarrow$ >70 K and an increase in abruptness ('smoothness' 55 K to 39 K) when compared with the control sample **7-Cl**. The observed change in $T_{1/2}\uparrow$ and $T_{1/2}\downarrow$ was significantly greater than the observed changes for **7-Cl**.
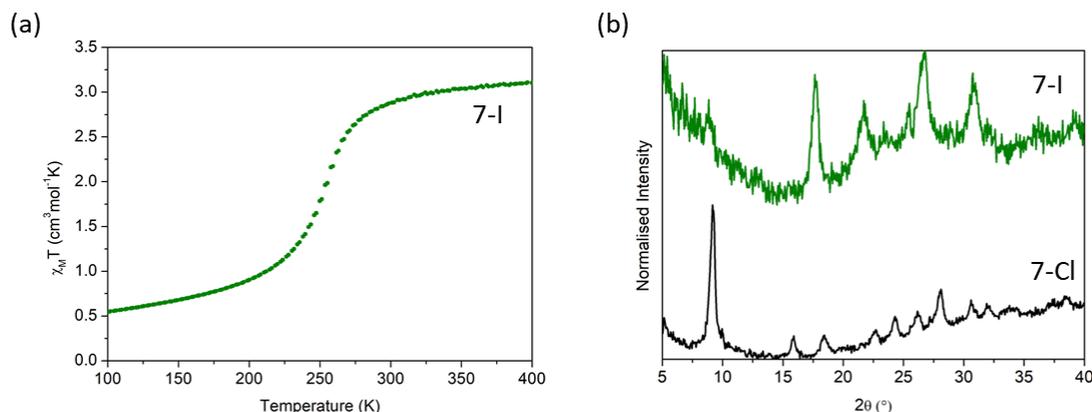

Figure 4.12: (a) X_MT vs T for compound **7-I**, second cycle. **(b)** Comparison of normalised PXRD data for compound **7-I** and **7-Cl**.

The PXRD pattern of **7-I** (Figure 4.12(b)) is significantly different from **7-Cl**, representing substantial differences in the structure of the product after SSM. PXRD data for $[Fe(atrz)_3]I_2$ is not available in literature and therefore comparison with previously reported data was not possible.

The complex $[Fe(atrz)_3]I_2$ has been previously reported with $T_{1/2}\uparrow$ = 270-280 K and $T_{1/2}\downarrow$ = 260-278 K.[23] The SCO properties of the **7-I** were identified as consistent with the complex $[Fe(atrz)_3]I_2$. Comparison between measured magnetic properties and those from literature[23] for **7-I** are shown in Table 4.3.

Table 4.3: Spin crossover properties of **7-Cl**, **7-I** and literature properties for $[Fe(atrz)_3]I_2$.[23]

	$T_{1/2}\uparrow$ (K)	$T_{1/2}\downarrow$ (K)	ΔT (K)
7-Cl	318	316	2
7-I	253	251	2
Lit [Fe(atrz)$_3$]I$_2$	Range: 270 to 280	Range: 260-278	Range: 8 to 20

4.2.2.3. Fluoride

Grinding with NaF was not expected to cause anion exchange. NaF is a stable salt and dissociation of the ions requires a significant amount of energy. Literature magnetic properties for the proposed SSM product $[Fe(atrz)_3]F_2$ are not available, and previous attempts to synthesise the complex were unsuccessful.[20] This was attributed to fundamental differences in the radii of the complex cation and anion which prevent the formation of a stable reaction product.

Compound **7** was ground with NaF for 15 minutes; yielding compound **7-F**. Analysis of the magnetic properties of the sample was carried out using SQUID magnetometry, as shown in Figure 4.13. The sample underwent a transition with $T_{1/2}\uparrow$ = 318 K, $T_{1/2}\downarrow$ = 316 K and with a 'smoothness' = 55 K. The properties of **7-F** were consistent with **7-Cl** including the transition temperatures and abruptness of transition. A significant difference in the values of $\chi_M T$ are shown, this is attributed the presence of NaF remaining in the sample, which affected the sample mass used in calculating $\chi_M T$; leading to a reduced response, as confirmed *via* EDX, *vide-infra*.
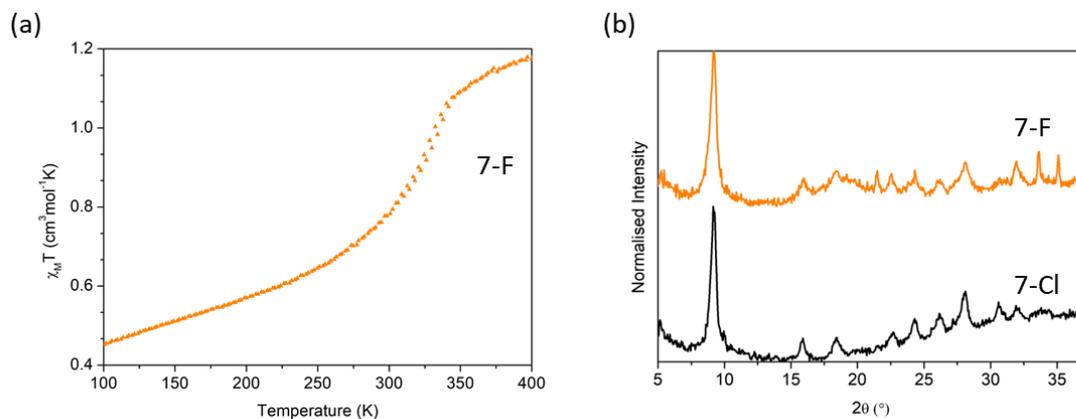
Figure 4.13: (a) $X_M T$ vs T for compound **7-F**, second cycle. **(b)** Comparison of normalised PXRD data for compound **7-F** and **7-Cl**.

As discussed in 4.2.1.1, previously reported magnetic properties of $[Fe(atrz)_3]Cl_2$ show significant cycling effects. However, the consistency in SCO properties between both **7-Cl** and **7-F** show both materials are the same composition, with Cl^- anions. Comparison between literature properties and both **7-Cl** and **7-F** are shown in Table 4.4.

Table 4.4: Spin crossover properties of **7-Cl**, **7-F** and literature properties for $[Fe(atrz)_3]Cl_2$. [20] *First cycle only.

	$T_{1/2}\uparrow$ (K)	$T_{1/2}\downarrow$ (K)	ΔT (K)
7-Cl	318	316	2
7-F	318	316	2
Lit [Fe(atrz)₃]Cl₂	300 and 306	355 and 315	55* and 9

After attempted exchange with NaF, the PXRD pattern was collected, as shown in Figure 4.13(b). The PXRD pattern was consistent with **7-Cl** confirming that no exchange had occurred. Three additional peaks at 22°, 33° and 35° 2θ are attributed to the presence of impurities, the peaks are consistent with α-Fe_2O_3.[38] It is also likely, NaF remains in the sample however, the pattern for NaF has peaks beyond the scanning range used.[39]

4.2.2.4.   Degree of Exchange

The degree of anion exchange in each sample was evaluated by energy-dispersive X-ray spectroscopy (EDX). An approximation for the relative elemental abundance was calculated based upon the characteristic elemental Kα emissions, and representative EDX spectra are shown in Figure 4.14.
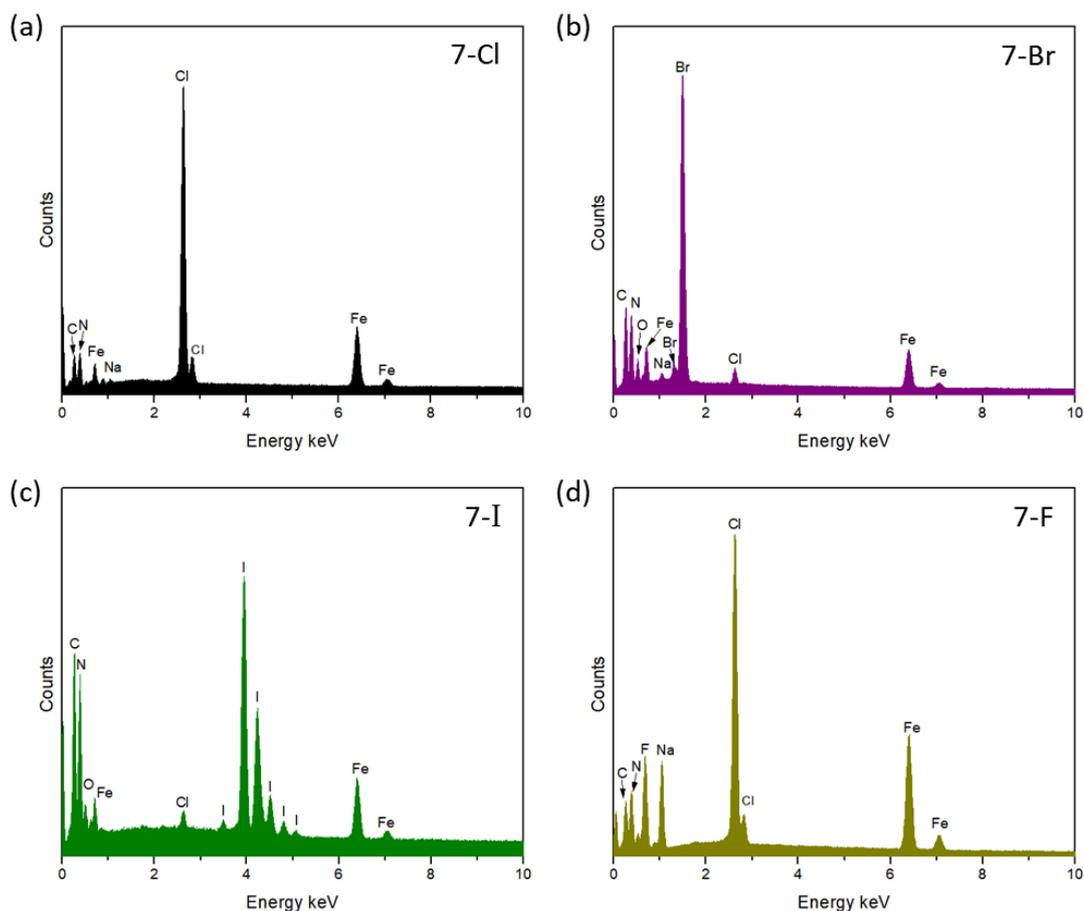

Figure 4.14: Representative EDX spectra for exchange products, with characteristic energies identified. (a) **7-Cl**, (b) **7-Br**, (c) **7-I** and (d) **7-F**.

For the control sample **7-Cl,** the only halogen observed is chlorine 16.70 ± 4.85% by weight. A representative EDX spectrum with characteristic atomic energies for **7-Cl**, after washing, is shown in Figure 4.14(a). The full elemental composition of **7-Cl** is similar to the calculated composition of [Fe(atrz)$_3$]Cl$_2$, with the differences within the standard deviation of the measurements taken. **7-Cl** also contains a small quantity of Na owing to the presence of some NaCl which was not

completely removed during washing. EDX analysis found (calc). C 23.24 ± 1.15 (19.00), N 42.99 ± 6.53 (44.35), Na 0.36 ± 0.10 (0.00), Fe 12.41 ± 3.63 (14.74) and Cl 16.70 ± 4.85 (18.71).

After exchange with NaBr, **7-Br** shows trace chlorine (1.22 ± 0.29 %) and a significant presence of bromine (27.52 ± 4.74 %). Both **7-Br** and **7-Cl** contain trace sodium (0.36 ± 0.10 % and 0.50 ± 0.10 % respectively), thus indicating unreacted NaBr is not present in significant quantities. Figure 4.14(b) shows a representative EDX spectrum for **7-Br**. The full elemental composition of **7-Br** was similar to the calculated elemental composition for $[Fe(atrz)_3]Br_2$. EDX analysis found (calc). C 20.60 ± 1.32 (15.39), N 37.09 ± 4.25 (35.92), Na 0.50 ± 0.10 (0.00), Fe 8.38 ± 1.71 (11.94), Cl 1.22 ± 0.29 (0.00) and Br 27.52 ± 4.74 (34.16).

Further, after exchange with NaI, **7-I**, also showed trace chlorine presence (0.59 ± 0.05 %) and a significant abundance of iodine (30.21 ± 4.10 %). In **7-I**, no significant presence of sodium was detected, indicating no unreacted NaI remained in the sample after washing, as shown in Figure 4.14(c). However, the full elemental composition measured was significantly different to the calculated composition for $[Fe(atrz)_3]I_2$. EDX analysis found (calc). C 18.42 ± 0.65 (12.82), N 40.34 ± 3.46 (29.91), Fe 6.22 ± 0.78 (9.94), Cl 0.59 ± 0.05 (0.00) and I 30.21 ± 4.10 (45.18). The lower abundance of iron and iodine are attributed to the partial oxidation of the complex $[Fe(atrz)_3]I_2$.

After attempted exchange with NaF, **7-F** showed a high quantity of chlorine in the system (11.62 ± 1.02 %), but lower than that observed in **7-Cl**. The amount of carbon and nitrogen also decreased, which is attributed to the presence of NaF in the system, supported by site dependent ratios of sodium and fluorine being consistent with the presence of NaF. Figure 4.14(d) shows a representative EDX spectrum of **7-F**, in which the proportion of impurities present in the washed sample can be observed. Increased presence of NaF was expected due to the relative insolubility of NaF in methanol (the washing solution used in this study). Additional workup of **7-F** was not carried out in order to maintain consistency throughout the exchange procedure and to limit the possibility of altering SCO properties as a result of solvent interactions, which has been frequently observed in SCO materials.[40–42] The result is an overall lower abundance of C, N, Fe and Cl within

the sample. EDX analysis found (calc). C 17.83 ± 0.30 (19.00), N 29.69 ± 0.48 (44.35), Na 6.68 ± 1.22 (0.00), Fe 13.41 ± 2.88 (14.74), Cl 11.62 ± 1.02 (18.71) and F 16.11 ± 3.05 (0.00). Full comparison between calculated and measured %weight for all samples are shown in Table 4.5.

Table 4.5: Average %weight of elements per sample based on EDX measurements. *The elemental composition of the **7-F** sample was strongly location dependent with significant variation in the presence of NaF. This is due to the relative insolubility of NaF in alcohol preventing sufficient washing.[43]

Sample	C %	N %	Na %	Fe %	Cl %	Br %	I%	F%
7-Cl	23.24 ± 1.15	42.99 ± 6.53	0.36 ± 0.10	12.41 ± 3.63	16.70 ± 4.85	-	-	-
7-F	17.83 ± 0.30	29.69 ± 0.48	6.68 ± 1.22	13.41 ± 2.88	11.62 ± 1.02	-	-	16.11 ± 3.05
[Fe(atrz)$_3$]Cl$_2$ Calculated	19.00	44.35	-	14.74	18.71	-	-	-
7-Br	20.60 ± 1.32	37.09 ± 4.25	0.50 ± 0.10	8.38 ± 1.71	1.22 ± 0.29	27.52 ± 4.74	-	-
[Fe(atrz)$_3$]Br$_2$ Calculated	15.39	35.92	-	11.94	-	34.16	-	-
7-I	18.42 ± 0.65	40.34 ± 3.46	-	6.22 ± 0.78	0.59 ± 0.05	-	30.21 ± 4.10	-
[Fe(atrz)$_3$]I$_2$ Calculated	12.82	29.91	-	9.94	-	-	45.18	-

4.2.2.5.   Summary of Halogen Exchange

In summary, SSM was carried out on [Fe(atrz)$_3$]Cl$_2$, using NaBr and NaI. This yielded products that exhibited properties significantly different to the control sample **7-Cl**. After exchange, **7-Br** underwent SCO with $T_{1/2}\uparrow$ = 298 K which was 20 K lower than the control sample **7-Cl**. The difference resulting from exchange with NaI was even greater with a change in $T_{1/2}\uparrow$ greater than 65 K ($T_{1/2}\uparrow$ = 318 to 253 K). The resulting properties for both **7-Br** and **7-I,** were comparable to

literature reported temperatures. Exchange with NaF did not modify the SCO properties ($T_{1/2}\uparrow$ = 318 K and $T_{1/2}\downarrow$ = 316 K), implying no anion exchange takes place. Due to the presence of impurities within certain samples, direct comparison of magnetic data proved difficult. In order to aid visualisation of effect of anion exchange on SCO properties, $X_M T$ was normalised within the range 150 – 400 K for all samples, as shown in Figure 4.15(a). Complete comparison between literature reported SCO properties and experimentally collected data are available in Table 4.6.
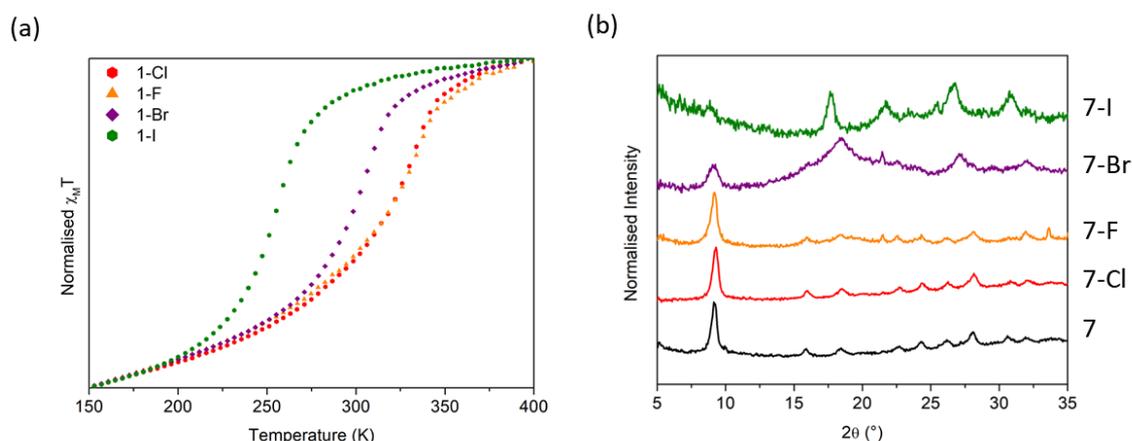
Figure 4.15: (a) Comparison of 2nd heating cycle $X_M T$ data normalised within the range 150 to 400 K for **7-Cl** (●), **7-F** (▲), **7-Br** (◆) and **7-I** (●). **(b)** Comparison of normalised PXRD data, bottom to top: **7** (Black), **7-Cl** (Red), **7-F** (Orange), **7-Br** (Purple) and **7-I** (Green).

PXRD analysis of **7** and **7-Cl** was carried out, revealing no structural changes except for increased Bragg peak broadening observed in **7-Cl**. The increase in peak width was attributed to a decrease in particle size, as confirmed by TEM analysis. Due to absence of available data, literature comparison of the patterns for **7** and **7-Cl** was not possible. However, both compounds **7** and **7-Cl** powders were crystalline. After exchange with sodium salts, the PXRD patterns for both **7-Br** and **7-**I were significantly different to **7-Cl**, as shown in Figure 4.15(b). The pattern of **7-Br** was consistent with previous literature reports. No PXRD pattern of **7-I** was previously reported, therefore comparison was not possible.

Table 4.6: SCO properties for Fe(atrz)$_3$]A$_2$, where A = Cl, Br and I, comparison between literature values and experimental values for anion exchange products.[20,21,23]

	Fe(atrz)$_3$]Cl$_2$			Fe(atrz)$_3$]Br$_2$	Fe(atrz)$_3$]I$_2$
Literature T$_{1/2}$ ↑ (K)	355			312-320	270-280
Literature T$_{1/2}$ ↓ (K)				304-313	260-278
Literature ΔT (K)				2-15	8-20
	Compound 7	Compound 7 - Cl	Compound 7 - F	Compound 7 - Br	Compound 7 - I
Experimental T$_{1/2}$ ↑(K)	334	318	318	298	253
Experimental T$_{1/2}$ ↓(K)	328	316	316	295	251
Experimental ΔT (K)	6	2	2	3	2
'Smoothness' (K)	39	55	55	41	39

4.2.2.6.   Driving Force for Anion Exchange

SSM was used successfully to exchange the Cl anions in compound **7**, for both Br (compound **7-Br**) and I (compound **7-I**). The exchange of anions followed the change in ionic radii, where F < Cl < Br < I, this approach represents a simple understanding of the exchange process and a more thorough understanding is required. In the SSM literature, $\Delta H_{rxn}°$ has been used as a tool to predict the exchange potential for a system. However, enthalpy calculations based on compound **7** are particularly difficult due to the complexity of the material and as such, calculating enthalpy of formation ($\Delta H_f°$) for compound **7** was beyond the scope of this project. This prevented the calculation of $\Delta H_{rxn}°$ and an alternative metric for describing the exchange was required. Total lattice potential energy (U_{POT}) was identified as a suitable alternative due to the availability of values for multiple sodium salts (Table 4.7). This term was used as a half reaction addressing the formation of NaCl from NaX (where X = F, Br, and I), the change in U_{POT} for this reaction is denoted by ΔU_{POT} and calculated as shown in Equation 4.3.

$$\Delta U_{POT} = U_{POT}(Product) - U_{POT}(Reactant)$$

Using this approach, the complex calculations required for calculating enthalpy of the SCO complexes could be bypassed with the assumption that differences in U_{POT} for exchanging anions in sodium salts represents the greatest change in energy occurring during the reaction. As such, U_{POT} was used to rationalise which anions would exchange with compound **7.** Both NaBr and NaI (NaBr - ΔU_{POT} = +37 kJ mol^{-1} and NaI - ΔU_{POT} = +87 kJ mol^{-1}) were predicted to exchange, whereas NaF would not proceed (NaF - ΔU_{POT} = -141 kJ mol^{-1}). The predictions were consistent with observations of magnetic properties and changing PXRD patterns, as previously discussed in 4.2.2.

Table 4.7: Total lattice potential energies, U_{POT}, for sodium halides (F, Cl, Br and I). [44]

	NaF	NaCl	NaBr	NaI
U_{POT} (kJ mol^{-1})	910	769	732	682

4.2.3. Additional Screening

Having demonstrated the ability to exchange halide anions, additional screening was attempted in order to expand the applications of SSM in the discovery of SCO materials. A series of anions that represented common and uncommon anions in the triazole family was explored. Successful exchange of the halogens was described using change in total lattice potential energy of the sodium salts (ΔU_{POT}). Using ΔU_{POT} as a metric to predict exchange, three sodium salts; NaBF$_4$ (ΔU_{POT} = -112 kJmol^{-1}), NaSCN (ΔU_{POT} = -87 kJmol^{-1}) and NaReO$_4$ (ΔU_{POT} = +132 kJmol^{-1}) were used to further test the SSM procedure and viability of the ΔU_{POT} metric for prediction of exchange. Unless stated, products remained unwashed to limit solvent effects. Without washing, excess sodium salts and impurities remained in the sample which affected the calculated $\chi_M T$ values. The absolute $\chi_M T$ values reported represent the product mixture which contains a high proportion of SCO-inactive by-products and therefore the response was considerably reduced. Additionally, the significant quantities of excess sodium salts prevented PXRD data collection.

The magnetic properties after SSM were explored by SQUID magnetometry and in instances where SSM modified the properties, work-up of the products was attempted. However, complete exploration of the potential applications of SSM was not undertaken due to time constraints. The huge number of possible exchanges predicted leaves plenty of scope for further research. Future work focusing on the exchanges described below could potentially yield new and exciting SCO materials, whereby previously unexplored anions and reaction pathways could be introduced to the triazole family of SCO materials.

4.2.3.1.   Tetrafluoroborate

After exchanging the Cl anion with $NaBF_4$, the magnetic properties of the material were modified, as shown in Figure 4.16. No indication of a SCO transition near 318 K is visible in SQUID data, which indicates no $[Fe(atrz)_3]Cl_2$ (compound **7**) remained in the sample. However, SCO behaviour was identified in the magnetic data. The first heating cycle showed a two-step transition with $T_{1/2}\uparrow$: 1 = 125 K and 2: 280 K. After repeated cycling, the second step was significantly suppressed, while the first step transition ($T_{1/2}\uparrow$ = $T_{1/2}\downarrow$ = 125 K) remained repeatable. Although supressed, a gradual transition for the second step ($T_{1/2}\uparrow$ = $T_{1/2}\downarrow$ = 250 K) was observed. The potential mechanism behind the differences between the first heating cycle and resulting cycling was explored further in 1.1.4.
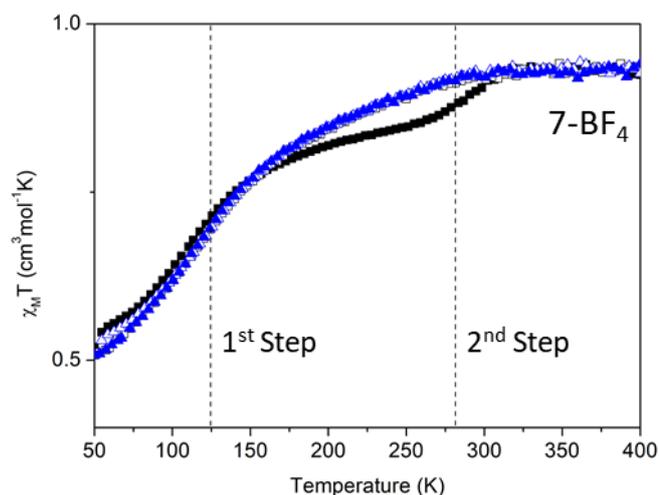
Figure 4.16: Temperature dependent SQUID data for **7-BF₄**, two cycles. Cycle 1 Heating ■ and Cooling □, Cycle 2 Heating ▲ and Cooling △.

The first-step transition temperature for **7-BF₄** did not correspond to transitions previously reported for either $[Fe(atrz)_3]Cl_2$ or $[Fe(atrz)_3](BF_4)_2$. However, the gradual second step has a similar temperature to the proposed α-form of $[Fe(atrz)_3](BF_4)_2$. The mechanochemical synthesis of the $[Fe(atrz)_3](BF_4)_2$ complex is discussed further in 3.2.6.1. Comparison of literature reports and **7-BF₄** are presented in Table 4.8. Based on the change in $\chi_M T$, the lower temperature first-step ($T_{1/2}\uparrow$ = 125 K) represented 70% of the SCO, with the remaining 30% attributed to the higher temperature second step ($T_{1/2}\downarrow$ = 280 K).

The low $\chi_M T$ values calculated strongly indicated the presence of impurities in the sample, as expected. However, repeated attempts to isolate the SCO active components of the product by washing were unsuccessful, due to complete oxidation of the material on addition of solvents. This significantly hampered research into the origins of these transitions. Attempts to use PXRD for further analysis were unsuccessful; instead presenting the PXRD patterns for $NaBF_4$, as predicted due to the excess $NaBF_4$ used in the SSM procedure.

	$T_{1/2}\uparrow$ (K)	$T_{1/2}\downarrow$ (K)	ΔT (K)
7-BF₄	1: 125, 2: 250	1: 125, 2: 250	0
Lit [Fe(atrz)₃](BF₄)₂ α	260	250	10
Lit [Fe(atrz)₃](BF₄)₂ β	245	239	6
7-Cl	318	316	2

The exchange with NaBF₄ was predicted to successfully exchange based on the total lattice potential energy (U_{POT} = 657 kJ mol⁻¹).[44] Using the half equation described in Equation 4.3., ΔU_{POT} = +112 kJ mol⁻¹. The exchange was confirmed by grinding with NaBF₄ and yielded approximately 30% conversion into the α-form of [Fe(atrz)₃](BF₄)₂, as calculated from the relative change in χ_MT. The remaining 70% of the sample displayed SCO properties with $T_{1/2}\uparrow$ = $T_{1/2}\downarrow$ = 125 K, which had not previously been reported. Although only 30% of the product displayed properties consistent with the predicted exchange products, the complex responsible for the transition at 125 K is currently unknown and should be the focus of future work, increasing grinding time using SSM would be a logical approach to improving percentage exchange.

4.2.3.2. Thiocyanate

Exchange with NaSCN (to form **7-SCN**) led to modification of the magnetic properties, as shown in Figure 4.17. It shows a very gradual transition with $T_{1/2}\uparrow$ = $T_{1/2}\downarrow$ = 180 K, and repeated cycling does not significantly modify the magnetic properties. Lavrenova *et* al[23] described the synthesis of a complex with the proposed formula [Fe(atrz)₃](NCS)₂, as discussed in 4.1.3.3. However, Mössbauer spectroscopy indicated the potential formation of a dimeric Fe²⁺ complex with SCO with $T_{1/2}\uparrow$ = 200 K and $T_{1/2}\downarrow$ = 200 K. The exchange between NCS and Cl was predicted to occur due to the total lattice potential energy of NaSCN (U_{POT} = 682 kJ mol⁻¹) being lower than NaCl, as such, ΔU_{POT} = +87 kJ mol⁻¹. Potentially offering a route to thiocyanate complexes with long chain structures.
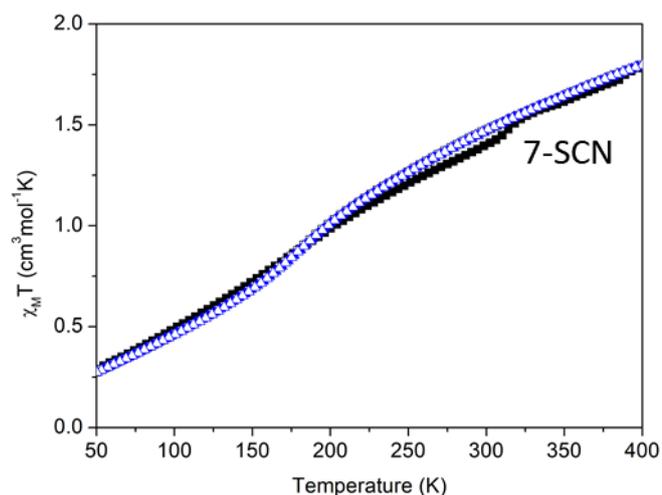
Figure 4.17: Temperature dependent SQUID data for **7-SCN**, two cycles. Cycle 1 Heating ■ and Cooling □, Cycle 2 Heating ▲ and Cooling △.

Without washing, **7-SCN** included residual NaSCN which caused a gradual increase in $\chi_M T$ as temperature increased and very gradual SCO, this is attributed to the difference between actual M_w and M_w used to calculate $X_M T$ which is emphasised as temperature increased. The SCO properties after SSM are clearly different to **7-Cl**, indicating exchange has occurred. Attempts to clean the sample led to oxidation of the iron and decomposition of the sample, limiting further analysis of **7-SCN**. The change in SCO properties suggests additional research into the changing properties caused by SSM with NaSCN is required. Due to difficulty in purifying **7-SCN** it was not possible to determine the structure of the resulting complex and whether the thiocyanate was bound or unbound. The change in magnetic properties imply a successful anion exchange, but, further research is required.

4.2.3.3.   Perrhenate

Exchange with NaReO$_4$ (to form **7-ReO$_4$**) modified the magnetic properties, with the first heating cycle being significantly different to subsequent cycles, as shown in Figure 4.18. The second cycle showed the presence of two transitions, with the 1st step: $T_{1/2}\uparrow = T_{1/2}\downarrow = 222$ K and the 2nd step: $T_{1/2}\uparrow = T_{1/2}\downarrow = 317$ K. The first transition was similar in temperature to previous literature reports on [Fe(atrz)$_3$](ReO$_4$)$_2$ ($T_{1/2}\uparrow = 228$ K, $T_{1/2}\downarrow = 223$ K).[27] The second step was

consistent with $[Fe(atrz)_3]Cl_2$ and the mechanical control sample, **7-Cl**. Comparison between literature transition temperatures and the exchange product are shown in Table 4.9. The small decrease in $T_{1/2}\uparrow$, $T_{1/2}\downarrow$ and loss of hysteresis observed for the first transition step was consistent with previously discussed effects of grinding on spin crossover properties, as described in 4.2.1.2.
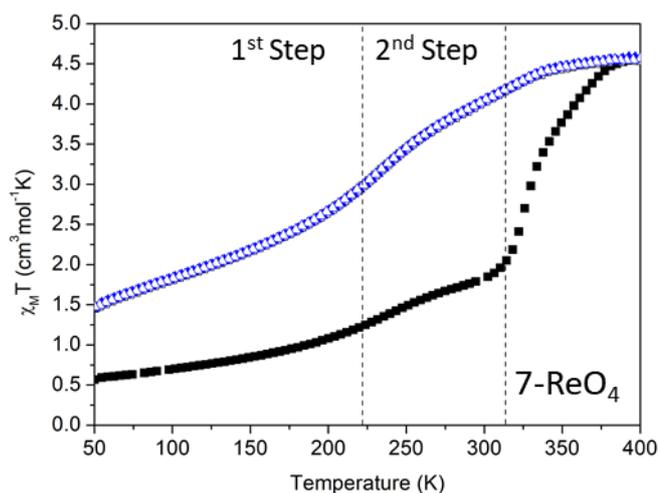

Figure 4.18: Temperature dependent SQUID data for **7-ReO₄**, two cycles. Cycle 1 Heating ■ and Cooling □, Cycle 2 Heating ▲ and Cooling △.

The presence of the first-step ($T_{1/2}\uparrow$ = 222 K) indicates partial anion exchange, based on differences in $\chi_M T$ the exchange with $NaReO_4$ was calculated at 64%. The exchange was predicted to successfully occur due to the U_{POT} = 637 kJ mol^{-1} for $NaReO_4$ (calculated using the Kapustinskii equation presented in [Equation 4.2.], representing ΔU_{POT} = +132 kJmol^{-1}. The partial exchange was attributed to a smaller excess of $NaReO_4$ used in the exchange attempt. A greater degree of exchange may have been possible with increased grinding and using a larger excess of $NaReO_4$. Further research is required.

Table 4.9: SCO properties for compound **7-ReO₄**, comparison with literature values for $[Fe(atrz)_3]Cl_2$[20] and $[Fe(atrz)_3](ReO_4)_2$.[27]

	$T_{1/2}\uparrow$ (K)	$T_{1/2}\downarrow$ (K)	ΔT (K)
7-ReO₄	1: 222, 2: 317	1: 222, 2: 317	0
Lit $[Fe(atrz)_3](ReO_4)_2$	228	223	5
Lit $[Fe(atrz)_3]Cl_2$	300 and 306	355 and 315	55* and 9

4.3. Conclusions and Prospects

In conclusion, SSM was used in the post-synthetic anion exchange of a triazole based SCO system. The effects of the proposed SSM procedure on SCO properties were investigated: leading to a slight decrease in $T_{1/2}\uparrow$, $T_{1/2}\downarrow$ and ΔT, in addition to a reduction in abruptness of transition, which is consistent with literature reports on the effects of post-synthetic grinding.[37] SSM was then used to exchange anions in $[Fe(atrz)_3]Cl_2$, using sodium halide salts as the anion source. Total lattice potential energies of the sodium salts (U_{POT}) was used as a metric to predict the likelihood of exchange. Based on the half equation for the formation of NaCl from compound **7** and NaX (where X = F, Br and I), the exchange with both NaBr and NaI was predicted and observed to be successful. The exchange using NaF was predicted to be unsuccessful and the resulting product **7-F** maintained SCO properties comparable to **7-Cl**, indicating the prediction was correct.

The properties of SSM halide exchange products were analysed using SQUID magnetometry and PXRD. Where possible, comparison to literature reported data was carried out. The SCO properties of both **7-Br** and **7-I** were comparable to literature values for $[Fe(atrz)_3]Br_2$ and $[Fe(atrz)_3]I_2$ respectively, when the effects of grinding during the SSM procedure are accounted for. The degree of exchange was investigated via EDX, in both **7-Br** and **7-I** the exchange was complete with only trace Cl remaining in the sample.

Further exchange using SSM was carried out using a variety of both coordinating and non-coordinating anions that were predicted to exchange based on ΔU_{POT} values. Application of the SSM procedure with $NaBF_4$ modified the magnetic properties, with **7-BF₄** displaying a 2-step transition (1: $T_{1/2}\uparrow$ = 125 K and 2: $T_{1/2}\uparrow$ = 250 K). The 2nd step was consistent with the previously identified β-form of $[Fe(atrz)_3](BF_4)_2$ whereas the origin of the 1st step ($T_{1/2}\uparrow$ = 125 K) remains unknown. Exchange with NaSCN also modified the magnetic properties but attempts to identify the product (**7-SCN**) were unsuccessful. Exchange with a smaller excess $NaReO_4$ led to partial exchange (64%), yielding a mixture of $[Fe(atrz)_3](ReO_4)_2$ and $[Fe(atrz)_3]Cl_2$.

SSM could be an especially useful tool for the rapid screening for novel materials. Carrying out reactions in the solid state allows for differences in solubility of reagents to be bypassed and allow for the formation of products that would otherwise by unfavourable *via* solution-state synthesis. The wide availability of sodium salts with complex anions has the potential to introduce additional anions to the triazole family of SCO materials, with the possibility of novel SCO materials being derived from both known and novel ligands. Additional research into the recovery of SCO properties after grinding could prove invaluable in the field of SCO.

4.4. References

1 R. E. Treece, E. G. Gillan and R. B. Kaner, *Comments Inorg. Chem.*, 1995, **16**, 313–337.

2 I. P. Parkin and A. M. Nartowski, *Polyhedron*, 1998, **17**, 2617–2622.

3 P. Parhi and V. Manivannan, *Solid State Sci.*, 2008, **10**, 1012–1019.

4 E. G. Gillan and R. B. Kaner, *Chem. Mater.*, 1996, **8**, 333–343.

5 L. Rao and E. G. Gillan, *J. Mater. Res.*, 1995, **10**, 353–361.

6 I. P. Parkin, *Chem. Soc. Rev.*, 1996, **25**, 199–207.

7 K. Gibson, M. Ströbele, B. Blaschkowski, J. Glaser, M. Weisser, R. Srinivasan, H. J. Kolb and H. J. Meyer, *Zeitschrift fur Anorg. und Allg. Chemie*, 2003, **629**, 1863–1870.

8 S. Ali, M. D. Aguas, A. L. Hector, G. Henshaw and I. P. Parkin, *Polyhedron*, 1997, **16**, 3635–3640.

9 L. Lei, W. Yin, X. Jiang, S. Lin and D. He, *Inorg. Chem.*, 2013, **52**, 13356–13362.

10 L. Lei and L. Zhang, *Matter Radiat. Extrem.*, 2018, **3**, 95–103.

11 A. M. Nartowski, I. P. Parkin, M. Mackenzie and A. J. Craven, *J. Mater. Chem.*, 2001, **11**, 3116–3119.

12 A. M. Nartowski, I. P. Parkin, A. J. Craven and M. Mackenzie, *ChemInform*, 2010, **29**, 805–808.

13 H.-J. Meyer, *Dalt. Trans.*, 2010, **39**, 5973–5982.

14 E. A. Guggenheim, in *Prinzipien der Thermodynamik und Statistik / Principles of Thermodynamics and Statistics*, ed. S. Flügge, Springer Berlin Heidelberg, Berlin, Heidelberg, 1959, pp. 1–118.

15 I. A. N. Mills, *Quantities, Units, and Symbols in Physical Chemistry: 3rd edition*, 2014, vol. 29.

16 A. F. Kapustinskii, *Q. Rev. Chem. Soc.*, 1956, **10**, 283.

17 L. Glasser, *Inorg. Chem.*, 2012, **51**, 10306–10310.

18 O. Roubeau, *Chem. - A Eur. J.*, 2012, **18**, 15230–15244.

19 P. Grondin, D. Siretanu, O. Roubeau, M. F. Achard and R. Clérac, *Inorg. Chem.*, 2012, **51**, 5417–5426.

20 L. G. Lavrenova, O. G. Shakirova, V. N. Ikorskii, V. A. Varnek, L. A. Sheludyakova and S. V. Larionov, *Russ. J. Coord. Chem. Khimiya*, 2003, **29**, 22–27.

21 T. Forestier, A. Kaiba, S. Pechev, D. Denux, P. Guionneau, C. Etrillard, N. Daro, E. Freysz and J. F. Létard, *Chem. - A Eur. J.*, 2009, **15**, 6122–6130.

22 A. Vallée, C. Train and C. Roux, *J. Chem. Educ.*, 2013, **90**, 1071–1076.

23 L. G. Lavrenova, N. G. Yudina, V. N. Ikorskii, V. A. Varnek, I. M. Oglezneva and S. V.

Larionov, *Polyhedron*, 1995, **14**, 1333–1337.

24 L. Salmon, G. Molnár, S. Cobo, P. Oulié, M. Etienne, T. Mahfoud, P. Demont, A. Eguchi, H. Watanabe, K. Tanaka and A. Bousseksou, *New J. Chem.*, 2009, **33**, 1283–1289.

25 L. G. Lavrenova, N. V. Ikorskii., V. A. Varnek., 1. M. Oglezneva. and S. V. Larinov, *Khoord Khim*, 1990, **16**, 654.

26 O. Kahn, J. Kröber and C. Jay, *Adv. Mater.*, 1992, **4**, 718–728.

27 L. G. Lavrenova, V. N. Ikorskiy, Y. G. Shvedenkov, L. A. Sheludyakova, V. V Volkov and S. V Larionov, *Chem. Sustain. Dev.*, 2002, **10**, 757–762.

28 J. R. Galán Mascarós, G. Aromí and M. Darawsheh, *Comptes Rendus Chim.*, , DOI:10.1016/j.crci.2018.07.005.

29 K. Nebbali, C. D. Mekuimemba, C. Charles, S. Yefsah, G. Chastanet, A. J. Mota, E. Colacio and S. Triki, *Inorg. Chem.*, 2018, **57**, 12338–12346.

30 J. J. A. Kolnaar, M. I. de Heer, H. Kooijman, A. L. Spek, G. Schmitt, V. Ksenofontov, P. Gütlich, J. G. Haasnoot and J. Reedijk, *Eur. J. Inorg. Chem.*, 1999, **1999**, 881–886.

31 H. S. Scott, T. M. Ross, B. Moubaraki, K. S. Murray and S. M. Neville, *Eur. J. Inorg. Chem.*, 2013, **1**, 803–812.

32 O. Roubeau, P. Gamez and S. J. Teat, *Eur. J. Inorg. Chem.*, 2013, 934–942.

33 A.-M. Li, T. Hochdörffer, J. Wolny, V. Schünemann and E. Rentschler, *Magnetochemistry*, 2018, **4**, 34.

34 J. G. Haasnoot, in *Magnetism: A Supramolecular Function*, 1996, pp. 299–321.

35 B. Michen, C. Geers, D. Vanhecke, C. Endes, B. Rothen-Rutishauser, S. Balog and A. Petri-Fink, *Sci. Rep.*, 2015, **5**, 9793.

36 L. Salmon and L. Catala, *Comptes Rendus Chim.*, 2018, **21**, 1230–1269.

37 M. S. Haddad, W. D. Federer, M. W. Lynch and D. N. Hendrickson, *Inorg. Chem.*, 1981, **20**, 131–139.

38 E. N. Maslen, V. A. Streltsov, N. R. Streltsova, N. Ishizawa and Y. Satow, *Acta Crystallogr. Sect. B*, 1993, **49**, 973–980.

39 Y. Shirako, Y. G. Shi, A. Aimi, D. Mori, H. Kojitani, K. Yamaura, Y. Inaguma and M. Akaogi, *J. Solid State Chem.*, 2012, **191**, 167–174.

40 E. Milin, B. Benaicha, F. El Hajj, V. Patinec, S. Triki, M. Marchivie, C. J. Gómez-García and S. Pillet, *Eur. J. Inorg. Chem.*, 2016, **2016**, 5282.

41 C. Bartual-Murgui, C. Codina, O. Roubeau and G. Aromí, *Chem. - A Eur. J.*, 2016, **22**, 12767–12776.

42 M. Fumanal, F. Jiménez-Grávalos, J. Ribas-Arino and S. Vela, *Inorg. Chem.*, 2017, **56**, 4474–4483.

43 G. J. Janz and R. P. T. Tomkins, *Nonaqueous Electrolytes Handb.*, 1973, **2**, 905–929.

44   D. P, *J. Mol. Struct.*, 1992, **268**, 320.

Chapter 5: Developing a Systematic Approach to Mechanochemical Screening for New Spin Crossover Materials

5.1. Introduction

5.1.1. Mechanochemical Screening

It has already been shown in 3.2 that synthesis of SCO materials using mechanochemistry can be extremely rapid, with synthesis occurring within 5 minutes, compared to solution-state methods, in which reactions can take days or weeks. Many families of complexes have been known to display SCO behaviour with small variations in anion, ligand substitutions, guest molecules, solvates and metal dilution.[1–4] However, while SCO properties primarily arise from ligand field considerations, there are important contributions from outer sphere affects such as packing and solvation. Polymorphism arising from packing differences can have significant effects on SCO properties[5] with a large variety of complexes reported to display polymorph specific SCO-activity.[6–9] This is exemplified by the complex $[Fe(BT)_2(NCS)_2]$ (where BT = 2,2'-bi-2-thiazoline, as shown in Figure 5.1), in which polymorph A undergoes SCO $T_{1/2}\uparrow$ = 185 K and $T_{1/2}\downarrow$ = 177 K and polymorph B remains in the HS state at all temperatures.[10–13]

Therefore, in pursuit of novel SCO materials, incremental modification of ligands and anions can be used to tune switching properties to a certain extent, the time required to screen all of the variables by solution-state techniques is substantial and without the guarantee of obtaining SCO-active products, the process becomes even more arduous. A substantial majority of complexes with a FeN_6 coordination sphere are not SCO-active and it is not possible to predict SCO-activity in a given complex, as the case of $Fe(BT)(NCS)_2$ illustrates.
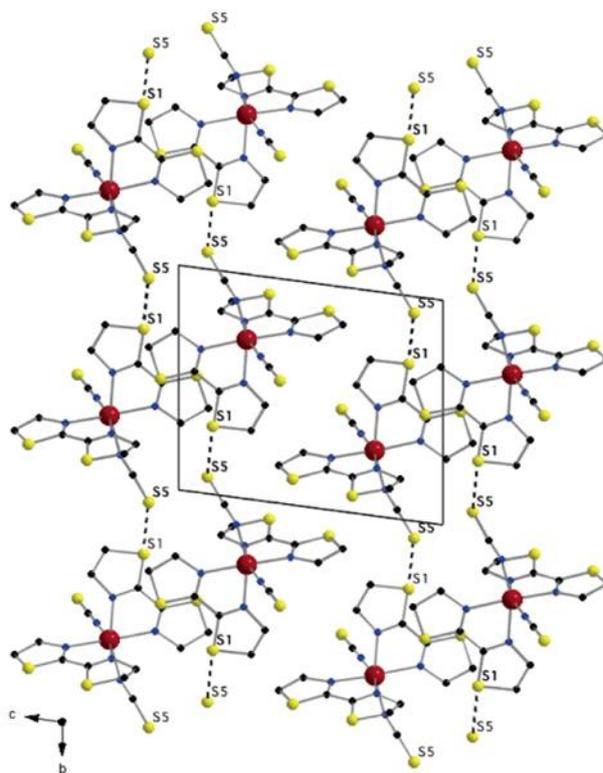
Figure 5.1: View of crystal packing of SCO-active polymorph A of [Fe(BT)$_2$(NCS)$_2$] in the (b, c) plane. Reproduced with permission from reference.[13]

Mechanochemistry presents an opportunity for rapid screening of variables including ligands, metal salts and solvent/guest molecules. In order to optimise the chances of discovery of novel SCO materials, a systematic protocol for the screening procedure is required. It should be rapid, cost effective and capable of identifying SCO-activity in both known and novel materials across families of SCO-active materials. Whereby the rate limiting step using solution-state techniques is the synthesis of compounds, the fast reaction times of mechanochemistry shifts the rate limiting step to characterisation of the material properties. Therefore, to optimise the screening process, characterisation of the properties must also be as efficient as possible. Using experience gained throughout this study, all characterisation techniques that were used will be evaluated for their speed and the information they provide and a systematic protocol for the identification of promising SCO candidates will be developed. The aims of this chapter are to assess characterisation techniques to develop a rapid mechanochemical screening protocol for use as a new tool for materials discovery. The protocol will then be tested using a wide variety of SCO

families with confirmation for the suitability of the protocol determined by screening of both known and novel compounds.

5.1.2. 2,6-di(pyrazole-3-yl)pyridine and Derivatives

The 2,6-di(pyrazole-3-yl)pyridine class of SCO materials hereby denoted **3-bpp**, represents the use of terimine ligands in preparation of SCO-active materials. Chelating two molecules of **3-bpp** and its derivatives around one Fe(II) centre provides the metal centre with the important FeN_6 first coordination sphere, which is commonly observed in SCO-active Fe^{2+} materials.[14] Derivatives of the **3-bpp** ligand have been researched less frequently for SCO than their regio-isomer **1-bpp**, due to difficulties in ligand synthesis.[15] However, significant steps have been made recently in the development of the synthetic techniques required for synthesis of **3-bpp** derivatives.[16] Structures of the corresponding Fe(II) complexes with **3-bpp** and **1-bpp** are shown in Figure 5.2.
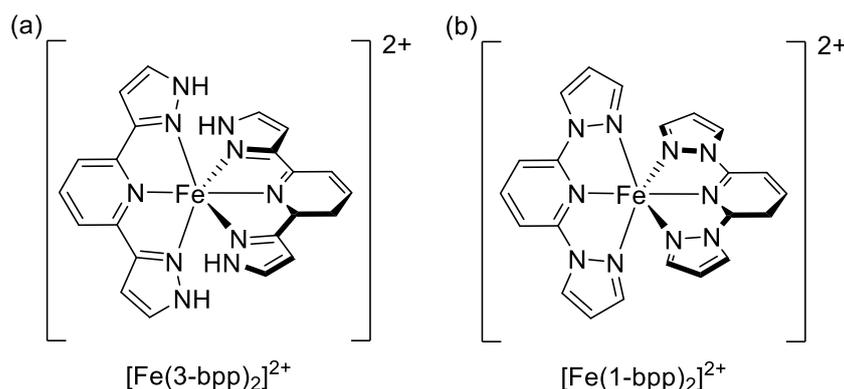
Figure 5.2: The structures of [Fe(3-bpp)₂]²⁺ (a) and [Fe(1-bpp)₂]²⁺ (b).

Synthesis of these systems is generally carried out using one of two methods. The first of which is the direct synthesis of the complex using the corresponding Fe(II) salts, such as $Fe(BF_4)_2$ or $Fe(ClO_4)_2$ in hot ethanol/water mixtures with the product precipitated using diethyl ether.[17] The second synthetic route consists of the mixing of the ligand with $FeCl_2$ followed by anion exchange with a corresponding Na salt, such as NaBr and $NaNO_3$. The resulting yellow and orange powders (depending on spin state) often contain excess moisture which darkens the colour of the powders, due to stabilising the LS state.[18] On drying the excess moisture can be removed, which is accompanied by a lightening in colour. The 2,6-di(pyrazole-3-yl)pyridine family undergoes visible

thermochromism from orange (in the LS state) to yellow (in the HS state) on heating. The magnetic properties of these complexes significantly depend on their degree of hydration and solvation, with $T_{1/2}\uparrow$ for [Fe(3-bpp)$_2$](BF$_4$)$_2$ in different solvents reported between 244 – 317 K.[18]

So far, all discussed **3-bpp** family complexes represent homoleptic complexes, where two equivalents of the same ligand are used. This is due to the more straightforward and traditionally favourable formation of homoleptic complexes using solution techniques.[19,20] Solution synthesis of iron-based heteroleptic complexes, where one equivalent of two different ligands is used, is often difficult due to the lability of Fe-N bonds.[21] This leads to a thermodynamic mixture of reaction products where the two homoleptic products and the one heteroleptic product are formed in a 1:1:2 ratio. Isolation of the complexes is often difficult and significantly increases the reaction work-up and time.
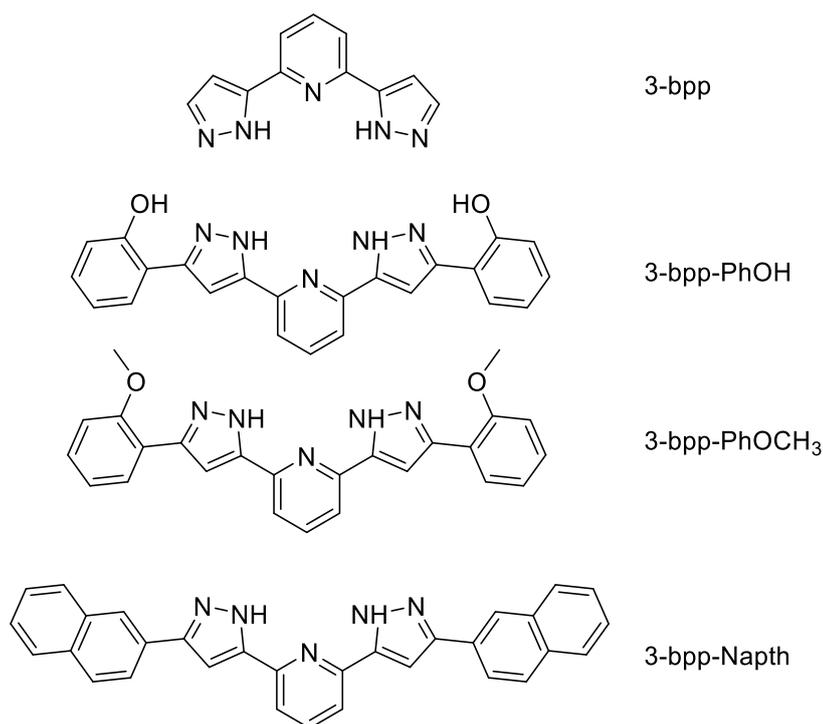
Figure 5.3: Structure of 2,6-di(pyrazole-3-yl)pyridine and the derivatives, with their representative abbreviations used throughout.

The **3-bpp** family presents an interesting contradiction to the belief of the homoleptic complexes being formed preferentially to heteroleptic complexes. The **3-bpp** family of complexes

generally organise into sheets according to the so-called terpyridine embrace.[22] The terpyridine embrace described an interlocked assembly which exhibits offset face-to-face and edge-to-face interactions forming a layered structure.[23] The differing dimensions of the different **3-bpp** ligands allows for secondary interactions which would otherwise not be possible.[24] This has been shown to lead to the preferential formation of heteroleptic complexes often without a significant homoleptic fraction.[24,25] The **3-bpp** derivatives screened in both homoleptic and heteroleptic complexes in this work are shown in Figure 5.3.

5.1.3. 2,2'-bipyridine Derivatives

$Fe(bipy)_2(NCS)_2$ (where bipy = 2,2'-bipyridine) was first reported by Baker *et al*. alongside $[Fe(phen)_2(NCS)_2$.[26] Further investigation by König *et al.* identified the possibility of three different polymorphs (I, II and III),[27] with crystallographic differences between polymorphs I and II later identified.[28] Preparation of $Fe(bipy)_2(NCS)_2$ has been reported using multiple techniques but all are based upon the conversion of $[Fe(bipy)_3](SCN)_2$ by either extraction or precipitation.[27] The ionic species $[Fe(bipy)_3]^{2+}$ undergoes LIESST in solution but has not been reported to display SCO as a neutral species with counter anions.[29] The SCO properties of $Fe(bipy)_2(NCS)_2$ have been shown to vary between different preparation techniques and different batches prepared using the same technique.[30] The polymorphs of $Fe(bipy)_2(NCS)_2$ display SCO with $T_{1/2}\uparrow \approx 214$ K with varying degrees of residual HS fraction at low temperatures.[27] Very few reports of simple complexes prepared using derivatives of bipy being SCO-active are available in literature. However, some reports on using bipy and bipy derivatives as building blocks in heteroleptic complexes have been presented. One such example is using the heteroleptic complex $[Fe(bipy)(CN)_4]^-$ as a building block for designing cyanide-bridged heterobimetallic complexes. But neither the building block nor resulting complexes display SCO-activity.[31]

The complexes discussed above and throughout this work represent the 2,2'-bipyridine isomer in the bipyridine family, which serves as a bidentate chelating ligand. The 4,4'-bipyridine isomer has also been used in SCO research with the ligand acting as a bridge between metal

centres, as reported in the Hofmann-type coordination polymers Fe(4,4'-bipridyl)[Au(CN)$_2$]$_2$.nGuest.[32] However, further investigation of the 4,4'-bipy ligand and complexes formed with it is not undertaken here.

2,2'-bipyridine

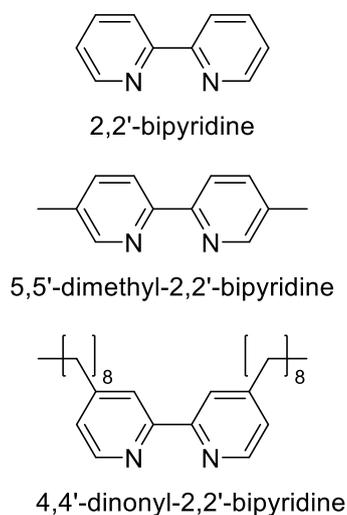5,5'-dimethyl-2,2'-bipyridine

4,4'-dinonyl-2,2'-bipyridine

Figure 5.4: Structure of 2,2'-bipyridine and the derivatives used for screening.

Many Fe^{2+} complexes ligated by substituted derivatives of bipy have been reported in literature.[33] Comparatively, few reports of their application in SCO research are available. Of the available SCO literature, a large amount focuses on heteroleptic. One such example was reported by Garcia *et al*.[34] in which a series of complexes with the general formula [Fe(H$_2$Bpz$_2$)$_2$(L)] (where pz = pyrazolyl and L = 5,5' substituted bipyridine derivatives) displayed interesting SCO properties. The derivatives of bipy investigated further in this work are presented in Figure 5.4, due to the absence of literature reports on the use of these ligands in proposed complexes with the general formula Fe(L)$_2$(NCS)$_2$, screening will be carried out.

5.1.4. Hydrotris(1-pyrazolyl)borates

Transition metal complexes with the tridentate ligand hydrotris(1-pyrazolyl)borates (general formula HB(pz)$_3^-$) were first investigated by Trofimenko.[35–37] Since their discovery, they have been intensively investigated with many papers describing the nature and coordination capabilities of these ligands,[38] with particular focus on iron and cobalt derivatives, due to their potential to display SCO.[39] The nature of these ligands was described by Trofiemnko[38] coining the term

'scopionates'. These ligands are usually at least bidentate with many tridentate ligands. The 'Scopionate' name originates from the coordination through two nitrogen atoms, in plane, acting as the claws of the scorpion, with the third coordination acting as the sting of the scorpion. A schematic representation of the structure is shown in Figure 5.5.
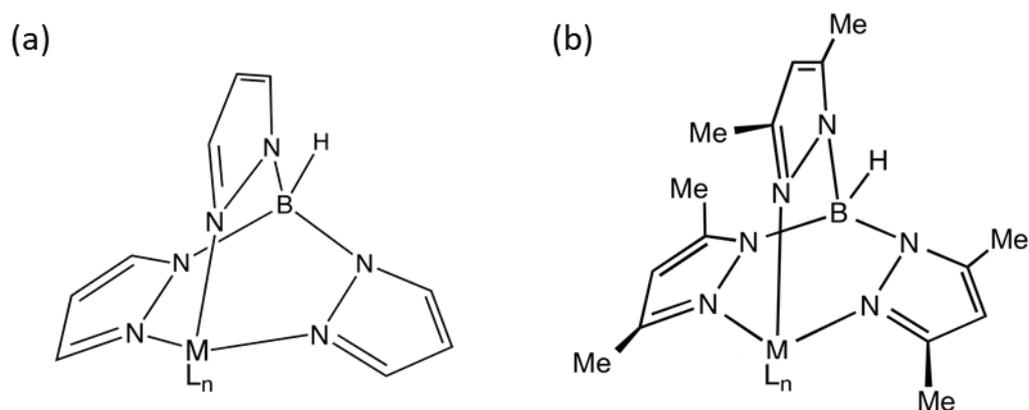
Figure 5.5: Structural representation of the hydrotris(1-pyrazolyl)borate metal complexes, displaying the scopionate structure - one equivalent of ligand is shown for clarity, with the second ligand denoted by L_n. (a) Fe[HB(pz)$_3$]$_2$ and (b) Fe[HB(3,5-(CH$_3$)$_2$-pz)$_3$]$_2$

The Fe[HB(pz)$_3$]$_2$ complex represents an early observation of SCO activity, with the identification of thermochromism on heating.[37] Confirmation of reversible SCO behaviour in Fe[HB(pz)$_3$]$_2$ was made by Hutchinson *et al*[40] with $T_{1/2}\uparrow$ ≈ 391 K and $T_{1/2}\downarrow$ ≈ 350 K. Further investigation of the complex by Grandjean *et* al.[41] confirmed the SCO properties and began studies into changes in optical absorption on SCO and identified a crystallographic phase transition accompanying SCO. Grandjean *et al.* also began investigation in the effects of grinding on this solution-synthesised complex with a lowering of $T_{1/2}\uparrow$ observed. In all literature reports of Fe[HB(pz)$_3$]$_2$, the first heating cycle was different to subsequent cycling, which gave the illusion of a large apparent hysteresis for the first cycle with no hysteresis observed for subsequent cycling. Grandjean *et al.* attributed this change to shattering the initial microcrystalline sample as a result of the SCO transition.[41] Reinvestigation of the system by Salmon *et* al[42] challenged this assumption, instead attributing the property change to rich polymorphism, with heating causing

an irreversible structural change from a metastable tetragonal form to a stable monoclinic form. After the first heating cycle, subsequent cycling displays SCO with $T_{1/2}\uparrow = T_{1/2}\downarrow = 358$ K.

Extensive modification of the ligand $[HB(pz)_3]^-$ has been carried out, with particular focus on substituent positioning and effects this has on SCO properties.[43] Of particular interest to this work is the methyl substitution on the 3 and 5 positions of the pyrazolyl ring. $Fe[HB(3,5-(CH_3)2-pz)_3]_2$ was first reported alongside $Fe[HB(pz)_3]_2$,[37] with $Fe[HB(3,5-(CH_3)2-pz)_3]_2$ reported to display SCO with $T_{1/2}\uparrow = 204$ and $T_{1/2}\downarrow = 173$ K,[44] the dimethyl derivative has not received as much attention in subsequent reports on the family. Further, interest in these materials in modern times arises due to their ability to be sublimed, which allows them to be used to fabricate high quality thin films for precise applications.[45]

5.1.5. Aims

The aim of this chapter is to create and develop a screening protocol that can be used with both thermochromic and non-thermochromic SCO families. Mechanochemical synthesis shifts the rate limiting step from synthesises of the complexes in traditional synthetic methods, to characterisation and analysis of the products. This shift is due to the significantly reduced reaction times. As a result, developing a method to identify promising complexes for further investigation becomes difficult and time consuming. The characterisation techniques used in SCO research are compared and evaluated for value of data, cost and time to collect data. Using this information, a protocol is designed and tested using a series of different thermochromic and non-thermochromic families of SCO materials.

5.2. Results and Discussion

5.2.1. Assessment of SCO Characterisation Techniques

As discussed in 1.1.3, a wide variety of techniques can be used to characterise SCO materials and their properties. Each technique provides insight into certain aspects of the material and no method can be solely used to completely characterise a compound. With mechanochemistry, the

rate-limiting step in screening novel compounds shifts from synthesis of the compounds to characterisation and identification of SCO properties. Using experience gained throughout this work, each in-house technique will be assessed for the characterisation potential and speed of analysis to allow for an optimised screening method to be developed.

5.2.1.1. SQUID Magnetometry

Superconducting quantum interference device (SQUID) magnetometry is a sensitive technique, which can be used to measure magnetic properties as a function of temperature. If the technique can be optimised for materials discovery, it would be an incredibly powerful technique. The device uses a liquid helium cooled superconducting magnet coupled with a Josephson junction to measure small changes in magnetic moment.[47] This allows for magnetic properties to be measured across a wide range of temperatures from as low as 5 K up to and exceeding 400 K depending on the instrument. Variable temperature SQUID magnetometry is able to detect the intrinsic changes in magnetic moment that occur during SCO; SQUID is not reliant on changes in optical properties such as visible thermochromism, which is not always observable.[48] This makes SQUID magnetometry an ideal method for detection of SCO allowing identification of small multi-step transitions in materials.[49] However, the required use of liquid helium significantly increases the operation costs (< £200 per measurement) for the instrument which reduces the availability of the instrument and considering the large number of negative results expecting during screening it is impractical to use SQUID magnetometry as an initial technique. Also, SQUID measurements take a long time to obtain data, with data collection times up to and beyond 20 hours, during which more than 40 samples could be mechanochemically synthesised, which would significantly slow identification of novel SCO materials. Modern SQUID magnetometers have begun to address these issues, do to operating on a closed system, modern systems do not require frequent helium filling and improvements in the technology has resulted in significantly reduced measurement times. The main issue remaining with modern systems is their availability, they are expensive to purchase.

5.2.1.2.   Differential Scanning Calorimetry

Differential Scanning Calorimetry (DSC) is a thermoanalytical technique that measures the differences in amount of heat required to increase the temperature of a sample relative to a reference.[48] The instrument can access a wide range of temperatures by cooling down to ≈ 77 K using liquid nitrogen and by heating up to 850 K, with the possibility of controllable repeated cycling. The use of liquid nitrogen significantly reduces operation costs compared to SQUID magnetometry. Regarding SCO, the transition between spin states is accompanied by a change in entropy (ΔS), which can be measured using DSC. Similar to changes in magnetic properties, the change in enthalpy is an intrinsic property of SCO materials. The transition from LS to HS induces an increase in metal-to-ligand bond distance ≈ 0.2 Å and this in turn is accompanied by a significant change in vibrational density of states. In calorimetry measurements, the large ΔS manifests as a discontinuity at the transition temperature, as shown in Figure 5.6.[50] DSC can either be used for very detailed analysis of thermodynamic properties, which requires significant analysis times, or as a crude method to observe the phase change associated with SCO.[48]
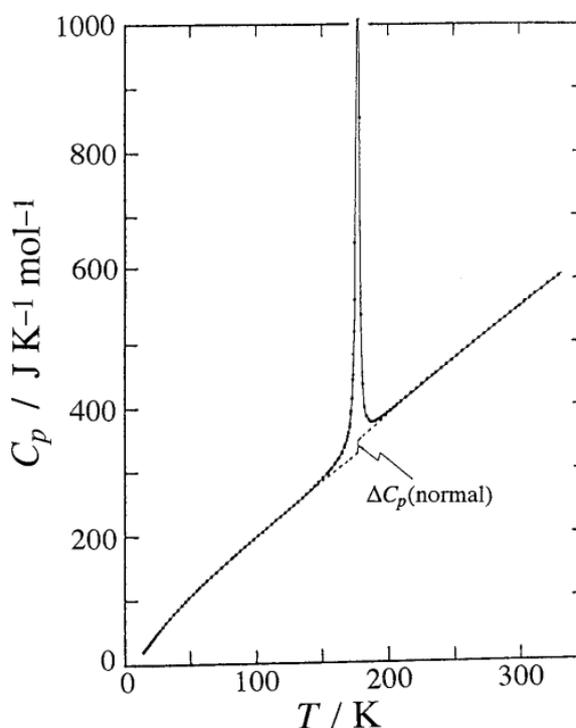
Figure 5.6: Molar heat capacity of [Fe(NCS)$_2$(phen)$_2$]. Displaying discontinuity attributed to SCO. Reproduced with permission from reference.[50]

5.2.1.3.   Thermochromism and Reflectivity

As discussed in 1.1.3, the characteristic thermochromic response to SCO can be used to rapidly identify SCO activity in a material. Cooling the compounds in liquid nitrogen or heating with a heat gun can be used to crudely observe the presence of SCO in a material. Visual observation of thermochromism is an ideal method for rapid identification of SCO activity in compounds, which allows quick screening of interesting materials. Rapid screening using this technique has some limitations including difficulties in testing complexes with significant charge transfer transitions, which mask the thermochromic response to SCO and the increased possibility of missing SCO active materials. The use of a reflectivity setup with precise temperature control and a high-quality camera could be used to reduce possibility of missing SCO active materials but this increased precision is accompanied by an increase in time required for each measurement. Precise temperature control combined with the reflectivity camera can be used to obtain SCO profiles by plotting response against temperature.[51] The camera allows for minute changes in colour to be recorded and using a greyscale, the SCO transition can be monitored.

5.2.1.4.   Powder X-ray Diffraction

PXRD is the one of the main techniques used for analysis of the structure of materials. Complete identification and refinement of a structure using PXRD is non-trivial, requires high-quality data, is time consuming and often requires a starting model for structure solution. However, using the technique to obtain a qualitative fingerprint to compare with reported patterns can significantly reduce times for identification of known materials. For unknown materials, the presence of previously unidentified peaks, not corresponding to starting materials or by-products, indicates the formation of a new product which should be investigated using additional techniques. Measurements using PXRD can take multiple hours for high quality data, depending on quality of the samples. But, for qualitative data scanning for approximately one hour is sufficient to obtain patterns for comparison. Further, the use of auto-sampling stages allows for large numbers of samples to be screened overnight. Variable temperature (VT) setups can be and have been used to characterise HS and LS states, which are structurally different due

to changing bond lengths and consequent distortion of the structure. The screening of mechanochemical reaction products using PXRD can rapidly provide valuable insight as to whether any chemical reaction has occurred. However, the presence of excess reagents and by-products introduced by the mechanochemical screening process could potentially mask the reaction product peaks. Therefore, it is important to note the possibility of false negatives in the screening process.

5.2.1.5.   Raman Spectroscopy

Raman spectroscopy is a non-invasive, non-destructive analytical technique that provides detailed information about chemical structure and in turn polymorphism, by probing the chemical bonding in a material.[52] Therefore, Raman spectroscopy does not depend on visibly changing properties such as thermochromism and can be used for non-thermochromic materials. A full description of the technique itself is presented in 2.1.6.3. For SCO research, standard room temperature Raman spectroscopy can be used to identify the bonding in a material, with the resulting spectra operating as a 'fingerprint' for the complex that can be compared with previous reports on the complex allowing for rapid identification of known materials. Full assignment of spectra to specific vibrational modes can be undertaken but this process requires extensive computational and/or experimental input and time for full interpretation.[53] For previously unreported materials, standard room temperature Raman spectroscopy does not provide significant information for rapid screening. However, variable temperature Raman spectroscopy (VT-Raman) can take advantage of the changing bond lengths induced by the occurrence of SCO, which results in a different spectrum for the HS and LS states.[52] This provides an interesting opportunity to use Raman spectroscopy for identification of SCO-active materials that have not previously been reported, by comparing spectra at different temperatures and identifying significant differences induced by the change in bonding. Variable temperature Raman spectroscopy is undertaken using a similar variable temperature stage as in reflectivity, *vide supra*. Screening of materials using VT-Raman is slower than thermochromic screening due to temperature being precisely controlled, which ultimately depends on the ramp rate of the

thermal stage. Collecting of the spectra themselves can also be time consuming and thus slow the screening process. However, in many cases, qualitative data can be collected quickly, which can allow rapid indication of SCO-activity. However, for detailed analysis higher quality data would be required. The information provided by Raman spectroscopy for non-thermochromic materials is crucial for identification of SCO-activity, therefore it can be used to optimise the screening procedure. However, the differences induced by SCO for many complexes is often difficult to observe due to noise and overlaying peaks. Therefore, in order to be rapidly identify the presence of SCO, a Raman active component should be present. One such example of this is the NCS^- ion, shows characteristic peaks which are well separated from the rest of the spectrum (at approximately 2000-2200 cm^{-1}). During SCO, the bonding of the thiocyanate significantly changes, which in turn changes the position of the thiocyanate peaks between both spin states, allowing rapid identification of SCO.

5.2.1.6. Summary

Each technique described above can provide valuable information for SCO materials. Some additional techniques non available in-house can be used to provide further characterisation such as EXAFS and Mössbauer. But access to these techniques are limited by availability at central facilities and for routine screening with mechanochemistry, they are not suitable. The technique which provides the most insight into SCO behaviour is SQUID magnetometry. But, the high cost of operation and long scanning times mean that using SQUID magnetometry for analysis of mechanochemical screening products is not feasible. As such, prior investigation using other techniques is required to identify promising candidates before using SQUID magnetometry. For thermochromic responsive materials rapid identification can be carried out using visual analysis on heating and cooling, this allows promising materials to be identified before confirmation of their SCO activity by SQUID magnetometry. For strongly coloured SCO materials that mask thermochromic response, such as $Fe(phen)_2(NCS)_2$, preliminary analysis by variable temperature Raman spectroscopy can be used to identify SCO activity before confirmation by SQUID magnetometry. Using the above discussion,

5.2.2.   Application of Screening Procedure

The flow chart presented in Figure 5.7 was developed based upon the discussion above, to optimise identification of SCO-active materials prepared by mechanochemistry. Once materials are identified as SCO-active, further analysis can be carried out to fully characterise the materials. The suitability of the screening procedure described in Figure 5.7, will be assessed by screening two families of potentially SCO-active materials. The thermochromic 4-R-1,2,4-Triazole family will be used to assess the thermochromic branch and derivatives of 1,10-phenantholine will be used to assess the non-thermochromic branch. Screening of previously active reported complexes for both families will be included to validate the procedure.
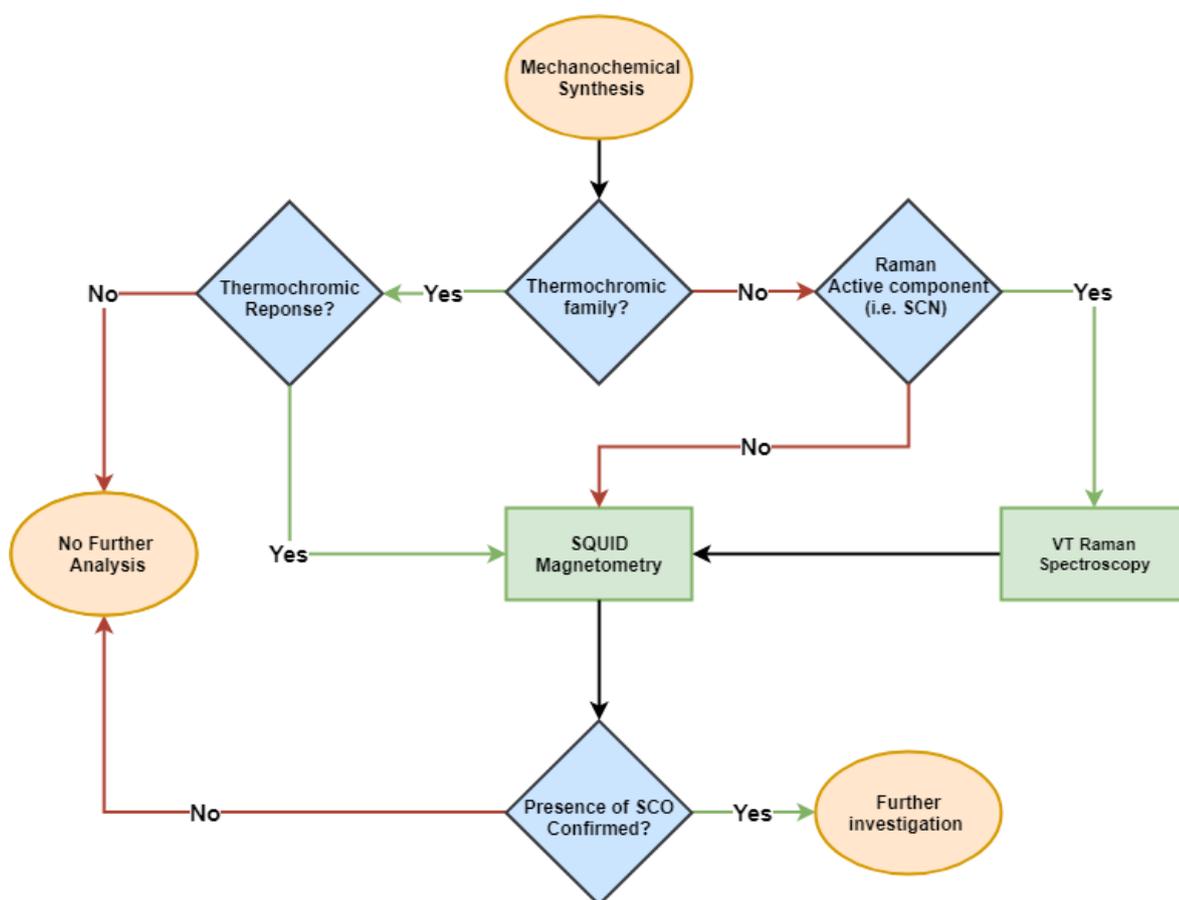
Figure 5.7: Flow chart describing the proposed screening procedure for both thermochromic and non-thermochromic SCO families.

5.2.2.1. 4-R-1,2,4-Triazole Family

The triazole family of SCO materials are ideal for rapid screening by mechanochemistry due to their large potential for modification and clear thermochromic response. Complexes in the triazole family have characteristic colours dependent on spin state, where HS complexes are typically white and LS complexes are typically purple.[3] The difference in colour allows for quick visual identification of SCO using the thermochromic branch of the flow chart shown in Figure 5.7. Depending on the initial colour, and therefore spin state, of the synthesised product, thermochromic screening of the complexes was carried out by heating LS (purple) products with a heat-gun ($\approx$ 500 K) or cooling HS (white) products in liquid nitrogen ($\approx$ 80 K). Screening with two triazole ligands, 4-H-1,2,4-triazole (Htrz) and 4-amino-1,2,4-triazole (atrz) and four Fe(II) salts; $Fe(BF_4)_2.6H_2O$, $FeCl_2.4H_2O$, $Fe(SO_4)_2.7H_2O$ and $(NH_4)_2Fe(SO_4)_2.6H_2O$ was done. Some of the complexes being screened had previously been reported as having SCO properties, this serves to assess the suitability of the screening procedure with successful identification of known materials confirming mechanochemical screening procedure can identify SCO-activity in mechanochemically synthesised materials. Further, two sulphate salts were used, this allows for comparison between anion sources with investigation on the attempts to reduce oxidation, with ammonium iron(II) sulphate less susceptible to oxidation due to the slightly acidic nature of (NH_4^+).

4-H-1,2,4-Triazole Complexes

Two of the proposed screening products, $[Fe(Htrz)_3](BF_4)_2$ and $[Fe(Htrz)_3]Cl_2$ have been previously reported as SCO-active, with multiple forms of $[Fe(Htrz)_3](BF_4)_2$ identified. The mechanical grinding of Htrz with all four Fe(II) salts, yielded purple powders, strongly indicating the presence of a LS species.[54] On heating, all four products underwent a purple $\rightarrow$ white colour change, as shown in Figure 5.8. After allowing to cool, the $Fe(BF_4)_2.6H_2O$ (**S1**) and $FeCl_2.4H_2O$ products (**S2**) reverted back to their initial purple colour. But, both $Fe(SO_4)_2.7H_2O$ (**S3**) and $(NH_4)_2Fe(SO_4)_2.6H_2O$ (**S4**) samples remained white. In accordance to Figure 5.7, after observation

of thermochromic response in all four samples, confirmation of SCO activity was determined using SQUID magnetometry, as shown in Figure 5.9.
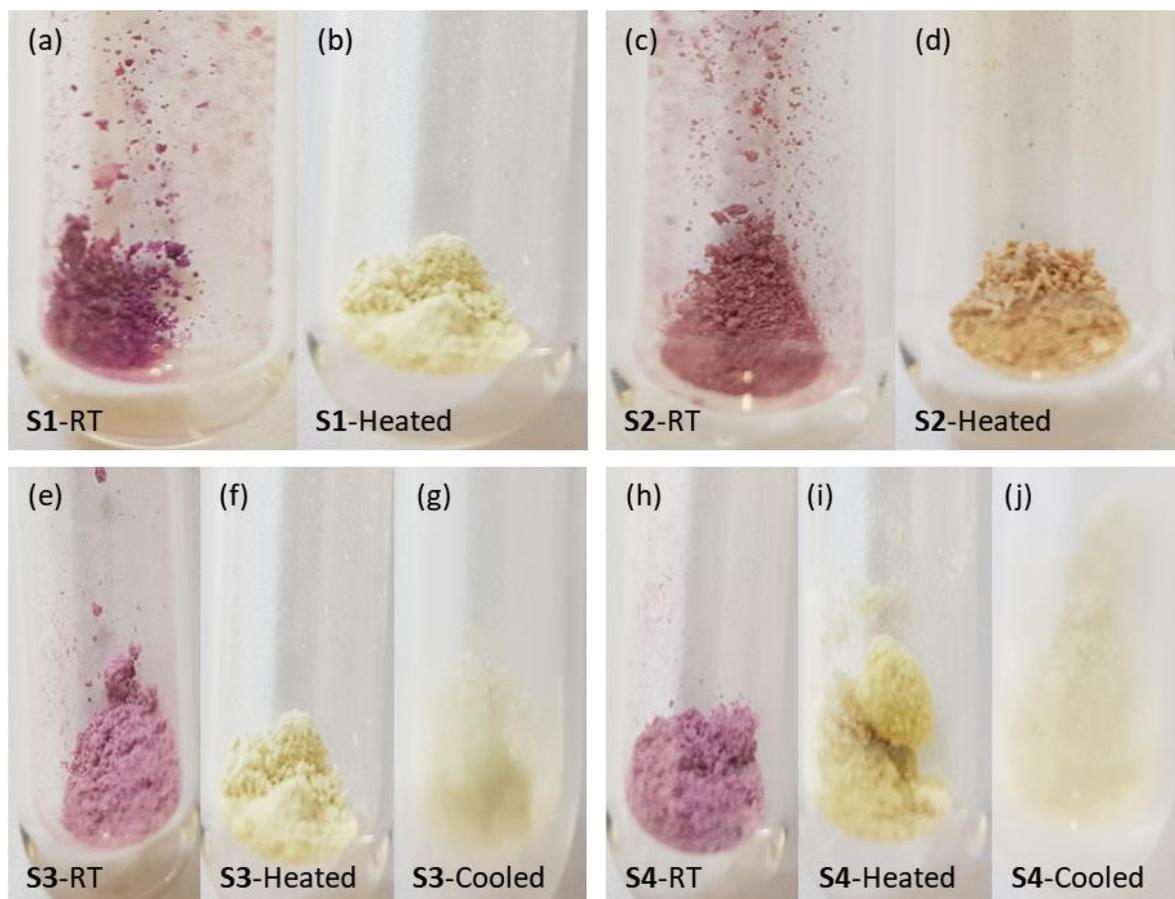
Figure 5.8: Thermochromic response. (a) **S1** – RT, (b) **S1** – Cooled in LN$_2$, (c) **S2** – RT, (d) **S2** – Heated, (e) **S3** – RT, (f) **S3** – Heated, (g) **S3** – Cooled in LN$_2$ after heating, (h) **S4** – RT, (i) **S4**-Heated and (j) **S4** – Cooled in LN$_2$ after heating.

SQUID analysis of the samples confirmed the presence of an initial SCO transition for all four complexes on heating above room temperature, as shown in Figure 5.9. **S1** is expected to show SCO activity,[51] which was identified using the visual thermochromism test. SQUID showed reversible SCO behaviour in temperature ranges consistent with some polymorphs of [Fe(Htrz)$_3$](BF$_4$)$_2$.[3] Ultimately, this screening procedure successfully identified the presence of SCO-activity in **S1** and further analysis of mechanically synthesised [Fe(Htrz)$_3$](BF$_4$)$_2$ is discussed in section 3.2.2.1, see Compound **2**. **S2** was also expected to exhibit SCO-activity and this was confirmed by SQUID magnetometry. **S2** underwent reversible SCO with a significant change in residual HS fraction and completeness of transition between the first heating cycle and

subsequent cycling. This difference is primarily attributed to mass loss owing to the removal of water at high temperatures, as shown by the increase in $\chi_M T$ at low temperature. Potential sources of water in mechanochemical synthesis are from the hydrated $FeCl_2.4H_2O$ salt used and atmospheric moisture. Although, the observed differences could also be attributed to the 'run-in' effect described in 1.1.4. The magnetic properties, including the differences between heating and cooling cycles, are consistent with previous reports on the complex $[Fe(Htrz)_3]Cl_2.xH_2O$.[55] As with **S1**, the screening procedure was successful in identifying and confirming SCO-activity in compound **S2**.
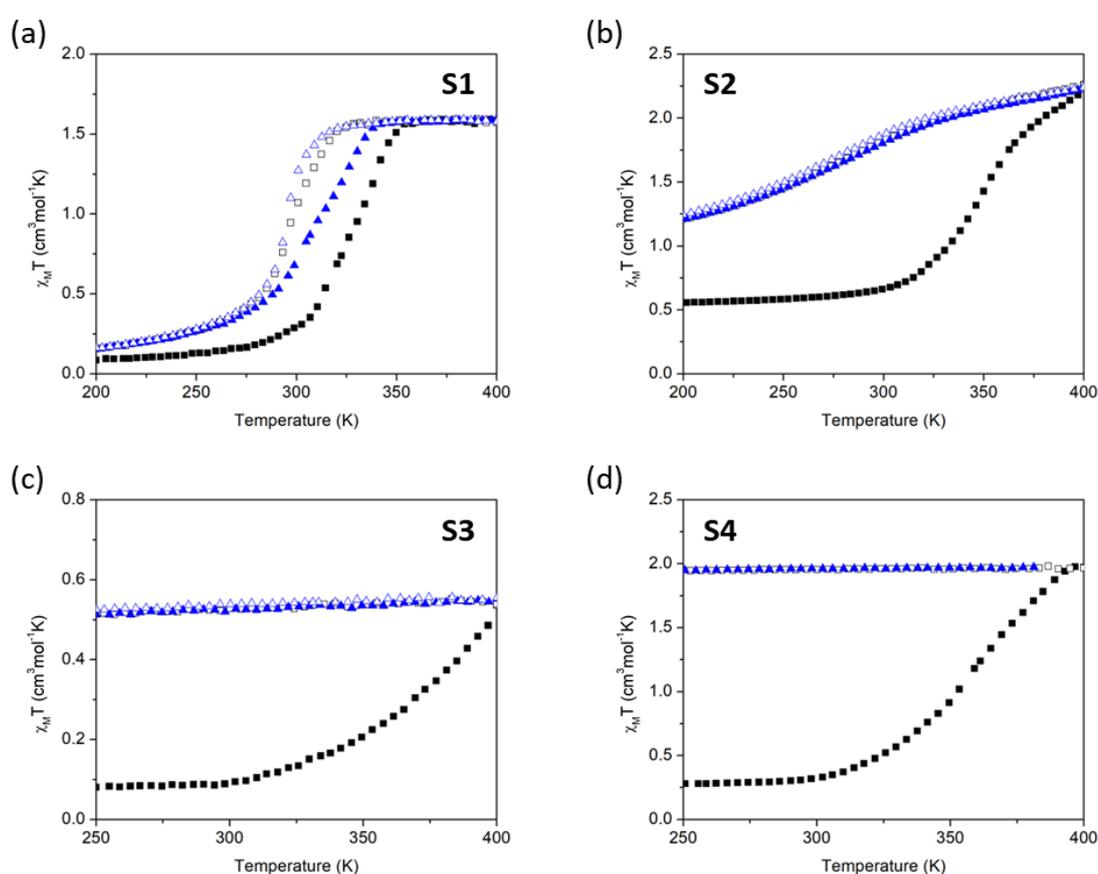
Figure 5.9: Temperature dependent SQUID data, two cycles. Cycle 1 Heating ■ and Cooling □, Cycle 2 Heating ▲ and Cooling △. **(a)** $[Fe(Htrz)_3](BF_4)_2$ – **S1**, **(b)** $[Fe(Htrz)_3]Cl_2$ – **S2**, **(c)** $[Fe(Htrz)_3]SO_4$ from $FeSO_4.7H_2O$ – **S3** and **(d)** $[Fe(Htrz)_3]SO_4$ from $(NH4)_2Fe(SO_4)_2.6H_2O$ – **S4**.

Neither **S3** nor **S4** represent materials previously reported in literature, but confirmation of the presence of SCO-activity was carried out using SQUID magnetometry. Both **S3** and **S4** undergo an irreversible transition. Transition onset temperatures for both complexes are similar (**S3** = 300

K and **S4** = 300 K) indicating the presence of the same material, which indicates both $(NH_4)_2Fe(SO_4)_2.6H_2O$ and $FeSO_4.7H_2O$ yield the same product, likely $[Fe(Htrz)_3]SO_4$. In the instance of **S3** and **S4**, further analysis of the properties was not carried out at this stage. The screening procedure was successful in identifying and confirming SCO-activity in a previously unreported material, as shown in Table 5.1.

Table 5.1: Measured transition temperatures for Htrz complexes. Two cycles of **S1**, **S2**, **S3** and **S4**.

Proposed Formula	Sample	Thermochromic Response	Reversible Transition	Cycle 1		Cycle 2	
				$T_{1/2}\uparrow$ (K)	$T_{1/2}\downarrow$ (K)	$T_{1/2}\uparrow$ (K)	$T_{1/2}\downarrow$ (K)
$[Fe(Htrz)_3](BF_4)_2$	**S1**	Yes	Reversible	330	301	314	297
$[Fe(Htrz)_3]Cl_2$	**S2**	Yes	Reversible	353	305	305	301
$[Fe(Htrz)_3]SO_4$ *$FeSO_4.7H_2O$*	**S3**	Yes	Irreversible	Onset: 300	-	-	-
$[Fe(Htrz)_3]SO_4$ *$(NH_4)_2Fe(SO_4)_2.6H_2O$*	**S4**	Yes	Irreversible	Onset: 300	-	-	-

4-Amino-1,2,4-Triazole

All four of the proposed reaction products prepared with atrz have previously been reported to display SCO-activity in literature. Thermochromic screening indicated the presence of reversible colour changes in **S5**, **S6**, **S7** and **S8** as shown in Figure 5.10. The reaction product of $Fe(BF_4)_2.6H_2O$ and atrz (**S5**), was previously reported as HS at room temperature.[56] This was consistent with the observed white → purple transition observed on cooling for **S5**. Similarly, $[Fe(atrz)_3]Cl_2$ (proposed product **S6**) and $[Fe(atrz)_3]SO_4$ (proposed product of the reactions with both $FeSO_4.7H_2O$ (**S7**) and $(NH_4)_2Fe(SO_4)_2.6H_2O$ (**S8**)) have reported SCO transitions above room temperature, consistent with the observed purple → white transitions on heating.[55]
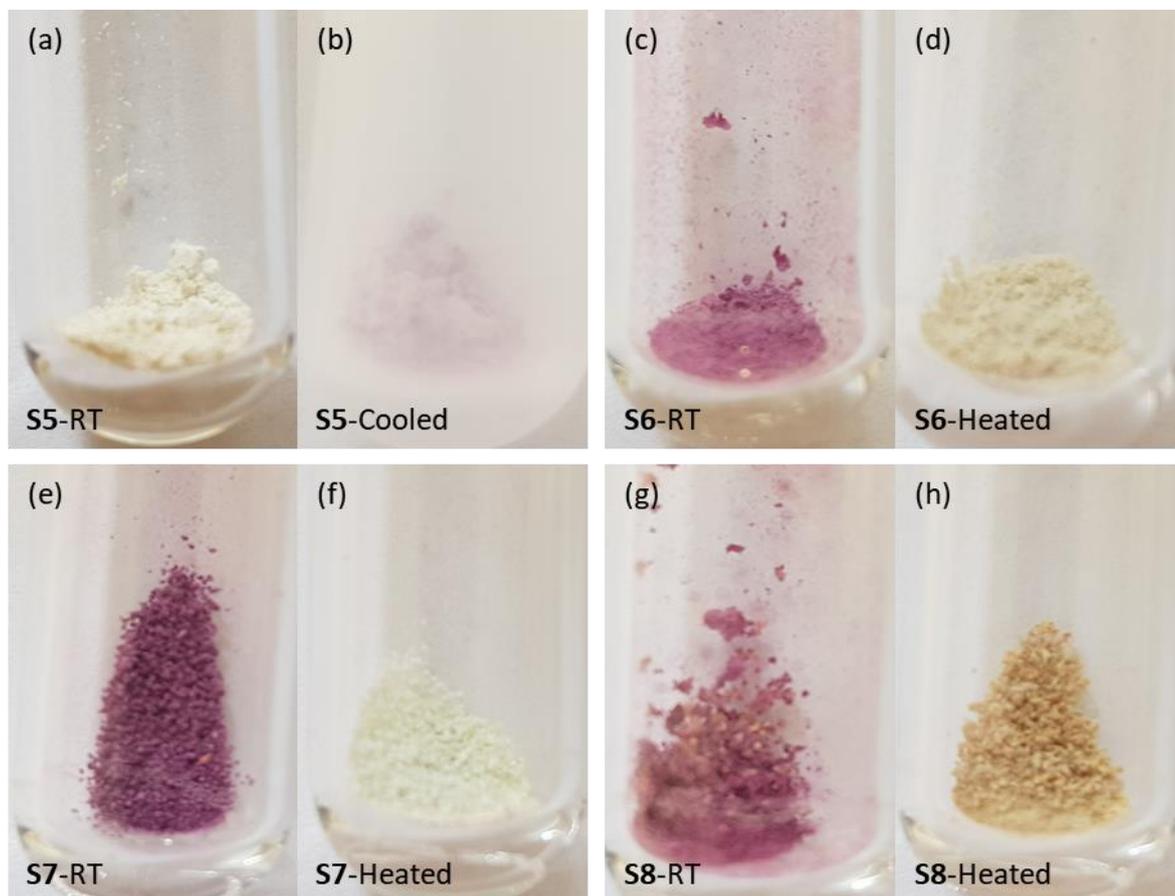
Figure 5.10: Thermochromic response. (a) **S5** – RT, (b) **S5** – Cooled in LN$_2$, (c) **S6** – RT, (d) **S6** – Heated, (e) **S7** – RT, (f) **S7** – Heated, (g) **S8** – RT and (h) **S8** – Heated.

Having identified the presence of a thermochromic response, variable temperature SQUID magnetometry was used to confirm the presence of reversible SCO transitions in all four products, as shown in Figure 5.11. **S5** underwent SCO with $T_{1/2}\uparrow$ = 201 K, which is consistent with a previously observed but uncharacterised form of [Fe(atrz)$_3$](BF$_4$)$_2$.[57] Further discussion on **S5** is presented in 3.2.2.2. **S6** underwent SCO with a two-step first heating cycle ($T_{1/2}\uparrow$ = 320 and 351 K), repeated cycling after the first heating cycle yielded reproducible results, displaying SCO behaviour with $T_{1/2}\uparrow$ = 331 K and $T_{1/2}\downarrow$ = 322 K consistent with previous literature reports. The magnetic properties of **S7** and **S8** are similar, with similar transition temperatures in the second cycle (**S7**: $T_{1/2}\uparrow$ = 335 K, $T_{1/2}\downarrow$ = 324 K and **S8**: $T_{1/2}\uparrow$ = 334 K, $T_{1/2}\downarrow$ = 317 K).
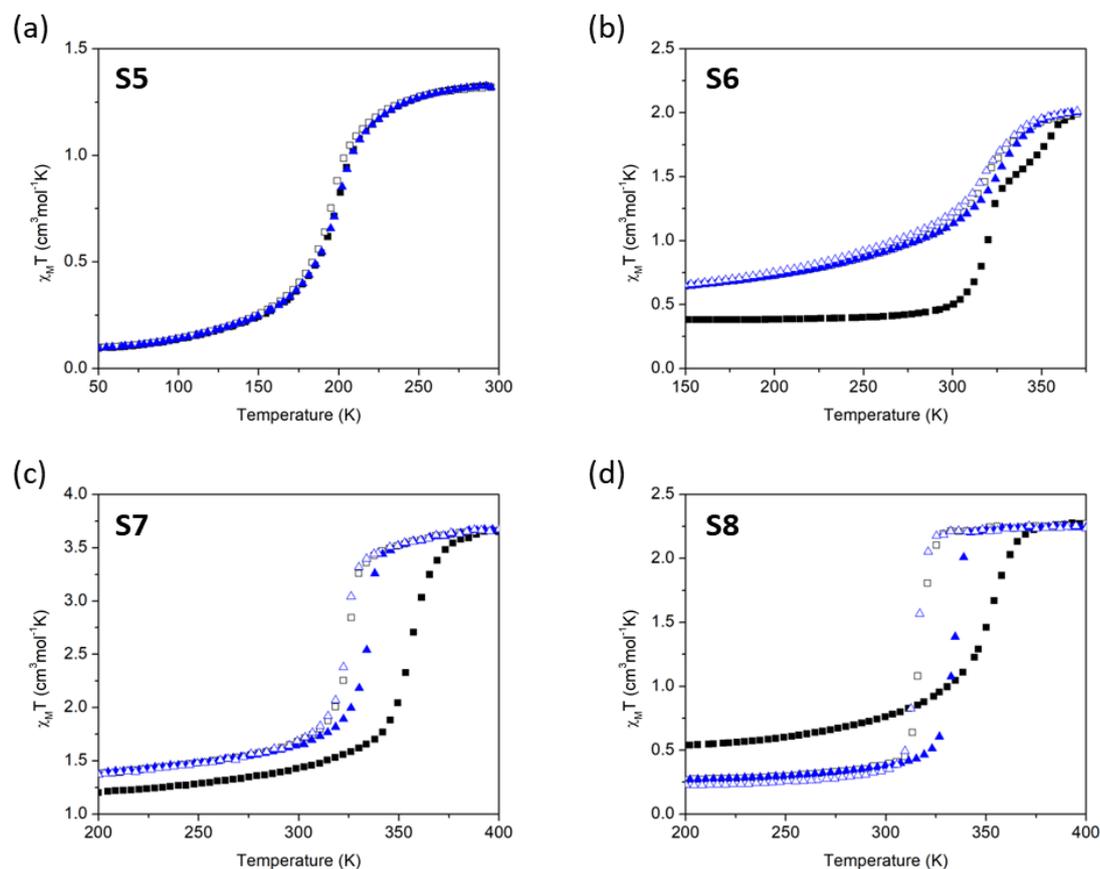
Figure 5.11: Temperature dependent SQUID data, two cycles. Cycle 1 Heating ■ and Cooling □, Cycle 2 Heating ▲ and Cooling △. **(a)** [Fe(atrz)$_3$](BF$_4$)$_2$ − **S5**, **(b)** [Fe(atrz)$_3$]Cl$_2$ − **S6**, **(c)** [Fe(atrz)$_3$]SO$_4$ from FeSO$_4$.7H$_2$O − **S7** and **(d)** [Fe(atrz)$_3$]SO$_4$ from (NH4)$_2$Fe(SO$_4$)$_2$.6H$_2$O − **S8**.

As discussed above, the values for $\Delta\chi_M T$ are lower than expected for triazole complexes due to the presence of impurities which were not removed during preliminary screening. However, this does not negatively affect the screening procedure as it is only used as a crude tool for materials discovery, any novel materials identified will be studied in much greater detail. Comparison of SCO properties for the screened complexes are shown in Table 5.2. The screening procedure successfully identified SCO-activity in all four products with confirmation of the properties made by variable temperature SQUID magnetometry.

Table 5.2: Measured transition temperatures for atrz complexes. Two cycles are shown for **S5**, **S6**, **S7** and **S8**. *2-Step transition.

Proposed Formula		Thermochromic Response	Reversible Transition	Cycle 1		Cycle 2	
				$T_{1/2}\uparrow$ (K)	$T_{1/2}\downarrow$ (K)	$T_{1/2}\uparrow$ (K)	$T_{1/2}\downarrow$ (K)
[Fe(atrz)$_3$](BF$_4$)$_2$	S5	Yes	Reversible	201	199	201	200
[Fe(atrz)$_3$]Cl$_2$	S6	Yes	Reversible	320 and 351*	326	331	322
[Fe(atrz)$_3$]SO$_4$ FeSO$_4$.7H$_2$O	S7	Yes	Reversible	357	326	335	324
[Fe(atrz)$_3$]SO$_4$ (NH$_4$)$_2$Fe(SO$_4$)$_2$.6H$_2$O	S8	Yes	Reversible	354	318	334	317

5.2.2.2.   Fe(phen)$_2$(NCS)$_2$ and Derivatives

The complex Fe(phen)$_2$(NCS)$_2$ is intensely coloured, which makes the colour change resulting from SCO difficult to observe, the strong colouration results from metal-ligand charge transfer. As discussed in Chapter 2, one solution-state synthetic route to the complex Fe(phen)$_2$(NCS)$_2$ requires synthesis of the complex [Fe(phen)$_3$](SCN)$_2$ before conversion to the SCO-active complex Fe(phen)$_2$(NCS)$_2$ by extraction of one phenanthroline ligand either by continuous solvent extraction[58] or thermal conversion.[59] Interest in mechanochemical screening of this complex arises due to the possibility for direct synthesis of the SCO-active complex, which was assessed by screening one-pot and two-spot synthetic routes. In accordance with the non-thermochromic branch of Figure 5.7, the reaction products for one-pot (**S9-1pot**) and two-pot synthesis (**S9-2pot**) were analysed by variable temperature Raman spectroscopy. In order to identify whether the products were the desired SCO-active complex or the inactive complex, the temperature-dependent magnetic properties were measured by SQUID magnetometry.
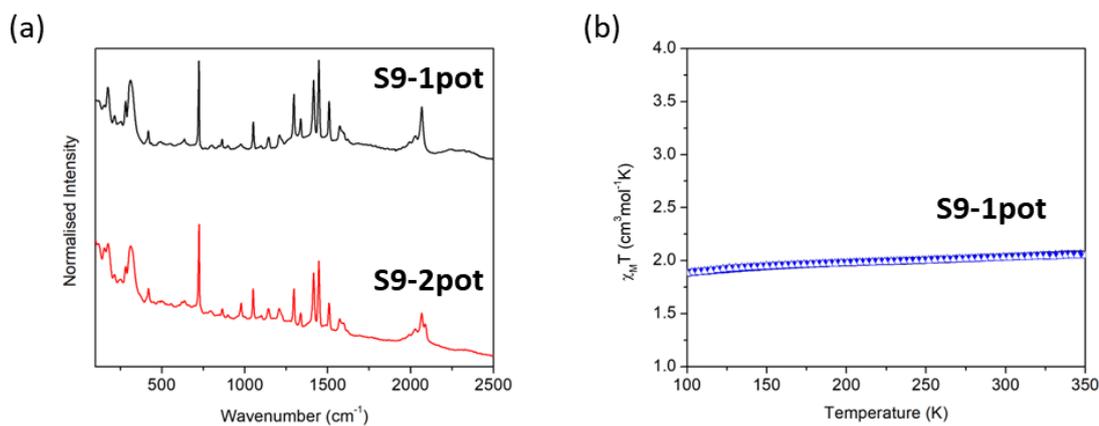
Figure 5.12: (a) Overlaid Normalised Raman Spectrum for one-pot product (**S9-1pot**) and two-pot product (**S9-2pot**). **(b)** Temperature dependent SQUID data for **S9-1pot**, two cycles. Cycle 1 Heating ■ and Cooling □, Cycle 2 Heating ▲ and Cooling △.

It can be seen in Figure 5.12(a) that independent of the reaction route taken, the product was the same. Small differences in the spectra at 2100 cm^{-1} are attributed to differences in quantities of reagents used, with a greater ratio of NCS present in **S9-1pot**. The magnetic properties of **S9-1pot**, shown in Figure 5.12(b), exhibited no SCO activity in the temperature range expected for Fe(phen)$_2$(NCS)$_2$.[60] Therefore, it was concluded that the product of both one-pot and two-pot synthesis was [Fe(phen)$_3$](SCN)$_2$, this was confirmed using a variation on a previously reported procedure for the thermal conversion of [Fe(phen)$_3$](SCN)$_2$ into Fe(phen)$_2$(NCS)$_2$.[59] A portion of **S9-1pot** was dried by heating to 80 °C for 3 hours, followed by heating to 200 °C for 10 hours. This yielded the product **S9-1pot-Heat**.

S9-1pot-Heat was first screened using variable temperature Raman spectroscopy, as shown in Figure 5.13(a). There are clear differences between the spectrum collected at 298 K and that at 130 K. Due to the significant differences, the magnetic properties were measured by SQUID magnetometry, as shown in Figure 5.13(b).
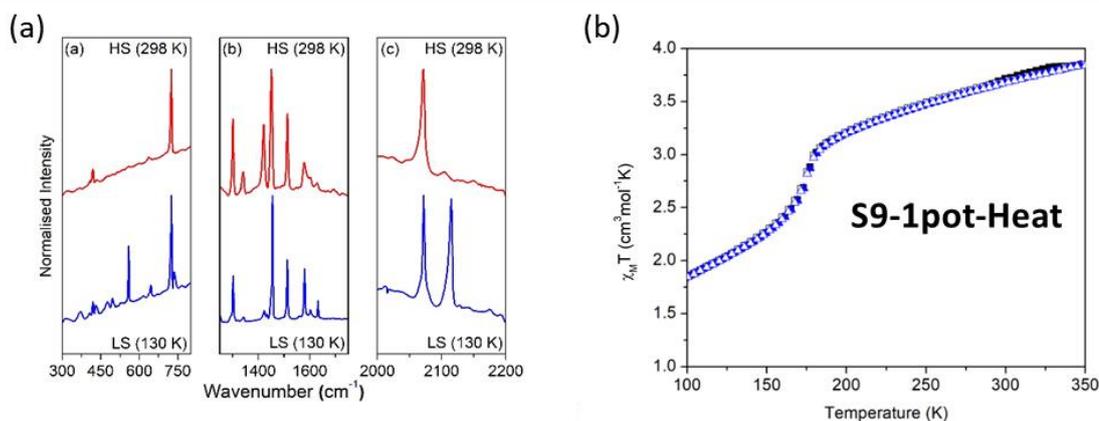
Figure 5.13: (a) Raman Spectra for **S9-1pot-Heat** taken at 298 K (Top) and 130 K (Bottom). Three sections shown to emphasise differences, full plots in 2.3.1.1. **(b)** Temperature dependent SQUID data for **S9-1pot-Heat**, 2 cycles. Cycle 1 Heating and ■ Cooling □, Cycle 2 Heating ▲ and Cooling △.

Variable temperature SQUID magnetometry confirmed the presence of SCO-activity in **S9-1pot-Heat**, with similar $T_{1/2}\uparrow$ = $T_{1/2}\downarrow$ = 175 K to previous literature reports.[26,60–62] Further discussion on the mechanochemical synthesis of $Fe(phen)_2(NCS)_2$, with comparisons to literature reports and solution synthesised samples, as well as the effects of washing can be found in 3.2.2.2. The proposed screening procedure was successful in identifying SCO-activity in **S9-1pot-Heat**.

5.2.2.2.1.   1,10-phenathroline Derivatives

Having identified SCO-activity in the previously reported complex $Fe(phen)_2(NCS)_2$, further screening was carried out using the phenanthroline derivatives 4,7-diphenyl-1,10-phenathroline (ph-phen) and 4,7-dimethyl-1,10-phenathroline (me-phen) the structures of both derivatives are shown in Figure 5.14. Screening of the complexes immediately after mechanochemical synthesis and after thermal treatment were undertaken. As with $Fe(phen)_2(NCS)_2$, the proposed products would be expected to be strongly coloured, which would mask the colour change resulting from SCO, therefore both derivatives were screened using the non-thermochromic branch of the screening procedure described in Figure 5.7.
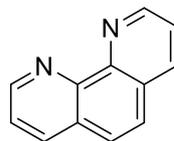
1,10-phenanthroline (phen)
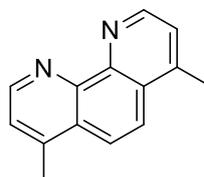
4,7-dimethyl-1,10-phenanthroline (me-phen)
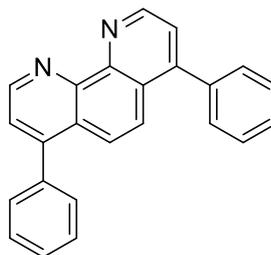
4,7-diphenyl-1,10-phenanthroline(ph-phen)

Figure 5.14: Structures of 1,10-phenathroline (top), 4,7-dimethyl-1,10-phenanthroline (middle) and 4,7-diphenyl-1,10-phenanthroline (bottom).

5.2.2.2.1.1.   4,7-diphenyl-1,10-phenanthroline

The screening product of ph-phen (**S10-As**) was screened using VT-Raman (at 123 K and 298 K), as shown in Figure 5.15(a). There are significant differences between the spectrum collected at 123 K and the second spectrum collected at 298 K. The area around 2000-2200 cm^{-1} underwent a drastic change, similar to changing bonding in the thiocyanate ion observed for Fe(phen)$_2$(NCS)$_2$.[59] Due to this, further investigation of **S10-As** was undertaken *via* variable temperature SQUID magnetometry. The thermally treated component of **S10-As**, sample **S10-Heat** did not display differences Raman spectra collected at 123 K and 298 K, as shown in Figure 5.15, therefore further investigation was not carried out on **S10-Heat**.
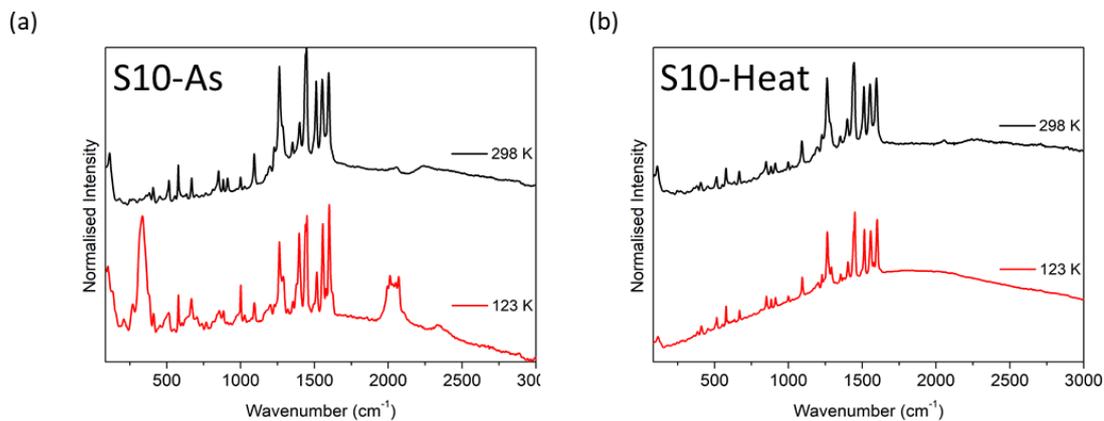
Figure 5.15: Raman spectra at 298 K (top) and 123 K (Bottom). (a) Compound **S10-As** and (b) Compound **S10-Heat**.

Analysis of the variable temperature SQUID data indicates **23-As** does not display SCO-activity across the range 50 K to 400 K, as shown in Figure 5.16. The constant and gradual increase in $\chi_M T$ is due to the sample being diamagnetic and the absence of a visible jump or sudden increase in $\chi_M T$ suggests the material does not undergo SCO. There is also no significant difference between the first and second heating cycle.
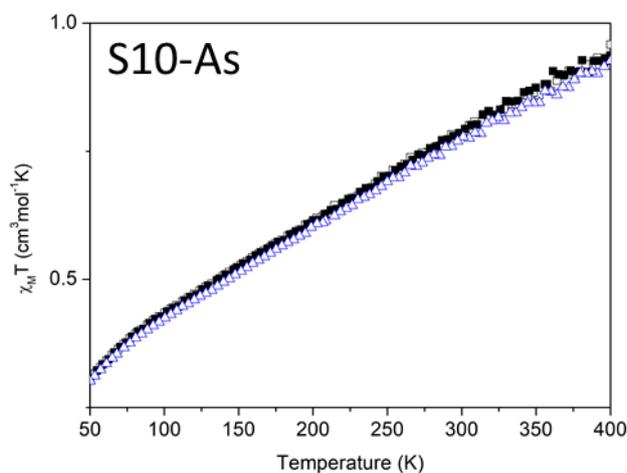
Figure 5.16: Variable temperature SQUID magnetometry for compound **S10-As**. Cycle 1 Heating ■ and Cooling □, Cycle 2 Heating ▲.

The origin of the difference observed in VT-Raman for **S10**, is not clear but may be due to sample inhomogeneity or an impurity introduced during the analysis. Multiple measurements at each temperature were made and each display the sample spectra consistent with the spectra

presented in Figure 5.15. Additional origins of the differences may be due to sample decomposition or oxidisation, as the Raman measurements were taken soon after synthesis whereas the SQUID measurements were taken some time after. However, repeated synthesis did not display the same differences in Raman spectra and no indication of SCO-activity was observed in the repeated SQUID measurements. This compound highlights potential limitations of the screening procedure and serves to emphasise the potential for false positive and the need to use several characteristic techniques. One such origin for the differences observed in the Raman data could be a structural phase transition, however, further investigation was beyond the scope of this work.

5.2.2.2.1.2.   4,7-dimethyl-1,10-phenanthroline

Screening of the complex prepared with the ligand 4,7-dimethyl-1,10-phenathroline (me-phen) was undertaken using the same general approach. Neither the as-synthesised product or the temperature treated complex showed significant differences in the Raman spectra collected at 298 K and 123 K. Therefore, no further analysis of the products was undertaken. Variable temperature Raman spectra are shown in Appendix C.

5.2.2.3.   Assessment of Screening Procedure

Application of the screening procedure described in Figure 5.7 to the 4-R-1,2,4-triazole family of SCO complexes proved the procedure successful and suitable for purpose, for thermochromic materials. SCO activity was identified in the previously reported complexes: $[Fe(Htrz)_3](BF_4)_2$, $[Fe(Htrz)_3]Cl_2$, $[Fe(atrz)_3](BF_4)_2$, $[Fe(atrz)_3]Cl_2$ and $[Fe(atrz)_3]SO_4$. The presence of an unreported irreversible SCO in $[Fe(Htrz)_3]SO_4$ was also identified. The thermochromic response of the 4-R-1,2,4-triazole family was very distinctive which reduced the possibility of a false negative classification.

For non-thermochromic materials, the screening procedure was not entirely optimised. However, the procedure was able to identify SCO-activity in a previously reported complex $(Fe(phen)_2(NCS)_2)$, screening of the ligand 4,7-diphenyl-phenathroline provided a false positive

response, with significant differences observed in the variable temperature Raman spectra without SCO-activity confirmed by SQUID magnetometry. This highlighted further analysis is required during the screening procedure, particularly for non-thermochromic materials.

Development of the screening procedure by including PXRD analysis prior to further analysis would allow for reduction of a false positive response. By comparing patterns of starting materials and reaction products, it is possible to confirm a reaction had occurred, which can be done by identifying peaks present in the pattern which are not from starting materials. The inclusion of PXRD analysis would not significantly alter the total screening time, due to the possibility of using auto-sampling systems for PXRD analysis. This significantly reduces the active time required whilst providing valuable information which can help to optimise the screening procedure. An improved screening procedure is presented in Figure 5.17.
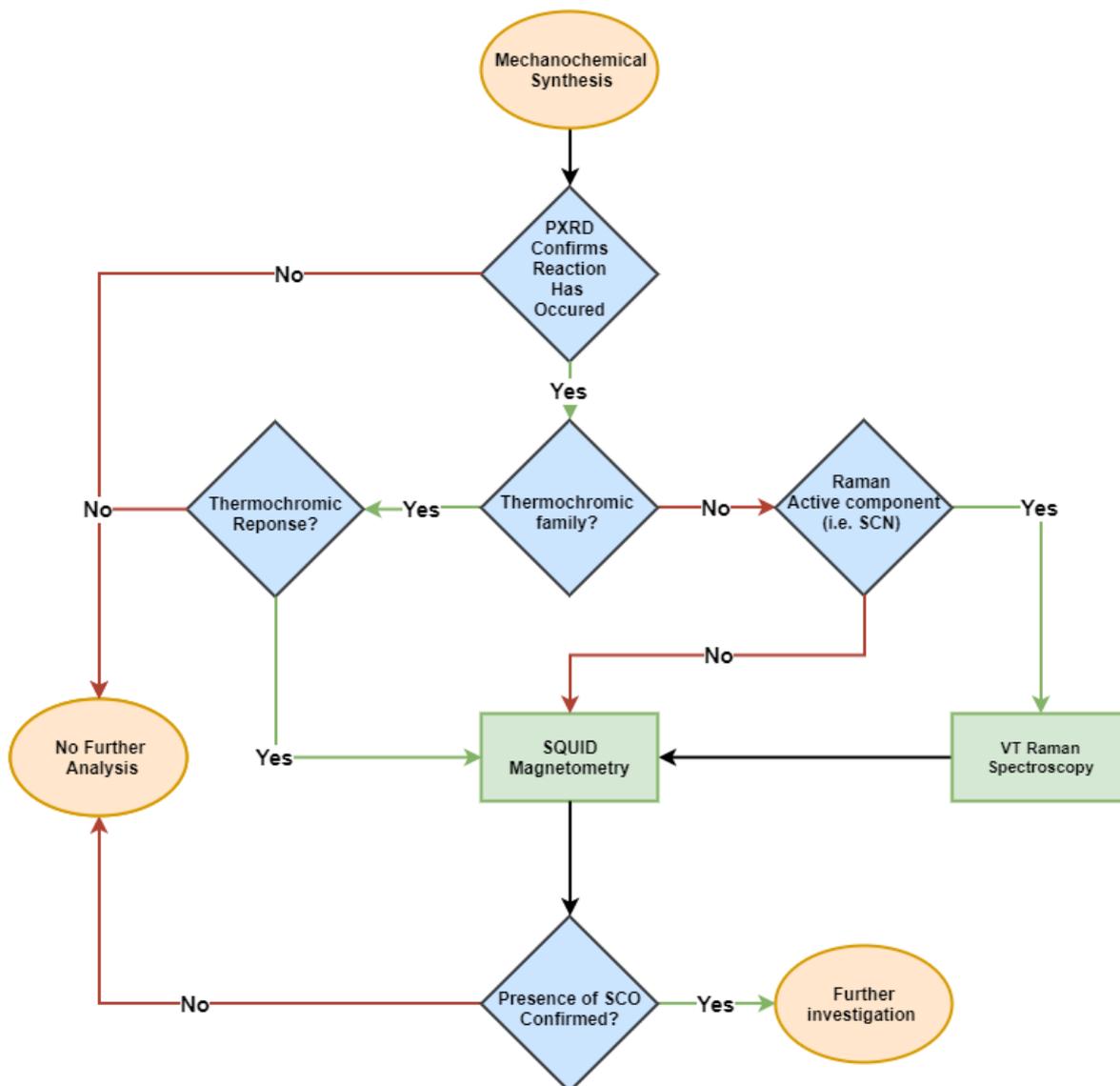
Figure 5.17: Developed Flow chart describing the proposed screening procedure for both thermochromic and non-thermochromic SCO families.

5.2.3. Testing Modified Screening Procedure

The suitability of the modified screening procedure described in Figure 5.17, was investigated by screening three families of potentially SCO-active materials. The thermochromic hydrotris(1-pyrazolyl)borate family, which undergoes purple to white thermochromism, was used to assess the thermochromic branch with particular interest in the possibility of forming mixed ligand complexes by mechanochemistry. Further, a second thermochromic family will be investigated, the 2,6-di(pyrazole-3-yl)pyridine (**3-bpp**) family undergoes a more subtle thermochromic response with a characteristic yellow-orange transformation, this will test the limitations of the screening

procedure for thermochromic materials. The final family investigated will be the non-thermochromic bipyridine family which will further test the non-thermochromic branch of the screening procedure.

5.2.3.1.   Fe[HB(pz)$_3$]$_2$

The complex Fe[HB(pz)$_3$]$_2$ (**S18**) has previously been reported as SCO-active, with $T_{1/2}\uparrow$ = 358 K.[42] Therefore it will be used to assess the suitability of the procedure and to serve as further evidence of mechanochemical synthesis of SCO-active materials. Mechanochemical synthesis yielded a pinkish powder which was purified by sublimation yielding **S18-Sublim**. Purification was done on this complex as an additional step to improve PXRD analysis. In accordance with the screening procedure, PXRD analysis was done, as shown in Figure 5.18. It is clear that the pattern for sample **S18-Sublim** is similar to that of the simulated pattern for Fe[HB(pz)$_3$]$_2$ (CSD Code: HPZBFE)[63] with multiple additional peaks likely resulting from the absence of a washing step. Comparison of PXRD indicates mechanochemical synthesis is promising and further analysis should be carried out.
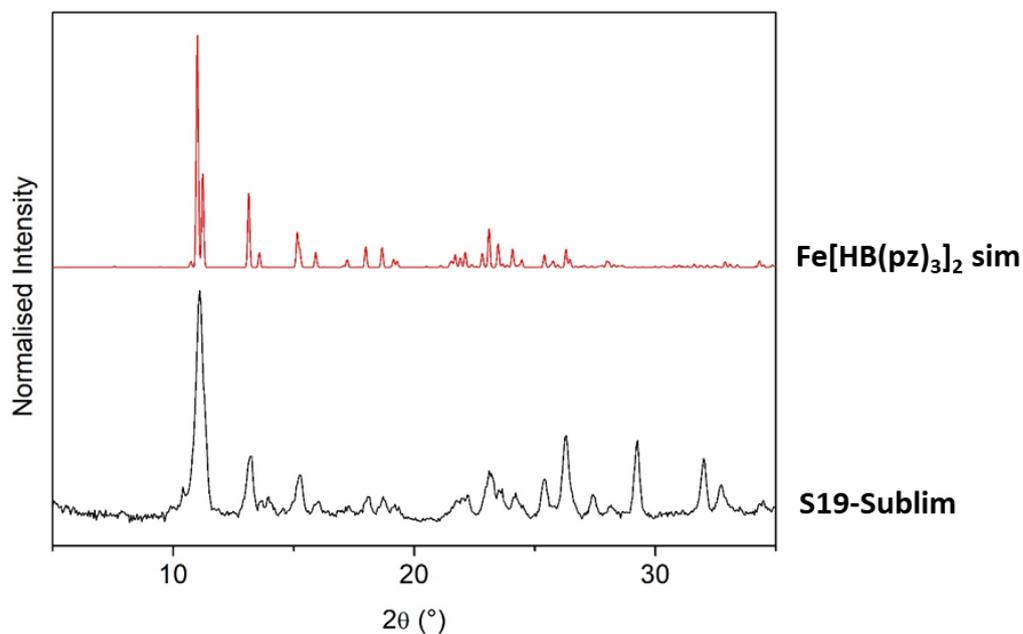
Figure 5.18: Comparison of normalised PXRD data for Top: Fe[HB(pz)$_3$]$_2$ complex, simulated from SC-XRD data (CSD Code: HPZBFE)[63] and Bottom: **S18-Sublim**.

The thermochromic response was investigated by heating the pink (proposed LS species) powder using a heat gun. In response to heating, the powder underwent a thermochromic response changing into a white (proposed HS species) powder, as shown in Figure 5.19. In accordance with the screening procedure described in Figure 5.17, further investigation was carried out to confirm SCO-activity in **S18-Sublim**.
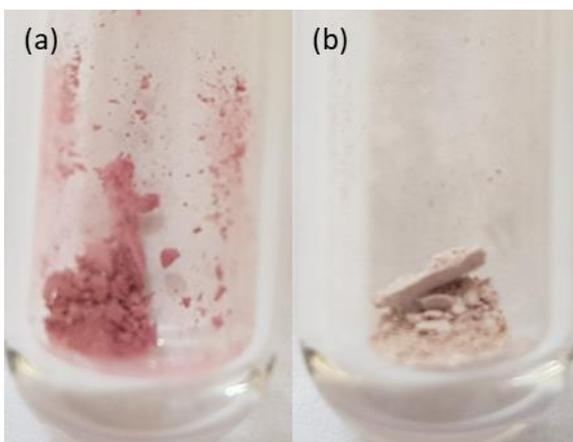
Figure 5.19: Thermochromic response for **S18-Sublim**. (a) RT and (b) Heated.

Confirmation of the presence of SCO-activity in **S18-Sublim** was done by variable temperature SQUID magnetometry, as shown in Figure 5.20(a). The first cycle transition temperature was reported in literature with $T_{1/2}\uparrow$ = 405 K which is a higher temperature than accessible in the SQUID magnetometer used, as shown in Figure 5.20(b). Therefore, it is only possible to observe the onset of the SCO-transition. Comparison of SCO properties are presented in Table 5.3. The screening procedure was successful in identifying SCO-activity in a previously reported SCO-active material.
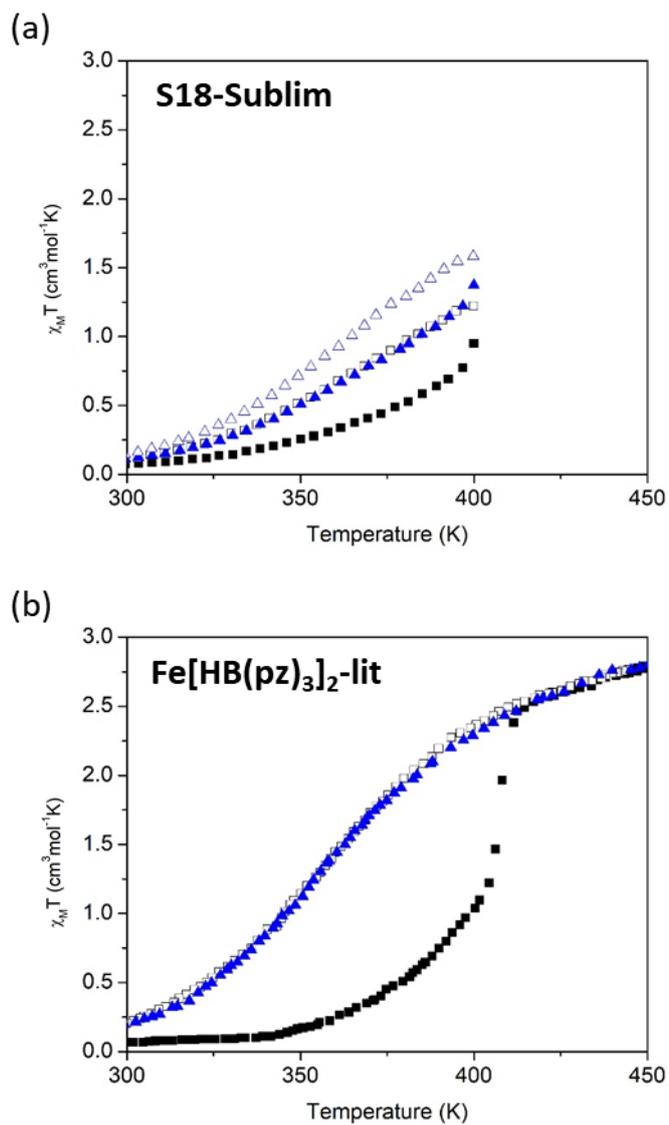
Figure 5.20: Temperature dependent SQUID data **(a) S18-Sublim** two cycles: Cycle 1 Heating ■ and Cooling □, Cycle 2 Heating ▲ and Cooling △, **(b)** Digitised literature plot for Fe[HB(pz)$_3$]$_2$-lit.[42]

Table 5.3: Comparison of SCO properties for **S18-Sublim** and literature reports on the complex Fe[HB(pz)$_3$]$_2$.[42]

	$T_{1/2}$↑ (K)	$T_{1/2}$↓ (K)	ΔT (K)	'Smoothness' (K)
S18-Sublim	>400	-	-	-
Literature Fe[HB(pz)$_3$]$_2$ First Cycle	405	-	-	24
Literature Fe[HB(pz)$_3$]$_2$ Subsequent Cylcing	358	358	0	52

5.2.3.2.   Fe[HB(3,5-(CH$_3$)$_2$-pz)$_3$]$_2$

The complex Fe[HB(3,5-(CH$_3$)$_2$-pz)$_3$]$_2$ (**S19**) has previously been reported as SCO-active, with T$_{1/2}$↑ = 358 K.[44] Therefore it was used to assess the suitability of the procedure and to serve as further evidence of mechanochemical synthesis of SCO-active materials. Mechanochemical synthesis yielded a white powder which was purified by sublimation (**S19-Sublim**). As previously discussed, purification *via* Sublimation was used as an additional step to improve PXRD analysis. In accordance with the screening procedure, PXRD analysis was done, as shown in Figure 5.21. The pattern for **S19-Sublim** shows some similarities to the simulated pattern of Fe[HB(3,5-(CH$_3$)$_2$-pz)$_3$]$_2$ (CSD Code: HMPBFE).[63] Comparison of PXRD indicates a mechanochemical reaction had occurred.
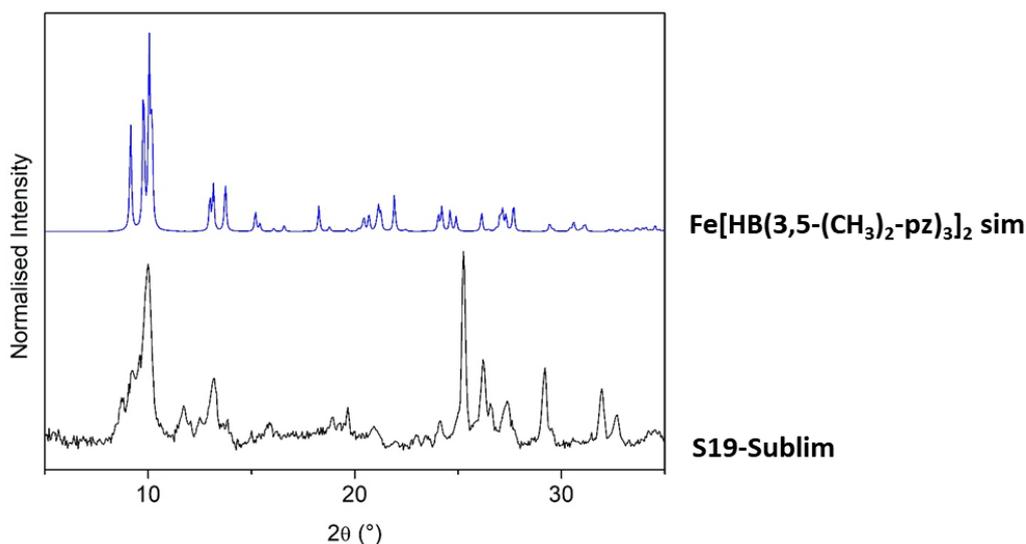
Figure 5.21: Comparison of normalised PXRD data for Top: Fe[HB(3,5-(CH$_3$)$_2$-pz)$_3$]$_2$ complex, simulated from SC-XRD data (CSD Code: HMPBFE)[63] and Bottom: **S19-Sublim**.

In accordance with the screening procedure described in Figure 5.17, the thermochromic response was investigated by cooling the white (proposed HS species) powder in liquid nitrogen. In response to cooling, the powder underwent a thermochromic response changing into a pink (proposed LS species) powder, as shown in Figure 5.22. Further investigation was carried out to confirm SCO-activity in **S19-Sublim**.
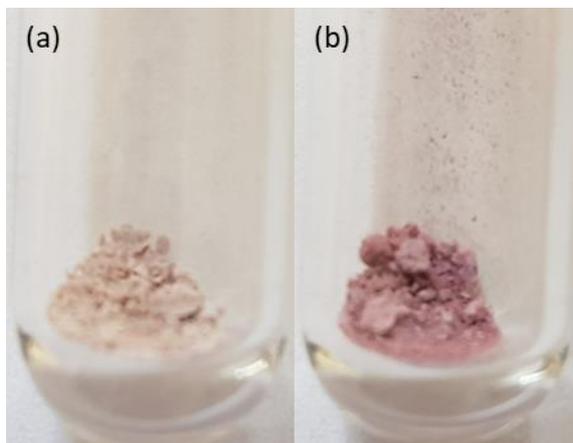
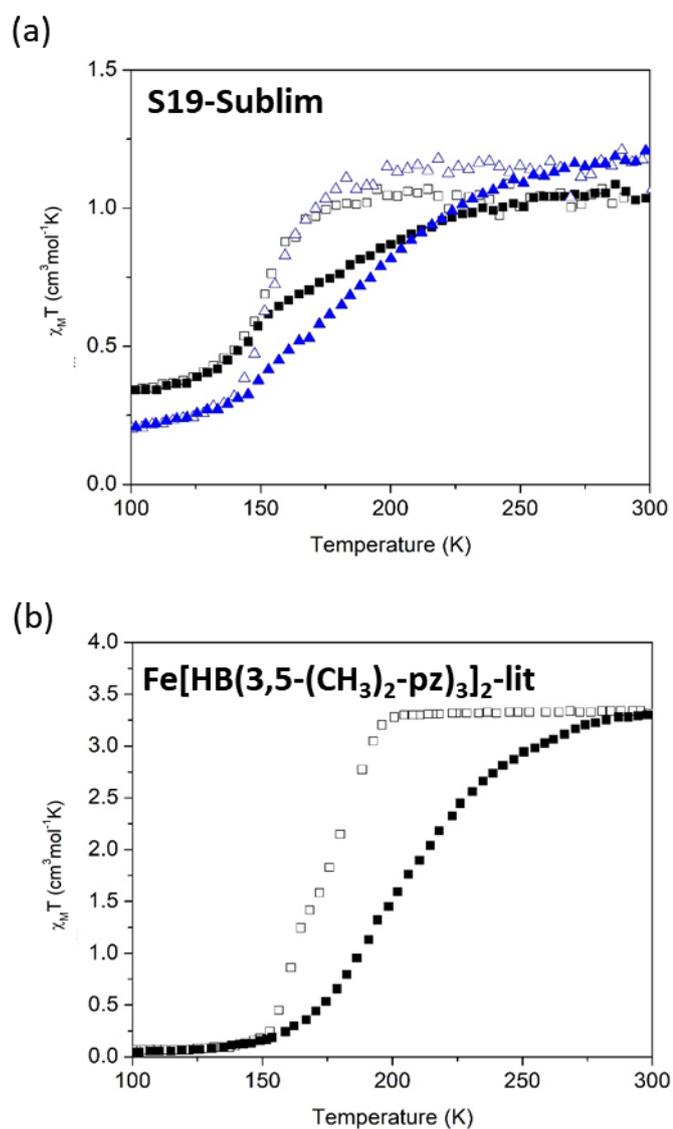**Figure 5.22:** Visible thermochromism for **S19-Sublim**. (a) RT and (b) Cooled in LN$_2$.

Figure 5.23: Temperature dependent SQUID data **(a) S19-Sublim** two cycles: Cycle 1 Heating ■ and Cooling □, Cycle 2 Heating ▲ and Cooling △, **(b)** Digitised literature plot for Fe[HB(3,5-(CH$_3$)$_2$-pz)$_3$]$_2$-lit.[44]

SQUID magnetometry was used to confirm SCO-activity in **S19-Sublim**, as shown in Figure 5.23. SCO-activity is clearly visible with differences between the first and subsequent cycles observed. Sample **32** undergoes a first cycle transition with $T_{1/2}\uparrow$ = 173 K, $T_{1/2}\downarrow$ = 154 K and 'smoothness' = 72 K. Subsequent cycling displays SCO with $T_{1/2}\uparrow$ = 180 K, $T_{1/2}\downarrow$ = 155 K and 'smoothness' = 65 K. The presence of SCO was successfully identified using the screening procedure, as shown in Table 5.4.

Table 5.4: Comparison of SCO properties for **S19-Sublim** and literature reports on the complex Fe[HB(3,5-(CH$_3$)pz)$_3$]$_2$.[44]

	$T_{1/2}\uparrow$ (K)	$T_{1/2}\downarrow$ (K)	ΔT (K)	'Smoothness' (K)
S19-Sublim First Cycle	173	154	18	72
S19-Sublim Second Cycle	180	155	25	65
Literature Fe[HB(3,5-(CH$_3$)$_2$pz)$_3$]$_2$	204	173	31	55

5.2.3.3.   Fe[HB(pz)$_3$][HB(3,5-(CH$_3$)$_2$-pz)]

The heteroleptic compound Fe[HB(pz)$_3$][HB(3,5-(CH$_3$)$_2$-pz)] (**S20**) has not previously been reported in literature. It was investigated as part of the screening process to identify whether mechanochemistry can be used as a synthetic route to compound not currently reported for solution-state synthetic methods. Mechanochemical synthesis yielded a reddish powder which was purified by sublimation (**S20-Sublim**). As previously discussed, purification was done on this complex as an additional step to improve PXRD analysis. In accordance with the screening procedure, PXRD analysis was done, as shown in Figure 5.24. The PXRD pattern for **S20-Sublim** does not solely match the patterns for either Fe[HB(pz)$_3$]$_2$ or Fe[HB(3,5-(CH$_3$)$_2$pz)$_3$]$_2$, therefore further interpretation should be undertaken.
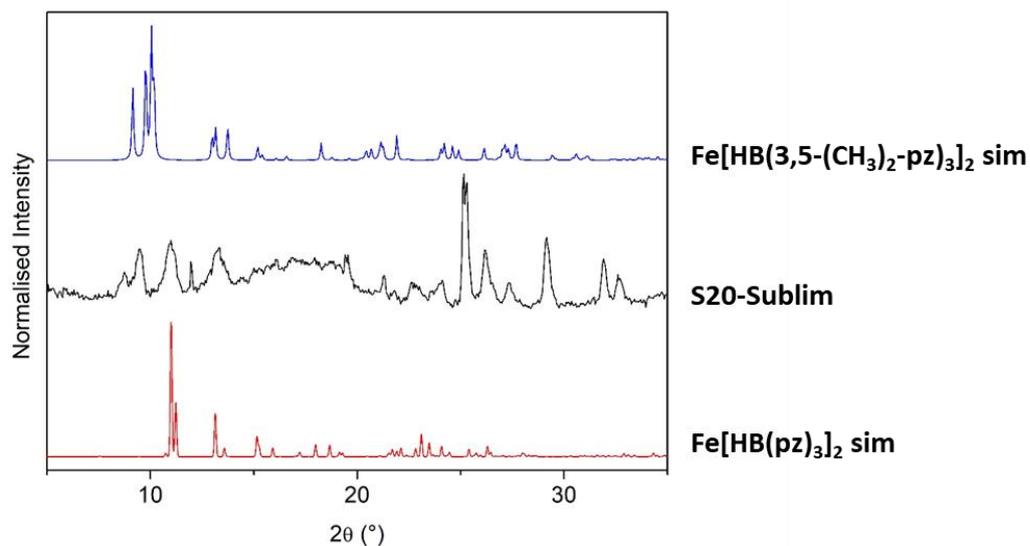
Figure 5.24: Comparison of normalised PXRD data for Top: Fe[HB(3,5-(CH$_3$)$_2$-pz)$_3$]$_2$ complex, simulated from SC-XRD data (CSD Code: HMPBFE),[63] Middle: **S20-Sublim** and Bottom: Fe[HB(pz)$_3$]$_2$ complex, simulated from SC-XRD data (CSD Code: HPZBFE).[63]

In accordance with the screening procedure, the thermochromic response was investigated by heating the reddish powder using a heat gun. In response to heating, the powder underwent a thermochromic response changing into a brownish powder, as shown in Figure 5.25. Further investigation was carried out to confirm SCO-activity in **S20-Sublim**.
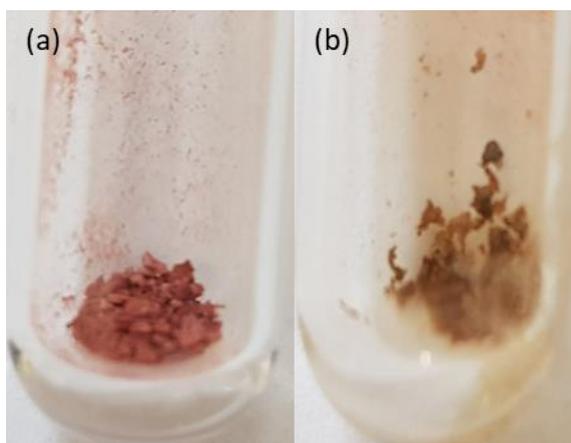
Figure 5.25: Visible thermochromism for **S20-Sublim**. (a) RT and (b) Heated.

Confirmation of the presence of SCO-activity was done by variable temperature SQUID magnetometry, as shown in Figure 5.26. The attempted synthesise of a heteroleptic complex yielded a SCO-active product which contained two distinct transitions. The first step displays SCO with $T_{1/2}\uparrow$ = 160 K, $T_{1/2}\downarrow$ = 159 K and 'smoothness' = 65 K, consistent with literature reports on the complex $Fe[HB(3,5-(CH_3)_2pz)_3]_2$.[44] The second step begins to occur at 350 K with $T_{1/2}\uparrow$ and $T_{1/2}\downarrow$ above 400 K, which is consistent with literature reports on $Fe[HB(pz)_3]_2$.[42] The screening procedure was successfully able to identify the presence of SCO-activity in **S20-Sublim**, with the presence of two distinct transitions, consistent with a mixture of the two reported homoleptic SCO-active materials. Comparison of the SCO properties with literature reports are shown in Table 5.5.
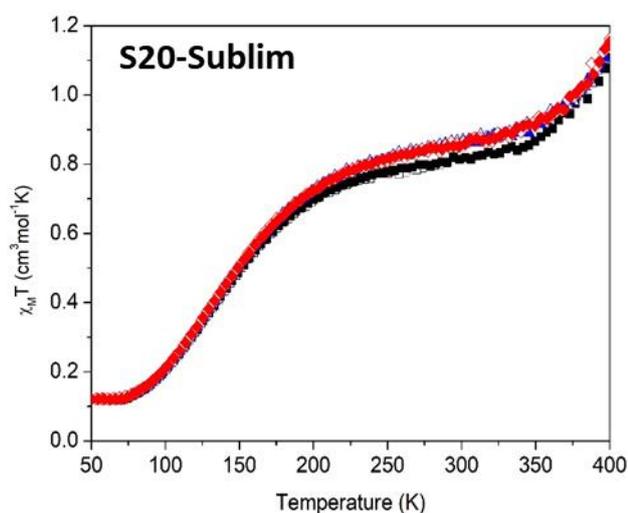
Figure 5.26: Temperature dependent SQUID data for **S20-Sublim** three cycles: Cycle 1 Heating ■ and Cooling □, Cycle 2 Heating ▲ and Cooling △, Cycle 3 Heating ◆ and Cooling ◊.

	T$_{1/2}$↑ (K)	T$_{1/2}$↓ (K)	ΔT (K)	'Smoothness' (K)
S20-Sublim First Step	160	159	1	65
S20-Sublim Second Step	< 400	< 400	-	-
Literature Fe[HB(pz)$_3$]$_2$ First Cycle	405	-	-	24
Literature Fe[HB(3,5-(CH$_3$)$_2$pz)$_3$]$_2$	204	173	31	55

5.2.3.4.   2,6-di(pyrazole-3-yl)pyridine and Derivatives

Fe^{2+} complexes of the **3-bpp** family, introduced in 5.1.2, usually undergo a characteristic SCO transition from yellow in the HS state to red in the LS state.[14] Here, this characteristic colour change was applied as the thermochromic branch of Figure 5.17. Complexes of **3-bpp** and three derivatives were screened using four different Fe(II) salts. The complexes screened included the ligands **3-bpp**, **3-bpp-PhOH**, **3-bpp-PhOCH₃** and **3-bpp-Napth** with Fe(BF$_4$)$_2$.6H$_2$O, FeCl$_2$.4H$_2$O, (NH$_4$)$_2$Fe(SO$_4$)$_2$.6H$_2$O and Fe(C$_2$O$_4$)$_2$.3H$_2$O. Each Fe(II) salt was used due to their relatively high stability under atmospheric conditions, low cost and wide availability from chemical suppliers, all factors which are important for commercial applications. Additionally, various solvates of complexes with BF$_4$$^-$ had previously been reported, making it an ideal candidate for discovery of novel SCO-active products.[14]

Stoichiometric ratios of the ligands and Fe(II) salts were ground in a pestle and mortar for 5 minutes. The resulting powders were collected, and one portion was heated using a heat gun until decomposition or a colour change and a second portion was cooled in liquid nitrogen. In the event of a colour change in either portion, further analysis was carried out by SQUID magnetometry. In accordance with the proposed screening procedure, if no thermochromism was observed, then no further analysis was carried out.

5.2.3.4.1.   [Fe(3-bpp)$_2$](BF$_4$)$_2$

Grinding **3-bpp** with Fe(BF$_4$)$_2$.H$_2$O yielded an orange powder. After allowing the sample to dry in air, a fine yellow powder was obtained (**S21-BF$_4$**). PXRD was used to characterise the reaction product of **S21-BF$_4$**, as shown in Figure 5.27. The collected pattern for **S21-BF$_4$** was consistent with previous literature reports for the complex [Fe(3-bpp)$_2$](BF$_4$)$_2$.[17] Comparison with a simulated pattern of **3-bpp** (CSD Code: QETVEQ01)[64] confirms the absence of a significant quantity of unreacted **3-bpp**.

Figure 5.27: Comparison of normalised PXRD data for Top: 3bpp ligand, simulated from SC-XRD data (CSD Code: QETVEQ01)[64] Middle: Sample **S21-BF$_4$** and Bottom: [Fe(3-bpp)$_2$](BF$_4$)$_2$ digitised from literature.[17]

Sample **S21-BF$_4$** was previously reported in literature,[17] with significant solvents effects. In fact, Halcrow *et al.*[18] observed significant stabilisation of the low-spin state (red) with different degrees of hydration. On cooling in liquid nitrogen, **S21-BF$_4$** underwent a yellow → orange colour change, characteristic of a SCO-transition for this family, as shown in Figure 5.28. Due to the presence of thermochromism, SQUID magnetometry was used to confirm SCO activity.
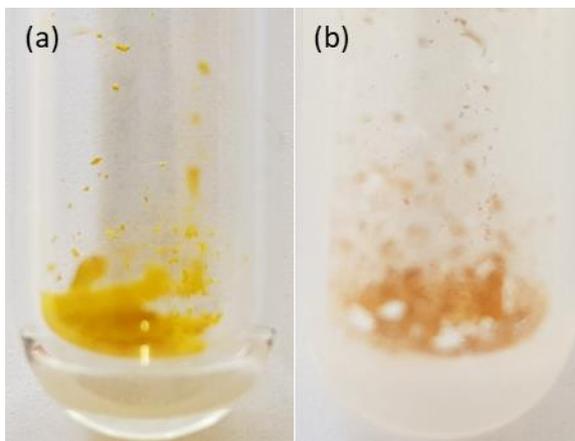
Figure 5.28: Thermochromic response for **S21-BF₄**. (a) Room temperature. (b) Cooled in liquid nitrogen.

The SCO behaviour of **S21-BF₄** was confirmed by temperature dependent SQUID magnetometry, as shown in Figure 5.29(a). **S21-BF₄** underwent SCO with $T_{1/2}\uparrow$ = 164 K, $T_{1/2}\downarrow$ = 153 K, ΔT = 11 K and a relatively gradual transition with 'smoothness' = 37 K. Previous literature reports on the complex [Fe(3-bpp)₂](BF₄)₂ has shown similar SCO behaviour with $T_{1/2}\uparrow$ = 185 K, $T_{1/2}\downarrow$ = 174 K, ΔT = 11 K and a comparably more abrupt transition with 'smoothness' = 15 K, as shown in Figure 5.29(b).[17] The effects of hydration were also described by Goodwin *et al*. with a partial transition observed with $T_{1/2}\uparrow$ = 287 K. The decrease in $T_{1/2}\uparrow$, $T_{1/2}\downarrow$ and 'Smoothness' observed for **S21-BF₄** are consistent with the effects of grinding and crystalline quality, further discussion on the effects of grinding is in 3.2.6. The developed screening procedure was successful in identifying a known SCO-active compound within the **3-bpp** family. PXRD analysis was able to confirm the formation of a product which was compared with previous literature reports, whilst the SCO properties were first identified by thermochromic response and confirmed by SQUID magnetometry, comparison of SCO properties with literature are shown in Table 5.6.
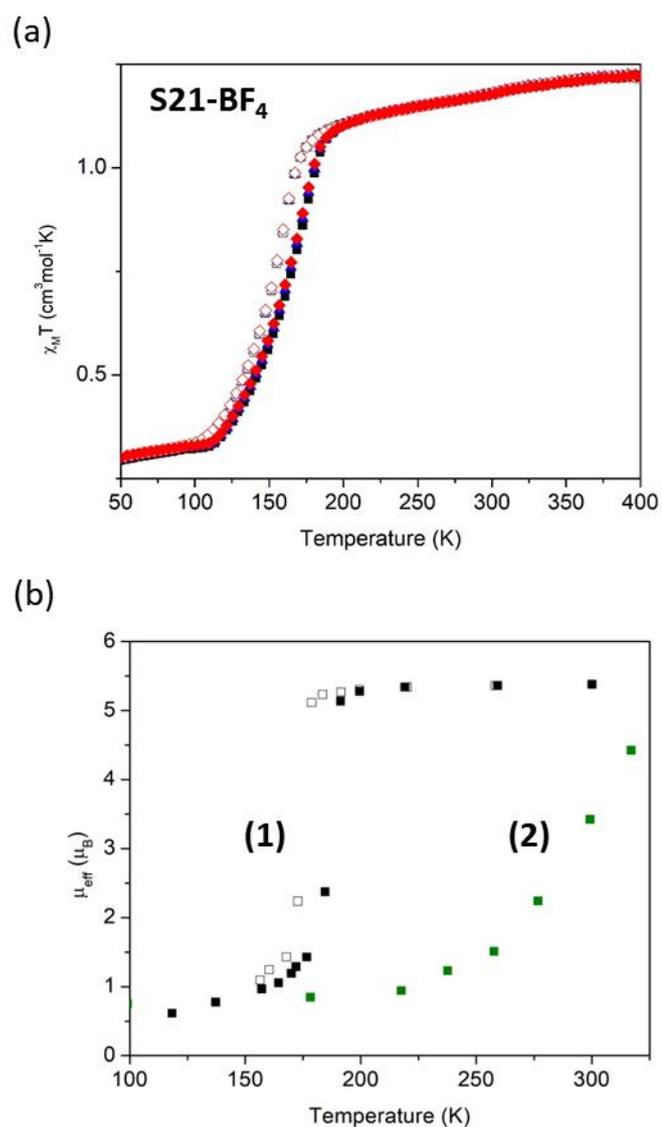
Figure 5.29: Temperature dependent SQUID data **(a)** [Fe(3bpp)$_2$](BF$_4$)$_2$, **S21-BF$_4$**, three cycles: Cycle 1 Heating ■ and Cooling □, Cycle 2 Heating ▲ and Cooling △, Cycle 3 Heating ▼ and cooling ▽. **(b)** Digitised literature plots **1**: [Fe(3bpp)$_2$](BF$_4$)$_2$ and 2: [Fe(3bpp)$_2$](BF$_4$)$_2$.2H$_2$O.[17]

Table 5.6: Comparison of SCO properties for **S21-BF$_4$** with literature reports of [Fe(3-bpp)$_2$](BF$_4$)$_2$.xH$_2$O (x = 0 and 2).[17]

	T$_{1/2}$↑ (K)	T$_{1/2}$↓ (K)	ΔT (K)	'smoothness' (K)
Sample **S21-BF$_4$**	164	153	11	37
Lit. [Fe(3-bpp)$_2$](BF$_4$)$_2$	185	174	11	15
Lit. [Fe(3-bpp)$_2$](BF$_4$)$_2$.2H$_2$O	287	-	-	-

Screening with FeCl$_2$.4H$_2$O, (NH$_4$)$_2$Fe(SO$_4$)$_2$.6H$_2$O and FeC$_2$O$_4$.2H$_2$O did not yield products which displayed thermochromism on either heating or cooling. The FeCl$_2$.4H$_2$O product (**S21-Cl**) was an off-white powder which partially oxidised to a brown powder when left in air. Similarly, both the (NH$_4$)$_2$Fe(SO$_4$)$_2$.6H$_2$O and FeC$_2$O$_4$.2H$_2$O products (**S21-SO$_4$** and **S21-C$_2$O$_4$** respectively) were off-white products and no change in appearance was observed when left exposed to air. In accordance with the proposed screening procedure, the absence of visible thermochromism on both heating and cooling, meant no further analysis of these products was carried out. The effects of heating and cooling all products made with **3-bpp** are described in Table 5.7.

Table 5.7: Test of thermochromism for **3-bpp; S21-BF$_4$**, **S21-Cl**, **S21-SO$_4$** and **S21-C$_2$O$_4$**.

	Original Appearance	Colour on Heating	Colour on Cooling
S21-BF$_4$	Yellow powder	No Change	Orange Powder
S21-Cl	Off-white powder. Turned slightly brown in air.	No Change	No Change
S21-SO$_4$	Off-white powder	No Change	No Change
S21-C$_2$O$_4$	Off-white powder	No Change	No Change

5.2.3.4.2.   [Fe(3-bpp-PhOH)$_2$]A$_x$

Similar to complexes formed with **3-bpp**, the ligand **3-bpp-PhOH** also forms complexes which undergo yellow (HS) → red (LS) thermochromism. As discussed in 5.1.2, the 3-bpp family have significant solvent sensitivity with multiple solvatomorphs exhibiting different SCO properties. **3pp-PhOH**, is no exception, with at least five solvatomorphs reported with the ClO$_4^-$ anion, investigation of the perchlorate anion cannot be routinely carried out using mechanochemistry due to the explosive risk. **3-bpp-PhOH** was screened with four iron(II) salts by mechanochemistry, and the resulting products were investigated using the protocol described in Figure 5.17.

Mechanically reacting **3-bpp-PhOH** with Fe(BF$_4$)$_2$.6H$_2$O, FeCl$_2$.4H$_2$O, (NH$_4$)$_2$Fe(SO$_4$)$_2$.6H$_2$O and FeC$_2$O$_4$.2H$_2$O yielded **S22-BF$_4$**, **S22-Cl**, **S22-SO$_4$** and **S22-C$_2$O$_4$** respectively. All four reactions initially yielded white powders but none of the products displayed thermochromic behaviour on either heating or cooling, as shown in Table 5.8. As observed with **S22-Cl**, the reaction product with

FeCl$_2$.4H$_2$O appeared to partially turn brown when left in air, which was attributed to partial oxidation. The proposed products of this reaction were not previously reported in literature. Due to the absence of thermochromism, no further analysis was carried out.

Table 5.8: Test of thermochromism for **3-bpp-PhOH; S22-BF$_4$, S22-Cl, S22-SO$_4$** and **S22-C$_2$O$_4$**.

	Original Appearance	**Colour on Heating**	**Colour on Cooling**
S22-BF$_4$	Off-white powder	No Change	No Change
S22-Cl	Off-white powder. Turned slightly brown in air.	No Change	No Change
S22-SO$_4$	Off-white powder	No Change	No Change
S22-C$_2$O$_4$	Off-white powder	No Change	No Change

5.2.3.4.3. [Fe(3-bpp-PhOCH$_3$)$_2$]A$_x$

Fe(II) complexes with the **3-bpp-PhOCH$_3$** ligand has previously been reported to display SCO activity with three different anions (ClO$_4$$^-$, CF$_3SO_3$$^-$ and BF$_4$$^-$).[65] The complexes reported with ClO$_4$$^-$ and BF$_4$$^-$ contain solvents and solvent-free forms were not described.[14] As previously discussed, the solvent effects on SCO activity are significant within the **3-bpp** family. Neither the solvent-free nor hydrated products of the anions screened have been previously been reported in literature. Screening carried out below explores the potential products without the addition of solvents, potential hydrates can occur due to the use of hydrated Fe^{2+} salts. Although anhydrous Fe^{2+} salts could be used, the use of anhydrous salt is non-trivial and would require special consideration which would drastically slow the screening process at this stage.

5.2.3.4.3.1. Samples S23-BF$_4$, S23-Cl, S23-SO$_4$ and S23-C$_2$O$_4$

The reactions between **3-bpp-PhOCH$_3$** and the four Fe^{2+} salts: Fe(BF$_4$)$_2$.6H$_2$O, FeCl$_2$.4H$_2$O, (NH$_4$)$_2$Fe(SO$_4$)$_2$.6H$_2$O and FeC$_2$O$_4$.2H$_2$O yielded **S22-BF$_4$, S22-Cl, S22-SO$_4$** and **S22-C$_2$O$_4$** respectively. In all four instances an off-white powder was obtained. Neither heating nor cooling caused a change in appearance for all four products, as shown in Table 5.9. In accordance with the screening procedure, without the presence of thermochromism, no further analysis was carried out.

Table 5.9: Test of thermochromism for **3-bpp-PhOCH$_3$; S23-BF$_4$**, **S23-Cl**, **S23-SO$_4$** and **S23-C$_2$O$_4$**.

	Original Appearance	Colour on Heating	Colour on Cooling
S23-BF$_4$	Off-white powder	No Change	No Change
S23-Cl	Off-white powder. Turned slightly brown in air.	No Change	No Change
S23-SO$_4$	Off-white powder	No Change	No Change
S23-C$_2$O$_4$	Off-white powder	No Change	No Change

5.2.3.4.4. [Fe(3-bpp-Napth)$_2$]A$_x$

Complexes of **3-bpp-Napth** were previously reported by Barrios *et al.*[66] with SO$_3$CF$_3^-$, ClO$_4^-$ and

BF$_4^-$ as the anions. In all instances the SCO-active complexes contained either acetone and water

or THF as solvent molecules. The complexes prepared with **3-bpp-Napth** were shown to crystallise

with the two equivalents of **3-bpp-Napth** in different conformations, as shown in Figure 5.30,

leading to an unusual crystal packing. Solvent-free complexes with the anions BF$_4^-$, Cl$^-$, SO$_4^{2-}$ and

C$_2$O$_4^-$ had not previously been reported in literature.

syn,syn

syn,anti

anti,anti
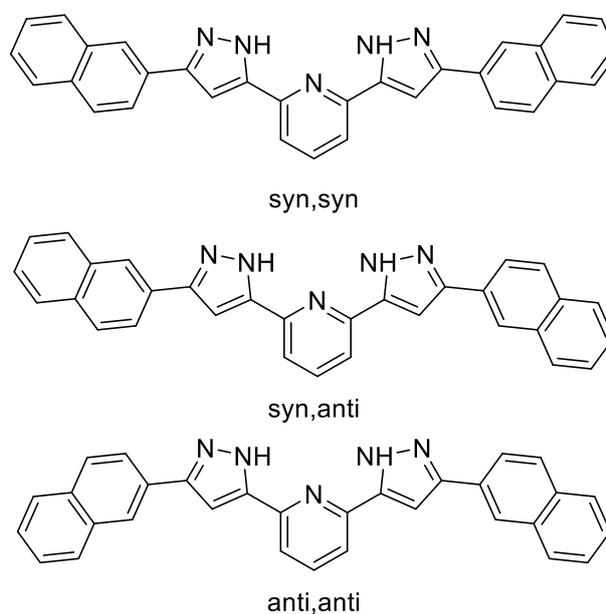
Figure 5.30: Conformations of the **3-bpp-Napth** ligand, as described by Barrios *et al.*[66]

5.2.3.4.4.1. Samples S24-BF₄, S24-Cl, S24-SO₄ and S24-C₂O₄

The reactions between **3-bpp-Napth** and the four Fe^{2+} salts: $Fe(BF_4)_2.6H_2O$, $FeCl_2.4H_2O$, $(NH_4)_2Fe(SO_4)_2.6H_2O$ and $FeC_2O_4.2H_2O$ yielded **S24-BF₄**, **S24-Cl**, **S24-SO₄** and **S24-C₂O₄** respectively. All four reactions yielded off-white powders which did not display thermochromism on either heating or cooling, as shown in Table 5.10. Due to the absence of thermochromism, no further analysis was undertaken.

Table 5.10: Test of thermochromism for **3-bpp-Napth; S24-BF₄**, **S24-Cl**, **S24-SO₄** and **S24-C₂O₄**.

	Original Appearance	Colour on Heating	Colour on Cooling
S24-BF₄	Off-white powder	No Change	No Change
S24-Cl	Off-white powder. Turned slightly brown in air.	No Change	No Change
S24-SO₄	Off-white powder	No Change	No Change
S24-C₂O₄	Off-white powder	No Change	No Change

5.2.3.4.5. Mixed Ligands

Here, a range of heteroleptic complexes prepared using the ligands **3-bpp**, **3-bpp-PhOH**, **3-bpp-PhOCH₃** and **3-bpp-Napth** were screened *vide supra*. To focus the screening process, only the $Fe(BF_4)_2.6H_2O$ salt was used. The BF_4 salt was chosen due to the various solvates of the BF_4 complexes representing a significant quantity of SCO-active complexes in the **3-bpp** family.[14,18,65,67–69] A potential explanation for the large number of SCO-active complexes in the **3-bpp** family including the BF_4 anion was proposed by Halcrow.[70] Halcrow compared the crystal structures of $[Fe(3-bpp)_2](BF_4)_2$, which display SCO, and $[Fe(3-bpp)_2](PF_6)_2$, which stays in HS state at all temperatures. This highlighted an unusual C_2-distorted, twisted structure in the PF_6 analogue, which Halcrow suggested stabilised the HS state. Similarly, the ClO_4 and SbF_6 analogues are isostructural with $[Fe(3-bpp)_2](PF_6)_2$ and also remain in the HS state across all temperatures.[71]

Heteroleptic complexes prepared with **3-bpp**, **3-bpp-PhOH**, **3-bpp-PhOCH₃** and **3-bpp-Napth** were screened with $Fe(BF_4)_2.6H_2O$, according to the screening procedure described in Figure 5.17. None of the proposed reaction products had previously been reported in literature. The ligand combinations and their assigned names are shown in Table 5.11.

Table 5.11: Sample names for heteroleptic screening of ligands.

Sample Name	Proposed Formula	Ligand One	Ligand Two
Sample **25**	[Fe(3-bpp)(3-bpp-PhOH)](BF$_4$)$_2$	3-bpp	3-bpp-PhOH
Sample **26**	[Fe(3-bpp)(3-bpp-PhOCH$_3$)](BF$_4$)$_2$	3-bpp	3-bpp-PhOCH$_3$
Sample **27**	[Fe(3-bpp)(3-bpp-Napth)](BF$_4$)$_2$	3-bpp	3-bpp-Napth
Sample **28**	[Fe(3-bpp-PhOH)(3-bpp-PhOCH$_3$)](BF$_4$)$_2$	3-bpp-PhOH	3-bpp-PhOCH$_3$
Sample **29**	[Fe(3-bpp-PhOH)(3-bpp-Napth)](BF$_4$)$_2$	3-bpp-PhOH	3-bpp-Napth
Sample **30**	[Fe(3-bpp-PhOCH$_3$)(3-bpp-Napth)](BF$_4$)$_2$	3-bpp-PhOCH$_3$	3-bpp-Napth

5.2.3.4.5.1. Heteroleptic Sample Screening

In all instances of mixed ligand screening with Fe(BF$_4$)$_2$.6H$_2$O, an off-white powder was obtained. On heating, all samples remained off-white until decomposition occurred. On cooling, no thermochromism was observed. This indicated an absence of SCO in these samples. As a result of the absence of thermochromism, no further analysis of Samples **25-30** was carried out.

5.2.3.4.6. Summary

A wide range of complexes, both homoleptic and heteroleptic, were screened. Although, no new SCO-active complexes were identified, all previously reported complexes were successfully identified. If this screening was done using traditional methods, then the time requirements would have been a lot more substantial. It is also worth noting than further screening could be carried out using LAG, other ligands and anions and screening of this family is not yet exhausted.

5.2.3.5. Bipy and Derivatives

Screening of 2,2'-bipyridine (bipy) and 2,2'-bipyridine derivatives was undertaken to prepare both homoleptic and heterolytic complexes with Fe(II) and the counter anion thiocyanate. As with 1,10-phenanthroline and derivates, the bipy family is strongly coloured due to charge transfer bands and visible thermochromism due to SCO is absent.

5.2.3.5.1. 2,2'-bipyridine

The complex Fe(bipy)$_2$(NCS)$_2$ is expected to display SCO-activity.[72] However, reported synthetic routes require the synthesis of the complex [Fe(bipy)$_3$](SCN)$_2$ which does not display SCO-activity in the solid state. Mechanochemical screening of 2,2'-bipyridine yielded **S12-As**.

Comparison of PXRD data patterns for **S12-As**, $Fe(BF_4)_2.6H_2O$ with simulated patterns of bipy (CSD Code: BIPYRL)[73] and KSCN (ICSD-16073)[74], as shown in Figure 5.31, showed the product of mechanochemical synthesis was significantly different to the reagents and a reaction had occurred.
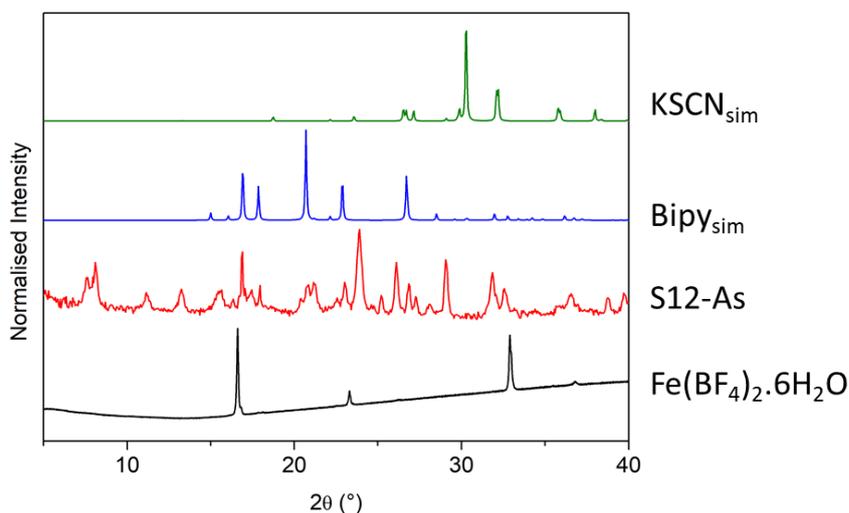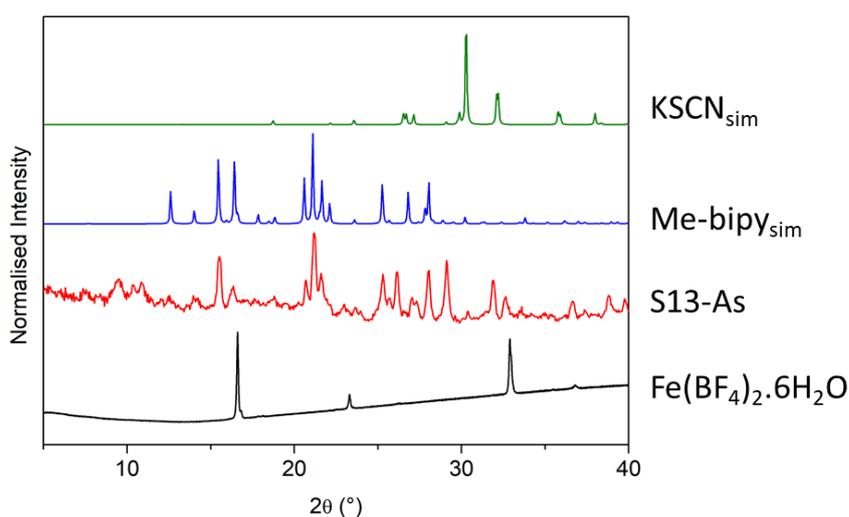

Figure 5.31: Comparison of normalised PXRD data for Top to bottom: KSCN, simulated from literature (ICSD-36073),[74] 2,2'-bipyridine (CSD Code: BIPYRL),[73] **S12-As** and $Fe(BF_4)_2.6H_2O$.

In accordance with the screening procedure, VT-Raman spectroscopy was used to investigate the presence of SCO-activity. Spectra were collected at 298 K and 123 K, as shown in Figure 5.32. There were no significant differences in the spectra, therefore no SCO-activity was identified, and no further investigation of the complex was undertaken. The bipy ligand was expected to produce a SCO-active complex due to previous literature reports. However, as observed with sample **S9-1pot**, mechanochemical synthesis did not directly yield a SCO-active product. Further processing of the product would be required which is beyond the scope of this current research.
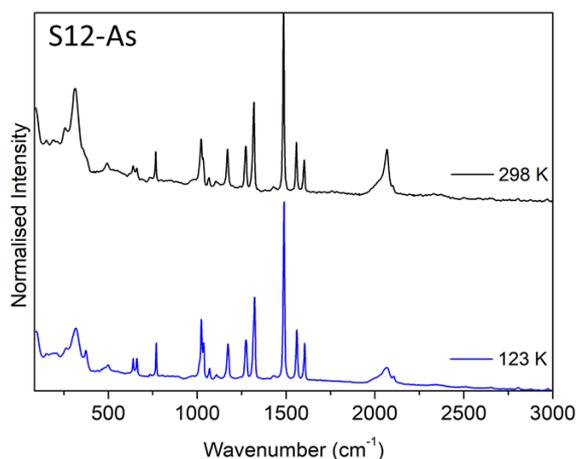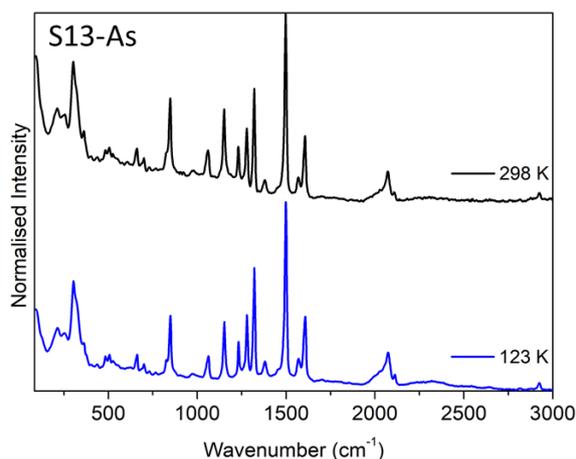
Figure 5.32: Raman spectra at 298 K (top) and 123 K (bottom) for **S12-As.**

5.2.3.5.2.   5,5'-dimethyl-2,2'-bypridine

Mechanochemical screening with 5,5'-dimethyl-2,2'-bipyridine (Me-bipy) yielded **S13-As**. The complex Fe(Me-bipy)$_2$(NCS)$_2$ has not previously been reported in literature. PXRD analysis of **S13-As** showed the resulting pattern was more than just a combination of the reagents, comparison of PXRD data patterns for **S13-As.** Fe(BF$_4$)$_2$.6H$_2$O with simulated patterns of Me-bipy (CSD Code: POWQAU)[75] and KSCN (ICSD-16073)[74]. Therefore, mechanochemical synthesis indicated a reaction had occurred, as shown in Figure 5.33.
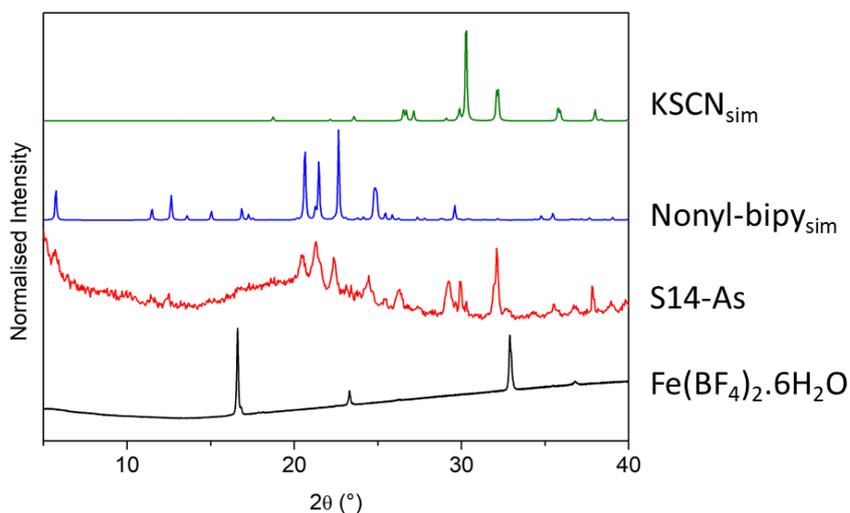

Figure 5.33: Comparison of normalised PXRD data for Top to bottom: KSCN, simulated from literature (ICSD-36073),[74] 5,5'-dimethyl-2,2'-bipyridine (CSD Code: POWQAU),[75] **S13** and Fe(BF$_4$)$_2$.6H$_2$O.

Investigation of SCO-activity in **S13** was undertaken by VT-Raman with spectra measured at 298 K and 123 K, as shown in Figure 5.34. No significant differences between the two different temperatures were identified. Therefore, **S13-As** is likely not SCO-active and no further investigation of the complex was undertaken.

Figure 5.34: Raman spectra at 298 K (top) and 123 K (bottom) for **S13-As**.

5.2.3.5.3.   4,4'-dinonyl-2,2'-bipyridine

Mechanochemical screening with 4,4'-dinonyl-2,2'-bipyridine (nonyl-bipy) yielded **S14-As**. The complex Fe(nonyl-bipy)$_2$(NCS)$_2$ has not been previously reported. Comparison of the pattern collected for **S14-As** with Fe(BF$_4$)$_2$.6H$_2$O with simulated patterns of Nonyl-bipy (CSD Code: FOHFAK)[76] and KSCN (ICSD-16073)[74] shows the presence of peaks not related to any of the starting materials, as shown in Figure 5.35. As such, as a rapid technique to show a reaction has occurred, comparison of the resulting powder with starting materials is a generally suitable method.

Figure 5.35: Comparison of normalised PXRD data for Top to bottom: KSCN, simulated from literature (ICSD-36073),[74] 4,4'-dinonyl-2,2'-bipyridine (CSD Code: FOHFAK),[76] **S14-As** and Fe(BF$_4$)$_2$.6H$_2$O.

Investigation of the presence of SCO-activity was undertaken using VT-Raman spectroscopy, as shown in Figure 5.36. Collection of spectra suitable for comparison was non-trivial due to the presence of fluorescence in **S14-As**, which has previously been observed in other bipyridyl derviatives.[33] Optimisation of the collection process required long data acquisition times which drastically increase the screening time for nonyl-bipy ligands. Suitable spectra for comparison were collected using a different laser setup with modifications on collection and laser exposure durations. The resulting spectra did not exhibit any significant differences, indicating the absence of SCO-activity in the temperature range investigated and no further investigation of **S14-As** was undertaken.
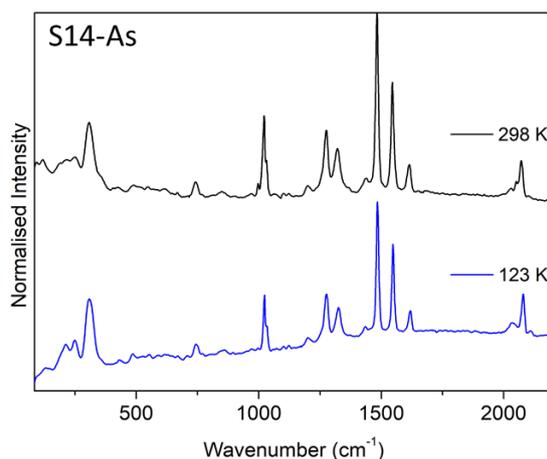
Figure 5.36: Raman spectra at 298 K (top) and 123 K (bottom) for **S14-As**. Collected using modified parameters (532 nm wavelength laser, x50 LWD NIR objectives).

5.2.3.5.4.   Heteroleptic Screening

The screening of heteroleptic complexes prepared with bipy and bipy derivatives was carried out using the procedure described in Figure 5.17. In all prepared samples, VT-Raman did not indicate the presence of SCO-activity and no further analysis was undertaken. PXRD patterns and Raman Spectra collected at 298 K and 123 K are presented in Appendix C. As with **S14-As**, heteroleptic complexes which included the nonyl-bipy ligand displayed fluorescence which significantly hampered the screening procedure and increased the screening time.

5.2.3.6.   Final Assessment

Screening of the ligands $HB(pz)_3^-$ and $HB(3,5-(CH_3)_2-pz)_3^-$ was carried out, yielding materials which display thermochromism on heating and cooling.   The procedure was successful in identifying and confirming SCO-activity in the screening procedure. Including PXRD as an initial screening step was important in confirming a mechanochemical reaction had occurred. The procedure was able to identify SCO-activity in all three mechanochemical attempts but was not able to differentiate a mixture of complexes formed when attempting heteroleptic complex synthesis without SQUID analysis.

Mechanochemical screening of the **3-bpp** ligand and three derivatives (**3-bpp-PhOH**, **3-bpp-PhOCH₃** and **3-bpp-Napth**) was carried out with four Fe(II) salts; Fe(BF₄)₂.6H₂O, FeCl₂.4H₂O, (NH₄)₂Fe(SO₄)₂.6H₂O and Fe(C₂O₄)₂.3H₂O. PXRD of the products was collected and compared with literature reports. The characteristic yellow (HS) → red (LS) thermochromism for the **3-bpp** family was used, allowing the possibility of identifying potential SCO materials in accordance with Figure 5.17. Mechanochemistry allowed for the rapid screening of 22 potential SCO-active materials, of which only one had previously been reported, [Fe(3-bpp)₂](BF₄)₂.[17] Screening of the homoleptic complexes indicated the presence of thermochromism in only one complex [Fe(3-bpp)₂](BF₄)₂ (**S21-BF₄**) which was consistent with previous literature reports. Having identified thermochromism in **S21-BF₄**, confirmation of SCO was made by SQUID magnetometry, confirming the formation of [Fe(3-bpp)₂](BF₄)₂. Similarly, heteroleptic screening was carried out using Fe(BF₄)₂.6H₂O. The BF₄ salt was chosen due to a large number of heteroleptic and homoleptic complexes in the **3-bpp** family containing the BF₄ anions.[14,18,65,68,69] None of the screened heteroleptic products displayed thermochromism so additional analysis was not carried out.

Screening of 2,2'-bipyridine and derivatives was carried out with attempted synthesis of both homoleptic and heteroleptic complexes with the formula Fe(L)₂(NCS)₂ (where L = 2,2'bipyridine, 5,5'-dimethyl-2,2'-bipyrdine and 4,4'-dinonyl-2,2'-bipyridine). The products were strongly coloured and thus thermochromism resulting from SCO-activity would be masked, therefore the non-thermochromic branch of screening was used. The inclusion of PXRD as an initial step was useful for identifying whether a reaction had occurred, by comparing the resulting pattern with the patterns for starting materials. Investigation of the presence of SCO was carried out using VT-Raman, which was not entirely suitable and suffered from difficulties in collection of data, due to problems with fluorescence and difficulties in collection data of sufficient quality for comparison.

Further development of the procedure was required for both the thermochromic and non-thermochromic branches of the screening procedure. For the thermochromic branch, the subtle colour change of some families such as the **3-bpp** family increased the possibility of false-negative results and more precise methods or recording thermochromism would drastically reduce the

possibility of false negative responses. In a similar direction, for investigation of heteroleptic complexes, the possibility of synthesising mixtures of products limits the possibility of using visible thermochromism for identification of novel materials from mixtures of known products, as observed for attempted mixed ligand synthesis in $HB(pz)_3^-$ and $HB(3,5-(CH_3)_2-pz)_3^-$. To address both issues, the use of a reflectivity setup could increase the accuracy of observations sufficiently for step-transitions to be observed, this could reduce the number of samples for SQUID analysis and speed up the screening procedure. The use of liquid nitrogen reduces the screening costs, compared to SQUID analysis.
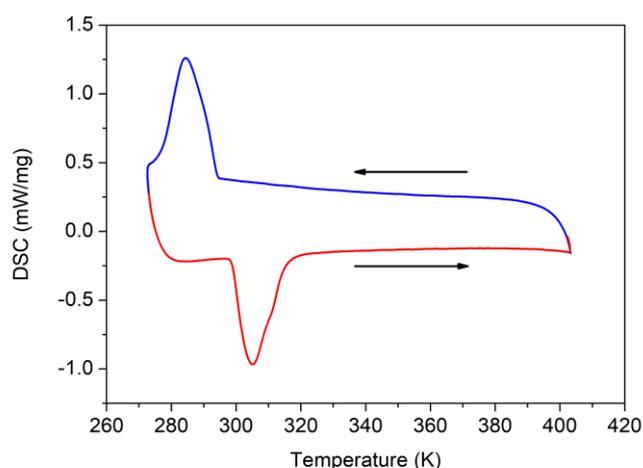
Figure 5.37: Plot of DSC data for **S6** with direction of heating (Red) and cooling (Blue) denoted by arrows.

To improve the non-thermochromic branch, the application of a calorimetric technique such as DSC analysis would overcome problems with fluorescence and sample impurities/inhomogeneity with the sample addressed as a whole. This would assist in reducing the possibility of false responses. The application of DSC analysis was preliminary tested using the compound $[Fe(atrz)_3]Cl_2$, as shown in Figure 5.37. It is clear than the presence of SCO activity in the compound is consistent with discussion of complex **S6** in Figure 5.11, with clear peaks indicated a SCO transition occurring. The temperature of transition is different to SQUID reports, due to the increased ramping rate used. However, for identification of the presence of SCO, confirming the presence of SCO is the main objective and the true transition temperature and full

SCO properties can be determined using additional methods. The optimised screening procedure
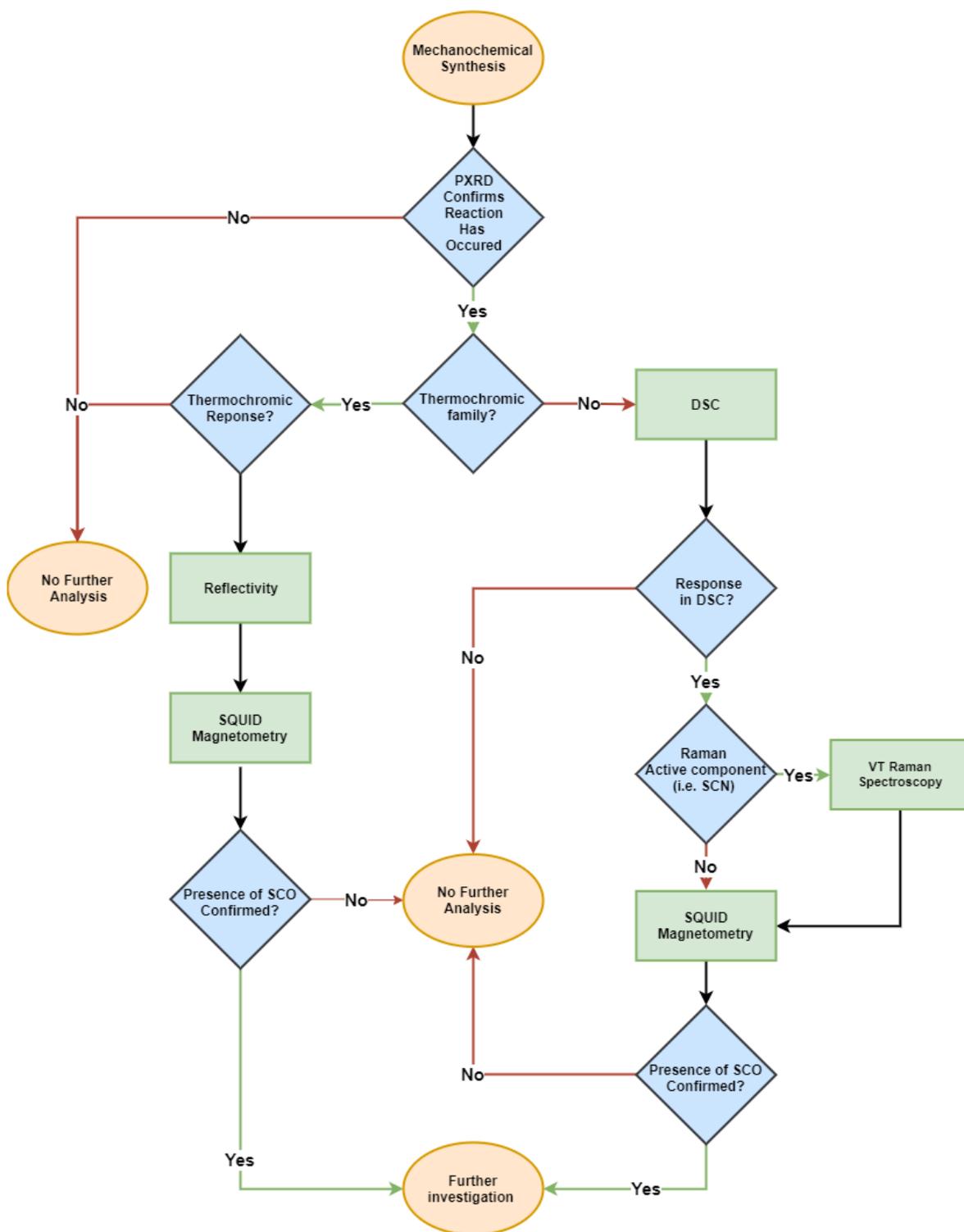including all of these points is presented in Figure 5.38.

Figure 5.38: Final optimised screening procedure for both thermochromic and non-thermochromic screening.
Optimised to reduced operation costs and provide the most analytical data about the screened materials within the
shortest amount of time.

5.3. Conclusions and Prospects

A screening procedure was proposed and developed for rapid identification of novel SCO-active materials. Development of the procedure using a range of different SCO-active families allowed for optimisation of the process, reducing screening times and costs whilst still providing sufficient information for the identification of SCO-activity. The families investigated included both thermochromic compounds, such as the 4-R-1,2,4-triazoles and **3-bpp** derivatives, and non-thermochromic compound, such as 1,10-phenanthroline derivatives and 2,2-bipyridine derivatives. Attempted screening of all previously reported SCO-active materials was successful, with the procedure able to identify SCO-activity. This validates the efficacy of the procedure.

The procedure itself is not perfect with the possibility of false responses. However, development of the procedure to include additional steps such as reflectivity measurements in thermochromic materials and DSC for non-thermochromic materials would serve to reduce the possibility of false-negative responses whilst still maintaining a relatively rapid screening time, compared to using SQUID magnetometry, although modern SQUID magnetometers can reduce measurement duration significantly. The aim of the proposed procedure is not to identify and fully characterise a novel material in one step. The procedure serves to reduce the screening time for the identification of interesting materials with re-synthesis and further analysis undertaken after identification of SCO-activity. Coupling the rapidity of mechanochemical synthesis with the proposed screening procedure could drastically reduce the arduous process of identification of promising SCO-materials. The success of identification of previously reported SCO-active materials serves to highlight the saved time using the procedure is worth the potential risk of false-negative responses.

Further research into screening potential SCO-active materials using this procedure could potentially drastically increase the number of SCO-active materials known by both screening of novel ligands and the possibility of novel solvatomorphs using LAG. The screening procedure highlighted the significant solvent effects in the **3-bpp** family.[65,77] The procedure in the current form represents an optimised approach for rapid mechanochemical screening of a range of

families of SCO-active materials showing great promise for application as a standardised screening procedure, which can identify known and novel complexes that display SCO-activity. The possibility of introducing different solvents to the synthesis of materials *via* LAG significantly expands the scope of potential SCO solvatomorphs. The application of LAG could introduce solvents to the complexes whilst bypassing the effects of insolubility.

5.4. References

1 E. König, G. Ritter and S. K. Kulshreshtha, *Chem. Rev.*, 1985, **85**, 219–234.

2 O. Roubeau, J. G. Haasnoot, E. Codjovi, F. Varret and J. Reedijk, *Chem. Mater.*, 2002, **14**, 2559–2566.

3 O. Roubeau, *Chem. - A Eur. J.*, 2012, **18**, 15230–15244.

4 J. R. Galán Mascarós, G. Aromí and M. Darawsheh, *Comptes Rendus Chim.*, 2018, **21**, 1209–1229.

5 J. Tao, R.-J. Wei, R.-B. Huang and L.-S. Zheng, *Chem. Soc. Rev.*, 2012, **41**, 703–737.

6 G. S. Matouzenko, A. Bousseksou, S. Lecocq, P. J. Van Koningsbruggen, M. Perrin, O. Kahn and A. Collet, *Inorg. Chem.*, 1997, **36**, 5869–5879.

7 C. F. Sheu, S. M. Chen, S. C. Wang, G. H. Lee, Y. H. Liu and Y. Wang, *Chem. Commun.*, 2009, **2**, 7512–7514.

8 R. Pritchard, H. Lazar, S. A. Barrett, C. A. Kilner, S. Asthana, C. Carbonera, J. F. Létard and M. A. Halcrow, *J. Chem. Soc. Dalt. Trans.*, 2009, 6656–6666.

9 E. Tailleur, M. Marchivie, P. Negrier, D. Denux, S. Massip, D. Mondieig, G. Chastanet and P. Guionneau, *CrystEngComm*, 2019, **21**, 6246–6251.

10 J. Nelson, S. M. Nelson and W. D. Perry, *J. Chem. Soc., Dalt. Trans.*, 1976, 1282–1289.

11 G. Bradley, V. McKee, S. M. Nelson and J. Nelson, *J. Chem. Soc., Dalt. Trans.*, 1978, 522–526.

12 E. W. Müller, H. Spiering and P. Gütlich, *J. Chem. Phys.*, 1983, **79**, 1439–1443.

13 A. Galet, A. Bele, M. C. Mun, G. Levchenko, U. De Vale and U. Polite, *Inorg. Chem.*, 2006, **45**, 9670–9679.

14 G. A. Craig, O. Roubeau and G. Aromí, *Coord. Chem. Rev.*, 2014, **269**, 13–31.

15 J. Olguín and S. Brooker, *Coord. Chem. Rev.*, 2011, **255**, 203–240.

16 M. A. Halcrow, *New J. Chem.*, 2014, **38**, 1868–1882.

17 K. H. Sugiyarto and H. A. Goodwin, *Aust. J. Chem.*, 1988, **41**, 1645–1663.

18 S. A. Barrett, C. A. Kilner and M. A. Halcrow, *Dalt. Trans.*, 2011, **40**, 12021.

19 R. Fallahpour, M. Neuburger and M. Zehnder, *New J. Chem.*, 1999, **23**, 53–61.

20 U. S. Schubert, H. Hofmeier and G. R. Newkome, *Modern Terpyridine Chemistry*, 2006.

21 I. M. Henderson and R. C. Hayward, *J. Mater. Chem.*, 2012, **22**, 21366–21369.

22 J. McMurtrie and I. Dance, *CrystEngComm*, 2005, **7**, 230–236.

23 H. A. Goodwin, *Spin Crossover Transit. Met. Compd. I*, 2004, **233**, 59–90.

24 J. S. Costa, S. Rodríguez-Jiménez, G. A. Craig, B. Barth, C. M. Beavers, S. J. Teat and G.

Aromí, *J. Am. Chem. Soc.*, 2014, **136**, 3869–3874.

25   L. A. Barrios, C. Bartual-Murgui, E. Peyrecave-Lleixà, B. Le Guennic, S. J. Teat, O. Roubeau and G. Aromí, *Inorg. Chem.*, 2016, **55**, 4110–4116.

26   W. A. Baker and H. M. Bobonich, *Inorg. Chem.*, 1964, **3**, 1184–1188.

27   E. König, K. Madeja and K. J. Watson, *J. Am. Chem. Soc.*, 1968, **90**, 1146–1153.

28   E. König and K. J. Watson, *Chem. Phys. Lett.*, 1970, **6**, 457–459.

29   C. De Graaf and C. Sousa, *Chem. - A Eur. J.*, 2010, **16**, 4550–4556.

30   A. T. Casey, *Aust. J. Chem.*, 1968, **21**, 2291–2292.

31   L. M. Toma, R. Lescouëzec, L. D. Toma, F. Lloret, M. Julve, J. Vaissermann and M. Andruh, *J. Chem. Soc., Dalt. Trans.*, 2002, **2**, 3171–3176.

32   K. Yoshida, D. Akahoshi, T. Kawasaki, T. Saito and T. Kitazawa, *Polyhedron*, 2013, **66**, 252–256.

33   C. Kaes, A. Katz and M. W. Hosseini, *Chem. Rev.*, 2000, **100**, 3553–3590.

34   S. Xue, Y. Guo, A. Rotaru, H. Müller-Bunz, G. G. Morgan, E. Trzop, E. Collet, J. Oláh and Y. Garcia, *Inorg. Chem.*, 2018, **57**, 9880–9891.

35   S. Trofimenko, *J. Am. Chem. Soc.*, 1967, **89**, 3165–3170.

36   J. P. Jesson, S. Trofimenko and D. R. Eaton, *J. Am. Chem. Soc.*, 1967, **89**, 3148–3158.

37   J. P. Jesson, S. Trofimenko and D. R. Eaton, *J. Am. Chem. Soc.*, 1967, **89**, 3158–3164.

38   S. Trofimenko, *Scorpionates: The Coordination Chemistry of Polypyrazolylborate Ligands*, 1999.

39   G. J. Long, F. Grandjean and D. L. Reger, *Spin Crossover Transit. Met. Compd. I*, 2004, **233**, 91–122.

40   B. Hutchinson, L. Daniels, E. Henderson, P. Neill, G. J. Long and L. W. Becker, *J. Chem. Soc. Chem. Commun.*, 1979, 1003.

41   F. Grandjean, G. J. Long, J. D. Holcomb, B. B. Hutchinson, L. Ohlhausen and P. Neill, *Inorg. Chem.*, 1989, **28**, 4406–4414.

42   L. Salmon, G. Molnár, S. Cobo, P. Oulié, M. Etienne, T. Mahfoud, P. Demont, A. Eguchi, H. Watanabe, K. Tanaka and A. Bousseksou, *New J. Chem.*, 2009, **33**, 1283–1289.

43   D. L. Reger, J. R. Gardinier, J. D. Elgin, M. D. Smith, D. Hautot, G. J. Long and F. Grandjean, *Inorg. Chem.*, 2006, **45**, 8862–8875.

44   O. Iasco, M.-L. Boillot, A. Bellec, R. Guillot, E. Rivière, S. Mazerat, S. Nowak, D. Morineau, A. Brosseau, F. Miserque, V. Repain and T. Mallah, *J. Mater. Chem. C*, 2017, **5**, 11067–11075.

45   T. Mahfoud, G. Molnár, S. Cobo, L. Salmon, C. Thibault, C. Vieu, P. Demont and A. Bousseksou, *Appl. Phys. Lett.*, 2011, **99**, 2009–2012.

46   Y. Lin and S. A. J. Lang, *J. Heterocycl. Chem*, 1977, **14**, 345.

47 R. L. Fagaly, *Rev. Sci. Instrum.*, 2006, **77**, 101101.

48 J. Sanchez Costa, *Comptes Rendus Chim.*, 2018, **21**, 1121–1132.

49 N. F. Sciortino, K. A. Zenere, M. E. Corrigan, G. J. Halder, G. Chastanet, J. F. Létard, C. J. Kepert and S. M. Neville, *Chem. Sci.*, 2016, **8**, 701–707.

50 M. Sorai, *Spin Crossover Transit. Met. Compd. III*, 2004, 153–170.

51 K. Jonas, A. Jean-Paul, C. Renée, C. Epiphane, K. Olivier, J. G. Haasnoot, G. Françoise, J. Charlotte, A. Bousseksou, L. Jorge, V. François and G. V. Anne, *Chem. Mater.*, 1994, **6**, 1404–1412.

52 J. A. Wolny, V. Schünemann, Z. Németh and G. Vankó, *Comptes Rendus Chim.*, 2018, **21**, 1152–1169.

53 J. A. Wolny, R. Diller and V. Schünemann, *Eur. J. Inorg. Chem.*, 2012, 2635–2648.

54 O. Kahn, E. Codjovi, Y. Garcia, K. P. J. van, R. Lapouyade and L. Sommier, in *ACS Symp. Ser.*, 1996, vol. 644, pp. 298–310.

55 L. G. Lavrenova, O. G. Shakirova, V. N. Ikorskii, V. A. Varnek, L. A. Sheludyakova and S. V. Larionov, *Russ. J. Coord. Chem. Khimiya*, 2003, **29**, 22–27.

56 O. Kahn, J. Kröber and C. Jay, *Adv. Mater.*, 1992, **4**, 718–728.

57 A. Grosjean, L'UNIVERSITÉ BORDEAUX, 2013.

58 B. Gallois, J. A. A. Real, C. Hauw and J. Zarembowitch, *Inorg. Chem.*, 1990, **29**, 1152–1158.

59 E. C. Ellingsworth, B. Turner and G. Szulczewski, *RSC Adv.*, 2013, **3**, 3745.

60 E. Konig and K. Madeja, *Inorg. Chem.*, 1967, **6**, 48–55.

61 E. König and K. Madeja, *Chem. Commun. (London)*, 1966, **3**, 61–62.

62 H. Köppen, E. W. Müller, C. P. Köhler, H. Spiering, E. Meissner and P. Gütlich, *Chem. Phys. Lett.*, 1982, **91**, 348–352.

63 J. D. Oliver, B. B. Hutchinson, D. F. Mullica and W. O. Milligan, *Inorg. Chem.*, 1980, **19**, 165–169.

64 K. H. Sugiyarto, M. L. Scudder, D. C. Craig and H. A. Goodwin, *Aust. J. Chem.*, 2000, **53**, 755–765.

65 G. A. Craig, J. Sánchez Costa, G. Aromí, O. Roubeau and S. J. Teat, *Trans Aca*, 2013, **44**, 69.

66 L. A. Barrios, E. Peyrecave-Lleixà, G. A. Craig, O. Roubeau, S. J. Teat and G. Aromí, *Eur. J. Inorg. Chem.*, 2014, **2014**, 6013–6021.

67 T. D. Roberts, F. Tuna, T. L. Malkin, C. A. Kilner and M. A. Halcrow, *Chem. Sci.*, 2012, **3**, 349–354.

68 G. A. Craig, J. S. Costa, O. Roubeau, S. J. Teat and G. Aromí, *Chem. - A Eur. J.*, 2012, **18**, 11703–11715.

69 P. King, J. J. Henkelis, C. A. Kilner and M. A. Halcrow, *Polyhedron*, 2013, **52**, 1449–1456.

70   M. A. Halcrow, *Coord. Chem. Rev.*, 2005, **249**, 2880–2908.

71   J. Elhaïk, C. A. Kilner and M. A. Halcrow, *Dalt. Trans.*, 2006, **5**, 823–830.

72   E. W. Müller, H. Spiering and P. Gütlich, *Chem. Phys. Lett.*, 1982, **93**, 567–571.

73   L. L. Merritt and E. Schroeder, *Acta Crystallogr.*, 1956, **9**, 801–804.

74   C. Akers, S. W. Peterson and R. D. Willett, *Acta Cryst*, 1968, **24**, 1125.

75   Z. Khoshtarkib, A. Ebadi, R. Ahmadi and R. Alizadeh, *Acta Crystallogr. Sect. E Struct. Reports Online*, 2009, **65**, o1586–o1586.

76   T. Fujihara, H. Suzuki and A. Nagasawa, *Acta Crystallogr. Sect. E Struct. Reports Online*, 2006, **61**, 1867–1868.

77   C. Bartual-Murgui, C. Codina, O. Roubeau and G. Aromí, *Chem. - A Eur. J.*, 2016, **22**, 12767–12776.

Chapter 6: Conclusions and Prospects

6.1. Conclusions and Prospects

Mechanochemistry represents a viable approach to the synthesis and discovery of spin crossover (SCO) materials. Mechanochemical synthesis has, for the first time, been used to synthesise a variety of SCO-active materials, which displayed SCO-activity consistent with previously reported solution-state synthesised materials (Chapter 3). The effects of mechanochemical synthesis were considered and investigated, with particular consideration on the role of crystal quality, particle size and solvent contributions. It was clear that current understandings of the factors contributing to SCO-activity and the role of cooperativity are not entirely conclusive (Chapter 3). The use of solid-state metathesis (SSM) as a route to materials inaccessible to solution state techniques was also explored with the successful exchange of anions in the $[Fe(atrz)_3]Cl_2$ system (Chapter 4). Finally, a screening protocol was proposed, tested, and optimised for the use of mechanochemical synthesis to rapidly screen potential SCO-active materials, with both thermochromic and non-thermochromic materials considered (Chapter 5).

The synthesis of previously reported SCO-active materials in three families; 0-D molecular systems, 1-D triazoles and 2-/3-D Hofmann-type clathrates was successfully carried out (Chapter 2). Synthesis of the 0-D molecular system $Fe(phen)_2(NCS)_2$ followed a similar synthetic route to standard solution-state synthesis in which the SCO-inactive complex $[Fe(phen)_3](SCN)_2$ was first prepared, followed by thermal conversion into the SCO-active form, yielding a product which displayed SCO-activity consistent with previous literature reports. Direct synthesis of 1-D triazole systems $[Fe(Htrz)_3](BF_4)_2$ and $[Fe(atrz)_3]SO_4$ using mechanochemistry was presented. Synthesis of $[Fe(Htrz)_3](BF_4)_2$ yielded a polycrystalline mixture of different known polymorphs, attempts to isolate specific polymorphs was not undertaken. The mechanochemically synthesised complex $[Fe(atrz)_3]SO_4$ displayed SCO-activity consistent with previous literature reports. Synthesis of the 2-D Hofmann-type clathrate $Fe(4-phpy)_2[Ni(CN)_4]$ required the use of liquid assisted grinding (LAG), in which a small amount of water was added to the grinding process, in order to obtain a SCO-active product. This was attributed the degree of hydration being integral for SCO-activity rather than an intrinsic requirement for mechanochemical synthesis of complex 2-/3-D materials.

The 3-D Hofmann-type clathrate complex $Fe(pz)[Au(CN)_2]_2$ was successful without the requirement of LAG.

The effects of mechanochemical synthesis on SCO properties presented a relatively complex perspective (Chapter 3). The proposed reduction in crystal quality, resulting from mechanochemical synthesis, did not result in consistent effects on SCO properties across all materials investigated. Previous studies on the effects of grinding solution-synthesised SCO complexes have presented detrimental effects of grinding, with substantial reductions in transition temperatures, hysteresis width and abruptness of transition. However, previous studies focused on the post-synthetic long duration high energy milling of materials, whereas synthetic grinding of materials did not present such severe consequences. Comparison between solution-state and mechanochemically synthesised samples did present a general trend in which $T_{1/2}\uparrow$ and $T_{1/2}\downarrow$ shifted to slightly lower temperatures and transitions became slightly more gradual. But it was also strongly sample dependent and in the case of $[Fe(atrz)_3]SO_4$ the mechanochemical sample displayed a larger ΔT. During investigation of the complex $[Fe(atrz)_3](BF_4)_2$, a different polymorph was observed in mechanochemical synthesis, potentially opening research into polymorphs that can be difficult to prepare using solution-state techniques.

As a route to introduce potentially inaccessible anions to the triazole family of SCO materials, SSM was investigated (Chapter 4). The complex $[Fe(atrz)_3]Cl_2$ was prepared by mechanochemistry, yielding a product with consistent batch-to-batch properties. The Cl anion was then exchanged using post-synthetic grinding with NaX salts (where X = Br, I). The degree of exchange was assessed and analysis with EDX proved complete exchange had occurred. Traditional application of SSM relies on a large change in enthalpy of reaction ($\Delta H°_{rxn}$) however the nature of the 1-D triazole 'infinite' chains prevented determination of enthalpy of formation for the triazole complexes. As such, as alternative metric was determined to predict the potential for exchange. It was determined that the change in total lattice potential (U_{POT}) for the sodium salts represented the greatest degree of change in energy. Therefore, ΔU_{POT} was used as a metric to predict the likelihood of exchange. This theory was confirmed using NaF in which exchange was expected not

to occur. Further exchange with NaSCN, NaBF$_4$ and NaReO$_4$ was undertaken, with partial exchange occurring.

Using mechanochemistry as a synthetic method changes the rate-limiting step of discovery of SCO materials. Prior to mechanochemistry, the limiting step was often synthesis of materials. Therefore, the analysis and characterisation of the synthesised materials was not a significant factor affecting discovery of novel materials. With mechanochemistry, it is possible to synthesise materials within 5 minutes of grinding in a pestle and mortar. This drastically alters the rate limiting step in the procedure, now identification of promising materials becomes the more onerous task. A screening protocol was devised which sought to streamline the screening procedure for both thermochromic and non-thermochromic materials, in an attempt to increase the rate of identification of promising materials whilst minimising potential for missing SCO-activity. The procedure was developed and tested against a wide range of materials in order to test its viability (Chapter 5).

The future prospects for the use of mechanochemistry in SCO are extremely promising. The ability to synthesise materials in a fraction of the time of traditional approaches can serve to drastically increase the potential for novel material discovery. The majority of work presented in this study was carried out using neat grinding of reagents. But, using techniques such as LAG it would be possible to further probe the solvent effects in materials, the effects of which have already be shown to be significant. The potential for introduction of previously inaccessible anions by using SSM could potentially create a surge of novel materials. A further avenue which was briefly touched upon is the potential for polymorph discovery with different SCO-properties and the synthesis of polymorphs inaccessible to traditional synthetic methods. This could also be investigated using LAG and variation of mechanochemical synthetic parameters such as milling duration.

Appendix A – Chapter 2
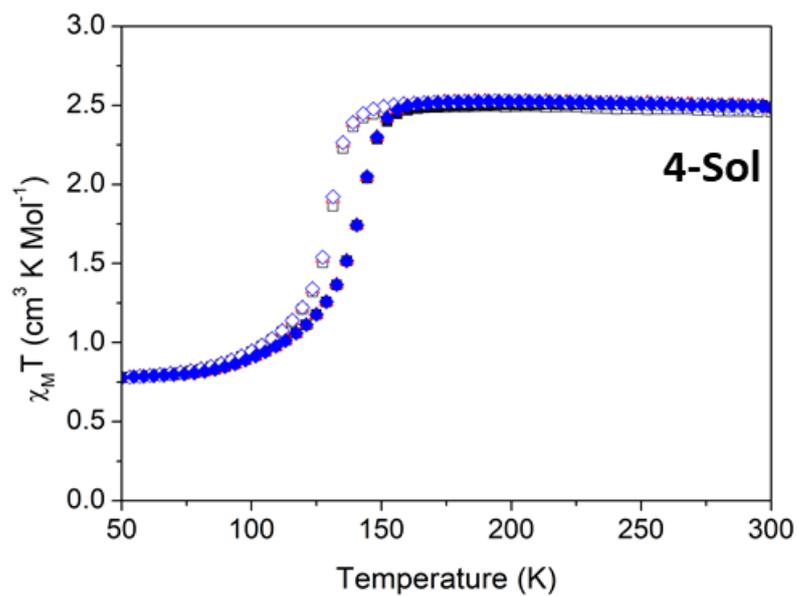
Additional SQUID
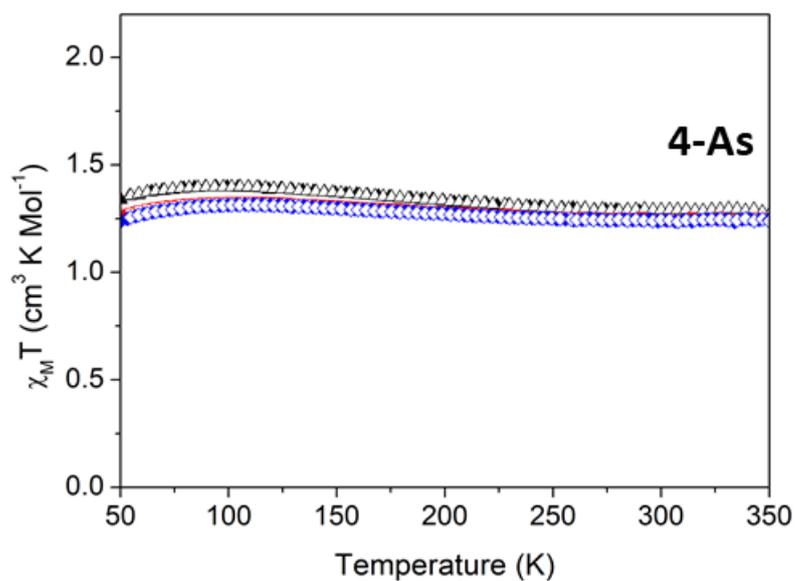
Figure A.1: Temperature dependent SQUID data for **4-As** three cycles: Cycle 1 Heating ■ and Cooling □, Cycle 2 Heating ▲ and Cooling △, Cycle 3 Heating ♦ and Cooling ◊.
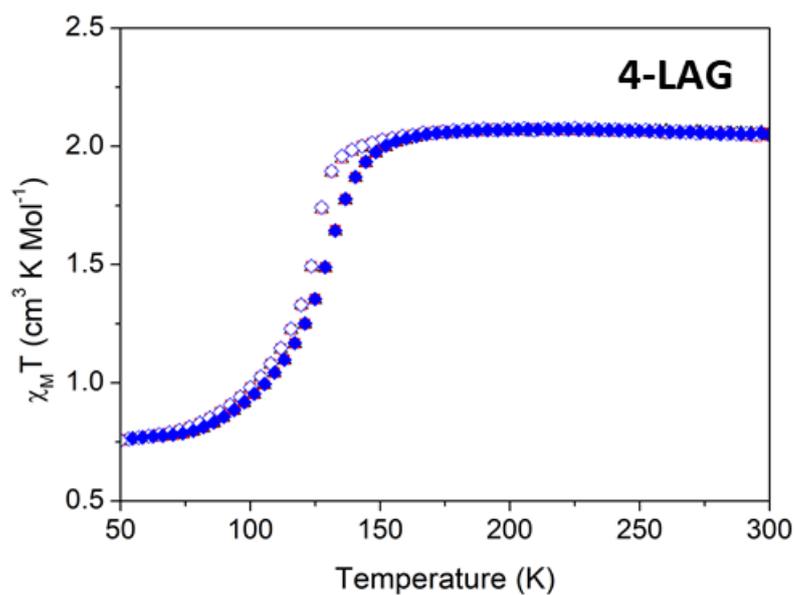
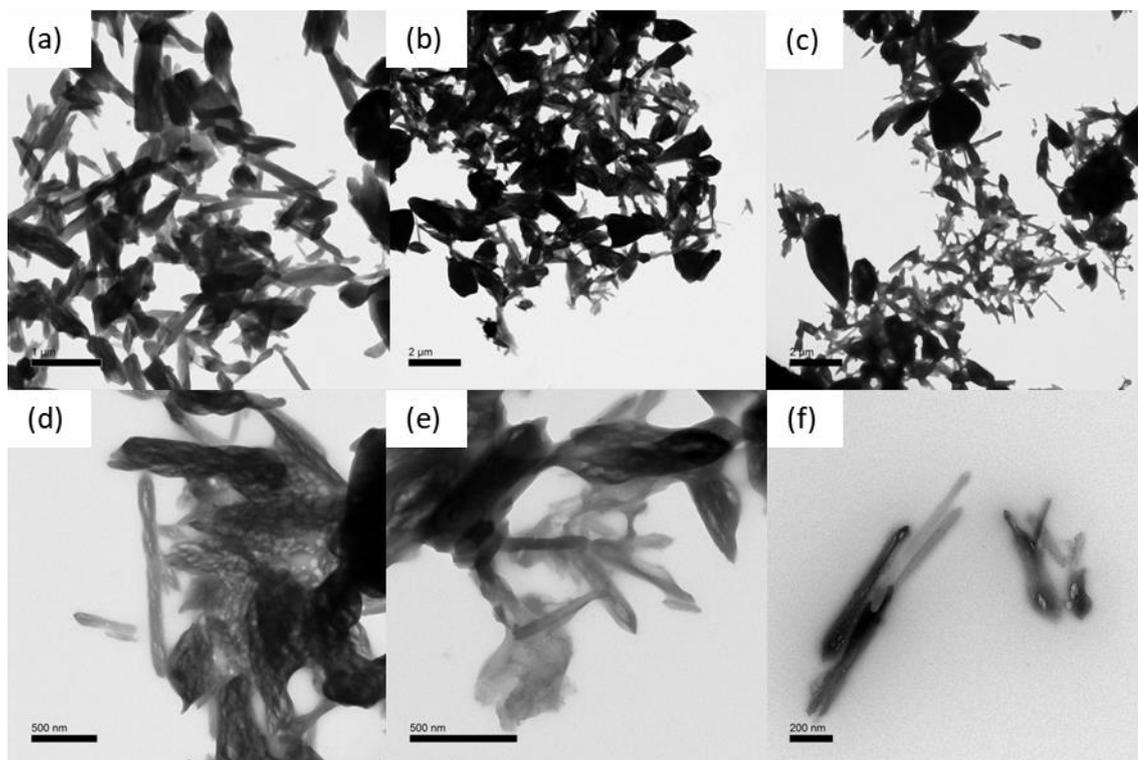**Figure A.2:** Temperature dependent SQUID data for **4-LAG** three cycles: Cycle 1 Heating ■ and Cooling □, Cycle 2 Heating ▲ and Cooling △, Cycle 3 Heating ♦ and Cooling ◊.

Figure A.3: Temperature dependent SQUID data for **4-Sol** three cycles: Cycle 1 Heating ■ and Cooling □, Cycle 2 Heating ▲ and Cooling △, Cycle 3 Heating ◆ and Cooling ◊.

Additional TEM images

3-Sol

Figure A. 4: Additional TEM images for compound **3-Sol**.

3-Mech
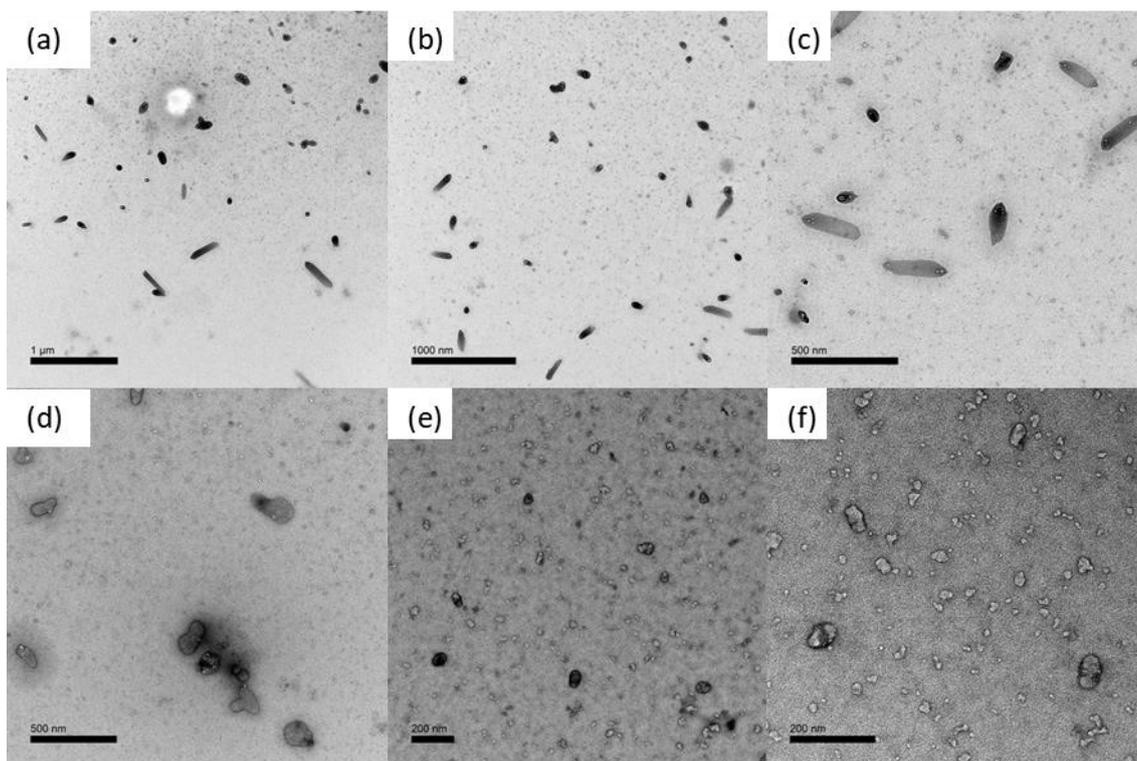
Figure A.5: Additional TEM images for compound **3-Mech**.

5-Sol
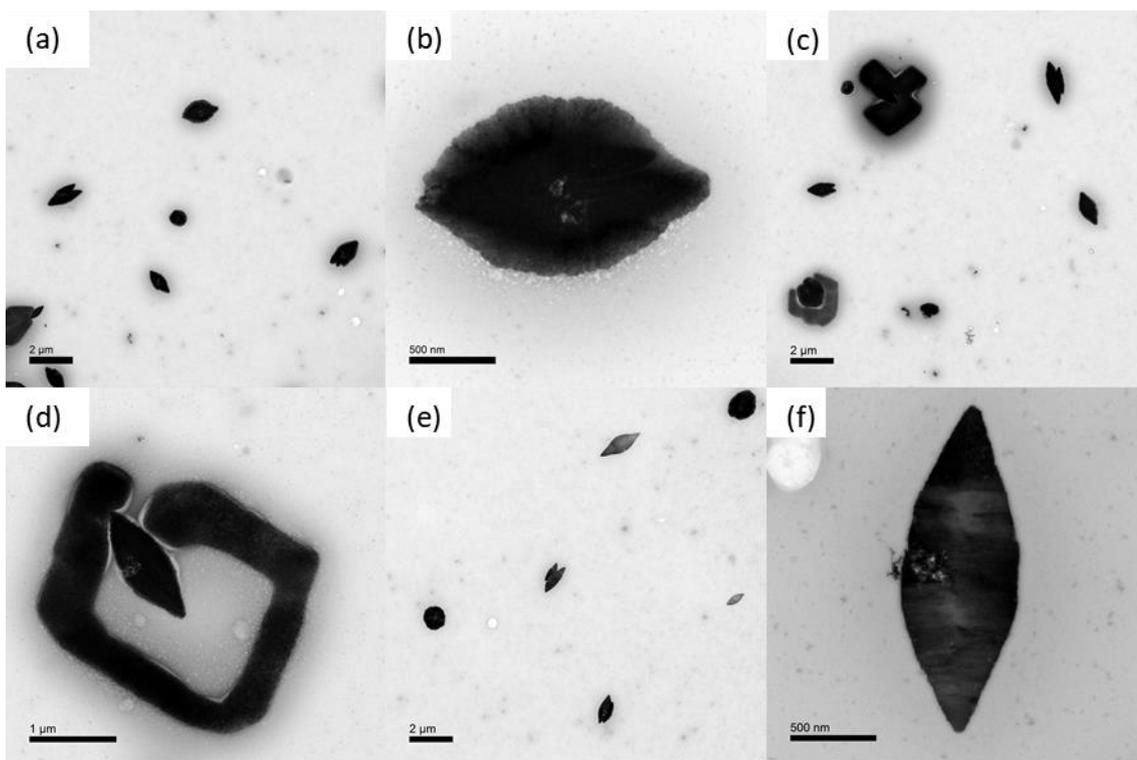
Figure A.6: Additional TEM images for compound **5-Sol**.

5-Mech
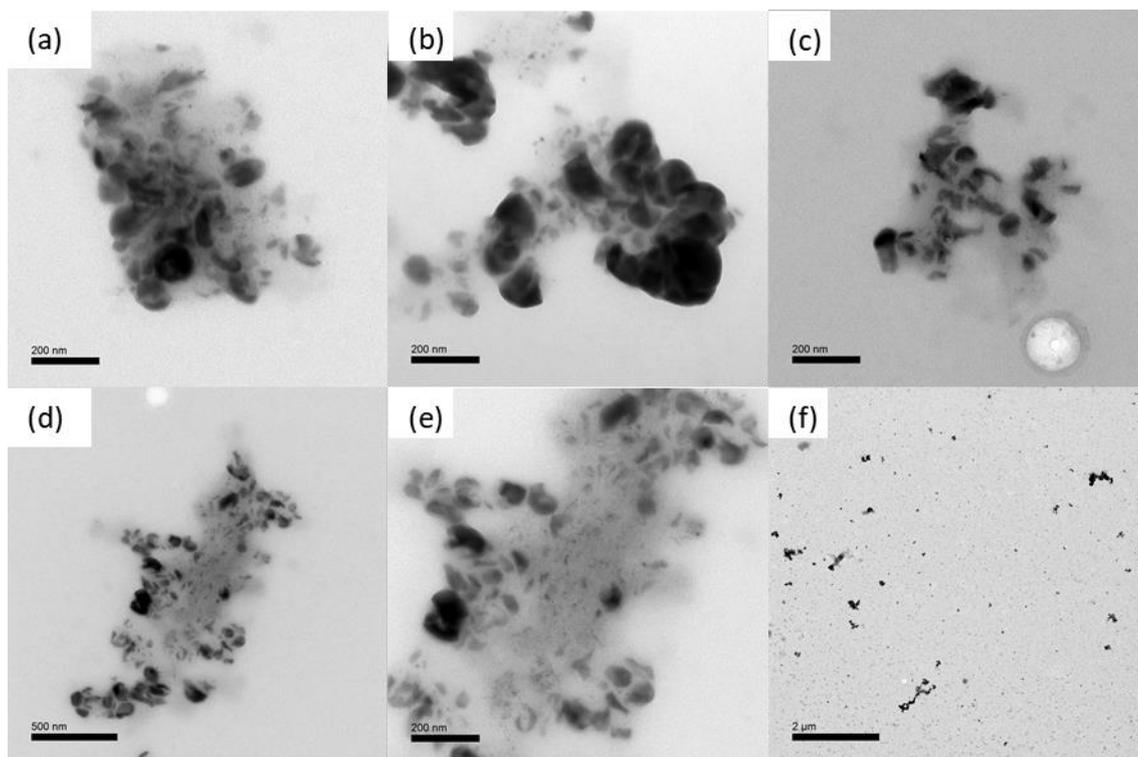
Figure A.7: Additional TEM images for compound 5-Mech.

6-Sol
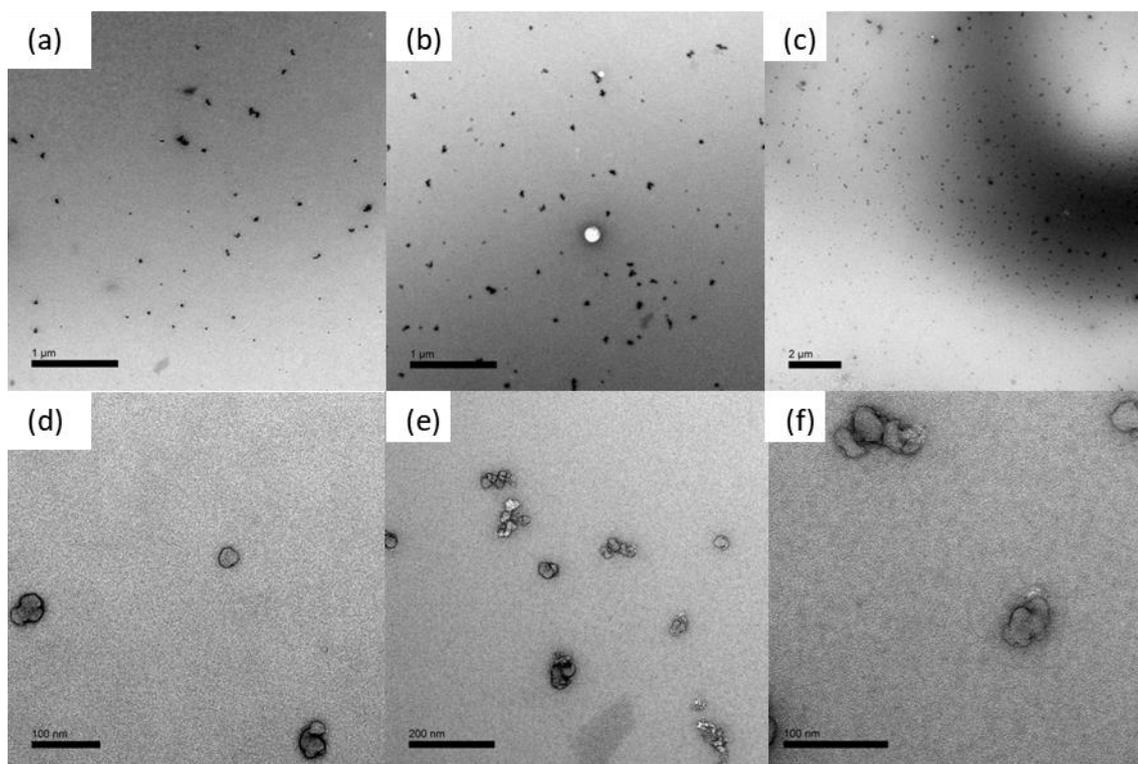
Figure A.8: Additional TEM images for 6-Sol

6-Mech
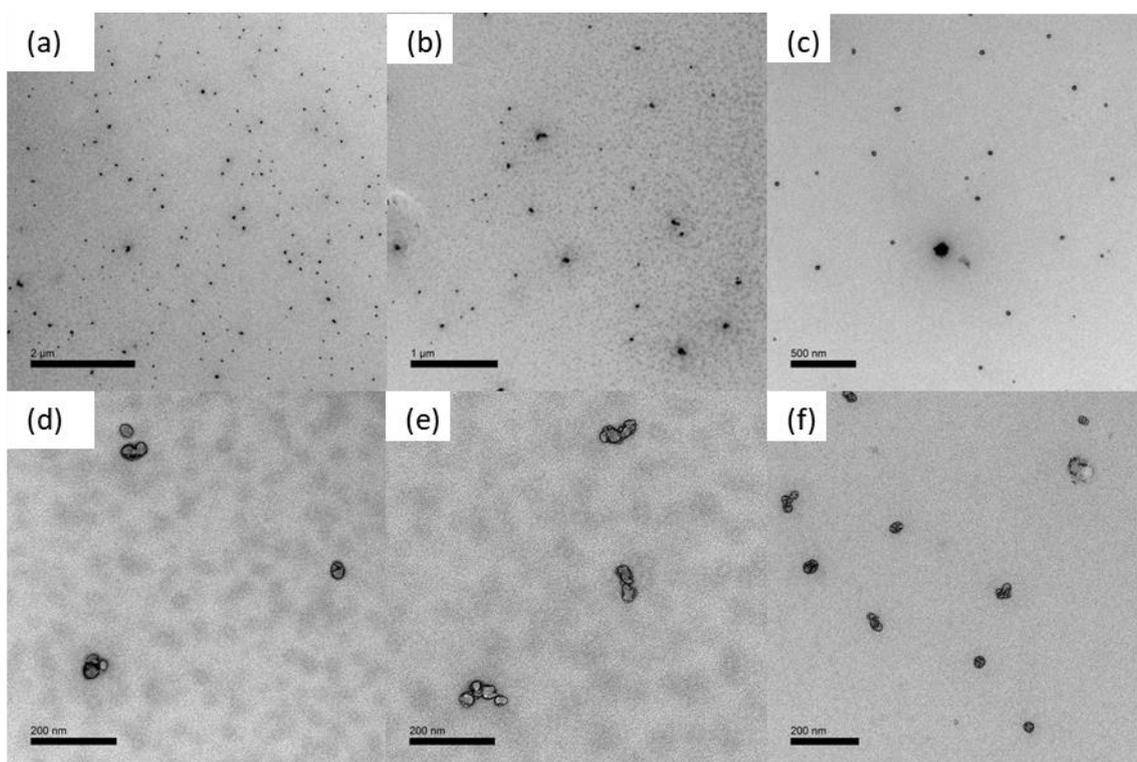
Figure A.9: Additional TEM images for **6-Mech**.

6-BM10
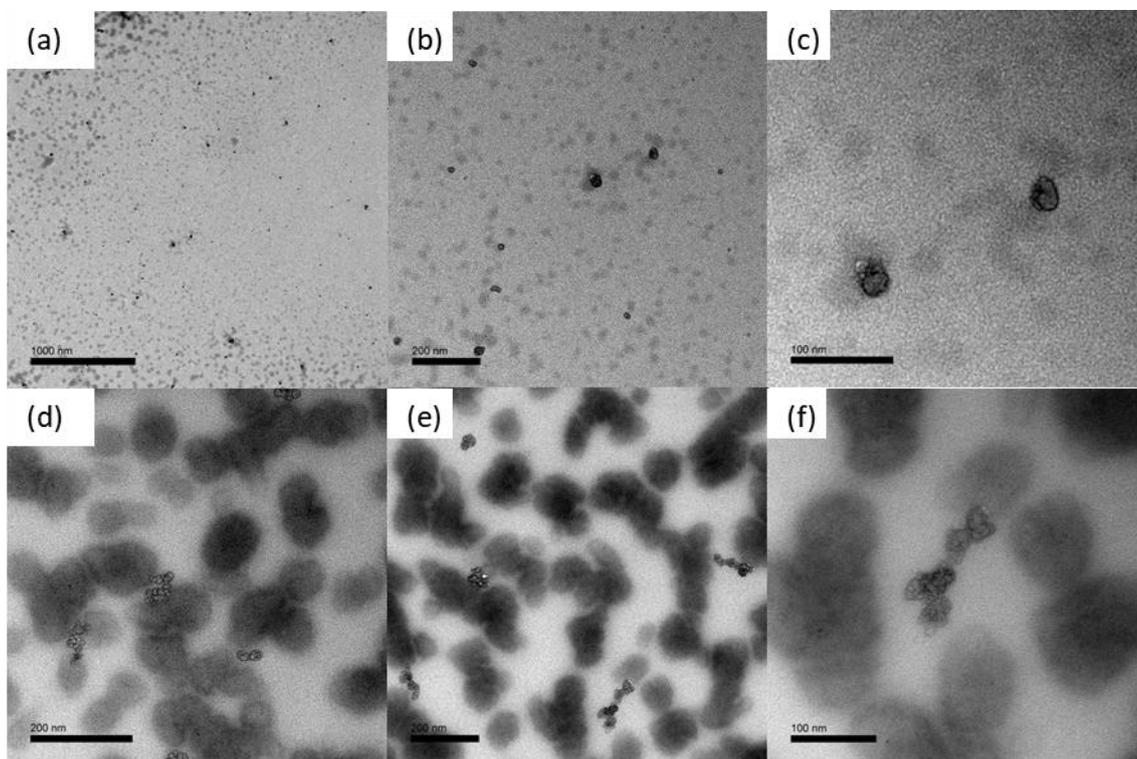
Figure A.10: Additional TEM images for **6-BM10**.

6-BM90
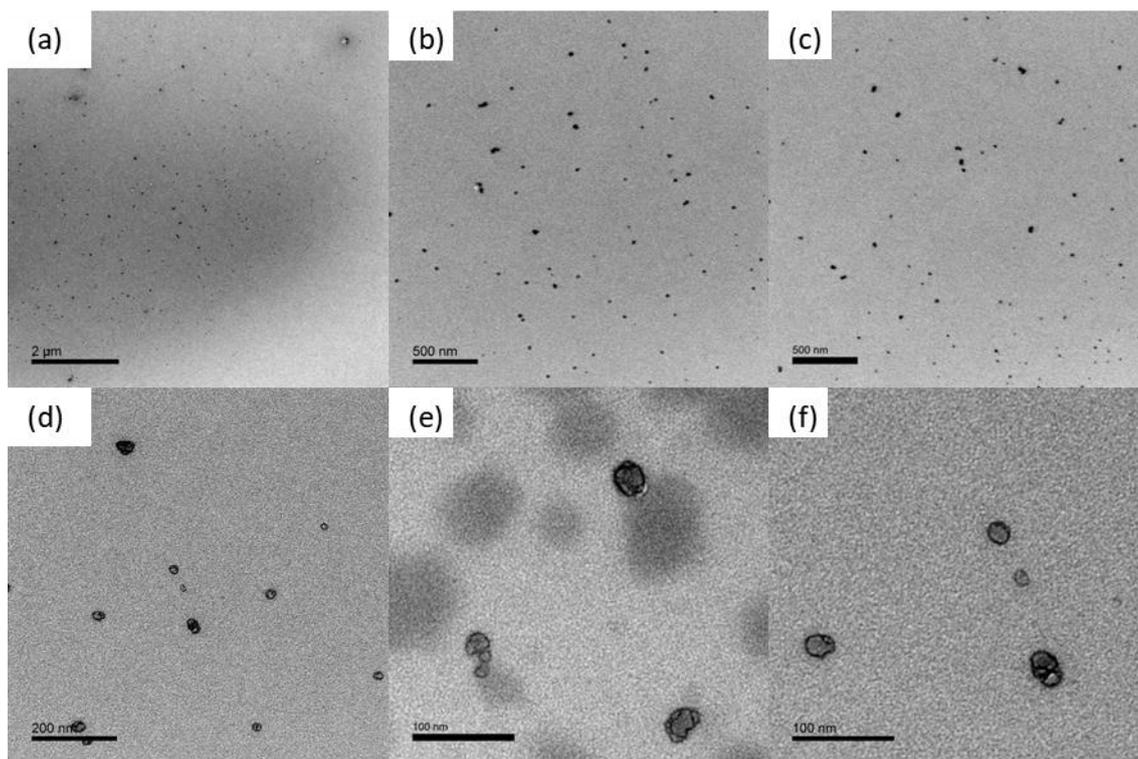
Figure A.11: Additional TEM images for **6-BM90**.

Appendix B – Chapter 5

NMR: 3-bpp and Derivatives
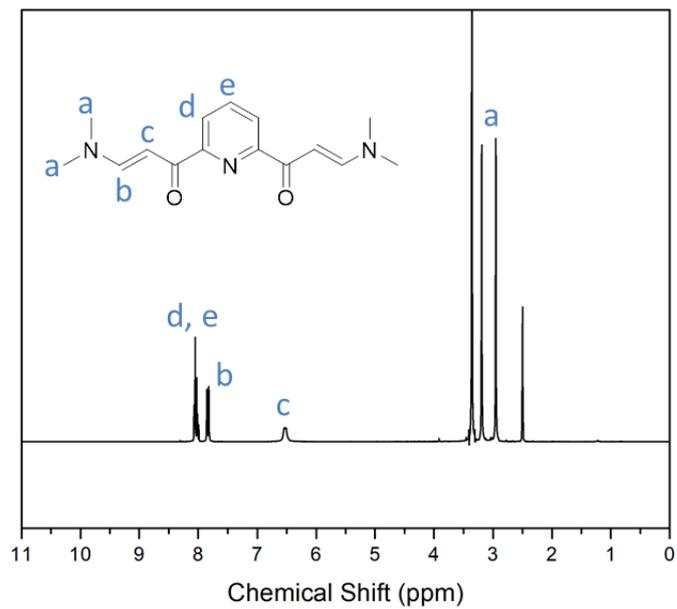
Figure B.1: ^{1}H NMR (DMSO-d[6]) for **3-bpp-intermediate**.
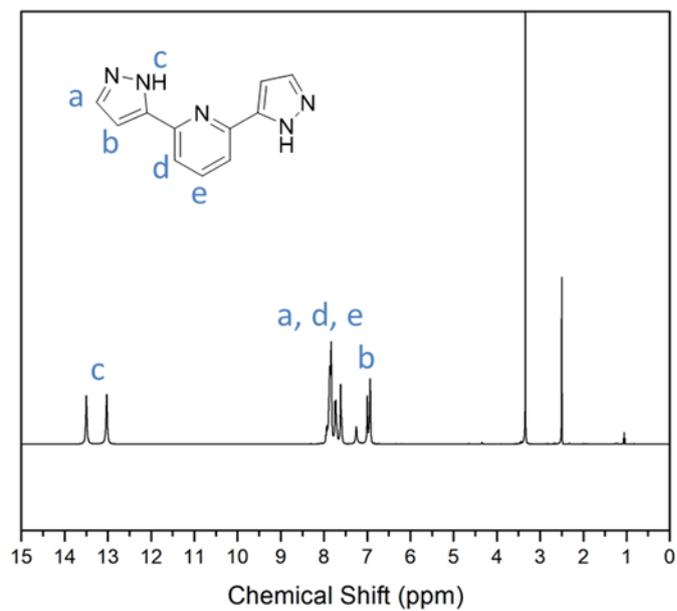
Figure B.2: ^{1}H NMR (DMSO-d[6]) for **3-bpp**.
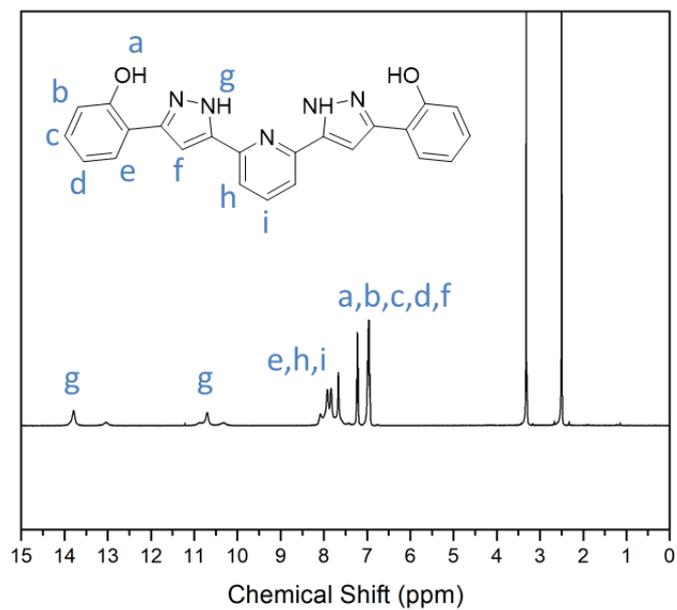
Figure B.3: ^{1}H NMR (DMSO-d[6]) for **3-bpp-PhOH**.
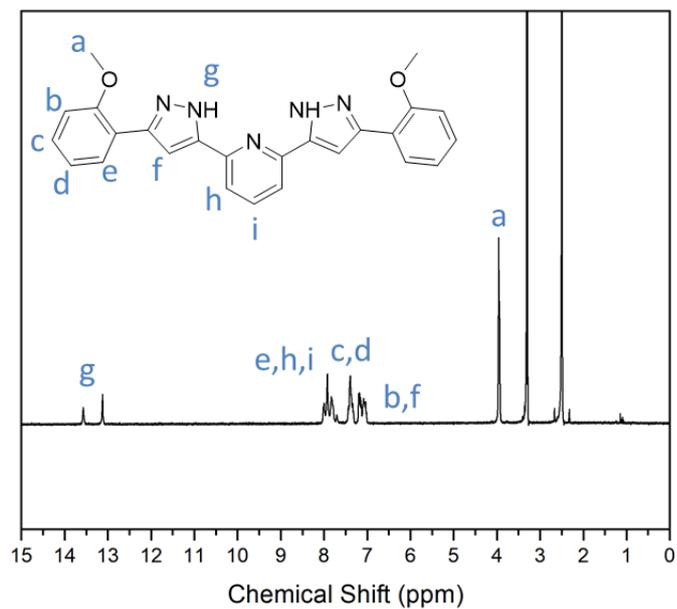
Figure B.4: ^{1}H NMR (DMSO-d[6]) for **3-bpp-PhOCH₃**.
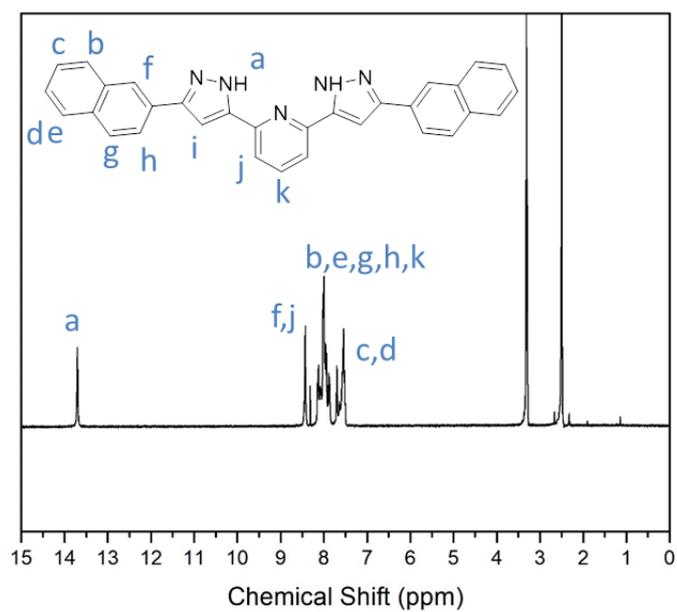
Figure B.5: ^{1}H NMR (DMSO-d[6]) for **3-bpp-Napth**.

4,7-dimethyl-1,10'-phenathroline VT-Raman
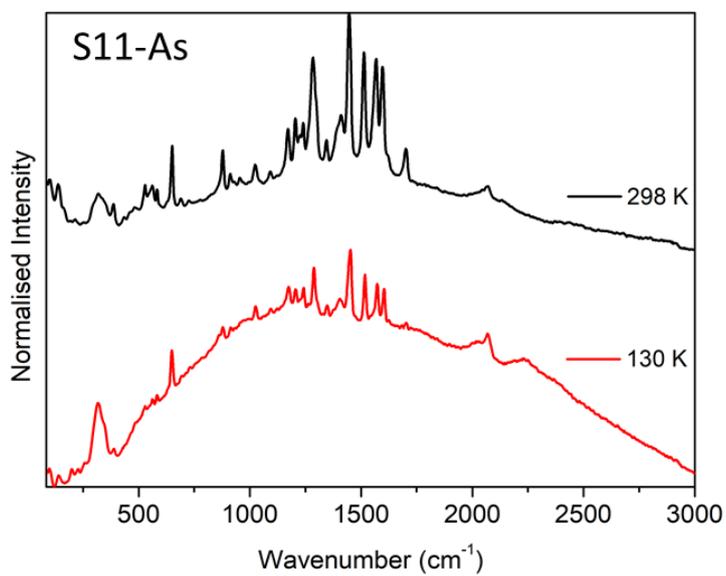
Figure B.6: Raman spectra at 298 K (top) and 123 K (Bottom) for **S11-As**.

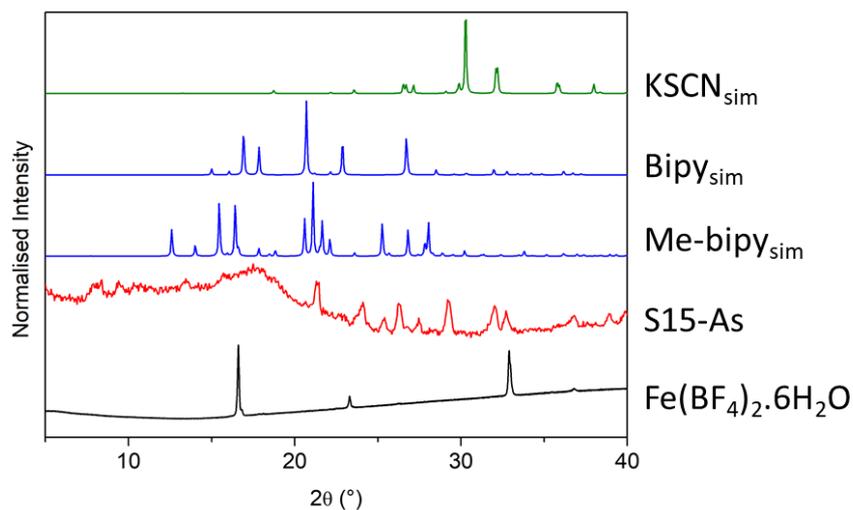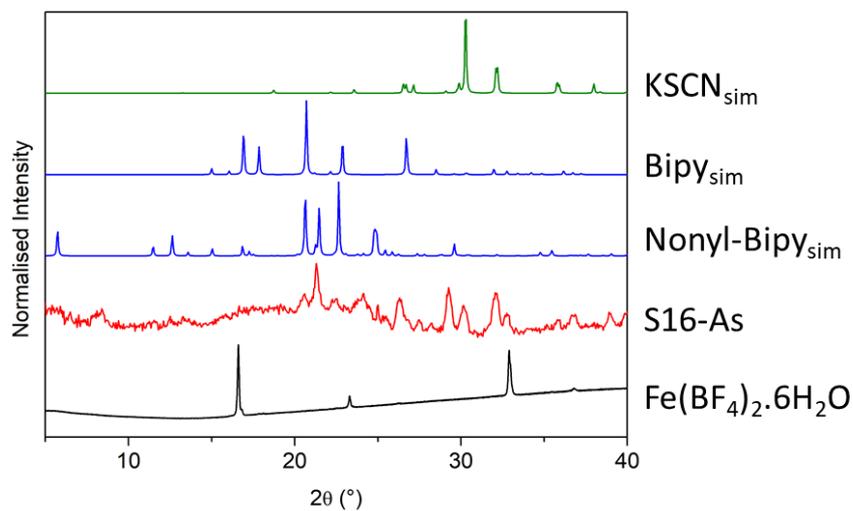# Heteroleptic bipy and Derivative Screening

Figure B.7: Comparison of normalised PXRD data for Top to bottom: KSCN, simulated from literature (ICSD-36073),[1] 2,2'-bipyridine (CSD Code: BIPYRL),[2] 5,5'-dimethyl-2,2'-bipyridine (CSD Code: POWQAU),[3] **S15** and Fe(BF$_4$)$_2$.6H$_2$O.

Figure B.8: Comparison of normalised PXRD data for Top to bottom: KSCN, simulated from literature (ICSD-36073),[1] 2,2'-bipyridine (CSD Code: BIPYRL),[2] 4,4'-dinonyl-2,2'-bipyridine (CSD Code: FOHFAK),[4] **S16** and Fe(BF$_4$)$_2$.6H$_2$O.
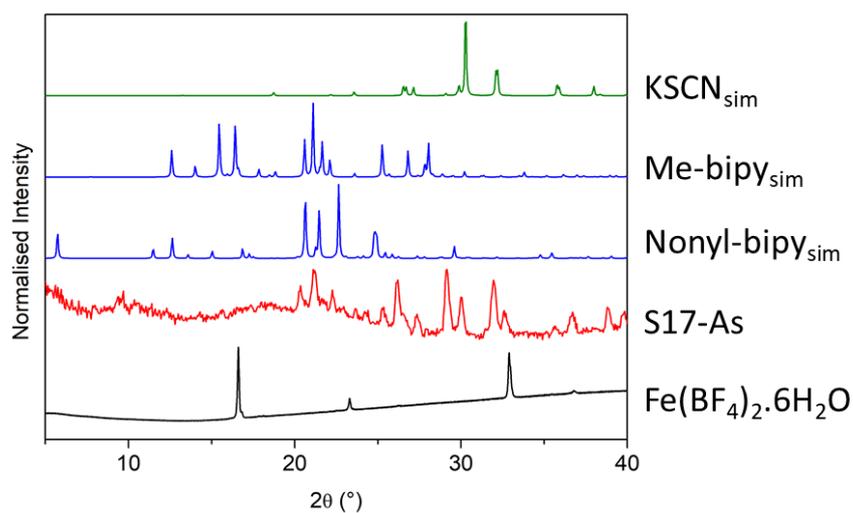
Figure B.9: Comparison of normalised PXRD data for Top to bottom: KSCN, simulated from literature (ICSD-36073),[1] 5,5'-dimethyl-2,2'-bipyridine (CSD Code: POWQAU),[3] 4,4'-dinonyl-2,2'-bipyridine (CSD Code: FOHFAK),[4] **S17** and Fe(BF$_4$)$_2$.6H$_2$O.

References

1   C. Akers, S. W. Peterson and R. D. Willett, Acta Cryst, 1968, 24, 1125.

2   L. L. Merritt and E. Schroeder, Acta Crystallogr., 1956, 9, 801–804.

3   Z. Khoshtarkib, A. Ebadi, R. Ahmadi and R. Alizadeh, Acta Crystallogr. Sect. E Struct. Reports Online, 2009,65, 01586-01586.

4   T. Fujihara, H. Suzuki and A. Nagasawa, Acta Crystallogr. Sect. E Struct. Reports Online, 2006, 61, 1867–1868.